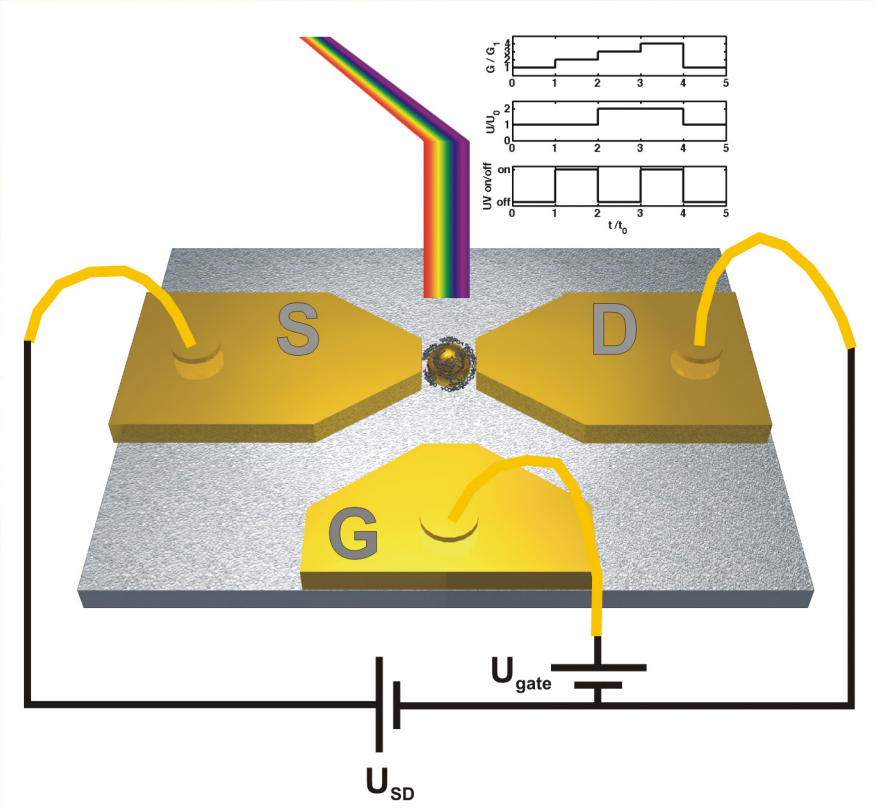

Optical and electrical addressing in molecule-based logic circuits

Marcel Manheller

Mitglied der Helmholtz-Gemeinschaft

JÜLICH
FORSCHUNGSZENTRUM

Schriften des Forschungszentrums Jülich
Reihe Information / Information Band / Volume 21

Forschungszentrum Jülich GmbH
Peter Grünberg Institute (PGI)
Eletronic Materials (PGI-7)

Optical and electrical addressing in molecule-based logic circuits

Marcel Manheller

Schriften des Forschungszentrums Jülich
Reihe Information / Information Band / Volume 21

ISSN 1866-1777 ISBN 978-3-89336-810-5

Bibliographic information published by the Deutsche Nationalbibliothek.
The Deutsche Nationalbibliothek lists this publication in the Deutsche Nationalbibliografie; detailed bibliographic data are available in the Internet at http://dnb.d-nb.de.

Publisher and Distributor:	Forschungszentrum Jülich GmbH Zentralbibliothek 52425 Jülich Phone +49 (0) 24 61 61-53 68 · Fax +49 (0) 24 61 61-61 03 e-mail: zb-publikation@fz-juelich.de Internet: http://www.fz-juelich.de/zb
Cover Design:	Grafische Medien, Forschungszentrum Jülich GmbH
Printer:	Grafische Medien, Forschungszentrum Jülich GmbH
Copyright:	Forschungszentrum Jülich 2012

Schriften des Forschungszentrums Jülich
Reihe Information / Information Band / Volume 21

D 82 (Diss., RWTH Aachen University, 2012)

ISSN 1866-1777
ISBN 978-3-89336-810-5

The complete volume is freely available on the Internet on the Jülicher Open Access Server (JUWEL) at http://www.fz-juelich.de/zb/juwel

Optische und elektrische Adressierung in molekülbasierten logischen Schaltungen

Moderne industrielle Herstellungsmethoden ermöglichen Strukturgrößen elektronischer Schaltkreise mit lateralen Dimensionen von momentan bis zu 22 nm. Eine weitere Verkleinerung dieser Bauteile ist nicht ohne eine fundamentale Veränderung elektronischer Eigenschaften über einen bestimmten Grenzwert hinaus möglich. Organische Moleküle bieten neue Möglichkeiten im Nanometerbereich. Der erste Schritt für die Entwicklung molekularer Elektronik ist die Definition zuverlässiger elektrischer Kontakte an einzelnen Molekülen. Es hat sich gezeigt, dass dies große Schwierigkeiteiten mit sich bringt. Aus diesen Gründen zielen die in dieser Arbeit vorgestellten Experimente darauf ab, zuverlässige Kontakte zwischen molekülbenetzten Nanopartikeln und metallischen Elektroden zu entwickeln und in solch einer Anordnung von Nanopartikel zwischen Elektroden logische Schaltkreise nachzuahmen.
Um dieses Ziel zu realisieren, wurden Nanoelektroden mit einem Abstand von nur wenigen Nanometern (3±1 nm) verwendet, welche in einem optimierten Elektronenstrahl-Lithographie-Prozess, unter Verwendung des Vektor-Grafik-Elektronenstrahlschreibers EBPG5000+ von Vistec, entwickelt wurden. Diese Präzision wurde durch ein optimiertes Zweilagen-Lacksystem in Kombination mit einem angepassten Entwicklersystem erzielt. Des Weiteren wurde eine optimale Geometrie der Elektroden, unter Einbeziehung von Nahbereichs-Streueffekten, erarbeitet.
In dieser Arbeit werden einzelne Nanopartikel mit einem Durchmesser von wenigen Nanometern in Elektroden mit einem geringeren Abstand immobilisiert. Die Immobilisierung der geladenen oder ungeladenen Nanopartikel geschieht durch Dielektrophorese, d.h. unter Anlegen einer AC, oder DC, Spannung über die Nanoelektroden. In dieser Konfiguration entstehen zwei Tunnelkontakte, welche auf wenigen (5-10) Molekülen pro Tunnelkontakt basieren. Im Fokus der Arbeit steht die Charakterisierung der Tunnelkontakte und die dezidierte Analyse der beteiligten Transportmechanismen, wie Arrhenius-, Superaustausch-, Granular-metal- oder auf Tunneln basierenden Transport. Die Leitfähigkeit des immobilisierten Nanopartikels ist entscheidend davon abhängig wie perfekt der Nanopartikel die Nanoelektroden ausfüllt. Molekülparameter wie die Höhe der Tunnelbarriere und das eventuell noch vorhandene Vakuumgap werden mittels einer iterativen Simmons Fitroutine und der Methode "Transition Voltage Spectroscopy" bestimmt. Erstaunlicherweise waren die Transporteigenschaften über den Elektrode/Molekül-Nanopartikel-Molekül/Elektrode Kontakt durch die molekularen Eigenschaften dominiert. Rastertunnel mikroskopische Messungen an den verwendeten Molekülen haben erstaunliche Übereinstimmungen gezeigt und haben die Zuordnung der molekularen Energieniveaus ermöglicht. Bei Nanopartikeln mit einem Durchmesser von weniger als 5 nm wurde Coulomb Blockade, "ein elektrostatisches Phänomen", bereits bei Raumtemperatur beo-bachtet. Coulomb Blockade Diamanten wurden an einem in Transistorgeometrie vermessenen Nanopartikel beobachtet. Es wurden unter anderem funktionalisierte Moleküle verwendet, welche unter Einstrahlung von UV-Licht die atomare Anordnung im Molekül reversibel verändern (Photoisomere). Die zwei Isomere zeigen dramatisch unterschiedliche Transporteigenschaften. Über die Anwendung als lichtgesteuerter Schalter hinaus kann dieses System mit geeigneter Wahl der Parameter einen kompletten Full-Adder-Schaltkreis ersetzen. Es wurde nicht nur eine Verkleinerung bestehender CMOS-Bausteine angestrebt, sondern die Implementierung komplexer logischer Schaltkreise in einem Baustein.

Optical and electrical addressing in molecule based logic circuits

By using state of the art industrial production methods it is possible to fabricate device geometries with lateral dimensions of 22 nm. A further reduction of these components is accompanied by a fundamental change of electronic properties, if a certain threshold is overcome. Organic molecules applied as functional components provide new possibilities in the nanometer scale. The first step, which is necessary for the development of molecular electronics, is the definition of reliable electrical contacts to individual molecules. It has been shown that this implicates major difficulties.Therefore, the aimed target of the presented experiments is to develop reliable contacts between molecular capped nanoparticles and metallic electrodes, and to mimic logic circuits in such an arrangement of nanoparticles and electrodes.

In order to realize this aim nano-electrodes with a distance of only a few nanometers (3 ± 1 nm) were developed in an optimized electron-beam lithography process, using the vector graphics EBPG5000+ electron beam writer from Vistec. This precision was achieved by developing an optimized two layer E-beam process, in combination with a customized system of developers. Moreover, an optimal geometry of the electrodes was elaborated including short-range scattering effects in the considerations.In this work, individual nanoparticles with a diameter of a few nanometer were immobilized between electrodes with a shorter tip separation. Charged and uncharged nanoparticles were immobilized applying dielectrophoretic trapping, i.e. the application of an AC, or DC, voltage over the nanoelectrodes. In this configuration the obtained tunnel junctions are based on a few (5-10) molecules per tunnel junction. The focus of this work is the characterization of tunnel junctions and the thoroughly analysis of the transport mechanisms involved, such as Arrhenius, super-exchange, granular metal-based transport or tunneling. The total conductivity across the gap formed by the nanoelectrodes is shown to be critically dependent upon how perfectly the NP fills the gap. For nanogaps partially and completely filled with a nanoparticle, respectively, representative measurements are shown. From transport measurements characteristic molecule parameters as the tunneling barrier height of the BP3 molecules and the remaining vacuum gap-width are obtained by a combination of Simmons fit and transition voltage spectroscopy. Surprisingly, the transport properties of the 'electrode/ molecule-nanoparticle-molecule/electrode'-contact were dominated by molecular properties. Scanning tunneling microscopic measurements on the applied molecules have shown astonishing similarities in the $I(U)$ characteristics. Furthermore, the observed energy levels could be assigned to molecular energy levels. Nanoparticles with a diameter of less than 5 nm have shown Coulomb blockade, an electrostatic phenomenon, already at room temperature. Coulomb blockade diamonds were observed in nanoparticle based devices with transistor geometry.Among others functionalized, photo-isomeric molecules, which reversibly change the atomic arrangement under irradiation of UV light, were applied. The two isomer conformations show dramatically different transport properties.Beyond the application as a light-controlled switch with such a type of device it is also possible to mimic, with a suitable choice of parameters, a complete full adder circuit. The aim in this work was not only a reduction of existing bricks of current CMOS devices, but the implementation of complex logic circuits in a single bricked unit.

Acknowledgement

It was a great experience to work in a research center, which offers a lot of scientific opportunities and a lot of kind persons supporting my work in a scientific or technical manner.
First of all I would like to thank Prof. Rainer Waser for the continuous interest of research in the field of Molecular Electronics at his institute and for providing the infrastructure.
Special credit is to my supervisor, Dr. Silvia Karthäuser for her ideas, which initiated this work, and hours of discussion that helped to understand my results. I am grateful for her personal and scientific report.
I have benefited a lot of the cooperation with Prof. Ulrich Simon and Dr. Melanie Homberger, firstly of the fruitful discussions we had and the synthesis of biphenyl-propanethiol capped gold nanoparticles.
Thanks are also to:
- Prof. Itamar Willner for the synthesis of spiropyrane capped gold nanoparticles,
- Prof. Francoise Remacle for the theoretical analysis of spiropyrane molecules,
- Prof. Rainer Weinkauf for spectroscopic measurements on spiropyrane based systems and fruitful discussions,
- Prof. Thomas Halfmann for technical support with the optical equipment
- Prof. Reinhard Carius for the theoretical analysis of slow plasmon polaritons in a nanoparticle-nanoelectrode system.
A thank you to Prof. Hermann Kohlstedt for the continuous interest he showed in my work and person. My special appreciation goes to my colleague Alexander Soltow for performing the STM and UV-VIS measurements, which created a strong affirmation of my work.
For the friendly working condition I would like to thank Christina Lennartz, Peter Kowalzik, Ninet Babajani and Alexander Soltow. Further afield, I am extremely grateful for my parents continuous support and facilitation of my education. Last but not least a big thank you is to my wife Annika and my kids Fiona and Miro for their never ending support, infinite patience and love.

Die Natur ist so gemacht, dass sie verstanden werden kann.

Werner Heisenberg

Achtung! Jetzt gibt es nur zwei Möglichkeiten:
Entweder es funktioniert oder es funktioniert nicht.

Lukas in "Jim Knopf und Lukas, der Lokomotivführer"

Contents

1. Introduction **1**

2. Theoretical description of a nanoparticle-nanoelectrode system **9**

2.1. Tunneling in a molecule-based device 9

2.1.1. Charge transport based on the Simmons model 10

2.1.2. Transition Voltage Spectroscopy 14

2.1.3. Orbital mediated transport 18

2.2. Influence of a surface dipole moment on the tunneling barrier height . . . 19

2.3. Temperature-dependent transport mechanisms 22

2.3.1. Temperature-dependent transport based on barrier suppression . . 22

2.3.2. Arrhenius/Poole-Frenkel type activated hopping-based transport process 24

2.3.3. Granular metal conductivity model 24

2.3.4. Sequential charge transport in molecular wires 26

2.4. Coulomb blockade 28

2.5. Influence of light on the NP-molecule-nanoelectrode system 30

3. Measurement equipment **32**

3.1. Motivation and concept of the measurement setup 32

3.1.1. Chip carrier 34

3.1.2. DEPT trapping-box 34

3.1.3. Interconnect-switch-box 38

3.1.4. Sub-picoampere cryostat setup 38

3.1.5. Optical setup 41

3.1.6. Measurement programming environment: Testpoint 41

4. Nanometer-Scaled Lithography **46**
4.1. Nanoelectrode Fabrication by E-beam Lithography 48
4.1.1. Fabrication route A: Standard resist layer 51
4.1.2. Fabrication route B: Optimized resist layer and developer 53
4.1.3. Fabrication route C: Proximity optimized pattern geometry . . . 55
4.1.4. Comparison of fabrication routes 58
4.2. Simulation of the effective dose pattern 60
4.3. Nanoelectrodes in multi-terminal devices 64
4.4. Tunneling characteristics between nanoelectrodes with small tip separations 66

5. Dielectrophoretic trapping of charged and uncharged NPs **68**
5.1. Detection of a trapping event 69
5.2. Immobilization of BP3 capped NPs (4 nm) 71
5.3. Immobilization of MES capped gold NPs (12 nm) 74
5.4. Immobilization of MES and Spiropyran (2:3) capped gold NPs (12 nm) . 77
5.5. Immobilization of Spiropyran capped CdSe NPs (4 nm) 78
5.6. Conclusion of DEPT 79

6. Transport measurements on BP3 capped NPs **80**
6.1. Temperature dependent transport measurement on single BP3 capped NPs 82
6.1.1. Molecular orbital mediated transport at 4K 89
6.1.2. Coulomb blockade at 4K 90
6.2. Transport measurement on single BP3 capped NPs at RT 92
6.2.1. Coulomb blockade at RT 92
6.2.2. Simmons fit of the $I(U)$ curve 95
6.2.3. Geometrical considerations out of electrical measurements 98
6.2.4. TVS 99
6.2.5. Photoconductivity in a single NP device 101
6.3. Conclusion of the BP3 capped NPs 104

7. Transport measurements on MES capped NPs **109**
7.1. Mercaptoethanesulfonic acid 109
7.1.1. UV-Vis spectroscopy on MES molecules 110
7.1.2. Approximation of the dipole moment of MES 111

7.2. Transport measurement on single MES capped NPs at RT 112
7.2.1. Simmons fit of the $I(U)$ curve 114
7.2.2. Transition Voltage Spectroscopy 115
7.3. Results and discussion 116

8. Transport measurements on SP / MES capped NPs **119**
8.1. DFT calculations of the SP/MC photoisomer and the MES / SP capped gold NP 120
8.2. UV - VIS spectroscopy on Spiropyran molecules 124
8.3. Excitation spectroscopy on SP/MES NP devices 125
8.3.1. Simulation of surface plasmon polaritons in the NP-nanoelectrode system 128
8.4. Transport measurements on Type A: SP/MES (3:2) with 12 nm Au core 129
8.4.1. Simmons fit of the $I(U)$ curve 131
8.4.2. Transition Voltage Spectroscopy 133
8.5. Electrical switch created by photo-isomerisation of spiropyran 135
8.5.1. Application as multi valued logic device / full adder 137
8.6. Transport measurements on Type B SP/MES (1:6) with 4 nm Au core . . 139
8.6.1. Device1: Current voltage characteristic and TVS at RT 141
8.6.2. Device1: Gundlach oscillations in molecular vacancies at 4K . . . 141
8.6.3. Device2: Current voltage characteristic and TVS at RT 143
8.6.4. Device2: Coulomb diamonds at 4K 148
8.7. Conclusion: Light induced conduction switch in devices with SP and MES capped NPs 150

9. Conclusion **159**

Bibliography **168**

Appendix **178**
A. Investigation of BP3-capped NP by Kerstin Blech 178
A.1. DSC Analysis using: UV/Vis, TEM, SAXS 178
A.2. Impedance spectroscopy measurement 181
B. Influence of light on the sample-temperature 183

Physical constants	
variable	declaration
$\hbar$	Planck constant
e	charge of an electron
m_e	mass of an electron
m^*	effective mass of the electron in the tunneling contact
k_B	Boltzmann constant
ϵ_0	dielectric constant

2. Theoretical description of a nanoparticle-nanoelectrode system	
variable	declaration
$I(U)$	current in dependence on the voltage
U	bias voltage
U_{sd}	source drain voltage
A	contact area of the tunneling barrier
l	width of the tunneling barrier
$G_{lin-Sim}$	conductance in the linear regime of tunneling
ϕ	height of the tunneling barrier
ρ	shape factor
β	decay constant
β_0	decay constant at zero bias (($\lvert U_{sd}\rvert \approx 0\,\mathrm{V}$))
(βl)	decay parameter
$I_{Sim,k}$	theoretical approximation of the current by the Simmons equation with parameter set k
$(\beta l)_k(i)$	result of the decay parameter in the i'th step of the iterative Simmons fit
$\phi_k(i)$	resulting height of the tunneling barrier in the i'th step of the iterative Simmons fit using parameter set $k \in [1, 2]$
$\rho_k(i)$	resulting shape factor in the i'th step of the iterative Simmons fit
β_n	decay constant of a molecular subunit

β_{vac}	decay constant of a vacuum gap
l_n	length of a molecular subunit
l_{vac}	length of a vacuum gap
phi_{Au}	work function of gold
R_{cont}	contact resistance in a metal-molecule-metal contact
U_{trans}	transition voltage (minimum of the Fowler-Nordheim plot)
α	exponent in calculations of the Fowler-Nordheim plot
η	division factor, fraction of voltage that drops over the molecule
U_{mol}	voltage drop over the molecule
R_l, R_r	contact resistance to the left and the right electrode
R_{mol}	'resistance' of the molecule
β_{mol}	decay constant of the molecule
l_{mol}	length of the molecule
C_{mol}	estimated capacitance of a molecular layer
C_{vac}	estimated capacitance of a vacuum gap
C_{tot}	total serial capacitance (C_{mol},C_{vac})
ϵ_r	permittivity of the molecule
β_{mol}	decay constant of the molecule
$\eta_{mol,sub}$	division factor, fraction of voltage that drops over a molecular subunit
$U_{mol,sub}$	fraction of voltage that drops over a molecular subunit
$R_{chemisorbed}$	contact resistance of chemisorbed molecules
$R_{physisorbed,vac}$	contact resistance of physisorbed molecules or a remaining vacuum gap
R_{BP3}	estimation of the resistance of a BP3 molecule
l_{alkane}	length of the alkane chain
l_{BP}	length of the biphenyl subunit chain
β_{alkane}	decay constant of the alkane chain
β_{BP}	decay constant of the biphenyl subunit chain
η_{BP3}	theoretical division factor calculated for the BP3 molecule
$\eta_{Meth,Prop,BP}$	theoretical division factor calculated for the methyl, propane or biphenyl subunit of a BP3 molecule
E_F	Fermi energy of electrons in metal

$E_{F,bulk}$	Fermi energy of electrons in bulk metal (without considering the surface dipole moment)
$E_{HOMO,LUMO}$	energy level of the molecular HOMO or LUMO energy level
f_{trans}	relation factor, (quotient of $E_{HOMO,LUMO}$ and E_F)
ϕ_{TVS}	tunneling barrier height calculated with TVS
T_n	transmission function regarding to the energy level ϵ_n
ϵ_n	n'th energy level
σ_n	broadening of the energy level ϵ_n
f_n	height of the Gaussian peak in the DOS
$D(U_{sd}, \epsilon_n, \sigma_n)$	Gaussian function
T	total transmission function
$I_{orbital-m}$	current estimated by orbital mediated tunneling
D_{int}	interface dipole moment
$\phi_{HOMO,LUMO}$	tunneling barrier height regarding to the molecular HOMO or LUMO energy level
E_A	electron affinity
I_P	ionization potential
W	work function
f_{red}	reduction factor
ΔE_i	energy shift due the surface dipole moment with $i \in$ {metal, metal-mol, mol}
P_i	surface dipole moment with $i \in$ {metal, metal-mol, mol}
Y	conductivity
T	temperature
E_a	Arrhenius type of activation energy
E_{PF}	Poole-Frenkel type of activation energy
C_{GM}	granular metal related parameter
E_{GM}	granular metal related activation energy
E_{SE}	super exchange related activation energy
$G_{lin,T=4\,\mathrm{K}}$	conductance at zero bias ($(\lvert U_{sd}\rvert \approx 0\,\mathrm{V})$) and $T = 4\,\mathrm{K}$
N_{mol}	number of molecules in the conduction path
τ	traversal time
E_c	charging energy
a	nonlinearity parameter

$C_{GM,low,high}$	granular metal related parameter for the low and high bias regime
$(\beta l)_{tot}$	sum of decay constants of the subunits
$V_{coupling}$	electronic coupling matrix element
$\Gamma_{N,N+1}$	charge transfer rate between the (N,N+1)'th phenyl
$C_{L,R}$	capacitive coupling of the NP to the left and the right electrode
Q_0	residual charge
C_Σ	sum of the capacitances between the NP, and the electrodes and the backgate
ΔU_c	distance in voltage between Coulom blockade peaks
$\Delta G_{CB-theory}$	theoretical value of the Coulomb blockade peak height
G_{lin-CB}	conductance at zero bias, related to Coulomb blockade transport
G_{lin-GM}	conductance at zero bias, related to granular metal transport
$G_{CB-meas}$	conductance at zero bias, related to Coulomb blockade transport
C_n	capacitance of the shell of a molecular subunit
$C_{sphere-plane}$	capacitance between a sphere and a plane

3. Measurement equipment

variable	declaration
R_{ref}	reference resistor
A_{ref-in}	voltage amplitude over the reference resistor at the input of the pre-amplification circuit
$A_{ref-out}$	voltage amplitude output of pre-amplifier
$U_{in}(t)$	time dependent bias voltage
A_{in}	amplitude of the bias voltage
$B_{DC}(t)$	time dependent DC-like offset
$B_{AC}(t)$	time dependent AC-like superposition

C_{guard}	stray capacitance between connection lines and guard (on-chip)
$C_{electrode}$	stray capacitance between the connection lines on the left and the right side of the nanoelectrodes
R_{n-el}	leak resistance over the nanoelectrodes
U_{sd}	source drain voltage
U_g	gate voltsage
I	source drain current
λ	wavelength

4. Nanometer-scaled Lithography

variable	declaration
I_b	current of the exposure beam
T_e	exposure time
d_b	beam step size
D	exposure dose
$d_s(X)$	beam step size of the coarse (C) or fine (F) pattern $X \in [C1, C2, F1, F2, F3, F4, F5]$
$RD(X)$	relative dose of the coarse (C) or fine (F) pattern $X \in [C1, C2, F1, F2, F3, F4, F5]$
$D(X)$	absolut dose of the coarse (C) or fine (F) pattern$X \in [C1, C2, F1, F2, F3, F4, F5]$
α_{beam}	Gaussian beam size
d	size of the designed electrode tip separation

5. Dielectrophoretic trapping of charged and uncharged NPs

variable	declaration
ϵ_m	permitttivity of the NP solvent
ϵ_p	permitttivity of the NP-shell (capping-molecules)

F_{DEP}	DEP force on a spherical NP
r_{NP}	radius of the NP
$\underline{CM}(\omega)$	Clausius-Mosotti factor
$\underline{E_0}$	electric field
$E_{th,NP}$	threshold field to trapp molecule capped NPs
U_{ref}	voltage drop over the reference resistor
U_{in}	total applied voltage to voltage divider circuit
$U_{AC-detect}$	AC detection-voltage for the Lock-in amplifier
U_{DC-DEP}	DC voltage ramp for DEPT
U_{AC-DEP}	AC voltage pulse for DEPT
A_{detect}	amplitude of the AC detection voltage
A_{DEP}	amplitude of the AC DEPT pulse
f_{detect}	frequency of the AC detection voltage
f_{DEP}	frequency of the AC DEPT pulse
Δt	duration of the AC DEPT pulse
$U_{DC,max}$	maximum of DC voltage ramp for DEPT
ω	wavelength of the applied AC voltage
ω_{n-el}	characteristic frequency related to the resistance of the nanoelectrodes
ω_{ref}	characteristic frequency related to the reference resistor
p_{ref}	phase drop over the reference resistor
R_{ref}, R_{n-el}	resistance of reference resistor and over nano-electrodes
C_{ref}, C_{n-el}	capacitance over reference resistor and nano-electrodes
Z_{ref}, Z_{n-el}	impedance of reference resistor and nano-electrodes
H	transfer function
$H_{\omega=0}, H_{\omega=\infty}$	value of the transfer function at low / high frequencies
Δp_{ref}	jump in phase
E_{n-el}	electrical field between the nanoelectrodes
ϵ_{alkane}	permittivity of alkane
ϵ_{phenyl}	permittivity of phenyl

6. Transport measurements on BP3 capped NPs

variable	declaration
Y	conductance
T	temperature
$l_{BP3-eff}$	effective length of tilted BP3 molecule
ϵ_{BP3}	permittivity of BP3
ϵ_{alkane}	permittivity of alkane
ϵ_{phenyl}	permittivity of phenyl
E_a	Arrhenius type of activation energy
E_{PF}	Poole-Frenkel type of activation energy
C_{GM}	granular metal related parameter
E_{GM}	granular metal related activation energy
E_{SE}	super exchange related activation energy
$(f_i, \sigma_i, \epsilon_i)$	parameter of a Gaussian bell
$\Delta U_{BP3,4K}(N, N+1)$	peak distance of Coulomb blockade peaks at 4 K
$C_{\Sigma,BP3-A,4K}$	sum of capacitances which defines Coulomb blockade at 4 K
$\Delta U_{BP3,RT}(N, N+1)$	peak distance of Coulomb blockade peaks at RT
$C_{\Sigma,BP3-A,RT}$	sum of capacitances which defines Coulomb blockade at RT
$C_{NP-plane}$	capacitance between a NP and an infinite plane
$U_{neg/pos,BP3-A/B}$	position of the first CB peak (neg/pos) around zero bias
Q_0	fractional charge
$C_{\Sigma,BP3-A/B,0}$	sum of capacitance calculated from the first step in device A/B
$G_{lin,BP3-A/B}$	conductance at zero bias in device A/B
$\Delta G_{CB,theo,A/B}$	theoretical peak height of CB in device A/B
$\Delta G_{CB,meas,A/B}$	measured peak height of CB in device A/B
$G_{CB-A,RT}$	conductance at zero bias, related to Coulomb blockade at RT
$G_{CB-A}(T)$	conductance at zero bias, related to Coulomb blockade transport in dependence of temperature
$G_{Arrhenius-A}$	conductance at zero bias, related to Arrhenius type of transport in dependence of temperature

$G_{GM-A}(T)$	conductance at zero bias, related to granular metal based transport in dependence of temperature
$G_{SE-A}(T)$	conductance at zero bias, related to sequential superexchange based transport in dependence of temperature
$I_{tunneling,A}$	current conttribution with tunneling mechanism
$I_{sd,A}$	measured current
$(G_{Sim,BP3-A/C}$	conductance at zero bias
$G_{Sim,BP3-A/C,theo.}$	theoretically calculated value of conductance at zero bias
$\rho_{BP3-A/C}$	shaping factor
$\phi_{BP3-A/C}$	height oh the tunneling barrier
$N_{molecules}$	number of molecules involved in charge transport
$A_{calotte}$	Area of calotte used to determine $N_{molecules}$
$r_{NP,BP3}$	radius of BP3-capped NP
$l_{vac,Sim,BP3,A/C}$	calculated vacuum gap using Sim theory
$\phi_{alkane,Lit}$	tunneling barrier height of alkane (from literature)
$\phi_{BP,Lit}$	tunneling barrier height of biphenyl (from literature)
$\phi_{gold,Lit}$	tunneling barrier height of gold (from literature)
$\phi_{BP3-NP-A/C,theo.}$	theoretical value of the tunneling barrier height of BP3 using barrier heights of the subunits (from literature)
$U_{TVS,BP3-A/B/C}$	transition voltage obtained in the Fowler-Nordheim plot of device A/B/C of BP3-capped NPs
$U_{DOS,BP3-B}$	DOS peak observed in the ndc-curve of device A/B/C

7. Transport measurements on MES capped NPs

variable	declaration
$l_{MES,trans}$, $l_{MES,cis}$	effective length of MES in the trans conformation
$\Delta E_{MES,2-1}$	distance between two energy levels, determined with the absorption spectra of MES
$f_i(E)$	Gaussian bell of the i^{th} MES energy level
H_i	height of the Gaussian bell of the i^{th} MES energy level
$\sigma_{MES,i}$	width of the Gaussian bell of the i^{th} MES energy level
$P_{MES,trans/cis}$	dipole moments of MES in the trans and cis conformation

$P_{MES,deprot.}$	dipole moment of deprotonated MES
$P_{MES-Au,trans/cis}$	surface dipole moments of MES in the trans and cis conformation SAM on a Au surface
$P_{MES-Au,deprot.}$	surface dipole moment of deprotonated MES SAM on Au
$W_{MES-Au,trans/cis}$	workfunction of a SAM of MES in trans or cis conformation on Au
$W_{MES-Au,deprot}$	workfunction of a SAM of deprotonated MES on Au
$\Delta W_{MES-Au,trans,cis}$	difference between the workfunctions of a SAM of MES in trans or cis conformation on a Au surface
dU, dt	measurement settings (step in voltage and waiting time)
$U_{MES,DOS,i}$	i^{th} peak of the ndc (counting from left to right)
G_{lin}	conductance at zero bias voltage
$G_{MES,lin-neg/pos}$	conductance at zero bias voltage obtained in the fit for $U_{sd} < 0\,\mathrm{V}$ or $U_{sd} < 0\,\mathrm{V}$ respectively
$\rho_{MES,neg/pos}(i)$	result of the shaping factor of the i^{th} iteration step for MES molecule capped NPs
$\phi_{MES,neg/pos}(i)$	result of the tunneling barrier height of the i^{th} iteration step for MES molecule capped NPs
$(\beta l)_{MES,neg/pos}(i)$	result of the decay parameter of the i^{th} iteration step for MES molecule capped NPs
$(\beta l)_{MES,tot}$	total decay parameter for MES NPs
β_{MES}	decay constant of MES molecule
γ	tilt angle of MES molecule
l_{ethane}	length of ethane subunit of MES
$l_{sulfonate}$	length of ethane subunit of MES
$l_{vac,MES,Sim-neg/pos}$	vacuum gap obtained by a Simmons fit of a MES-capped NP in nanoelectrode configuration
$U_{MES,TVS-up/down}$	transition voltage of MES, determined
$l_{vac,MES,TVS}$	vacuum gap obtained by a TVS fit of a MES-capped NP in nanoelectrode configuration

variable	declaration
λ	wavelength of the light
λ_i	peak position observed in excitation spectroscopy
$U_{DOS,SP-A,i}$	observed peak i in the ndc of a type A SP/MES NP-nanoelectrode device
$\Delta U_{DOS,SP-A,i-j}$	difference between the observed peaks i, j in the ndc of spiropyrane
$U_{DOS,MC-A,i}$	observed peak i in the ndc of a type A MC/MES NP-nanoelectrode device, thus the conformer merocyanin
$\Delta U_{DOS,MC-A,i-j}$	difference between the observed peaks i, j in the ndc of merocyanin
$G_{Sim,SP-A}$	conductance at zero bias
$\rho_{SP-A,neg/pos}$	shaping factor
$\phi_{SP-A,neg/pos}$	tunneling barrier height
$(\beta l)_{SP-A,neg/pos}$	decay parameter
$l_{vac,Sim,SP-A}$	vacuum gap determined by Simmons fit
$U_{TVS,SP-A,neg/pos}$	transition voltage
$l_{vac,TVS,SP-A}$	vacuum gap determined by TVS
$T_{1/2,MC-A}$	half life time of MC in type A (SP/MES) NPs
$U_{0,1}$	input voltage 0,1
(A_{in},B_{in},C_{in})	binary input parameter
(S,C_{out})	binary output parameter
S_n	multi valued output parameter
$\Delta U_{DOS,SP-B1/2}$	observed peak in SP/MES Type-B NPs in device 1/2
$U_{TVS,SP-B1/2}$	transition voltage
U_N	bias voltage where the N^{th} Gundlach peak is observed
ϕ	tunneling barrier
F	field strength
l_tot	distance between the metal contacts where the volatge drops
$U_{DOS-HOMO,SP-B}$	observed peak in the ndc for negative bias

Table 0.8.: Chapter wize declaration of used variables.

1. Introduction

The reduction of device sizes in complementary metal oxide semiconductor (CMOS) technology according to Moore's law finds its natural limit in molecular length scales. Current optical lithographic methods in industrial fabrication have reached a technological barrier. They have halted temporarily at 22 nm technology since the implementation of 11 nm optical lithography technology currently involves a much higher fabrication effort and cost [1]. However, the sizes of industrially fabricated devices are already comparable to those of nanoelectrode devices used in scientific investigations [2–4] to study molecules or molecule-capped nanoparticles. However, including the width of the connecting wires to the nanoelectrodes and the possible pitch between the devices in the considerations does not lead to significant improvements in the device size of molecule-based systems. As a consequence, molecular electronics currently do not aim to reduce device geometry, but rather to increase logic density.

In 1960, Herwald and Angello published an article in Science stating that 'The trend in electronics circuit construction is toward microminiaturization and molecular electronics.' [5]. In the early 1970s, Mann and Kuhn [6], as two of the first experimentalists, published measurements on molecule-based systems. In their work, an exponential decrease in the transport current was obtained with increasing molecular length, clearly demonstrating the tunneling nature of molecule-based systems. In 1974, Aviram and Ratner [7] were the first, to suggest that an organic molecular system shows current rectification and diode-like characteristic. Since then, hundreds of scientific researchers have been inspired to face the challenges that emerge with molecule-based transport in order to find suitable molecular systems for application.

Compared to current CMOS technology, charge transport mechanisms in molecule-based systems are fundamentally different. In such systems, electron transport is based on tunneling [8], orbital mediated transport [9], superexchange coupling [10] and intramolecular hopping [11]. Although the idea that molecules are the bricks of CMOS technology is already 50 years old, charge transport in molecule-based devices is still not

fully understood. One reason is that molecules cannot be contacted in a reproducible way in a nanometer-sized CMOS compatible device. As a consequence, current-voltage ($I(U)$) characteristics often do not respond as expected to a controlled change in experimental conditions. Furthermore, charge transport is influenced by a wide range of parameters that dictate the electrical properties of molecule-based devices. Possible influences can be summarized in three categories:

- Contact resistance (anchoring group, detailed atomic structure of the atoms at the interface, vacuum gap, electrode material)
- Molecular composition (σ- and π-bonded subunits, donor/acceptor subunits, polarizability, dipole moment and the length of the molecule)
- experimental conditions (temperature, surrounding medium).

The wide range of influences on charge transport often allows a variety of possible interpretations of the experimental work. The generic features described in the literature have been extracted from experimental studies on rather unique individual samples. However, enough data have been published to clearly show that the molecular properties influence the charge transport properties. In principle, it should be possible to design and synthesize molecules with the transport properties required to implement, for example, logical devices or sensors. The current challenge in single organic molecules is to understand the observed variety of electronic transport phenomena in molecule-based devices, such as cotunneling [12], quantum interference, coherent and incoherent transport [13], Kondo effect [14], Coulomb blockade [15, 16], negative differential resistance [17] and temperature-dependent transport (hopping/superexchange) [11,18]. The field is far away from mass production of identical devices, until the molecule-electrode contact must first be brought under control. Experiments on the same molecule using different probing methods, such as: nanoelectrodes, nanopores and large area junctions [19] show significant differences in current transport, such as the magnitude of the current and the shape of the $I(U)$ curve, for each type of device. The molecule-electrode system-related characteristics [20], such as the exact geometry at the electrodes, the type of coupling (physisorbed/chemisorbed) to the electrodes, molecular parameters (acceptors/donors /σ-/π-bonded molecular subunits, (photo)isomer molecules and the surrounding medium [21]), have a tremendous influence on charge transport in specific systems.

The previously itemized categories are understood as a toolbox to create molecule-based

working devices with tailored functionalities for the intended application for, example, as logic circuit. In such circuits, a simple reduction in device geometry, for example to create a diode or a transistor, is not intended. Instead, the aim is to create complex logical circuits, for example, a Full-Adder or a ternary multiplier. Further possible applications of molecule-based devices are as add-ons in CMOS technology, in energy conversion techniques (OLED) or as chemical sensors [22]. The boundaries between materials and devices, and between devices and circuits are fading, and we will see an integration of disciplines in the future development of molecular electronics.

The most established investigation method for molecular conductance is scanning tunneling microscopy (STM) [23–25]. The substrate (commonly atomic flat Au, Cu, Si, GeSe single crystal) acts as one of the electrodes and is covered with a self-assembled monolayer of molecules. A scanning probe tip is used as the other electrode. Such systems have the potential to perform both topographic imaging and charge transport measurements. This bottom-up approach is suitable for fundamental analysis, but not usable in commercial devices.

In the past decade, various creative nanofabrication techniques, such as break junction [4, 26, 27], nanopore [28], electrodeposition [29–31] and electromigration [32, 33], have been developed to investigate charge transport in single or bundled molecules. The generic features described in experimental studies have been obtained using rather unique individual samples, and there is much to be done before we can mass produce identical devices based on single or bundles of molecules [34].

Charge transport measurements on large-area junctions, in which a large number ($> 10^6$) of molecules are involved in the transport process in parallel, have shown a high reproducibility. Deviations in the sub-nm scale, which can dominate the transport in a single electrode-molecule-electrode contact are averaged out over the large number of parallel molecular channels [35, 36].
This also holds for an array of molecule-capped nanoparticles (NPs) in micrometer-scaled, large-area-junction devices. In such devices, sub-nm-scaled deviations in the subsequent NP-molecule-NP junctions average out over various percolation paths, meaning the tunneling paths through the 3D nanoparticle array, which have the highest transmission probabilities. Such systems have been shown to be directly dependent on the cap-

ping molecule, and on the size and size distribution of the molecule-capped NPs [37–40]. In both types of large-area junctions (characterizing molecules and molecule-capped nanoparticles), the transport currents are typically in the order of hundreds of microamperes and do not show distinct exponential behavior.
The combination of optical and electrical characteristics of a molecule-based system, and a 3D array of molecule-capped NPs, such as shown by Nakanishi et al. [37], provides new insights into electron transport in nanostructured (molecule-based) devices. On the one hand, the current transport is dependent on plasmonic resonances in the metal NP/nanoelectrode configuration, and on the other hand, on photoexcitation or photoisomerization of the capping molecule [41].

The intention of my work was to achieve a working device in which transport is based on a bundle of a few molecules and that is highly reproducibility and stability. The aim was to combine the advantage of the reproducibility of large-area junctions with the high quality of charge transport measurements of single or a bundle of molecules by applying STM or break junction technology. Charge transport in a single molecule-capped nanoparticle with a diameter in the range of 4 nm-12 nm was investigated in a nanoelectrode configuration. In such a device, two metal-molecule-metal contacts were created by a bundle of a few molecules. When the size of the nanoparticle was considerably greater than the tip separation of the nanoelectrodes, the device geometry in each individual system of a single trapped nanoparticle was comparable. Therefore the number of molecules involved in charge transport and the coupling between the molecule and the electrodes was similar for each device and thus the device properties were also similar. Furthermore, the nanoparticle was fixed between the nanoelectrodes by electrostatic forces, which led to a good device stability. Charge transport measurements on single molecule-capped nanoparticles with a diameter smaller than 7 nm, in a nanoelectrode configuration were still not very good. The currently relevant publications [3, 16, 42–47] , regarding the measurement of single-nanoparticle devices, investigate nanoparticles with diameters in the order of 10 nm. The reason for this might be the challenge to fabricate nanoelectrodes, which have a tip separation of smaller than 10 nm [42].

Forschungszentrum Jülich gave me the opportunity to use state-of-the-art E-beam technology, the vector scan system EBPG5000+ from Vistec. The development and opti-

mization of each of the E-beam lithographic steps (pattern layout, resist-layer stack and developer, settings of the E-beam machine) led to the fabrication of devices with an electrode separation of 2-4 nm, a yield of $\approx 55\,\%$ and a geometric control of the electrode shape in the nm scale. Worldwide there is no device fabricated in a direct write process capable of competing with these properties. Additionaly, a full plain backgate enabled three terminal measurements.
Other groups working in the field of single- and few-nanoparticle devices in nanoelectrode configuration [3, 16, 42–47] are investigating Coulomb blockade behavior at low temperatures. The size of the particles is typically in the order of 7-10 nm.
As a nanoparticle material gold has the advantage that it is commonly applied (in addition to silicon, copper, silver and carbon) as a substrate in current STM measurements. A variety of experiments are discussed in the literature, which investigate charge transport through mercapto-bonded molecules on gold surfaces. Alkanes are known for their insulating properties and have been well characterized in various types of devices. Their molecular properties are well documented in the literature [48]. It has been shown that the conductivity of a molecule correlates to the length of its chain. The delocalized π-electron system of phenyl has been discussed as a good conductor, if two or more phenyl units are coupled over a π-conjugated unit. However, if the two phenyl units are coupled via a sigma bonded unit, the delocalization of the π-system strongly depends on the torsion angles between the phenylene. A recent study measured the conduction of a molecule linked to the electrode by either a mercapto group or by a fullerene [49, 50]. Fullerene anchoring led to a considerably lower spread in low-bias conductance compared to the thiol-anchored molecule. The contact between the electrode and the molecule was created with the π-electron system of the fullerene, i.e. a ring of six carbons such as in phenyl.

Another fascinating aspect of molecular electronics is combining electrical and optical studies of molecular states, i.e. using a photoisomer as a capping molecule for NPs. One of the spectroscopically most studied families of photoisomers are the spiropyrans [51–56]. After irradiation with ultraviolet (UV) light, the bond between the spirocarbon and the oxazine breaks, the ring opens and its π-orbitals form a conjugated electron system. This zwitterionic isomer species, namely merocyanin, is colorful as the conjugated system has the ability to absorb photons of visible light, with which backward isomerization can be induced. This class of photoisomer are thermodynamically

unstable in one form and revert to the stable form in the dark unless cooled to low temperatures.

In the present work, charge transport in a nanoelectrode-molecule-nanoparticle-molecule-nanoelectrode device was investigated in relation to source-drain voltage, gate voltage, temperature and under illumination with light of a discrete wavelength. It was shown that charge transport in such a system is strongly dependent on molecular properties. The distance of the molecular energy levels to the Fermi level of the electrodes and their localization on the molecule play a central role in the conduction mechanism. First, a tailored species of molecules, namely biphenyl propanethiol, was applied as a functional unit to couple NP to the gold electrodes. The spacer group propanethiol was found to create the dominating part of the tunneling barrier and thus to limit the magnitude of conductance through the molecule. The delocalized π-electron system of the biphenyl unit was assumed to create a reproducible contact to the electrodes [49,50]. A fundamental understanding of charge transport was developed in current-voltage characteristics and temperature-dependent conductance measurements using a composition of the well-studied alkanethiol- and phenyl-based subunits.
Finally, the capping molecule spiropyrane was used as a functional element. Under irradiation with UV light, the molecule isomerizes to the zwitterionic isomer species, namely merocyanin. The distance between the molecular energy level and the Fermi level of the electrode has a high impact on the magnitude of the charge transport through the molecule. The molecular energy levels of merocyanin are different from those in the spiropyrane state, as a consequence a 'switch' was generated with which between two different molecular species with significantly different properties, based on the illumination of UV light, can be chosen. Additionally, the coupling of the molecule in the case of hydrogen, to the nanoelectrode is enhanced by the use of an alloy of Au_3Pd_2 [57,58].

Outline of the thesis

The thesis is structured as follows:

- Chapter 2 gives a brief introduction to the physics of charge transport mechanisms in a molecule-based nanoscale junction. Three evaluation tools for current trans-

port in molecule-based systems with constant temperature are described: normalized differential conductance, adapted Simmons equation for molecule-based systems and improved transition voltage spectroscopy. When the decay constants of the molecular subunits were known, these methods revealed geometrical and molecular properties, such as the length of the vacuum gap and of the HOMO-LUMO gap. Under rather simple but realistic assumptions, the theoretical description was extrapolated to a 'nanoelectrode-molecule-nanoparticle-molecule-nanoelectrode' system. Temperature-dependent charge transport properties in the molecule-nanoparticle system, i.e. hopping, granular metal-based transport for arrays of nanoparticles, as well as temperature-dependent charge transport properties of the molecule itself, i.e. intramolecular hopping, are discussed.

- Chapter 3 deals with the construction of two experimental setups with which molecule-capped nanoparticles (a) were immobilized between two nanoelectrodes and (b) were electrically and optically addressed in transistor geometry at variable temperatures.
- Chapter 4 introduces the state-of-the-art direct-write E-beam technology. The lithographic fabrication process was optimized technologically side, the chemically, i.e. the electron-sensitive resist and the applied developer as well as geometrically based on Monte Carlo simulations of backscattered electrons in the resist and substrate stack. The simulation of the exact dose pattern gives an estimation of the machine parameters of the E-beam pattern generator.
- In Chapter 5, the immobilization methods based on AC and DC dielectrophoretic trapping for charged and uncharged molecule-capped NPs are described. Furthermore, examples are shown of typical trapping procedures for each molecule and nanoparticle system.
- Chapter 6 reports on the current transport characteristics of biphenylpropanethiol-capped gold nanoparticles with a core size of $\sim 4\,\mathrm{nm}$ in nanometer-sized gold nanoelectrodes. Even at room temperature, the $I(U)$ measurements on such small gold nanoparticles showed Coulomb blockade. The current transport was investigated for constant temperatures ($298\,\mathrm{K}$, $4\,\mathrm{K}$) using the above mentioned methods to extract physical parameters, such as the tunneling barrier height and length of the vacuum gap. In temperature-dependent transport measurements, an understanding of current transport mechanisms was developed for single nanoparticle devices.

- In Chapter 7, transport properties of mercaptoethane sulfonic-acid-capped gold nanoparticles with a core size of 12 nm are studied. Fundamental analysis methods, such as UV/VIS spectroscopy, were applied to correlate the results obtained by the electrical characterization of the mercaptoethane sulfonic-acid-capped nanoparticle. For the electrical characterization, several investigation tools were applied.
- Chapter 8 discusses the experimental results of spiropyrane and mercaptoethane sulfonic-acid-capped (3:2) gold nanoparticles with a core size of 12 nm. When illuminated with UV light, spiropyrane isomerized to merocyanin, which is a zwitterionic molecule with a delocalized π-electron system. This change in the electronic properties of the isomer has a high impact on charge transport, as is clearly shown in the current voltage characteristics.
- In Chapter 9, two parameters of the NP device were altered. The size of the gold nanoparticle was reduced to (4 ± 1) nm and the relation between spiropyrane and mercaptoethane sulfonic acid was changed to (1:6). Nanoparticles with a diameter of (4 ± 1) nm were expected to show Coulomb blockade even at room temperature. These NPs were characterized in transistor geometry, under illumination of light with discrete wavelength at variable temperatures. By applying a gate voltage, the energy levels of the molecules could be shifted. This effect is known as molecular orbital gating. At low temperatures, two different types of devices were observed. On the one hand, the nanoelectrodes were not completely filled by the nanoparticle, i.e. a vacuum gap remained. In the case of resonant tunneling, an interference phenomenon, namely Gundlach oscillations, was observed at low temperatures ($T \approx 4K$). On the other hand, where almost (< 0.2 nm) no vacuum gap remained, Coulomb diamonds were observed at 4 K.

2. Theoretical description of a nanoparticle-nanoelectrode system

2.1. Tunneling in a molecule-based device

Various current transport phenomenas in molecule-based systems are described in several studies [8, 48, 59–62], which provides a basic understanding of electronic charge transport across molecular systems. The magnitude and properties of the transport current depend on the junction's parameters (for example, the type of contact to the electrodes, the position of the bond, the conjugation of the molecular orbital and the density of the energy levels). The question that must be addressed is to what extent this is the case.

Seemingly minor structural changes, such as the change of the adsorption position that may shift the HOMO level of the adsorbed molecule [63] or a vacuum gap of 0.1 nm. For both effects an exponential effect on the molecular conductance is expected. Currently, experiments on molecule-capped NPs are not controllable with the necessary precision to clearly differentiate between all possible influences in the tunneling barrier that affects current transport. Experiments, in which current-voltage $I(U)$ characteristics are measured, do not often respond in a controllable and reproducible manner to a controlled change in conditions. The experimentalist faces the problem of how to quantify the observations and assign them to specific properties such as:

(i) the relative positions of the molecular energy level to the Fermi energy level of the electrode, which dictate the barrier height and

(ii) inter-molecular coupling between energy levels of different molecules, i.e. superexchange coupling, something that may well affect the contact area in which charge transport occurs.

An arbitrary complex theoretical model can be created by a comprehensive in-depth analysis. However, this leads to a decreasing reliability of each applied parameter. The most probable scenarios, from the point of view of the authors, are described in current literature.
Currently, the two most relevant tools for interpreting tunneling transport measurements in metal-molecule-metal (MMM) contacts are:

- the linear Simmons equation [8], which was adapted to molecule-based tunneling by Vilan [59],
- transition voltage spectroscopy (TVS) [62, 64, 65], which visualizes the transition between off-resonant tunneling and Fowler-Nordheim tunneling [66].

2.1.1. Charge transport based on the Simmons model

The use of the Simmons model to analyze tunneling transport across molecular junctions is underlying inherent limitations, specifically in cases where data, such as the decay parameter of the molecular subunits, is unknown. A. Vilan [59] derived a detailed theoretical model, based on the Simmons model [8], which is reduced to a few averaged characteristic parameters, such as, the conductance in the linear regime $G_{lin-Sim}$, the barrier height ϕ and the decay parameter βl with the length l of the tunneling barrier. This enables the experimentalist to decompose experimentally measured $I(U)$ curves into a few basic parameters, which are then averaged over the width of the tunneling barrier. The conductance in the linear regime ($|U_{sd}| \approx 0\,\mathrm{V}$) was calculated as [59]:

$$G_{lin-Sim} = \frac{e^2}{4\pi h} \frac{Am^*\phi}{(\beta l)} \exp(-\beta l) \tag{2.1}$$

where l is the width of the tunneling barrier, m^* is the effective electron mass and A is the contact area.
The decay constant β describes the exponential decay of the wave function of an electron during tunneling through the barrier ϕ and thus, the exponential decay of the current I with the length l of the tunneling barrier: $I \sim \exp(-\beta l)$. According to A. Vilan [8, 59], the potential barrier across a molecular junction and thus the decay constant is strongly bias-dependent:

$$\beta = \beta_0 \sqrt{1 - \frac{U_{sd}}{2\phi}} \tag{2.2}$$

where β_0 is the decay constant at zero bias.
The decay parameter (βl) and the tunneling barrier ϕ must be understood as averaged values over the tunneling barrier with the length l. The decay parameter is proportional to the tunneling barrier height [59]:

$$(\beta l) = \rho\phi \tag{2.3}$$

where ρ is the shape factor. The 'shape factor' designates the influence on the shape of the $I(U)$ curve: the higher the value of the shape factor, the steeper the $I(U)$ curve. Hence for different values of ϕ and βl with the same ratio ρ, the $I(U)$ curves are indistinguishable. Finally, the linear Simmons equation using a field-dependent tunneling barrier height is [59]:

$$\begin{aligned} I_{Sim,1}(G_{lin-Sim},\phi,\rho) \;=\; & \tfrac{2G_{lin-Sim}\phi}{\rho\phi-2}\Bigg\{ \left(1-\tfrac{U}{2\phi}\right)\exp\left[\rho\phi\left(1-\sqrt{1-\tfrac{U}{2\phi}}\right)\right] \\ & -\left(1+\tfrac{U}{2\phi}\right)\exp\left[\rho\phi\left(1-\sqrt{1+\tfrac{U}{2\phi}}\right)\right]\Bigg\} \end{aligned} \tag{2.4}$$

and with equation (2.3) a second form is defined

$$\begin{aligned} I_{sim,2}(G_{lin-Sim},\phi,(\beta l)) \;=\; & \tfrac{2G_{lin-Sim}\phi}{(\beta l)-2}\Bigg\{ \left(1-\tfrac{U}{2\phi}\right)\exp\left[(\beta l)\left(1-\sqrt{1-\tfrac{U}{2\phi}}\right)\right] \\ & -\left(1+\tfrac{U}{2\phi}\right)\exp\left[(\beta l)\left(1-\sqrt{1+\tfrac{U}{2\phi}}\right)\right]\Bigg\}. \end{aligned} \tag{2.5}$$

Fitting routine based on the Simmons model

An exponential fit with the Simmons model is associated with high uncertainties. The outcome of a single fit to the Simmons equation (2.4) depends heavily on the choice of starting parameter and is therefore inconclusive. However, it is possible to make the outcome of the Simmons fit more reliable by: (i) a good estimation of the starting parameter and of the range where conduction is based on pure tunneling, and (ii) by applying two different sets of three independent parameters using an iterative fit sequence.

(i) According to Vilan [59], the power expansion to the Simmons model shows that $I/U vs. U^2$ plots is linear over a range where conduction is based on pure tunneling:

$$I/U = G_{lin-Sim}(1 + \frac{\rho^2}{96}U^2). \tag{2.6}$$

Thus, a linear fit to the plot of I/U vs U^2 yields two functional parameters $G_{lin-Sim}$ and $\rho_1(i = 0)$, where $i = 0$ denotes the first start value of the iterative fitting sequence. The starting value for the decay parameter $(\beta l)_2(i = 0)$ is estimated using [59]:

$$(\beta l)_2(i = 0) = \ln(e^2/(4\pi\hbar)) - \ln(G_{lin-Sim}l^2/A). \tag{2.7}$$

In this study the contact area was typically $A \approx 1 - 10\,\mathrm{nm}^2$ for a molecule-capped NP with a diameter of 4-12 nm.

(ii) Two sets of three independent parameters were chosen:

$$(G_{lin-Sim}, \phi, \rho)_1 \text{ and } (G_{lin-Sim}, \phi, (\beta l))_2,$$

according to [59], using equations (2.4) and (2.5). The shape factor ρ was a stable fit parameter, however the height of the tunneling barrier ϕ was rather undefined in this fitting procedure, as shown in Fig. 2.1a). Therefore, the fit of only one parameter set is strongly dependent on the choice of the values of the starting parameters.
In the second set of fitting parameters, the decay constant times the length of the tunneling contact (βl) and the height of the tunneling barrier was chosen. The grayscale plot of the mean square error (MSE) for this parameter set is shown in Fig. 2.1b). A clear valley along the diagonal axis was observed. When the results of these two fitting methods were combined a conclusive result was achieved with an iterative fitting sequence, as described below.

In the iterative fit sequence, the conductance in the linear regime was set to a constant value $G_{lin-Sim}$, which was determined by the linear fit (see equation (2.6)). The starting parameters for the two sets in the iterative fitting sequence were chosen as $(\phi_1(i = 0) = 0\,\mathrm{eV}, \rho_1(i = 0))$ and $(\phi_2(i = 0) = 7.5eV\,\mathrm{eV}, (\beta l)_2(i = 0))$. The results of the i'th iteration step of the fitting routine were $(\phi_1(i), \rho_1(i))$ and $(\phi_2(i), (\beta l)_2(i))$, respectively. The subsequent (i'th) starting parameters were calculated using the previous (i-1)'th

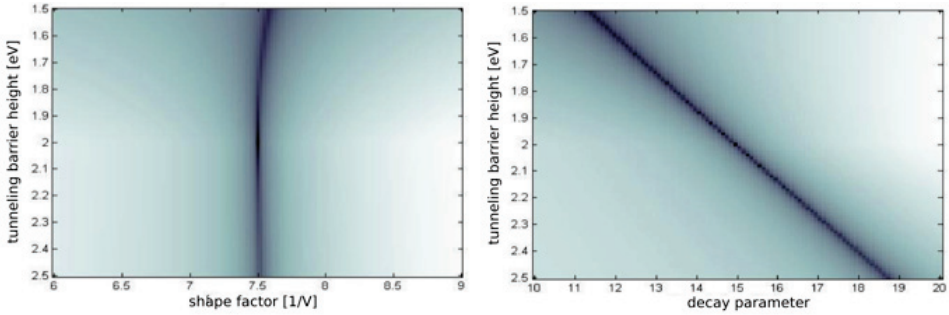

(a) **(b)**

Figure 2.1.: The graphs show the mean square error (MSE) between a 'target' I-V curve and the $I(U)$ curve based on the parameters given in the X-Y coordinates for that pixel plotted in grayscale. The barrier height is plotted on the Y coordinate and either a) the shape factor ρ or b) the decay parameter on the X coordinate. a) The MSE grayscale plot shows a clear valley for the shape factor and a rather unpronounced valley for the tunneling barrier. b) The MSE grayscale plot shows a clear valley, the tunneling barrier height with the lowest MSE is linearly dependent on the decay parameter ((βl)). These results were taken from *Vilan. Analyzing molecular current-voltage characteristics with the simmons tunneling model: Scaling and linearization. J Phys Chem C (2007) vol. 111 (11) pp. 4431-4444*

results of the fit:

$$\begin{aligned} \phi_{[1,2]}(i) &= (\phi_1(i-1) + \phi_2(i-1))/2 \\ \rho_1(i) &= (\beta l)_2(i-1)/\phi_{[1,2]}(i-1) \\ (\beta l)_2(i) &= \rho_1(i-1)\phi_{[1,2]}(i) \end{aligned} \tag{2.8}$$

After a fitting sequence of 20 iterations, the result converges to a set of parameters:

$$(\phi, \rho, (\beta l)).$$

The achieved shape factor was typically 10% lower than to the value ρ_{start} achieved by the linear fit.

If the decay constant of the molecular system is known, geometrical conclusions can be

drawn based on the result of the iterative Simmons fitting routine using:

$$(\beta l)_{tot} = \sum_n \beta_n l_n + \beta_{vac} l_{vac} \tag{2.9}$$

where β_n and β_{vac} are the decay constants and l_n and l_{vac} are the length of the subunits of the molecule (vacuum gap), respectively. The vacuum decay constant is estimated as:

$$\beta_{vac} = \frac{2}{\hbar}\sqrt{2m_e e\phi_{Au}} \approx 23nm^{-1} \tag{2.10}$$

where $\phi_{Au} = 5.2\,\mathrm{eV}$ is the work function of gold. The total conductance in the linear regime is calculated as:

$$G_{lin-Sim} = R_{cont}^{-1} e^{-(\beta l)_{tot}}. \tag{2.11}$$

where R_{cont} is the contact resistance of the molecule to the electrodes, which is calculated as the sum of contact resistance, i.e. the resistance of the molecule-NP contact (chemisorbed), which is typically in the range of $26..1000\,k\Omega$ [67–69] and the molecule-electrode contact (physisorbed), which is typically in the range of $1\,M..10\,T\Omega$, depending on the remaining vacuum gap.

2.1.2. Transition Voltage Spectroscopy

Transition voltage spectroscopy (TVS) is a spectroscopic tool with which the distance of the Fermi energy to the molecular orbital with the closest energy level is determined for metal-molecule-metal contacts. Often the condition for resonant tunneling requires a bias voltage up to a few volts over a molecule, which has a length typically below 2 nm. Therefore, the huge electric fields ($\sim 10^9\,\mathrm{V/m}$), might cause a breakdown before the molecular level is actually accessed. The main advantage of TVS is that, even if the bias voltage is moderate and a resonance to the energy level of the molecular orbital is not yet reached, the position of the nearest molecular energy level in a two-terminal device is derived. In principle the minimum U_{trans} on a Fowler-Nordheim plot, where $\ln(I/U^2)$ is plotted against $1/U$, is related to the closest molecular energy level to the Fermi level. The principle is based on the transition between off resonant tunneling and Fowler Nordheim tunneling (orbital mediated tunneling).
The required voltage to determine the molecular levels is reduced by $\sim 30\,\%$, using the mathematical trick of finding the minimum $U_{trans}(\alpha)$ of $\ln(I/U^\alpha)$ with the exponent $\alpha < 2$, which is described by Markussen et al. [62] as the improved TVS.

In order to gain quantitative information of the molecular junction the order of magnitude of the contact resistance is taken into account using the division factor $\eta \in [0, 1]$. The factor η describes the fraction of the bias voltage which drops over the molecule, i.e. $U_{mol} = \eta U_{sd}$. In other words, for devices with ideal contact to both electrodes ($R_l + R_r = 0\,\Omega$), the division factor is $\eta = 1$, as a consequence, the applied voltage completely drops over the molecule. If the sum of the contact resistances becomes dominating compared to the resistance of the molecule ($R_l + R_r >> R_{mol} \approx \frac{h}{2e^2} exp(\beta_{mol} l_{mol})$), i.e. due to a vacuum gap, the division factor η approaches $\eta = 0$. Compared to the size of the molecule the electrodes, on both side of the molecule, is approximated as two plates of a parallel plate capacitor containing two layers of medium: the molecule and vacuum [70, 71]. Using this model, the division factor η is estimated with:

$$\eta = \frac{U_{mol}}{U_{sd}} = \frac{C_{tot}}{C_{mol}} = \left(1 + \frac{\epsilon_r l_{vac}}{l_{mol}}\right)^{-1} \tag{2.12}$$

with the relative permittivity ϵ_r and the length l_{mol} of the molecule, l_{vac} the length of the vacuum gap and $l = l_{vac} + l_{mol}$. Another consideration to describe the division factor is the ratio between the decay parameter:

$$\eta = \frac{U_{mol}}{U_{sd}} = \frac{(\beta l)_{mol}}{(\beta l)_{mol} + (\beta l)_{vac}} = \left(1 + \frac{\beta_{vac}}{\beta_{mol}} \cdot \frac{l_{vac}}{l_{mol}}\right)^{-1} \tag{2.13}$$

Comparing equations (2.12) and (2.13) the permittivity of the molecule might be approximated by:

$$\epsilon_r = \frac{\beta_{vac}}{\beta_{mol}} \tag{2.14}$$

The equation is proven by experimentally obtained values in literature,e.g alkanethiol ($\epsilon_r = 2.8$, $\beta_{alkane} = 8.1\,\mathrm{nm}^{-1}$), phenyl ($\epsilon_r = 4.5$ [72], $\beta_{phenyl} = 4.7\,\mathrm{nm}^{-1}$) which is in excellent agreement with equation. The fraction ηU_{sd} of the bias voltage drops over the molecule, which will cause an electric field in the molecule. However, a more realistic picture is drawn considering subunits in the molecule with localized orbitals, where no voltage will drop [20]. Hence, in an electric field, the energy levels of the molecular subunits are shifted by the applied field by ($\eta e U_{sd}$), the shift of each subunit might be

approximated in a first step in analogy to equation (2.12) using:

$$\eta_{mol,sub} = \frac{U_{mol,sub}}{U_{mol}}\eta = \frac{(\beta l)_{mol,sub}}{(\beta l)_{mol}}\eta \tag{2.15}$$

The fraction $(1-\eta)$ of the applied voltage that does not drop over the molecule, drops over a resistor, which is commonly referred to as contact resistance. The contact resistance in a metal-molecule-metal (MMM) is composed of two contributions: (i) the chemisorbed Au-S bond ($R_{chemisorbed} = 5 - 100\,\mathrm{k\Omega}$ [67–69]) and (ii) a physisorbed molecule (typically $54M\,\mathrm{M\Omega}$) or a remaining vacuum gap $R_{physisorbed,vac}$.
However, the resistance in the linear regime of the $I(U)$ characteristic, for example of an biphenylpropanethiol unit is calculated using

$$R_{BP3}(U_{sd} \approx 0V) = \frac{h}{2e^2}\exp(\beta_{alkane}l_{alkane} + \beta_{BP}l_{BP}) \approx 19\,\mathrm{M\Omega}$$

and

$$R_{physisorbed,vac}(U_{SD} \approx 0V) = e^2/\hbar\exp(\beta_{vac}l_{vac}).$$

The biphenylpropanethiol unit consists of an alkane chain of a length $l_{alkane} = 0.56\,\mathrm{nm}$ and a biphenyl (BP) unit of a length $l_{BP} = 0.83\,\mathrm{nm}$ length, which have a decay constant of $\beta_{alkane} = 8.1\,\mathrm{nm}^{-1}$ [48] and $\beta_{BP} = 4.7\,\mathrm{nm}^{-1}$ [73]. Therefore the resistance over the whole molecule R_{BP3} is a few orders of magnitude greater as the contact resistance $R_{chemisorbed}$, which is dedicated to the Au-S bond. Though the dominating part of the contact resistance is created by the remaining vacuum gap / physisorbed molecule $R_{physisorbed,vac}$. The voltage drop over each subunit is considered separately [74], see Fig. 2.2. As shown by [75], there is no voltage drop over a delocalized π-electron system, i.e. over a single phenyl-unit, therefore it is assumed that the voltage drop at the connection of the phenyl rings.

Finally two statements are drawn:
The higher the contact resistance, the smaller is the division factor η and thus the smaller is [62]:

- the difference between the transition voltage U_{trans} and the voltage $U_{resonance}$, which is necessary to observe resonant transport [62]
- the peak-width of the measured DOS.

Markussen et al. [62] calculated the relation factor $f_{trans}(\alpha, \eta)$ between the transition

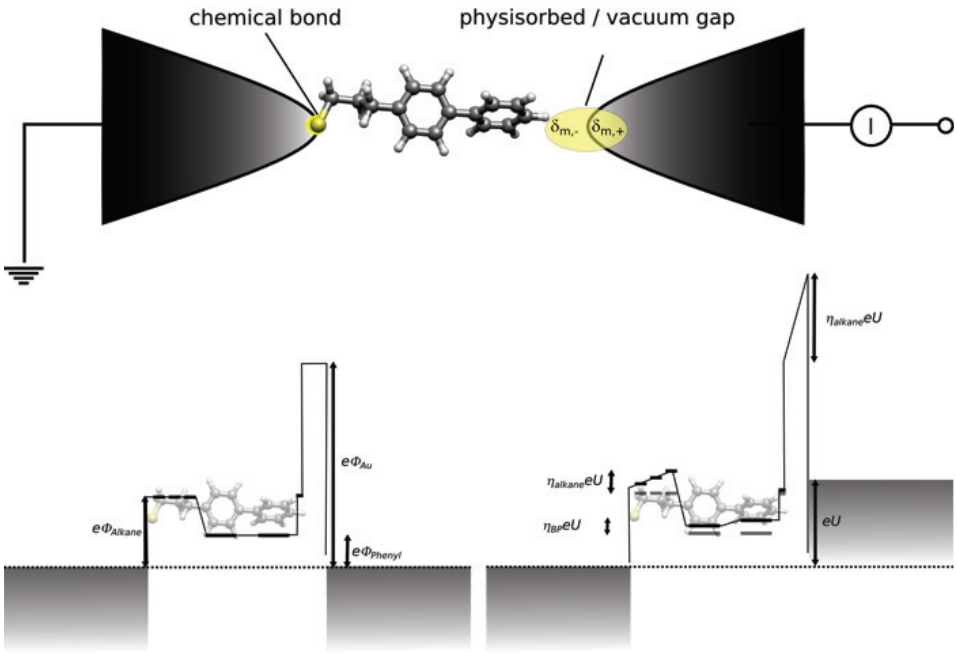

Figure 2.2.: (top)Schematic illustration of the metal molecule metal contact. The molecule is chemisorbed at one electrode and potentially has a vacuum gap to the other electrode. In the case of a small vacuum gap $\approx 0.1nm$, the molecule is physisorbed, thus interacting with the electrode.(bottom) A more realistic barrier profile for a BP3 molecule in a tunneling contact is depicted. The main potential drop is suggested over the vacuum gap $l_{vac} = 0.2\,\mathrm{nm}$ and the alkane subunit. In contrary, in the delocalized π electron system of a single phenyl unit, no voltage drop is assumed. According to the text the division factors where calculated : $\eta_{BP3}(l_{vac}) = 0.64$, $\eta_{Prop} = 0.27$, $\eta_{Meth} = 0.07$, $\eta_{BP}(l_{vac}) = 0.30$ using equation (2.15).

voltage $U_{trans}(\alpha)$ and the difference of the molecular level to the Fermi level $|E_n - E_F|$:

$$f_{trans}(\alpha, \eta) = \frac{|E_n - E_F|}{U_{trans}(\alpha)}.$$

We shall assume that the closest molecular level to the Fermi level is the HOMO level ($E_n = E_{HOMO}$), which is the typical case for alkanes.

With known relation factor f_{trans}, the division factor η can be determined using:

$$\begin{aligned} f_{trans}(\alpha = 1.5, \eta) &= 1.9 - 1.15\eta \\ f_{trans}(\alpha = 2, \eta) &= 2.95 - 1.85\eta \end{aligned} \tag{2.16}$$

Furthermore, in the case, where the tunneling is dominated by a vacuum gap, the correlation between the tunneling barrier height and the transition voltage is [65]:

$$\phi_{TVS} = \frac{e^2 m l^2 U_{trans}^2}{8\hbar} \tag{2.17}$$

Equation (2.17) is remarkably different from the results Beebe et al. [76] obtained, who exclusively considered molecule-based tunneling contacts. It is observed that the determined value of the tunneling barrier height ϕ_{TVS} is not:
(i) proportional to the transition voltage U_{trans}, though to its square;
(ii) independent of the length of the barrier l, though proportional to its square.

2.1.3. Orbital mediated transport

A common model for current transport in molecule-based systems via electronic levels is considered in the work of Huisman et al. [65]. The transmission function is assumed to be Gaussian:

$$T_n(U_{sd}, \epsilon_n, \sigma_n, f_n) = f_n D(U_{sd}, \epsilon_n, \sigma_n)\Gamma_{tot} \tag{2.18}$$

where $\Gamma_{tot,n} = (\Gamma_{vac}^{-1} + \Gamma_{mol,n}^{-1})^{-1}$ is the total tunneling rate, the gaussian function is $D(U_{sd}, \epsilon_n, \sigma_n) = 1/(\sqrt{2\pi}\sigma_n)\exp(-1/2((eU_{sd} - \epsilon_n)/\sigma_n)^2)$, σ_n is the broadening of the energy level ϵ_n and f_n is a factor to account for the different impacts (e.g. localization) of the molecular orbitals on the current transport. In the case of several molecular levels, the transmission function is described as a linear combination of DOS distributions:

$$T(U_{sd}, \underline{\epsilon}, \underline{\sigma}, \underline{f}, \eta) = \Sigma_n T_n(U_{sd}, \epsilon_n, \sigma_n, f_n) \tag{2.19}$$

where $\underline{\epsilon} = (\epsilon_0 \,..\, \epsilon_n)\underline{\sigma} = (\sigma_0 \,..\, \sigma_n)$ and $\underline{f} = (f_0 \,..\, f_n)$. The total amount of voltage drop over the molecule is denoted by the division factor $\eta \in [0, 1]$ such that the current is given by:

$$I_{orbital-m} = \frac{2e^2}{h}\int_{-\infty}^{\infty} T(U_{sd}, \underline{\epsilon}, \underline{\sigma}, \underline{f}, \eta)dE \tag{2.20}$$

2.2. Influence of a surface dipole moment on the tunneling barrier height

The interface dipoles formed at the molecule-metal interfaces play a key role in determining the barrier for charge (hole or electron) injection between the metal electrodes and the active organic layers. Numerous photoelectron studies and probe measurements [77] have demonstrated that the interface dipole D_{int} at the molecule-metal interface affect the charge injection barrier. An interface dipole in parallel to the surface normal, with its negative pole pointing towards the organic layer, shifts the HOMO energy of the organic layer relative to the Fermi level of the metal by adding an electrostatic energy. This reduces the hole injection barrier ϕ_{HOMO}. Accordingly, an interface dipole, with the negative pole pointing towards the metal, reduces the electron injection barrier ϕ_{LUMO} [71, 77]. There are at three possible contributions to the dipole moment in a MMM device, which influences the charge transport:

- (i) The surface dipole moment of the pure metal (m) and the change in metal surface dipole because of the modification of the metal electron density tail that is induced by the presence of the adsorbed organic molecules (physisorption),
- (ii) The metal-molecule (m-m) contact dipole moment along the chemical bond between the organic layers and the metal (chemisorption), which is induced by a partial charge transfer,
- (iii) the dipole moment of the molecule (mol).

The influence of the three types of contributions on the energy levels of the system is illustrated in Figure 2.3. The previously itemized dipole moments are influencing the work function of the metal, which is calculated using [71, 77]:

$$W = f_{red}\Delta E_m + \Delta E_{m-m} + \Delta E_{mol} - E_{F,bulk}, \tag{2.21}$$

where each contribution is calculated using:

$$\Delta E_i = \frac{eP_i}{\epsilon_0} \tag{2.22}$$

where $E_{F,bulk}$ is the bulk Fermi level [78] and P_i is the surface dipole moment at (i) the metal-vacuum interface (m), (ii) the metal molecule (m-m) interface and (iii) the molecule (mol) meaning $i \in$ {metal, metal-mol, mol}, respectively. The polarization

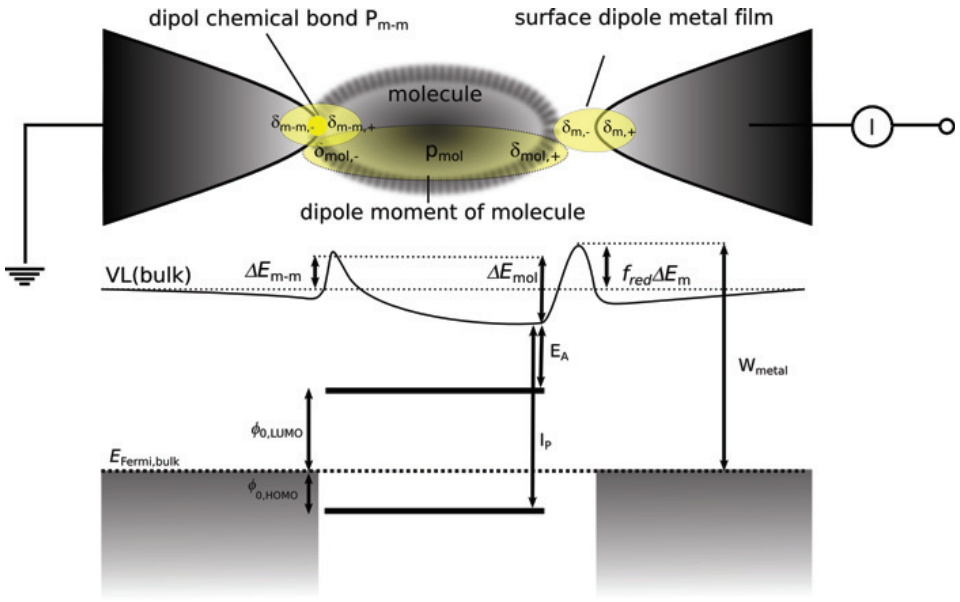

Figure 2.3.: Schematic of the influence of the dipole moments of a thiol-bonded molecule on the injection barrier heights, the electron affinity E_A, the ionization potential I_P. On the left (thiol-bonded) side of the MMM contact, the negative pole of the metal-molecule bond dipole points in direction of the vacuum. This dipole moment influences the relative position between the Fermi-level and the HOMO LUMO level, i.e. ϕ_{HOMO} and ϕ_{LUMO}. On the right side of the MMM contact, the surface dipole moment of the metal is reduced due to the metal electron density tail being repelled at the metal electrode on the right.

P_{mol} is estimated by a simple parallel plate approximation, using the capping density of the molecules on the surface and the calculated dipole moment of a single molecule. The reduction factor f_{red} is equal to one when the metal is free of adsorbent molecules and equal to zero for completely covered surfaces. However, physisorbed molecules are reducing the surface dipole moment ($f_{red} < 1$) [20].
The alignment of the HOMO-LUMO gap relative to the Fermi-level dependent on the contact dipole moment P_{m-m} is influenced by the contact dipole moment of the molecule and thereby by the bonding mechanism itself, as described by Crispin et al. [77].

Conduction mechanism	conductance behavior	temperature range [K]
Arrhenius	$Y \sim \exp\left(-\frac{E_a}{k_B T}\right)$	100 - E_a/k_B
Poole Frenkel	$Y \sim U_{sd} \exp\left(-\frac{E_{PF}-\sqrt{eU_{sd}/(\pi\epsilon_{mol}\epsilon_0 l_{tot})}}{k_B T}\right)$	100 - E_{PF}/k_B
Granular metal	$Y \sim \exp\left(-2\sqrt{\frac{C_{GM}}{k_B T}}\right)$	50 - 330 K
Sequential superexchange	$Y \sim E_{SE} T^{-1/2} \exp -\frac{E_{SE}}{4k_B T}$	$<$ 300K
Coulomb blockade / barrier suppression	$Y \sim T G_{lin,T=4K} \cdot \frac{\sinh(eU_{sd}\tau/\hbar)}{\sin(2\pi\tau k_B T/\hbar)}$	depends on, where CB is observed

Table 2.1.: Possible transport mechanisms in solid state insulators.

2.3. Temperature-dependent transport mechanisms

In the last decade, several studies on temperature-dependent transport in devices consisting of nanoscaled subunits have been performed [12, 16, 61, 79–81]. In the following subsections, several temperature-dependent transport mechanisms are described. These include:

- barrier suppression in Coulomb blockade systems
- Arrhenius-/Poole-Frenkel- type of activated hopping
- Granular metal conductivity model
- Sequential superexchange based transport in molecular wires

2.3.1. Temperature-dependent transport based on barrier suppression

Direct tunneling is described as a temperature-independent process by Simmons [8]. In 'nanoelectrode-molecule-NP-molecule-nanoelectrode' devices, the coexistence of single electron tunneling and barrier suppression was analyzed theoretically by Korotkov and Nazarov [82] and shown experimentally [16]. The $I(U)$ curve of such a system is described by the modified Stratton formula [82]:

$$I(U) = \frac{N_{mol} 2\pi k_B T G_{lin,T=0K}}{e} \frac{\sinh(eU_{sd}\tau/\hbar)}{\sin(2\pi\tau k_B T/\hbar)} \tag{2.23}$$

N_{mol} is the number of molecules (tunnel junctions) involved in the tunneling process, T is the temperature, $G_{lin,T=0K}$ is the junction conductance at zero bias and $T = 0K$, the tunneling traversal time is $\tau = l/\sqrt{2\phi/m_e}$, $\hbar$ is the Planck constant and k_B is the Boltzmann constant. The important feature of the tunneling barrier in molecular systems, compared to systems with native oxide barriers deposited on the metal surface, is that the typical barrier height ϕ is much lower and the typical width l_{mol} is much wider than the corresponding parameters for oxide barriers. Therefore the tunneling traversal time τ is large in molecule-based systems. As distinct from the metal systems, this large traversal time plays a role in single charge transport phenomena. In the case of:

$$a = E_c\tau/\hbar < 1$$

for metal-oxide barriers, a Coulomb staircase with a linear slope is expected. According to [82], barrier suppression is observed when the tunneling traversal time becomes greater than the characteristic timescale $\hbar/E_c$ and thus the nonlinearity parameter a is:

$$a = E_c\tau/\hbar > 1,$$

where E_c is the charging energy. In this regime, staircase peculiarities are only observed for voltages below $\hbar/e\tau$, as shown in Fig. 2.4, and a clear nonlinearity is observed in the $I(U)$.

A typical ratio between the traversal times for a SET system based on transport through a molecular system can be estimated using $l = 1\,\mathrm{nm}$, $\phi = 1\,\mathrm{eV}$ and $E_c = 60\,\mathrm{meV}$ as $a = 0.15$. This is the weak nonlinearity case, i.e. $I(U)$ is slightly nonlinear and the peculiarities are remarkable. The $I(U)$ of such a type of device is illustrated in Fig. 2.4.

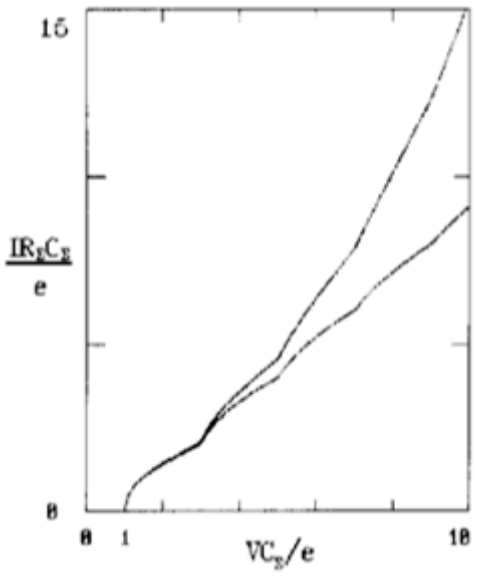

Figure 2.4.: Characteristic $I(U)$ for the two different regimes nonlinear parameters. The lower curve shows a conventional SET $\tau/(\hbar/E_c) > 1$, where barrier suppression is observed. The upper one illustrates the weak nonlinear case of $a = 0.125$. The picture is taken from Korotkov, Nazarov *(NPhysica B 173 (1991) 217-222)*.

2.3.2. Arrhenius/Poole-Frenkel type activated hopping-based transport process

Conduction through an insulating material in bulk is described considering localized states (traps) that are occasionally occupied by electrons due to thermal fluctuations. These fluctuations will provide to the electron enough energy to get out of its localized state into the conduction band, until it relaxes back into a localized trap. This effect is described by Arrhenius in the case, where the applied voltage between each conducting island is significantly smaller, then the barrier height of the trap. A temperature-dependent Arrhenius type of activated hopping process in an NP array structure was first discussed in [81]. It is based on a model of temperature-dependent transport in amorphous metal-semiconductor films according to [83, 84], which changes the conductivity with $\exp(-(E_a/k_BT))$.
The activation energy E_a is described as the mean excess energy of the moving charges. The higher the extent of disorder the higher is the transition temperature to an activated conduction.
In the case of a large electric field the necessary thermal energy, to move the electron into the conduction band, is reduced. The quantitative expression for this transport is called the Poole-Frenkel effect [85]

$$I \sim U_{sd} \exp(-\frac{E_{PF} - \sqrt{eU_{sd}/(\pi\epsilon_{mol}\epsilon_0 l_{tot})}}{k_BT}) \tag{2.24}$$

In molecule-based system the Poole-Frenkel energy E_{PF}, is associated with the tunneling barrier height $E_{PF} = \phi$.

2.3.3. Granular metal conductivity model

The temperature-dependent, electrical properties of a granular metal film with a thicknesses of 5-20 nm was investigated by B. Abeles et al. [86]. Their theory was adapted by Murray et al. [61] to solid-state films of alkanethiol-capped gold NPs with a core size of 1-2 nm. In such devices, the electronic conductivity σ is dependent on (a) the core-to-core tunneling of electronic charges along alkanethiol chains and (b) the electrostatic repulsion of electrons (Coulomb blockade). The number of charge carriers in a granular metal film (GMF), the generation of which requires an energy of E_{GM}, is proportional to the Boltzmann factor $\exp(-E_{GM}/k_BT)$. The charge transport occurs along the per-

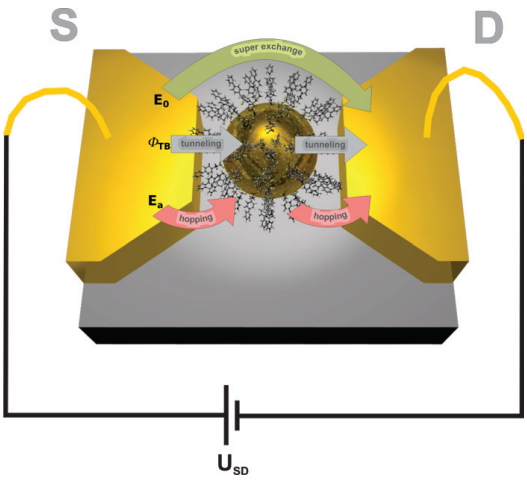

Figure 2.5.: Schematic of tunneling, hopping and superexchange coupling in a 'nanoelectrode-molecule-NP-molecule-nanoelectrode' device. The tunneling barrier height ϕ, the activation energy E_a and the superexchange coupling E_{GM} are the relevant energies on which current transport is dependent in such a system.

colation path, i.e. the path where the charging energies have the least deviations [86]. When the temperature is lowered, the number of charge carriers decreases and so too does the conductance. The temperature-dependent conductance is given by [86]:

$$\sigma = \sigma_0 \exp(-2(C_{GM}/k_B T)^{1/2}) \tag{2.25}$$

where C_{GM} is the scaled energy, which is dependent on the voltage drop between neighboring particles.

In the low field regime (see Fig. 2.6) the applied bias produces voltage drops between neighboring particles that are smaller than the thermal energy, $k_B T_{298} \approx 25\,\mathrm{mV}$, so that charge carriers are generated by thermal activation. In an array of NPs with a core diameter of 4 nm and a length of 500 nm, a bias of $\pm 1\,\mathrm{V}$ corresponds to a voltage drop of $\Delta U < 10\,\mathrm{mV}$ between neighboring NPs, while the Coulomb-blockade-related energy requirement for such a system is in the range of 60 mV [61]. The activation barrier energy E_{GM} is proportional to the parameter C_{GM}:

$$C_{GM,low} = (\beta l)_{tot} E_{GM} \tag{2.26}$$

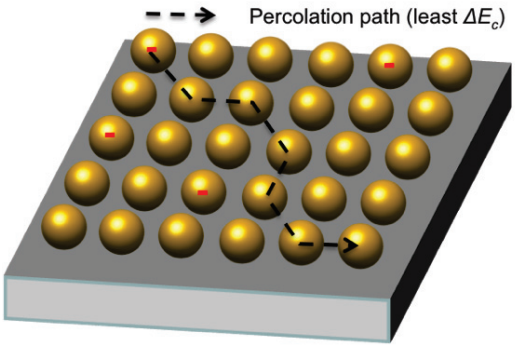

Figure 2.6.: Schematic of charge transport in an NP array according to granular-metal-based transport theory. Negative charges are produced according to Boltzmann statistics. The charges have the highest mobility along the percolation path, where ΔE_c is minimal.

where $(\beta l)_{tot}$ is the decay parameter in the adjacent barriers between the metal grains (tunneling contact), as used in the section 2.1.1.

In the high field regime, where $\Delta U > k_B T$, an additional mechanism becomes important, field-induced tunneling. The parameter C_{GM} becomes:

$$C_{GM,high} = C_{GM,low}(1 + 0.5(\beta l)_{tot}). \tag{2.27}$$

In GMF, the transport is dependent on the number of available charges and thus the temperature-dependent mobility of the electrons along the percolation path. The characteristic energy E_{GM} is a measure of the effective coupling between next-nearest neighbors, suggesting that conduction occurs by superexchange coupling in delocalized electronic states. With increasing temperature, there is a crossover to an activated regime.

2.3.4. Sequential charge transport in molecular wires

Charge transport in molecular wires comprising π-conjugated structural units interlinked by σ-bonded spacers are described in [11, 79] using a superexchange model. The model suggests that each elementary charge transfer step is based on superexchange cou-

pling, and is treated as an electron-transfer reaction between ionic and neutral states of π-conjugated structural units (C_i). Charges generated by an electrical field are localized exclusively on the π-conjugated subunits. The rate $\Gamma_{N,N+1}$ of charge motion between neighboring π-conjugated units, in terms of the reorganization energy E_{SE} and the electronic coupling matrix element $V_{coupling}$ is described by:

$$\Gamma_{N,N+1} = \frac{V_{coupling}^2}{\hbar} \left(\frac{\pi}{E_{SE} k_B T} \right)^{1/2} \exp - \frac{E_{SE}}{4 k_B T} \tag{2.28}$$

for temperatures that are high enough to allow vibrational modes be treated classically [87]. The charge transfer process for elementary hole and electron conduction mechanisms are symbolized as:

$$\begin{array}{rcl} Phenyl_i^- + Phenyl_{i+1} & \rightarrow & Phenyl_i + Phenyl_{i+1}^- \\ Phenyl_i^+ + Phenyl_{i+1} & \rightarrow & Phenyl_i + Phenyl_{i+1}^+ \end{array} \tag{2.29}$$

Thus, no ion pairs were produced in this transport mechanism. Instead, transport is based on charge displacement rather than on charge separation. Therefore, it is not surprising that the charge transfer rate $\Gamma_{N,N+1}$ remains field-independent. The ability of the molecule to transport a charge depends on the internal reorganization energy E_{SE}. The highest recombination rate is expected for coplanar alignment of aromatic rings. In this configuration, the electronic matrix element is maximal. Large deviations in the twist angles from the equilibrium value represent a bottleneck for the transport process.

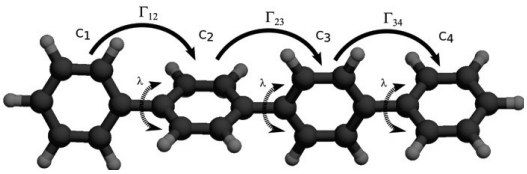

Figure 2.7.: Schematic of charge transport in a molecule comprising π-conjugated structural units that are coupled through σ-bonded spacers. The rate $\Gamma_{N,N+1}$ for sequential charge recombination from ionic to neutral species is dependent on the reorganization energy E_{SE}.

2.4. Coulomb blockade

The tunneling characteristics of a gated two-junction system created with a small, molecule-capped metal NP in electrode configuration shows single electron tunneling (SET), which is manifested as a $I(U)$ characteristic with staircase-like features. In a voltage range $|U| < 2E_c/e$, the current transport is blocked due to electrostatic repulsion [88]. The charging energy $E_c = e^2/2(C_L + C_R + C_{gate}) = e^2/2C_\Sigma$ is dependent on C_Σ the sum of the capacitive coupling to the left and the right electrode C_L,C_R and the coupling to a gate electrode C_{gate}. The shape as well as the width of the Coulomb staircase varies with the fractional residual charge Q_0, which is manipulated by the gate electrode. According to Tinkham et al. [89], the voltage of the NP as it gains or loses an electron is:

$$\Delta U_\pm(Q_0) = \frac{(Q_0 \pm e)^2}{2eC_\Sigma} - \frac{Q_0^2}{2C_\Sigma} = \frac{e \pm 2Q_0}{2C_\Sigma} \tag{2.30}$$

This means that varying the residual charge Q_0 on the central island will change the relative distance between the staircase, as well as the offset to zero bias voltage. The charging energy is calculated with the voltage difference between two peaks:

$$\Delta U_c = (\Delta U_+ - \Delta U_-)e = \frac{2Q_0 e}{C_\Sigma} = 4E_c/e \tag{2.31}$$

For temperatures in the range $k_BT << E_c(Q_0)$, which is the 'strong' Coulomb blockade regime, the theoretical value of the Coulomb blockade peak height $\Delta G_{CB-theory}$ is calculated using [88]:

$$\Delta G_{theory} = G_{lin-Sim} E_c(Q_0)/6k_BT \tag{2.32}$$

with the fraction of conductance in the linear regime G_{lin-CB}, which is related to Coulomb blockade based transport. The total charge transport in the linear regime is calculated by the sum of the contributing transport mechanisms:

$$G_{lin-tot} = G_{lin-Sim} + G_{lin-A} + G_{lin-GM}$$

with the Simmons, Arrhenius and granular metal related transport conductance in the linear regime $G_{lin-Sim}, G_{lin-A}$ and G_{lin-GM}, respectively. The contribution of charge transport via CB is estimated in the linear regime ($|U_{sd}| < 0.1$) using:

$$G_{lin-Sim} = G_{lin-tot} \frac{\Delta G_{meas-CB}}{\Delta G_{CB-theory}} \tag{2.33}$$

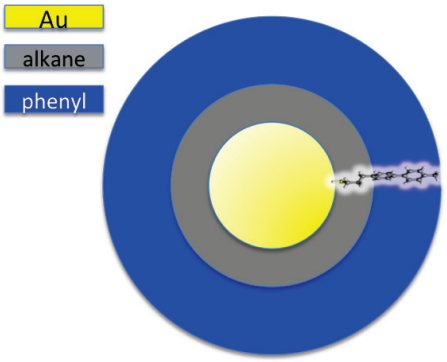

Figure 2.8.: Illustration of a multishell capacitor, created by a gold NP, which is capped by a molecule, which consists of two subunits

with the measured Coulomb blockade peak height $\Delta G_{CB-meas}$.
There are two channels for SET transport (i) elastic, where one and the same electron tunnels through the left and the right barrier, and (ii) inelastic, involving two different electrons for current transport and leaving an electron-hole excitation. The transport current in the case of elastic tunneling process (i) is predicted to be linear, in the case of the inelastic process (ii) the current is proportional to U^3 [90].
The related capacitive coupling is simulated by a spherical multi shell capacitor with different permittivities ϵ_n of the shells. According to Fig. 2.8, the total capacitance is calculated by the serial capacitance of the subsequent shells:

$$C_\Sigma = (\Sigma_n C_n^{-1})^{-1}, \tag{2.34}$$

using the capacitance of one shell $C_n = 4\pi\epsilon_0\epsilon_n(r_{n-1}^{-1} - r_n^{-1})^{-1}$, with the inner and outer shell radii r_{n-1},r_n, respectively. For the case where the molecule-capped NP (with a radius r_{NP}) is in physical contact with one electrode, and a vacuum gap of l_{vac} remains at the electrode, the capacitive coupling is calculated using:

$$C_{sphere-plane} = 4\pi\epsilon_0\epsilon_r k(r, l_{vac}) \tag{2.35}$$

The coupling of the NP to an infinite plane is numerically approximated with:

$$k(r_{NP}, l_{vac}) = \sum_{n=1}^{\infty} \frac{\sinh\left(\ln\left(\frac{r+l_{vac}}{r_{NP}} + \sqrt{\left(\frac{r_{NP}+l_{vac}}{r_{NP}}\right)^2 - 1}\right)\right)}{\sinh\left(n \cdot \ln\left(\frac{r_{NP}+l_{vac}}{r_{NP}} + \sqrt{\left(\frac{r_{NP}+l_{vac}}{r_{NP}}\right)^2 - 1}\right)\right)} \tag{2.36}$$

2.5. Influence of light on the NP-molecule-nanoelectrode system

In normal photodiodes, mobile charge carriers in the valence and/or conduction bands are generated by the incident light, which increases the conductivity. This type of photoconductance was also observed in nanostructured photoconductors by Nakanishi et al. [37]. The conductivity through 3D NP arrays is either increased or decreased on irradiation with visible light of wavelengths close to the particles' surface plasmon resonance. The reactance in conductance due to illumination of light in such systems is dependent on the properties of the capping molecule, i.e. on the charging of the molecule. The conductivity of electrically neutral (polar and nonpolar) molecules increases on irradiation using plasmonic frequencies, due to the photo current effect [37]. In contrast, in the case of electrically charged (either negatively or positively) groups, the conductivity decreases on irradiation. These observations are explained in terms of the light-induced creation of mobile charge carriers, the transport of which through the charged capping molecules is inhibited by carrier trapping in transient polaron-like states [37]. However, it is remarkable that even nanostructured devices, based on molecule-capped NPs, with of a length scale two orders of magnitude smaller than the incident light exhibit photoconductance.

The generation of heat in NPs and arrays of gold nanoparticles under illumination is investigated theoretically by Murphy et al. [91]. In these considerations the NPs are embedded in a homogeneous dielectric medium and illuminated by a standard xenon flash lamp. The temperature of the nanoparticle is strongly influenced by the thermal resistance at the nanoparticle-medium interface. Optical interactions are found to be important, if the centers of the particle are separated by about twice the particle diameter or less. Thermal interactions between NPs via the medium are found to be relevant for the temperature increase in the dielectric medium, see 2.9a). The maximum temperature increase is proportional to the volume fraction of the NPs in the medium [91]. The calculated increase in temperature of a single NP and two touching NPs as a function of the nanoparticle radius is shown in Fig. 2.9b). The segmented lines represent the power absorbed by a single nanoparticle or each individual nanoparticle in the two nanoparticle case. Further experimental investigations on the temperature change due to exposure of light is shown in the supplementary information. The temperature change of the substrate is investigated using the critical temperature of a

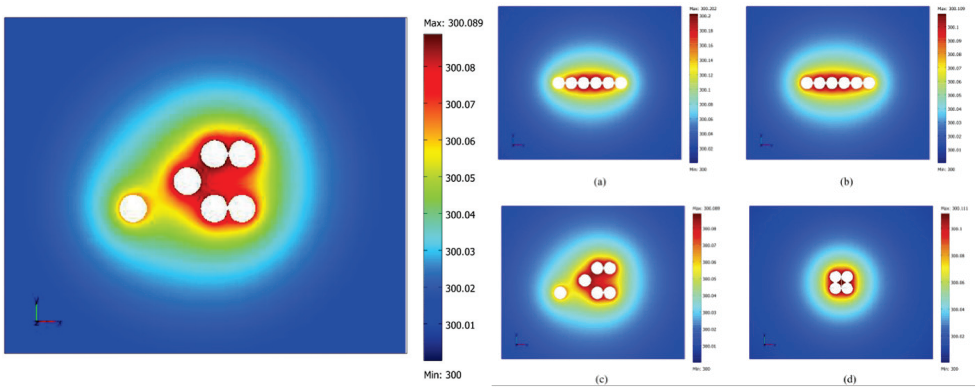

Figure 2.9.: (left) Temperature increase after a flash pulse in dependence on the NP radius for a single nanoparticle (circle) and two touching nanoparticles (triangle). Absorbed power (dashed line) of the single nanoparticle (square marker) and of two nanoparticles divided by two (cross marker). (right)Temperature distribution in a cluster of six NPs placed on a plane in a less-ordered arrangement. The nanoparticle radius is 20 nm and the cell dimension is 40 nm in each direction (only the area surrounding the cluster is shown in each subfigure). The color scale gives temperature in kelvin. [91]

superconducting Nb film to the metal state on a SiO_2 substrate, which is covered by 50% with Nb.

3. Measurement equipment

In the beginning of my work as PhD student I had to start all the experimental work that is described in the following chapters from the scratch. That means a new laboratory, including all measurement setups, had to be established. Therefore a facility plan for e.g. inert gas, Helium recovery, electricity, compressed air etc., was created. In the laboratory four facility areas are equipped: (i) an electro static dis-chargement (ESD) protected work bench for the dielectrophoretic trapping (DEPT) setup as well as for sensitive electrical equipment, (ii,iii) two areas are equipped with a helium recovery line and gas supply (helium, argon, nitrogen) suitable for cryostat setups, (iv) a secondary facility work bench for e.g. battery charging, soldering and a PC for data analysis and measurement controlling.

3.1. Motivation and concept of the measurement setup

In the proposed experiments a molecular capped NP is measured in a transistor like geometry at different temperatures and under illumination of light with a discrete wavelength. Therefore two measurement setups had to be created. The performance of one experiment involves: (1) the immobilization of NPs from solution in a nanoelectrode configuration by dielectrophoretic trapping (DEPT), (2) interconnecting between measurement setups and (3) performing transport measurements on a NP-nanoelectrode system in transistor geometry under inert gas atmosphere, for a temperature range of 4 K- 300 K and using the possibility to illuminate the system with light of discrete wavelength.
The immobilization technique by DEPT is different for i.e. various solvents, size of the NP and charged/uncharged NP. The DEPT trapping-box was tailored for the respective demands of each molecule-NP-solvent system. After successfully trapping of the

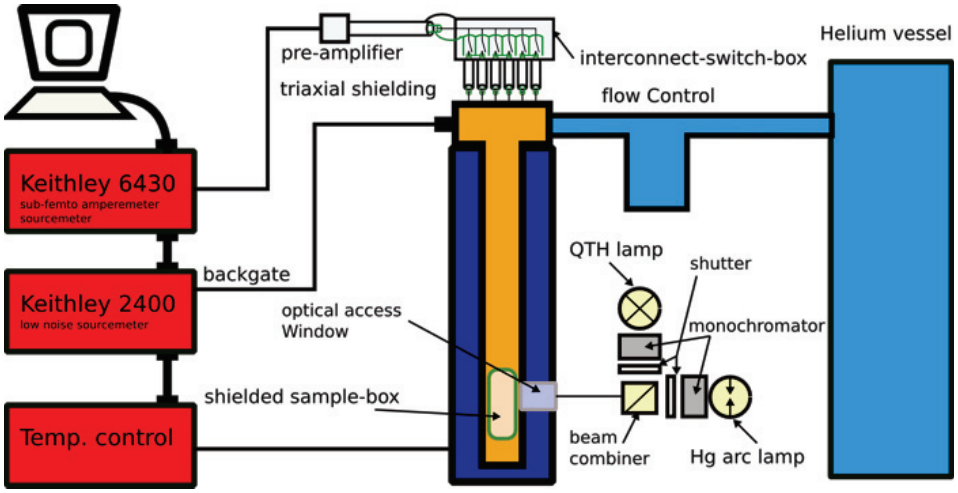

Figure 3.1.: Schematic illustration of the main measurement equipment. The sample was measured in a continuous flow cryostat in a helium gas atmosphere at variable temperatures between 4 K and 300 K. The triaxial shielding of the connection wires was continued thoroughly in the shielded sample-box as well as in the interconnect-switch-box, which permits switching between different input lines. The sample can be illuminated with light of discrete wavelength and intensity in two separately tunable beam lines through an optical access window, which has a homogeny bandpass for UV up to NIR.

NP the transfer of the chip carrier to the measurement equipment was a critikal-point in each experiment. Nanoelectrodes that have tip separations of smaller than 10 nm are sensitive to electrostatic dis-chargement (ESD), since even small fluctuations in voltage may generate high electric fields. In the case that a NP is immobilized in between the nanoelectrodes the distance between the metal objects is reduced to ≈ 1 nm, according to the molecular length. Since the electrical field increases with the inverse of the distance between two metal objects, the generated electric field is even higher. The risk of a damage to the sample was reduced by following an interconnection route, involving the creation of additional equipment, i.e. the interconnect-switch-box. The main measurement of sub-picoampere currents of devices with transistor geometry during illumination with light was performed in a continuous flow cryostat under a Helium gas atmosphere. Through the optical access window of the cryostat the sample is illumi-

nated with light of discrete wavelength and intensity, using the optical setup.
In the following sections the DEPT-trapping-box, interconnect-switch-box, sub-pico-ampere cryostat setup and the optical-setup for the proposed measurements, see Fig. 3.1, were described. Beside these measurement equipments a chemical inert chip-carrier was designed, which connects the nanoelectrodes with the measurement equipment. All parts of the equipment described below were created with carefully chosen materials to ensure an isolation resistance ($> 100\,\mathrm{T}\Omega$) and a chemically inert environment, which can be baked up to 520 K in order to eliminate organic residuals, improve vacuum properties and minimize chemical contaminations.

3.1.1. Chip carrier

The chip carrier bridges the nanoelectrodes with the different measurement equipments. The circuit board as well as the circuit path were created by chemically inert materials, since they are in contact with various solvents, e.g. toluol, hexane, chlorbenzol and water during: (i) deposition of the NP solution, (ii) DEPT in saturated gas atmosphere of the solvent, or (iii) rinsing with the solvent for cleaning . As circuit board the commercially available RUBALIT® (Al_2O_3) fulfilled these requirements. The circuit path was created by a company (Beratronic GmbH), which is specialized in prototype fabrication, in thick film technology of Pt/Pd. The organic rest in the Pt/Pd film was removed by four cycles of each 2h in a plasma etcher at 200 W. Gold plated mini smp plugs (Rosenberger GmbH) interconnected the chip carrier with the measurement equipment. On the contrary the sample was connected via commonly used Al wires, which were soldered by an ultrasonic bonder (Manual Wire Bonder 4500 by Kulicke & Soffa). The triaxial shielding was consecutively followed down to the sample. The chip carrier is created by the printed circuit board, which is mounted on a V2a board. A picture of a 'ready-to-measure' prepared chip carrier is shown in Fig. 3.2.

3.1.2. DEPT trapping-box

Dielectrophoresis is the motion of particles due to the interaction of an induced dipole in the particle with a nonuniform electric field. The electric field between the electrode tips was generated by applying a AC or DC voltage over the nanoelectrodes.
The trapping event was measured in a voltage divider circuit, as depicted in the equivalent circuit Fig. 3.4a) by a lock-in amplifier. The serial reference resistor R_{ref} was chosen

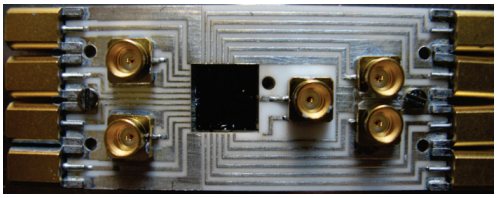

Figure 3.2.: An Al_2O_3 chip carrier with printed Pt/Pd circuit path is shown. The measurement setup was connected by mini-smp plugs and the sample is bonded by Al wires. The carrier is mounted on a 1 mm thick V2a plate, which is electrically connected by four M1 screws to the guard line of the triaxial shield on the circuit path.

in the same order of magnitude as the NP-molecule-nanoelectrode system (>10 MΩ). Since the input impedance of the lock-in amplifier is 10 MΩ the voltage drop over a high ohmic reference resistor was measured in a pre-amplification circuit. Therefore a combination of two operation amplifiers was applied: the 'ultra low input bias current instrumentation amplifier' INA116 (Texas instruments) and the 'low noise operational amplifier' OP37 (ANALOGDEVICES), as depicted in Fig. 3.4b). The output voltage $A_{\text{ref-out}}$ was measured by the lock-in amplifier SRS830 (Stanford Research Systems, Inc.). Both the twelve nanoelectrodes and the eight different reference resistors ((1, 10, 100) MΩ, (1, 10, 100) GΩ, 1 TΩ) and one inter-changeable resistor, which was shunted with a 1 nF capacitance, were computer controllable, accessed by 20 ceramic reed relays (Meder electronic AG). The reed relays have a leak resistance > 500 TΩ, see Fig. 3.4c). The computer interface of the trapping-box was optically isolated in order to reduce 50Hz noise generated by the computer. The stray capacitance C_{guard} of the twelve input lines to the guard shield is depicted in Fig. 3.4c). Due to the line capacitance of the Kapton coated connection wires and the on-chip capacitance between AuPd lines, the stray capacitance was estimated to $C_{guard} > 200$ pF. The capacitance between each input line is half of this value, thus the magnitude of coupling between the input lines inhibits a separate detection of the trapping event for a single electrode pair. This problem was solved by setting the guard line to ground potential, as depicted by the green colored circuit in Fig. 3.4 c). Thereby the stray capacitance between the nanoelectrodes and the guard was parallel to the voltage source (see green colored part in circuit depicted in Fig. 3.4 a)) and the input lines became decoupled.
Additionally, triaxial shielding of the blue (opposite) part of the electrode reduced the

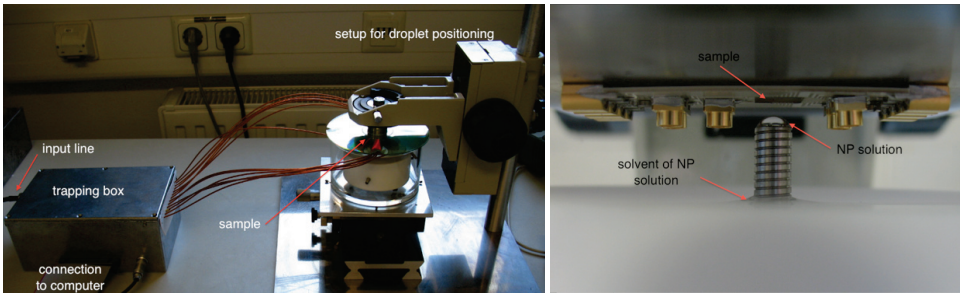

Figure 3.3.: (left) DEPT setup to suspend the nanoelectrodes with NP solution, in a bottom-drop and top-sample approach. The twelve nanoelectrodes and eight reference resistors in the trapping box for DEP trapping are controllable by computer. The trapping procedure is monitored by a lock-in amplifier in a voltage divider circuit over a reference resistor. (right) The bottom-drop and top-sample approach is depicted. The droplet of NP solution is in a saturated gas atmosphere of the same solvent as the NP solution. Thereby the evaporation rate is minimized.

stray capacitance over the nanoelectrode $C_{electrode}$ (between the blue and the red colored line) to $<0.1\,\mathrm{pF}$. The stray capacitance over the reference resistor was determined to $\approx 8\,\mathrm{pF}$ depending on the choice of reference resistor. The leak resistance over the nanoelectrodes was $R_{n-el} > 1\mathrm{T}\,\Omega$, which was quite good for a coaxial cable, thus without triaxial shielding.

The nanoelectrodes were suspended with solution by two different strategies. The favored deposition method depended on the properties of the solvent of NP solution. Solutions, which have a high surface tension and a low vapor pressure, were suspended with the drop-on-sample method. That means a small amount (between $5 - 15\mu\mathrm{l}$) of NP solution was deposited with an Eppendorf pipette on the sample.

For solvents, i.e. toluol with a high vapor pressure speed, the time window for trapping was too small ($<5\,\mathrm{min}$) for this type of deposition. Therefore the opposite approach of deposition was followed. A small amount of NP solution was deposited in a small mold, the sample was approached from the top, the bottom-drop top-sample approach. In a saturated gas atmosphere of the solvent the time window for DEPT was increased for toluol to $>45\,\mathrm{min}$. Fig. 3.3 shows the setup for the bottom-drop top-sample approach.

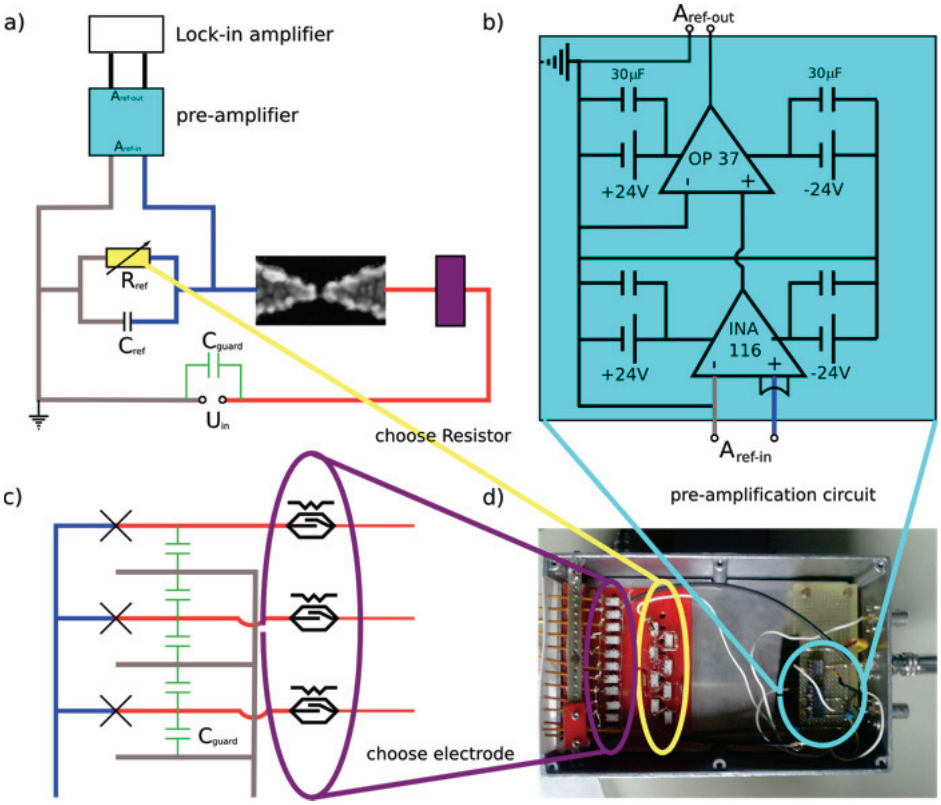

Figure 3.4.: a) Equivalent circuit of the DEPT electrical circuit. A combination of AC and DC $U_{in}(t) = A_{in}\cos(\omega t) + B_{DC}(t)$ or two AC voltages $U_{in}(t) = A_{in}\cos(\omega t) + B_{AC}(t)\cos(\omega t)$ was applied to a voltage divider circuit. During the DEPT a voltage drop over the reference resistor (R_{ref} $(1, 10, 100)\,\mathrm{M\Omega}, (1, 10, 100)\,\mathrm{G\Omega}, 1\,\mathrm{T\Omega}$) was measured by a pre-amplification circuit and handed over to a lock-in amplifier. In the equivalent circuit diagram the connection lines are color coded to identify electrical connections in the different sketches. b) the voltage drop A_{ref-in} over a high ohmic resistor R_{ref} was measured by a pre-amplification circuit converting the signal to a voltage $A_{ref-out}$ with low output impedance to the lock in amplifier. c) Schematic illustration of stray capacitance (green colored line) between the connection lines and the triaxial guard. The guard is set to ground potential (compare a)). d) Image of the DEP trapping measurement box, containing the electrode switching relays (purple), reference resistor switching relays (yellow) and the pre-amplification circuit(light blue).

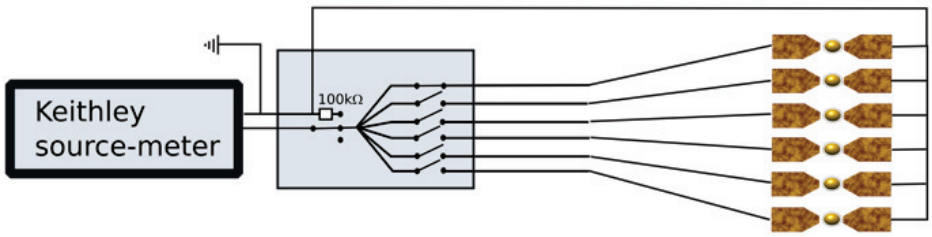

Figure 3.5.: The picture shows the interconnect-switch-box, the triaxial shielding was consequently followed for each of the six lines, which are switchable individually to the connected/isolated state. The leads to the nanoelectrodes are either (i) shorted by a a 100 kΩ resistor, for interconnection of the measurement equipment or change of the input line, (ii) isolated from the measurement equipment, to change the battery, or set to measurement position.

3.1.3. Interconnect-switch-box

The interchange between different measurement setups was a critical point in the experimental process, due to electrostatic dis-chargement (ESD). During the connection to the measurement setup the leads of the nanoelectrodes and the measurement equipment were set to the same electrostatic potential (over a 100 kΩ resistor), which reduces the risk of a damage of the device. This procedure was also necessary during the interchange between the six input lines of the cryostat, see Fig. 3.7. The input line was chosen by a mechanical switch, which opens and closes the power supply to a ceramic reed relay (Meder). Thereby the triaxial shielding was thoroughly followed.

3.1.4. Sub-picoampere cryostat setup

The proposed experiments on a molecular based system in a three terminal configuration require transport measurements at variable temperatures and under illumination of light with discrete wavelength. The transport currents in such systems ranges from sub-pico-ampere to several μA. In order to achieve a current resolution in the sub-pico-ampere range the leak resistance and stray capacitance to the ground was reduced by triaxial shielding. But inert, low temperature stable triaxial cables were commercially not available for cryogenic systems. The triaxial shielding was imitated by a teflon®

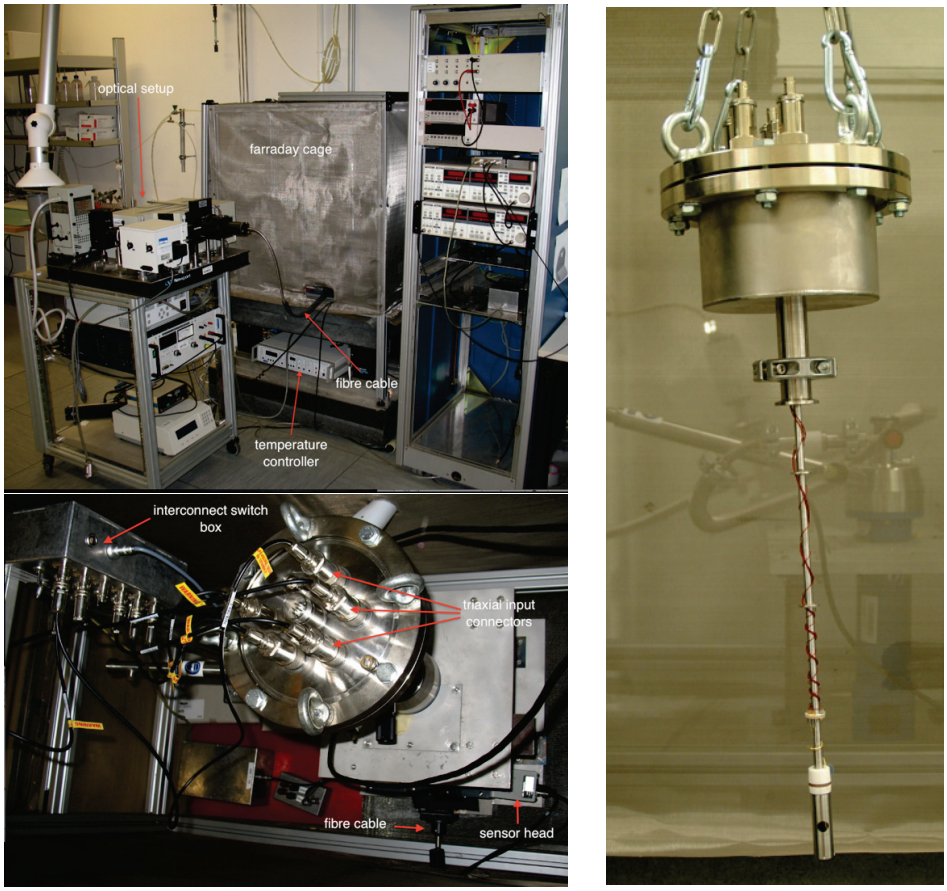

Figure 3.6.: The top left picture shows the Sub-pico-ampere cryostat setup, with the two stage vibration damping system. The base plate (335 Kg granite) was damped with elastic rubber dampers, the top plate (195 Kg granite) with pneumatic isolators. The cryostat, the interconnect-switch-box and the preamplifier of the Sub-femtoampere sourcemeter is shielded in a Faraday cage. The optical setup is coupled via a fibre cable to the optical cryostat. The bottom left image depicts the triaxial shielded input connectors of the probe stick and the switch box. At the bottom optical input fibre cable and the radiometry sensor head for life monitoring is visible. The complete probe stick is shown in the right image. The shielded sample box was electrically isolated from the (grounded) probe stick by a technical ceramic (Macor). The metal tube of the shielded sample box has a hole to expose the sample to light.

coated coaxial cable, which was densely fitted in a V2A tube. Thereby microphone noise, which is originated by changes in capacitive coupling between ground and input line due to relative movement, was minimized. The concept of triaxial shielding was continued in the sample chamber of the cryostat. The chip carrier was placed in a shielded metal box, which was connected to the guard potential. Therefore a new probe-stick was designed, where the sample space was electrically isolated from the grounded top of the probe stick, see Fig. 3.6. The mounting plate of the chip carrier and the shielding metal tube at the end of the probe-stick were set to guard potential. Electrical contact between the shielding tube and the grounded cryostat shell was avoided by teflon® space holders. The shielding tube has a hole at the position of the optical access windows (Suprasil WF), which have a transmission range from 200 nm to 4.5 μm, of the cryostat. Six triaxial shielded inputs are provided in the cryostat setup. Additionally 5 DC twisted pair input lines are available for e.g. gating, application of magnetic field etc.

The continuous flow cryostat Optistat CF (Oxford Instruments) was applied for variable temperature measurements. In this cryostat the heat conduction is realized by inert Helium exchange gas, therefore a vacuum shielding ($< 10^{-5} mBar$) of the sample chamber is necessary. The sample chamber of the cryostat was evacuated by a turbo molecular pump to a base pressure of $< 10^{-5}\, mBar$ and flushed with 400 mBar Helium, before it was cooled. A full range pressure sensor was mounted to monitor the pressure during pumping. The pressure of the Helium exchange gas is sensed by a mechanical Gauge. The cryostat is operated in two different modes: (i) pump mode (for T > 2 K), (ii) push mode (for T > 4.2 K). During measurement the push mode was favored, since less mechanical vibrations were generated. The temperature in the continuous flow cryostat was controlled by a computer and regulated between 4 K and 300 K.Due to heat conduction via He exchange gas the sample was homogeneously cooled in a He bath, which prevented the previously observed melting of the NP-nanoelectrode device in a vacuum cryogenic system.
The complete sub-pico-ampere measurement setup is shielded by a Faraday cage to reduce the influence of electromagnetic radiation. The damping system consists of two stages: (i) the base plate (330 Kg granite) is damped by a rubber damper BRB110 40SH (STS Schwingungstechnik Schuster GmbH) and (ii) the top plate (195 Kg granite) is damped with a light load OEM pneumatic isolator I-125A (Newport Corporation).

The total weight on the top dampers is estimated to 255 Kg (Cryostat, cryostat stand, Pb accu-pack, inter-connect-switch-box). This is the maximum load for the dampers, whereby the resonance frequency is reduced to below 2Hz. The total weight on the bottom rubber dampers (pneumatic isolators, stand for isolators, faraday cage, equipment) is estimated to 660 Kg. Therefore the resonance frequency of the base plate with the rubber dampers is 7 Hz. The resonance frequency of the complete setup was measured with an acceleration cube to 3 Hz.

3.1.5. Optical setup

In cooperation with Uwe Paetzold in the group of Thomas Halfman from the TU Darmstadt an optical equipment was created to illuminate the molecule capped NP in transistor geometry with light of discrete wavelength and adjustable intensity. As depicted in Fig. 3.7 two beam lines with different light sources were applied: (i) a mercury arc lamp in the UV-light-line and (ii) a quartz tungsten halogen (QTH) lamp in the VIS-light-line. In each beam line a discrete wavelength was chosen by a monochromator. In the VIS-line the monochromator SpectraPro ® 150 of Acton Research Cooperation was applied. The bandwidth of the incident light was chosen by a micrometer slit between 1 nm to 120 nm. In the *UV-line* a $\lambda/4$ monochromator MS257 of Oriel was used, the bandwidth was chosen between 1 and 30 nm. In this beam line the second order maxima are filtered by an automated filter wheel, which is controlled by the monochromator MS257. Both beams were turned on/off separately by a fast shutter setup (M-76994) provided by Oriel with a maximum frequency of 40 Hz in burst mode and a single raise/fall times of respectively 3 ms / 5 ms. The beam lines were combined by a 50/50 polka dot beam splitter (PDOT-2) with wavelength independent transmission in the range of 250 nm to 2500 nm. The combined beam was coupled to a Fused silica fibre bundle, thereby the optical setup was flexible for use in other measurement setups. A second polka dot beam splitter close to the viewport of the cryostat enabled the monitoring of the intensity of the incident light by the Merlin radiometry system of Oriel with a 1x1 cm silicon detector head (M-70336).

3.1.6. Measurement programming environment: Testpoint

The interface to the measurement equipment was programmed in a script-like program environment called Testpoint. To achieve the requirements of each step of the

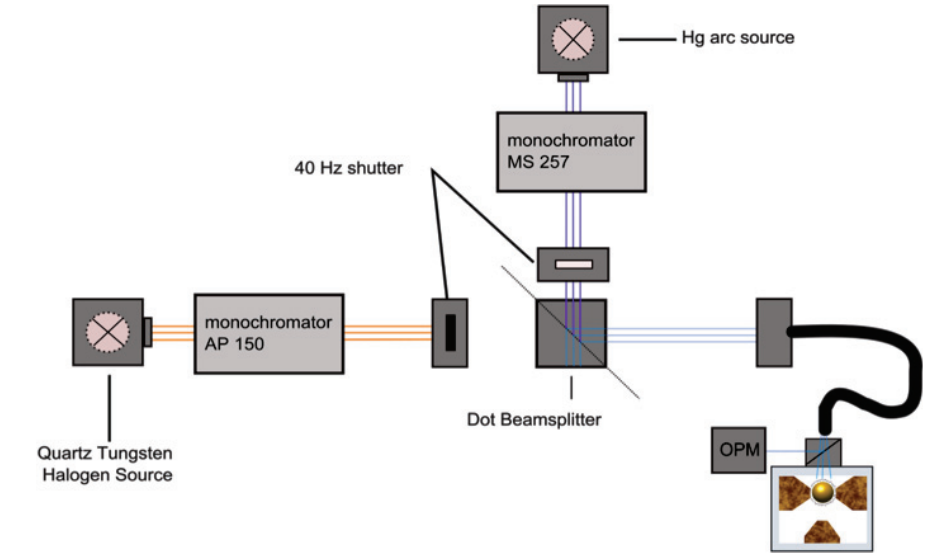

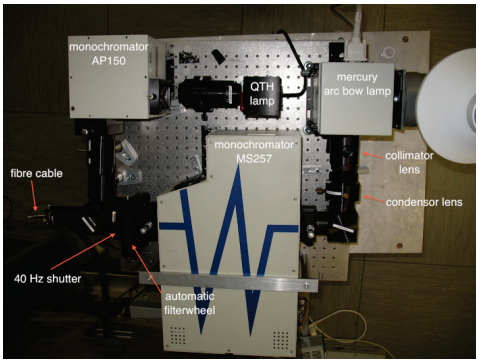

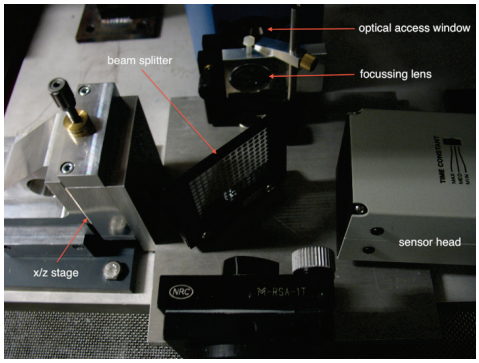

Figure 3.7.: The optical setup is depicted in the top sketch. (bottom left) The setup contains two beam lines (UV / VIS), where the wavelength of each is set by a monochromator to a discrete value. The light exposure is turned on/off by a fast shutter system. (bottom right) The intensity of the light was measured with a radiometry system (OPM) close to the sample space and adjusted by tuning the supplied power to the QTH lamp and the mercury arc lamp.

experiment three different programs were coded: (i) Impedance spectroscopy Measurement, (ii) AC/DC dielectrophoretic trapping, (iii) $I(U_{sd}, U_g, \lambda(t))$, $I(U_{sd}, U_g, \lambda(t))$, $U_{sd}(I_{sd}, U_g, \lambda(t))$ measurement under illumination of light with discrete wavelength λ.

(i) Completely automated impedance spectroscopy measurements , with the possibility to choose the start / stop frequency, reference resistor(s) and electrodes. The output was a frequency-dependent measurement of voltage and phase drop over the reference resistor.

(ii) The AC/DC dielectrophoretic trapping program controls the amplitude and frequency of the lock-in signal with which the trapping event is detected, as well as either the amplitude and frequency of the AC trapping pulse or the voltage ramp for the DC trapping, which are applied to the DEPT trapping box to generate the electric field for DEPT trapping. The output was a time-dependent measurement of voltage and phase drop over the reference resistor.

(iii) The main program for transport measurements in a three terminal device under illumination with light of discrete wavelength had three different measurement modes for source drain transport measurements: cyclic ($I(U)$), constant ($I(U_{sd}, t)$ and $U_{sd}(I, t)$). In cyclic ($I(U)$) mode it is possible to choose the backgate voltage automatically. Two beam lines were applied to expose the sample. In each beam line the wavelength was chosen by a separate monochromator, the intensity of the incident light was monitored by a radiometry system and adjusted by controlling the power supply. The beam lines were turned on/off in a constant or alternating mode with frequencies up to 40 Hz.

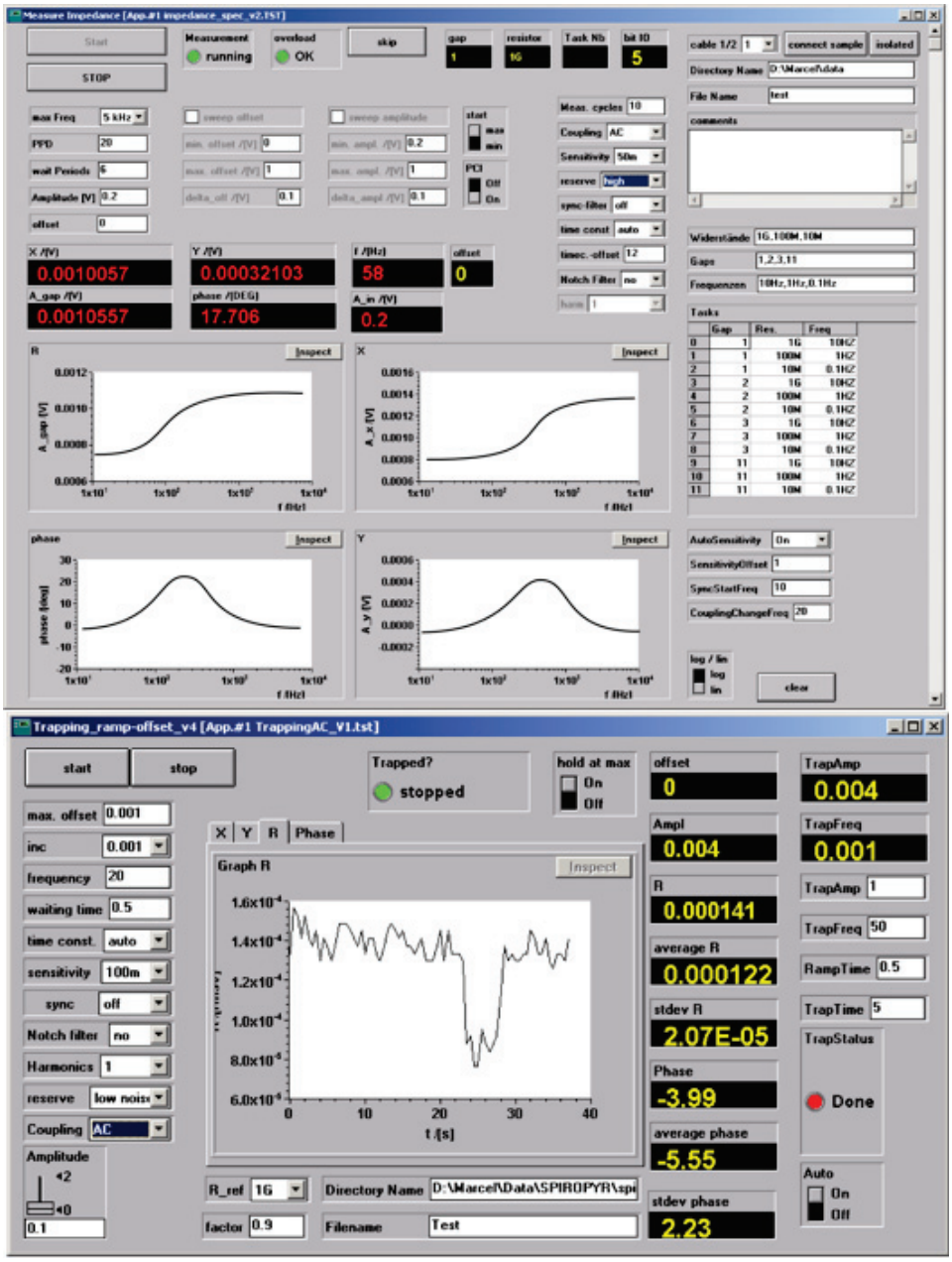
Measure Impedance [App.#1 impedance_spec_v2.TST]
Start
STOP
Measurement
running
overload
OK
skip
gap
resistor
Task Nb
bit IO
cable 1/2
connect sample
isolated
Directory Name
File Name
test
comments
max Freq
5 kHz
PPD
20
wait Periods
Amplitude [V]
offset
sweep offset
sweep amplitude
start
max
min
PCI
Off
On
Meas. cycles
Coupling
AC
Sensitivity
reserve
high
sync-filter
time const
auto
timec.-offset
Notch Filter
no
X /[V]
0.0010057
Y /[V]
0.00032103
f /[Hz]
58
offset
0
A_gap /[V]
0.0010557
phase /[DEG]
17.706
A_in /[V]
0.2
Widerstände
1G,100M,10M
Gaps
1,2,3,11
Frequenzen
10Hz,1Hz,0.1Hz
Tasks
R
X
phase
Y
Inspect
AutoSensitivity
SensitivityOffset
SyncStartFreq
CouplingChangeFreq
log / lin
log
lin
clear
Trapping_ramp-offset_v4 [App.#1 TrappingAC_V1.tst]
start
stop
Trapped?
stopped
hold at max
On
Off
offset
0
TrapAmp
0.004
max. offset
0.001
inc
0.001
frequency
20
waiting time
0.5
time const.
auto
sensitivity
100m
sync
off
Notch filter
no
Harmonics
1
reserve
low noise
Coupling
AC
Amplitude
0.1
X
Y
R
Phase
Graph R
Ampl
0.004
TrapFreq
0.001
R
0.000141
TrapAmp
1
average R
0.000122
TrapFreq
50
RampTime
0.5
stdev R
2.07E-05
TrapTime
5
Phase
-3.99
TrapStatus
Done
average phase
-5.55
Auto
On
Off
R_ref
16
Directory Name
factor
0.9
Filename
Test
stdev phase
2.23

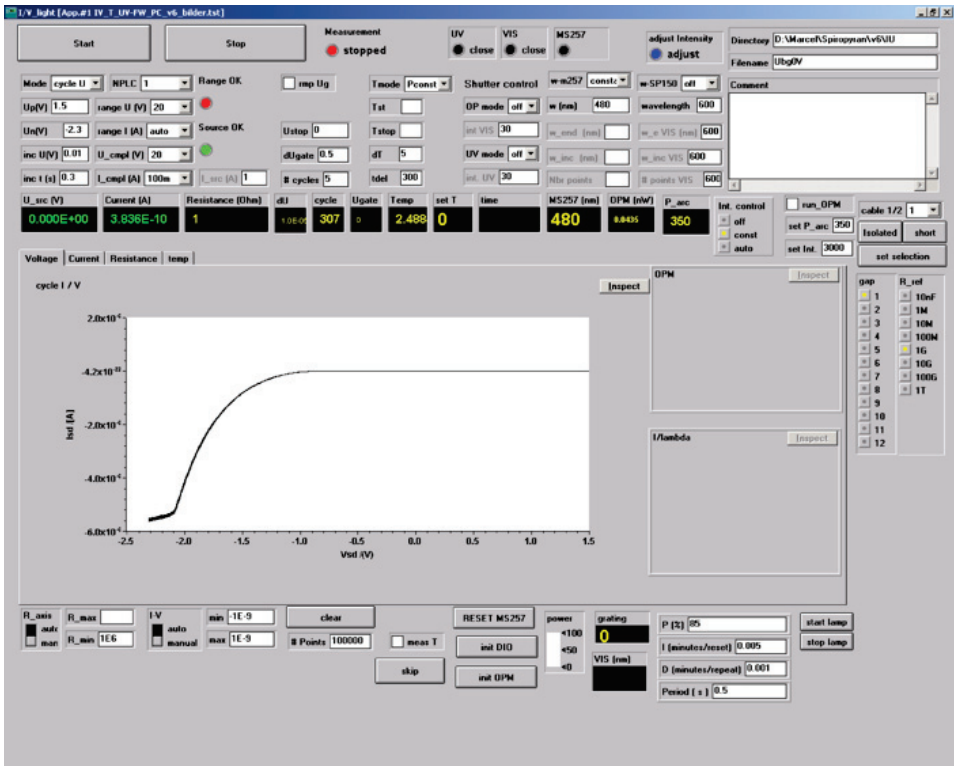

Figure 3.8.: Testpoint program user interface of the Impedance spectroscopy measurement program and the AC/DC dielectrophoretic trapping (top) and the main measurement program (bottom).

4. Nanometer-Scaled Lithography

The emerging field of molecular electronics focuses on the possibility of using organic molecules as functional units to supplement CMOS devices, to create sensors and to fabricate solar cells. However, reliably contacting molecules or molecule-capped NPs for transport measurements remains challenging in CMOS compatible device geometry. Beyond the scientific challenges, such as exploring new functionalities and new application fields, demanded by such measurements, state-of-the-art lithography techniques are essential for creating new devices with a tip separation of only a few nanometers. Nanolithography is the branch of nanotechnology concerned with the fabrication of nanometer-scaled structures. It involves the creation of patterns with at least one lateral dimension between the size of an individual atom and approximately 100 nm. Currently, there are several lithographical methods for patterning nanometer-scaled devices [92].

- **Optical lithography at ultraviolet (UV) wavelengths** is the standard process for patterning 22 nm state-of-the-art devices in the semiconductor industry. It is claimed that the miniturisation to 11 nm will be reached in industrial fabrication within the next decade [93]. The resolution limit $W_{res} = (0.25\lambda)/\mathrm{NA}$ is dependent on the wavelength $\lambda = 193\,\mathrm{nm}$ (ArF) of the incident light, the resolution factor of 0.25 and the numerical aperture NA $\propto n$ with the refractive index n. The optical immersion technique allows optical lithography on a scale of a few nm (currently 22 nm). By immersing the lens in a high-refractive-index liquid [1], an ultimate limit of 11 nm can be reached by a 157 nm(F_2) based technology [93]. However enormous problems have been encountered by optical lithography in going beyond 193 nm. A problem with the sole lens material for 157 nm lithography, for example, is attaining the required quality in sufficient quantities and at affordable prices. Another problem with 157 nm lithography is the lack of soft pellicle for the mask. A hard pellicle has a lower NA, which reduces the resolution. Since

the whole waver is exposed in one shot UV lithography has a high throughput, currently 100-180 wafers (300 mm)/hour.

- The application of **extreme ultraviolet (EUV) light** (ranging from 10 nm to 100 nm) in lithographic processing was pioneered by L.R. Hughey in the early nineteen eighties [94]. EUV overcomes diffraction problems during circuit manufacture, since the designed structures are in the same order of magnitude as the applied wavelength. The resolution is five times greater than the commonly used UV technology. With such high resolution, the inherent high throughput as compared to optical lithography will enable the development of a broad range of applications beyond semiconductor electronics.
- **E-beam Lithography (EBL)** has a low throughput of 1 wafer/1300 hours due to vector scan pattern generation. Therefore, EBL is mainly applied for prototype, mask and mold fabrication, e.g. for UV, EUV and NIL. A threefold increase in throughput can be achieved by a new type of chemically amplified resist (UV1116) [95], which requires an exposure dose that is three times lower compared to the necessary dose for the PMMA 950K. Efforts are focussing on developing a multiple beam pattern generator [96] to speed up EBL fabrication (currently by a factor of 110) in a pre-alpha prototype. The aim is to extend the multiple beam pattern generator to 13,000 parallel electron beams, which would make it possible to fabricate 10-30 wafers/hour.

- **Nanoimprint lithography (NIL)** has been developed as a cost-effective alternative to high-resolution ebeam lithography for printing sub-20 nm geometries in a pattern. Imprinting is based on the principle of mechanically pressing a thin polymer film with a stamp containing the nanopattern in a thermo-mechanical or UV curing process. The patterned polymer can be used as a final device, e.g. lens for imaging sensors, microfluidic chip, biomedical array etc. It can also be used as a high-resolution mask for subsequent steps of the fabrication process. Due to the at-once pattern generation, a throughput of 50 wafers(300 mm)/hour can be achieved [92].

4.1. Nanoelectrode Fabrication by E-beam Lithography

For the study of molecules, molecule-capped NP or nanocrystals, the fabrication of nanoelectrodes with a tip separation in the range between 1 and ~ 5 nm has attracted much attention. Currently, tip separations in this range are difficult to achieve using a single direct write EBL step. Further fabrication steps are required, such as narrowing the gap further by, for example electroless gold plating [97], metal evaporation [98] and shadow evaporation [99] or sculpting using a transmission electron microscope (TEM) [100], electromigration, and self breaking techniques [2].

The EBL technique involves direct writing with a focused beam of electrons in a layer of electron sensitive resist, to achieve the desired structures. On one hand, the resolution was limited by the generated dose pattern. The contrast between exposed and unexposed areas was dependent on the (i) beam shape, (ii) beam step size of the writing machine and (iii) the exposure dose (stray dose) related to the proximity effect, which is generated by interactions of the electron beam with the substrate.
On the other hand, structural control was also limited by the fabrication process itself, e.g. contrast and sensitivity of the developer, homogeneity of the resist film, grain size of the metal film, and the stability of the mask layer resist. Due to these influences, the geometry of the metal structure differs from the pattern design.

The fabrication of the nanostructure was performed in two steps. The nanoelectrodes were first created by EBL in a 'lift off' process, whereby the connection pads, which creates the contact to the connection lines that are fabricated by optical lithography, measuring $10x30\,\mu\text{m}^2$ were also created (Fig. 4.1 blue, red and yellow). Second, macroscopic connection lines, which overlap the previously created pads, were fabricated by optical lithography (Fig. 4.1 gray). Simultaneously guard lines for the triaxial shielding were processed. The metal structure on the sample was connected to the measurement equipment by bonding wires.
The nanostructures were fabricated on a 1x1 inch p-doped Si substrate ($1 - 5\Omega\text{cm}^{-1}$), which was coated with a 400 nm thermally oxidized insulating SiO_2 layer. An array of 3x3 samples with a dimension of 6x6 mm were placed on each substrate . On each sample, eleven nanoelectrodes and one shortcut were fabricated with a pitch of $300\,\mu$m by

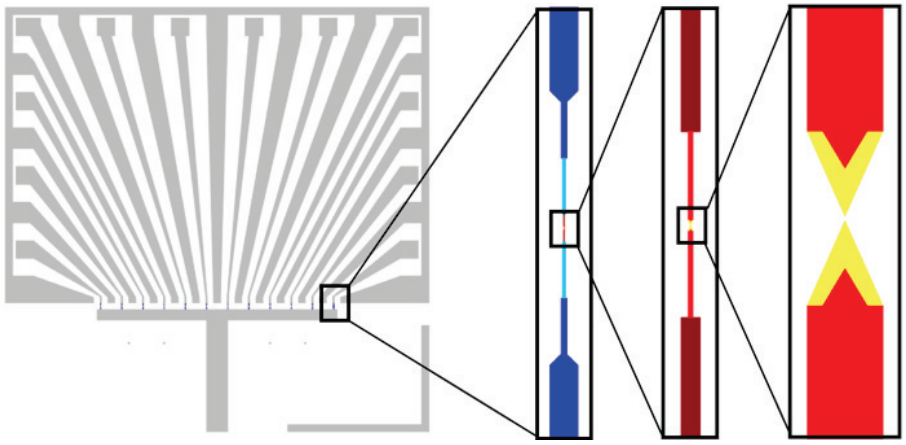

Figure 4.1.: Schematic of the pattern layout of a 6x6 mm sample. Gray colored structures were created by optical lithography. On the right side the nanoelectrode pattern for the EBL process of fabrication route A are shown. The pattern was composed of two parts: (C) the coarse pattern (blue (C1), light blue (C2)) were written with a coarse beam (5 nA beam current) and (F) the fine pattern (red (F1), light red (F2), yellow(F3)) with a fine electron beam (60 pA beam current). Lighter colors have a higher exposure dose (C2,F2). The dark/light red lines have a width of respectively 200 nm, 50 nm and a length of $4\,\mu m, 1\,\mu m$.

EBL. The line width in the pattern design was subsequently reduced: $2\,\mu m$ (dark blue), $1\,\mu m$ (light blue), $200\,nm$ (dark red), $50\,nm$ (light red), as shown in Fig. 4.1. Hence, the contrast in the exposure dose pattern was increased by a reduction in the stray dose.Additionally, for writing speed reasons, the pattern was divided into two parts: coarse structures (C), (blue) and fine structures (F), (red and yellow). The desired coarse pattern C was exposed to an electron beam with a diameter of 35 nm and a current of 5 nA. The fine structure F was generated by the smallest stable beam, which had a current of 60 pA and an estimated beam diameter of < 5 nm. The exposure dose for the C and F patterns was optimized for the thickest lines $2\,\mu$m and 200 nm, respectively. Secondly the 'missing' stray exposure dose in the thinner lines was compensated by a higher dose (coded by lighter colors in Fig. 4.1). Both types of lines (light/dark colors) were written in the same writing process, but with a different exposure dose, which was

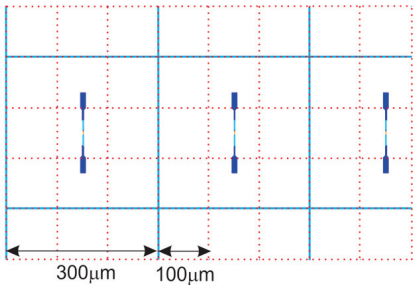

Figure 4.2.: Schematic illustration of the relative position of the pattern to the main-fields. Astigmatism in the beam shape is reduced by a centered beam according to the main field. The red/blue colored dashed lines show the main-field of the fine/coarse structure respectively. The dimensions of the squared fields were $100\mu m$ and $300\mu m$ respectively.

set into a relation to a relative dose factor. Finally, the electrode tip separation was fine-tuned by adjusting the relative dose of the arrow-shaped tip (yellow).
The writing dose of each pattern pixel was specified by the beam current I_b, the exposure time T_e and the beam step size d_b:

$$D = \frac{I_b T_e}{d_b^2} \tag{4.1}$$

The relative dose was adjusted by scaling the exposure time T_e. The Gaussian vector scan system writes the pattern section wise in so call 'main-fields'. The substrate is mounted on a xy-stage, which rasters the main-field positions. In each main field the structure was exposed in a meander type path. The tips of the nano-electrode structure were arranged in the center of a main field as shown in Fig. 4.2. At this position the electron beam pointed perpendicular to the substrate, thus the astigmatism was minimal. In addition the same beam shape for each nanoelectrode structure was guaranteed .
In this chapter three different production routes (A,B,C) of nanoelectrode fabrication were described. In production route A a 'first approach' fabrication recipe was applied. In route B the resist layer stack and developer was optimized. Thereby the mask-bridge, which is creating the tip separation, was strengthened. As a result the yield of the fabrication process was increased. In route C the proximity effect related exposure dose was reduced by an improved dose pattern and device geometry. Consequently a reduction of the electrode tip separation to only 3 nm with a yield of 55 % was achieved. On the whole with the optimized fabrication recipe and machine settings it was possible to achieve a geometrical control over the metaled structures in the nanometer scale.

4.1.1. Fabrication route A: Standard resist layer

In fabrication route A of the nanoelectrode fabrication a 'standard' bilayer resist system was applied. The top layer defines the desired structure (mask layer), therefore the high resolution resist polymethyl-methacrylate (PMMA) 950K was chosen. The bottom layer resist was 33 % methacrylic acid (MAA) in PMMA, in short PMMA/MAA (2:1). Due to the higher sensitivity of the PMMA/MAA (33%) compared to PMMA 950K an undercut in the resist layer profile was created, which is mandatory for a lift-off process. Therefore the bottom layer is further referred to as undercut layer. The predefined tip separation of the electrode structure was 5 nm.
The employed EBL procedure basically consists of five steps: 1. Spin coating resist on the substrate, 2. Exposing pattern to an electron beam, 3. Development of resist, 4. Metal deposition and 5. Lift off:

1. The polymers PMMA/MAA 1 % in 2-methoxyethanol and PMMA 950K 1 % in ethyl-lactate were spin coated to 40 nm (0-2000 RPM in 5 s,2000 RPM for 55 s) and 20 nm (0-4000 RPM in 10 s,4000 RPM for 50 s), respectively on the Si/SiO_2substrate. The solvent of the polymer layers was baked out for 7 min at 210 °C and 180 °C respectively.

2. The pattern layout (Fig. 4.1) of the electrode structure was designed by CleWin. The desired nano-electrode exposure pattern was generated in a meander type raster with the Gaussian vector scan system EBPG 5000+ from Vistec. The electron beam was accelerated with 50 kV and the aperture of the beam was chosen to 200 μm.
   The coarse pattern C was written with a dose of 370 μ/C cm^2, a beam current of $I_b = 5\,nA$ (a beam diameter of 35nm) and a beam step size of $d_s(C) = 20\,nm$. The exposure dose of pattern $C2$ had a relative dose factor of C2 $r(C2) = 1.1$ compared to layer $C1$, the corresponding relative dose is calculated as follows: $D(C2) = 1.1D(C1)$.
   The fine pattern F was written with an exposure dose of 390 μC/cm^2, a beam current of $I_b = 60\,pA$ and a beam step size of $d_s(F) = 1\,nm$. The relative dose factors for each section in the fine layer were $RD(F2) = 1.2$ and $RD(F3) = 2.7$. The tip electrode separation can be fine tuned by the relative dose factor r(F3).The

smallest beam, thus the lowest stable beam current of 60pA, was applied. This leads to a beam diameter of below 4nm [101], with which the high resolution dose pattern was created.

3. PMMA/PMMA-MAA were positive working resists. The exposed areas of the mask layer and the undercut layer was developed under gently shaking with the commercially available developer AR 600-56 (Allresist GmbH) for 150 s. The development was stopped in isopropanol (IPA) for 30s. Next the sample was blow dried with nitrogen and baked for 2 min at 50 °C.

4. The complete structure was covered by a two layer metal film deposited by electron beam evaporation in a vacuum chamber under a pressure of $< 1 \cdot 10^{-7} mBar$. A 1 nm thick Ti layer, which was deposited with a rate of 0.05 nm/s, served as sticking layer. Second, the actual electrode material, a 20 nm thick Au layer was evaporated at a rate of 0.3 nm/s. In the evaporation machine the substrate is cooled to avoid a potential damage of the mask bridge, due to the heat, which is generated by the irradiation of the hot evaporating metal ($T \approx 2850K$).

5. The sacrificial material (i.e. PMMA/PMMA-MAA) together with the covering metal was washed out with acetone for two hours, rinsed with IPA and blow dried with nitrogen. After this process only the predefined electrode structures remained.

The applied developer AR 600-56 has shown a low dark development of unexposed areas, therefore the contrast is higher for long development times. A dose test was applied for three different development times (90 s, 120 s and 150 s). The best result was achieved for a development time of 150 s and a dose of 390 μC/cm^2. The structures were characterized with a scanning electron microscope (SEM) of Zeiss Gemini I. In this fabrication route tip separations of 5-9 nm with a reproducibility of approximately 45% have been observed (Fig. 4.3), the remaining nanoelectrodes were mostly shorted. In conclusion we can state, that the tip electrode separation and the yield was limited by the fragility of the mask bridge (Fig. 4.4).

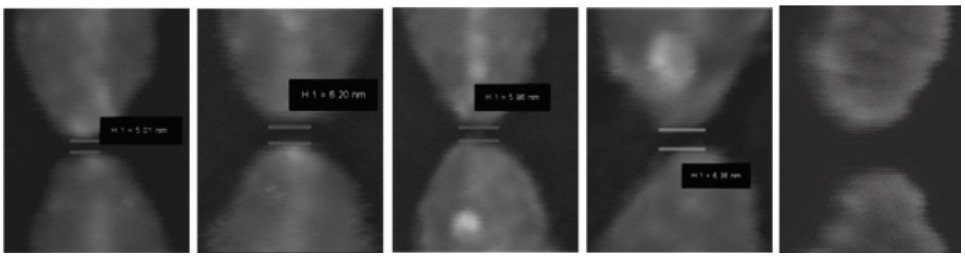

Figure 4.3.: SEM micrographs of nanoelectrodes of a single sample fabricated in route A, a tip separation of 5-9nm within 45% was achieved by the standard developer and standard resist layer stack.

4.1.2. Fabrication route B: Optimized resist layer and developer

The low reproducibility of nano-electrode structures that were fabricated as described in route A can be explained by an instability of the PMMA mask bridge (Fig. 4.4). Since the top and the bottom resist were developed simultaneously the mask bridge was developed from the bottom as well, which makes the bridge more fragile.
In fabrication route B the mask bridge became more rigid by following two strategies: (i) The undercut layer resist was exchanged to polymethyl-glutarimide (PMGI), which is solvable by an alkaline metal free developer. Therefore the mask layer (PMMA 950K) and the undercut layer (PMGI) were developed in two independent steps. The effect of this was that the mask bridge was not developed from the bottom side. (ii) A new type of developer based on IPA/water (7:3) was applied. As reported by Yasin et al. [102] the contrast as well as the sensitivity was higher compared to the previously used developer AR600-56. Thereby dark development was reduced.

1. The thickness of the polymers PMGI 1 % in cyclopentanone and PMMA 950K 1 % in ethyl-lactate was adjusted by spin coating to 45 nm (0-4000 RPM in 2 s, 4000 RPM for 58 s) and 25 nm (0-2000 RPM in 5 s, 2000 RPM for 55 s) respectively. The solvent of the polymer layers were baked out for7 min at 260 °C and 180 °C

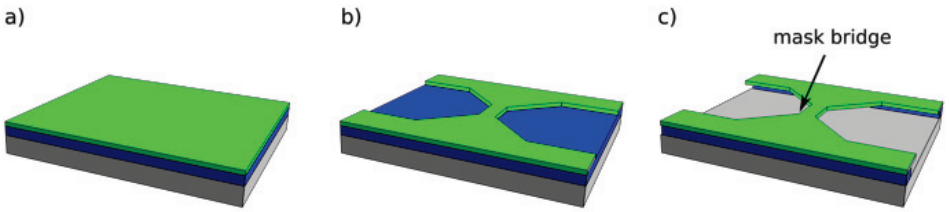

Figure 4.4.: The schematic a) depicts the resist layer stack PMMA 950K (green) and PMGI (blue). In b) only the PMMA mask layer was developed in water/IPA (7:3), c) development of the PMGI undercut layer in alkaline developer. The remaining mask bridge was forming the electrode tip separation.

respectively. Before the PMMA 950K layer was spin coated, the PMGI layer was pre-exposed with UV-light 320 nm in a mask aligner for 1min. Thereafter the PMGI layer becomes solvable by the developer and hence the dimension of the undercut profile in the resist layer will scale with the development time.

2. The exposure dose of the coarse layer can be reduced to $350\,\mu\mathrm{C/cm^2}$, due to the higher sensitivity of the developer. The beam current of $I_b = 5\,nA$, the beam step size of $d_s = 20\,\mathrm{nm}$ and the relative dose factor of $RD(C2) = 1.1$ was the same as in route A. The fine layers F were now written with a dose of $370\,\mu\mathrm{C/cm^2}$, a beam current of $I_b = 60\,pA$, a beam step size of $d_s = 1\,nm$ and the relative dose factors were $r(F2) = 1.2$ and $r(F3) = 2.75$.

3. The exposed areas of the PMMA were developed for 80 s using the high contrast, sensitivity developer IPA/water (7 : 3). The development was stopped for 30 s in demineralized water and blow dried with nitrogen. Later the PMGI was developed for 40 s using the metal-free alkaline developer MF21a (MicroChem), the development was stopped for 60 s in a demineralized water bath, blow dried with nitrogen and baked for 2 min at 50 °C.

t

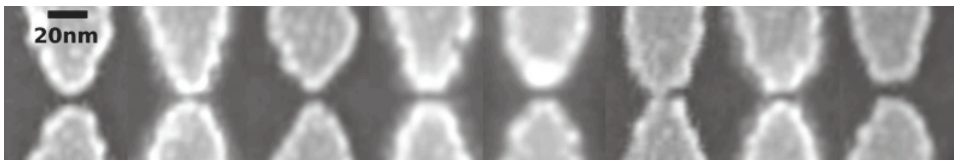

Figure 4.5.: SEM micrographs of nanoelectrodes of a single sample fabricated in route B, a tip separation of 4-6nm within 45% was achieved by the new developer and resist layer stack.

4. The deposition of the metal film was performed as described in route A. The electrode material was exchanged to Au_3Pd_2, which is less ductile and has a lower mobility. Furthermore a new sample holder for the evaporation machine was created, which improved the thermal conduction between the cooling system and the substrate.

5. In the lift-off process the sacrificial material (PMMA/PMGI) together with the covering metal was washed out with N-methyl 2 pyrrolidone (NMP) for two hours, dipped in acetone in an ultrasonic bath for 2 min, rinsed with IPA and blow dried with nitrogen. Only the exposed electrode structures remain.

In this fabrication route we were able to achieve nanoelectrodes with a tip separation of 4 nm - 6 nm with a yield of 45 %. The thin PMMA bridge became more rigid due to the separate development step of the PMGI and the new IPA/water based developer [102]. As a consequence a higher fabrication yield and a better structural control were achieved.

4.1.3. Fabrication route C: Proximity optimized pattern geometry

After the optimization of the resist layer stack and the application of a high contrast developer the remaining limit in patterning accuracy was mainly due to proximity effects. The proximity effect related exposure dose in EBL is a consequence of electron

scattering due to their interactions with each other and with atoms in the resist and substrate. Coulomb interaction between electrons within the beam causes a spreading of the electron beam to a Gaussian dose profile (forward scattering). The incident electrons were back scattered due to interactions with the atoms in the substrate, thereby the mask layer resist was exposed a second time over a large area with a radius of tens of μm. These effects reduce the contrast in the exposure dose pattern. The most commonly used proximity correction program PROXECCO is based on dose adjustment. However this method significantly fails to correct features below 65 nm accurately [103]. Proximity effect correction in sub 65 nm structures requires not only a geometrical optimization but also a gradient in dose at the edges of structures [104].

Scattering of a point sized electron beam in a realistic material stack (25 nm PMMA 950K, 45 nm PMGI, 400 nm SiO_2 on a bulk Si substrate(Fig. 4.6 a)) was calculated in a Monte Carlo simulation. The proximity effect included exposure dose profile was achieved by folding the result of the Monte Carlo simulation with a Gaussian beam (green line). As first approximation a beam spot size of 3 nm was chosen. As a result the proximity effect corrected exposure dose profile of each exposure pixel was achieved in dependance on the radial distance, compare Fig. 4.6a,b). In this Figure three different sections in the exposure dose profile can be denoted: (I) a Gaussian shape in the central profile section for ($r_{dp} < 20\,nm$), (II) an exponential decay in the intermediate profile section for (20 nm $< r_{dp} <$ 2 μm) and (III) a cut off in the section for 2 μm $< r_{dp} <$ 20 μm.
In fabrication route C the contrast in the dose pattern was increased by two mechanisms: (i) a reduction of the exposed area and (ii) a minimization of the necessary exposure dose in the region with a diameter of 40 μm around the nano-electrode:

(i) According to the dimensions of the section II/III in the Monte Carlo simulation the length of the 50 nm, 200 nm wide line was set to 1.98 μm and 18 μm respectively, see Fig. 4.6 c). The new tip design (central section I in the Monte Carlo simulation) was formed as a sharp spike with three segments of 8 nm length and a line width of 2 nm, 6 nm and 8 nm respectively. In a region of 20 μm radius around the electrode tip position the total pattern area was reduced by approximately 77 % compared to the design, which was used in routes A and B. In each section I,II,III the magnitude of area was reduced by 47 %, 60 % and 77 % respectively

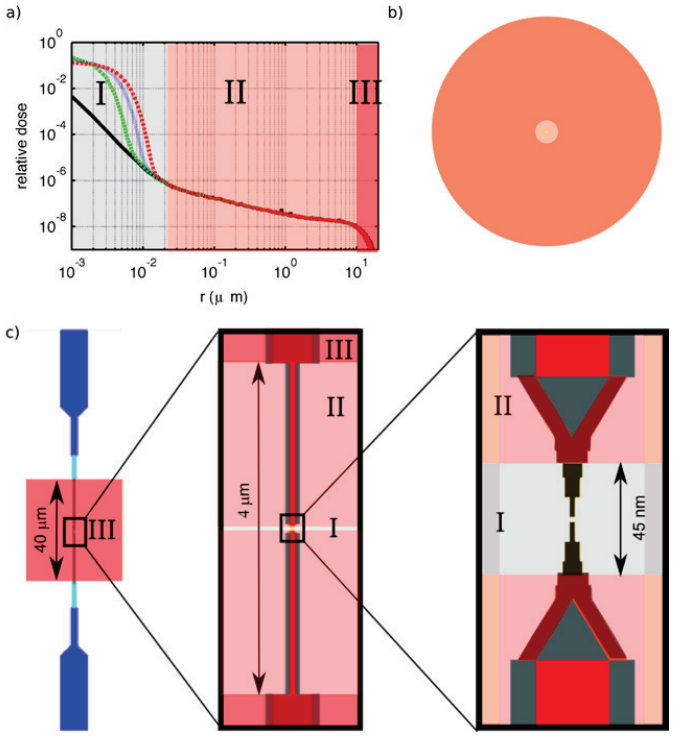

Figure 4.6.: a) Monte Carlo Simulation of a point shaped electron beam, which was backscattered in the material stack: 25 nm PMMA, 45 nm PMGI, 400 nm SiO_2, 100μm Si. In the dose profile three different sections (I-III) can be dedicated: (I) Gaussian (light gray), (II) exponential decay (light red) and (III) a cut-off section (red). The green curve shows a realistic dose profile for a Gaussian beam(3 nm). b) This 2d-schematic illustrates the dose pattern of one exposure pixel. The different colors denote the sections (I-III) of the dose profile. c) In the new pattern design the length of the 200 nm and 50 nm lines and the tip geometry were chosen according to the dimensions of the sections I-III in the Monte Carlo simulation (background colors). Each line with different coloration (red, gray, brown, black) was exposed with a different relative exposure dose. The relative dose factors (r) of the Coarse Pattern (C1-2, dark/ligth blue) were RD(C1) = 1.0, RD(C2) = 1.1 respectively. Fine Pattern connection lines (F1, red) RD(F1) = 1.0, the outline stripes (F2, gray) RD(C2) = 1.3, and the tip (F3-4, brown/black) RD(C3) = 3.2 and RD(C4) = 6.0.

compared to the pattern area in the previous design.

(ii) The amount of dose per area was reduced by a proximity correcting trick. Due to missing stray dose the outlining area (with a width of 10 nm around the structure) was less exposed compared to central regions of a line. According to this fact 60 %, 90 % and 98 % of the 50 nm, 200 nm and 1 μm lines respectively were slightly over exposed in the previous design. The outline stripes had a width of 10 nm (green colored line) and a relative dose factor of RD(F2) = 1.3, compare Fig. 4.6c). The dose at the core of the 50 nm and the 200 nm line was RD(F1) = 1.0 (red colored line). The brown colored arrow shaped part has a relative dose factor RD(F3) = 3.2 and the spike like black part RD(F4) = 6. Thereby the total amount of exposure dose applied in the region of interest ($r < 20\,\mu$m) was reduced by approximately 7 % compared to a design without an outline stripe. Finally the geometry in the central section I was optimized in order to sharpen the electrode tip.
The exposure dose of the coarse beam ($I_b = 5\,nA$) was similar as applied in route B (355 μC/cm^2). The dose for the fine layers F(1-4) had to be increased to 380 μC/cm^2, due to the reduction in the stray dose.

In this fabrication route an electrode tip separation of 2-4 nm with a yield of 55 % was achieved. The rest of the structures were shortened. This points to the fact, that the PMMA mask bridge was still a limiting factor in nanoelectrode fabrication. Due to the high contrast developer and the improved contrast in the dose pattern a structural control in the nm scale was achieved.

4.1.4. Comparison of fabrication routes

In the previous sections three different fabrication routes have been presented. In route A a standard double layer resist and a high resolution commercial available developer was applied. In the exposure pattern design a concept to reduce stray dose was developed. In this first approach nanoelectrodes with a tip separation down to 5nm have been observed, but the fabrication yield was only 45 % for tip separations of $5 - 9\,nm$. In route B the undercut layer resist was changed to PMGI, which is developed in a separate step. Additionally a developer with higher contrast and higher sensitivity was

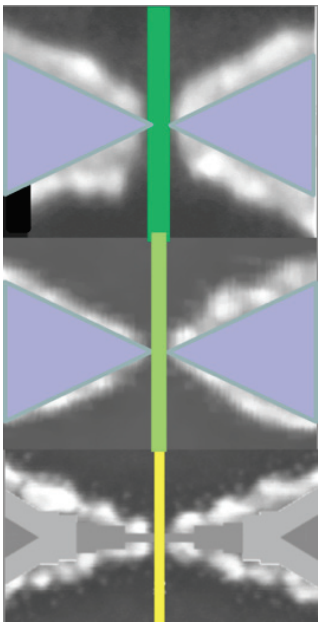

route A

- Standard double layer resist:
  20nm PMMA 950K // 40nm PMMA-MA
- **Electrode tip separation:** 5-9 nm 45%

route B

- optimized resist layer stack:
  20nm PMMA 950K // 45nm PMGI
- high contrast developer (H_2O/IPA)
- **Electrode tip separation:** 4-6 nm 45%

route C

- optimized resist layer stack
- high contrast developer
- optimized pattern design
- **Electrode tip separation:** 2-4 nm 55%

Figure 4.7.: The fabrication history shows a reduction in tip separation from 7 nm to 3 nm, while the fabrication yield was improved to 55%. This was achieved by a new resist layer stack (route B) and an optimized pattern geometry/dose (route C).

applied to develop the mask layer. Thereby the mask bridge became more rigid compared to route A. This improved the tip separation to 4-6 nm within 45 % in route B. In both fabrication routes the predefined tip separation of the pattern was 5 nm. However a smaller design of the nanoelectrode tip separation did not lead to a better result.
In route C the geometrical design of the connection lines was optimized based on the analysis of a Monte Carlo Simulation. Additionally a higher relative dose at the outlines reduces the overall necessary dose further. With this two improvements a tip separation of $2-4\,nm$ with a yield of 55 % was reached.

As depicted in Fig. 4.7 the yield in nanoelectrode fabrication was increased by the resist layer stack (PMMA950K / PMGI), due to a more rigid mask bridge. A more accurate

structural control was achieved by applying the new type of developer (H_2O/IPA). The contrast between exposed and unexposed areas i.e. in the electrode tip region was enhanced by a reduction of:

(i) the pattern area, whereby line dimensions were chosen according to the sections of a Monte Carlo simulation (77 %) ,

(ii) the exposure dose by an increased outline dose (7 %).

Thereby an electrode tip separation of 2-4 nm within 55 % and a structural control within the nm scale was achieved.
Next a smaller tip separation of 2 nm or even 1 nm in the design pattern is to be tested. There might still be some possibilities to increase the yield and decrease the tip separation of the fabricated nanoelectrodes. The PMMA mask bridge might become more rigid, if the thickness of the mask layer is increased. Furthermore the electron beam might be defocused due to a systematic error in focus alignment as described in [101]. Empirical studies of V. Sidorkin et al. [101] have shown three possible reasons for a defocused beam in the EBPG 5000+: (1) a contaminated holder marker prohibits a correct focussing on the marker and therefore on the sample as well. (2) An incorrect recalculation of the focus point to work distance, which usually differs from marker height position. (3) Sample not perfectly aligned perpendicular to ebeam axis. An adjustment of the focal point of the E-beam pattern generator might eliminate systematic focal adjustment errors and improve the structural control further [101]. Within the optimization of the fabrication route a hardmask process was tested as well. The application of Cr or Pt was intended to stabilize the mask bridge. However, the control over the shape as well as the yield of the fabrication was not improved. The reason for that is the increased amount of backscattered electrons during electron beam exposure and the additional edge process, using Crome edge (Cr) and reactive ion beam edging (RIBE) for Pt.

4.2. Simulation of the effective dose pattern

The fabrication of nanometer scaled structures by EBL underlies several limitations as described in the previous sections. In this section the realistic beam shape of the pattern generator and the proximity effect corrected exposure dose is discussed. The intended exposure dose pattern of both the first and the proximity effect optimized

pattern is shown in Fig. 4.1,4.6. The realistic dose pattern was generated pixel by pixel of the design pattern. At each pixel a dose profile was applied such as calculated in the Monte Carlo simulation for different beam spot sizes of α_{beam} = 2 nm, 3 nm, 4 nm. In this simulation also the relative dose settings were taken into account , see Fig. 4.8.

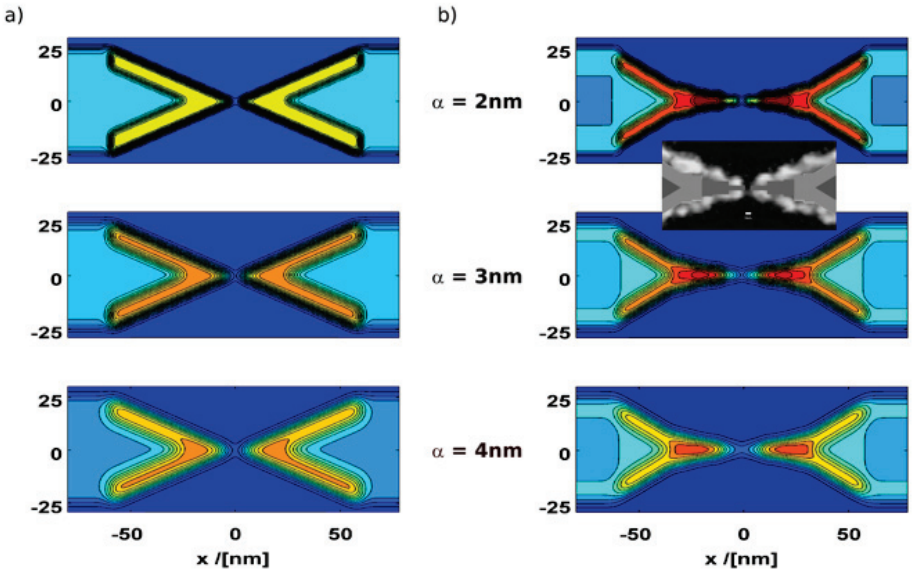

Figure 4.8.: Simulation of the realistic exposure dose pattern. The Monte Carlo simulated exposure dose profile using beam diameters of α_{beam} = 2 nm, 3 nm, 4 nm was applied at each pixel of a) the first pattern and b) the second pattern design. The dose patterns were normalized so that the center of the 50 nm line in 100 nm distance to the tip electrodes has the value 1.2 RD (Relative Dose) in the first and 1 RD in the second design. Comparing a scanning electron micrograph of a device that is fabricated with the second design and the simulated dose patterns, the beam size is estimated to 2 nm - 3 nm.

In the simulation a pattern with the size of 40 μm x 200 nm was used. A comparison of the simulated exposure dose pattern, for electron beams with different spot sizes (in Fig. 4.8), with a scanning electron micrograph, the spot size is estimated between 2 nm and 3 nm. This estimation is in accord with the measured 3.9 nm for a 140pA beam at 100kV acceleration voltage by Sidorkin et al. [101]. The higher the beam current

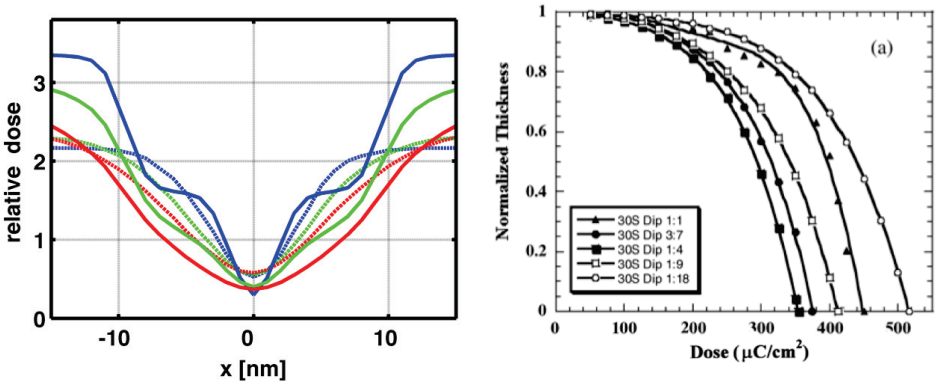

Figure 4.9.: The cross section of the proximity effect corrected exposure dose pattern through the gap position is plotted (left side) for the first pattern design (dashed line) and the optimized pattern design (solid line). The different beam sizes of $\alpha_{beam} = 2\,\text{nm}, 3\,\text{nm}, 4\,\text{nm}$ (blue, green, red) show a significant difference in contrast. The graph on the right side was published by *Elsevier, Microelectronic Engineering 61-62 (2002) 745 - 753.* Contrast curve for PMMA developed with various compositions of water/IPA. In our specific case a composition of IPA/water (7/3) was applied (graph with filled dots).

the bigger are Coulomb interactions between electrons of the incident beam, therefore a slightly bigger beam is expected. In Fig. 4.9 a cross section of the exposure dose pattern through the nanoelectrodes is shown for the new design (solid lines) and the old design (dashed lines) for beam sizes of $\alpha_{beam} = 2\,\text{nm}, 3\,\text{nm}, 4\,\text{nm}$ (blue, green, red).
Comparing the previous design with the optimized design a clear improvement in contrast was observed, i.e. the crossover from exposed to unexposed resist between the nanoelectrode tips was steeper, and the dark exposure in the center of the electrode tips was reduced from 0.52 RD, 0.54 RD, 0.56 RD to 0.30 RD, 0.35 RD, 0.40 RD relative dose for the different beam sizes respectively. The relative dose where the distance in the cross section plot equals 5 nm in the old design was 0.90RD for $\alpha_{beam} = 2\,\text{nm}$, 0.84RD for $\alpha = 3\,\text{nm}$, similarly calculated for a 3 nm Gap in the new design was 0.79RD for $\alpha = 2\,\text{nm}$, 0.52RD for $\alpha = 3\,\text{nm}$. The applied exposure dose in fabrication routes B($370\,\mu\text{C/cm}^2$), C($380\,\mu\text{C/cm}^2$) was in good accord with literature ($380\,\mu\text{C/cm}^2$) [102].

	relative dose at gap in dose pattern			
	previous design		new design	
	d = 0 nm	d=5 nm	d = 0 nm	d=3 nm
α_{beam} = 2 nm	0.52	0.90	0.3	0.79
α_{beam} = 3 nm	0.54	0.84	0.35	0.52
α_{beam} = 4 nm	0.56	0.75	0.40	0.41

Table 4.1.: Relative exposure doses (RD) extracted from the exposure dose pattern Fig. 4.9, at the center the (d=0) of the gap. The relative dose, in the cross section of the proximity effect corrected exposure dose pattern, for an electrode tip separation of d=5 nm such as observed in fabrication route B (first design) and a tip separation of of d=3 nm such as observed in fabrication route C (second design) is shown.

As shown in Fig. 4.9 a relative dose of 80 % of the necessary exposure dose corresponds to a remaining relative thickness of the resist layer of approx. 60 % (12 nm), which seemed to be a stable thickness of the mask-layer resist in outlining structures. The relative exposure dose in the center of the gap ($d = 0$ nm) and for a distance of ($d = 5$ nm) (first design) / ($d = 3$ nm) (second design) is shown in Tab. 4.1. The remaining thickness of the central part of the mask-bridge was estimated with Tab. 4.1 and Fig. 4.9 to 80 % (∼20.0 nm) for the previous design and to 98 % (∼ 24.5 nm) for the new design. Comparing the values of the relative dose for the second pattern for ($d = 0$ nm) and for ($d = 3$ nm), as shown in Tab. 4.1, a beam spot size of 2-3 nm is reasonable. Having taken all these factors into account a smaller electrode tip separation and a better structural control in the second pattern design was reasonable, even a further reduction of the nanoelectrode tip separation seems to be possible. In the second design the lines with a width of 2-8 nm, in the region of the nanoelectrodes, has to be exposed with a relative dose of 6 RD, which might be an indication that the beam is slightly out of focus or is not shaped homogeneously.

4.3. Nanoelectrodes in multi-terminal devices

The fabrication of a gated electrode structure was performed by a similar fabrication route as described above. Three different approaches have been followed: (i) a lithographically confined backgate, (ii) sidegates, and (iii) a full plain backgate.

(i) The lithographically confined backgate was fabricated, applying the EBL technique. The overlap between the gate and the nanoelectrodes was designed to approximately 50x150 nm^2, which ensures a safe alignment between the two ebeam fabrication steps. As gate material Pt was chosen, which do not tend to migrate into the isolation barrier. As electrical isolation between the backgate and the nanoelectrodes a 25 nm thick sputtered SiO_x as well as a SiN_x film deposited by plasma enhanced chemical vacuum deposition (PECVD) was tested. The RMS roughness of the combined Pt / insulator layer was below 1 nm therefore a similar yield in tip separation, as in fabrication route B was achieved, Fig. 4.10. The leak resistance between the backgate and the nano electrodes by application of small Voltages ($|U_{bg}| < 3$V) was in the order of $1\,T\Omega, 1\,G\Omega$ for the deposited SiO_x,SiN_x, respectively. Thus on the first view SiO_x as isolating barrier seemed to be a proper material, however unfortunately for higher voltages ($U_g > 3V$) a permanent short cut was observed.

(ii) The sidegates were fabricated by an EBL process similar to fabrication route B, in one run with the nanoelectrodes, see Fig. 4.10b)). Due to a higher proximity effect related exposure dose, the dose at the arrow shaped tip had to be slightly corrected to a relative dose of RD(F3) = 2.6. The size distribution of the electrode tip separation was about 7 ± 5nm, while often two of the four electrodes were shorted. The tip separation perpendicular to the transport direction was designed to 30 nm. With a relative dose at the arrow shaped tip of $RD(F3) = 2.8$ two junctions with a tip separation of ~ 10 nm (50%) were created, see Fig. 4.10c).

(ii) A thin insulating layer was necessary, since a good coupling between the backgate and the NP is mandatory. Best results for epitaxical oxide layers, which have a low defect density, were obtained by thermally grown oxides. Therefore as final approach a full plain backgate of thermally grown 26 nm thick SiO_2 was chosen,

see Fig. 4.11. The yield and tip separation was identical with fabrication route C. A leak resistance greater than 10 TΩ was measured for negative backgate voltages down to -20V. For positive voltages ($U_g > 3\,V$) a creation of a permanent short cut between the backgate and the nanoelectrodes was observed.

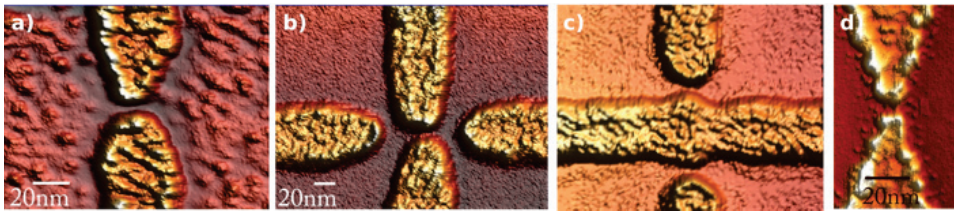

Figure 4.10.: Scanning electron micrographs, which were plotted by a commercially available program to display atomic force micrographs. a) nanoelectrode pair with 4 nm electrode tip separation with Pt backgate and 20 nm thick SiO_2 is shown. b) Side-gate structure achieved with proper exposure dose, and c) slightly overexposed, so that a two junctions were created. d) Nanoelectrode pair on a p-doped silicon full plain backgate with a thermally grown SiO_2 insulating layer.

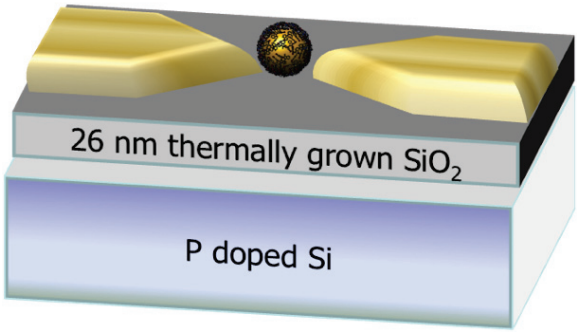

Figure 4.11.: Three terminal device realized with a full plain backgate of a p-doped Si ($1-5\Omega cm^{-1}$) substrate, utilizing a 26 nm thermally grown oxide layer as galvanical isolation between the backgate and the nanoelectrodes.

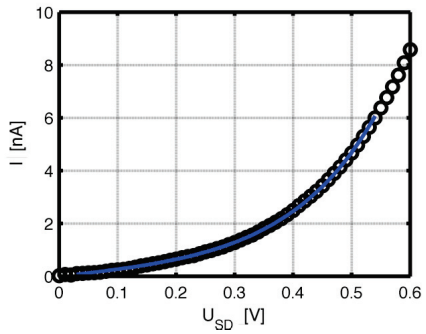

Figure 4.12.: Tunneling characteristic in nanoelectrode with a $< 3\,\mathrm{nm}$ tip separation measured after all lithographic steps, bonding on chip carrier and connected to measurement equipment. The blue line represents a fit by an automated Simmons fit routine described in section 2.1.1, yielding a barrier height of $\varphi_{vac} = (4.9 \pm 0.1)\,e\mathrm{V}$ and a separation $d = (2.2 \pm 0.01)\,\mathrm{nm}$.

4.4. Tunneling characteristics between nanoelectrodes with small tip separations

Nanoelectrodes with a tip separation of $< 3\,\mathrm{nm}$ were accessible in electrical measurements and tunneling characteristic according to the Simmons Model [8, 59] was observable. Fig. 4.12 shows an I(U) characteristic of nanoelectrodes with nanometer sized tip separation. This measurement was performed after all lithographic steps and bonding of the sample to the chip carrier and connecting it to the measurement equipment. The iterative fitting sequence as described in section 2.1.1 revealed an electrode tip separation of $d = (2.2 \pm 0.01)\,\mathrm{nm}$ and a barrier height of $\varphi_{vac} = (4.9 \pm 0.1)\,e\mathrm{V}$. It is demonstrated, that nanoelectrodes with tip separations have been fabricated by pure EBL, with which even transport investigations on long chained molecules were possible. In this thesis the performed investigations of NPs with dimensions in the nanometer-scale were analyzed, where coulomb blockade is visible even at room temperature.

Conclusion of the fabrication of nanoelectrodes

An essential part of this work is the establishment of a fabrication recipe for metallic nanoelectrodes that have a tip separation of a few nanometer, in CMOS compatible technology. An E-beam lithographical fabrication process have been worked out to provide nanometer-spaced metal electrodes and multi-terminal devices. The E-beam lithographical fabrication process was optimized to fabricate nanoelectrodes with a tip separation of only a few nanometer with an accuracy in the nanometer scale. The optimization included the enhancement of (i) the contrast in the exposed pattern, (ii) the

optimization of E-beam machine parameter and (iii) the resist/developer combination. (i) The increase in contrast of the dose pattern by a factor of 1.5, was achieved, on the one hand by reducing the exposed area around the electrode tip position according to the regimes obtained by a Monte Carlo based simulation of backscattered electrons in the substrate. On the other hand by a reduction of the applied dose using an enhanced dose setting, i.e. a higher dose at the outline of the structures.
(ii) The exposure dose pattern with best contrast and steepest steps at the border region is created with the lowest possible beam current and beam step size.
(iii) The new type of developer (H_2O/IPA) enhances the sensitivity by 15 % and the contrast by 10 %. Almost no dark development is observed. A double layer resist was chosen that is developed in two subsequent steps. Thereby the stability of the mask bridge is increased.
The contrast of the realistic exposure dose pattern was improved with (i), (ii). In combination with (iii) the sidewall of the mask layer bridge became steeper and therefore the mask layer bridge itself remained thicker. Thus in sum it is more rigid which results in a higher yield fabrication process ($\sim$ 55 %) of nanoelectrodes that have a tip separation of 2-4 nm and a geometric control, which is in the nanometer scale. These results are unrivaled in comparison with other E-beam lithographic fabricated nanoelectrodes.
There are indications that the limiting factor is the beam shape/focus. The dose in the 2 nm and 4 nm lines have to be increased by a factor of two compared to the previous tip design. This might indicate a defocused or deformed beam.

Three different methods were investigated to fabricate multi terminal devices, using 4-terminal-in-plane sidegates, lithographically defined metal backgate and semiconducting full plane backgate. In the case of four terminal devices (in plane gating), the yield was noticeably reduced, due to the increased stray dose. Additionally the attempt to contact the four electrodes with the measurement equipment leaded to the destruction of the device, probably due to electrostatic dis-chargement. Contrary, in metaled backgated structures that were isolated by a 25 nm thick SiO_2 layer, the yield did not change dramatically, but in such devices the applied voltage to the backgate was limited to a few volt (3 V - 4 V) before a breakdown of the device was observed. The best choice was the approach using the semiconducting full-plane as backgate, here no influence on the yield was observed and the device was stable for an applied gate voltage of -20 V to 2 V at room temperature.

5. Dielectrophoretic trapping of charged and uncharged NPs

In the first approaches to immobilize NPs in between nanoelectrodes, the metallic leads were covered with a self assembled monolayer of di-thiolate molecules in a mono-thiolate matrix by immersion. The di-thiol molecules serve as glue, binding the NPs to the electrodes [43]. In this approach at least two different molecules are present in the tunneling barrier and contribute to the transport current.
To avoid the complicated tunnel barrier structure, an alternative assembly of NPs between nanoelectrodes was developed by applying an electric field [105–109]. The motion of polarizable particles suspended in a solvent can be induced by a nonuniform electric field, this process is called dielectrophoresis (DEP) [105]. The electric field in the electrode tip region is generated by either an AC or DC voltage applied to the nanoelectrodes. The dipole approximation of the DEP force for a spherical particle of radius r_{NP}, in a media of permittivity ϵ_m is given by [106]:

$$F_{DEP} = 2\pi\epsilon_m r_{NP}^3 Real\{\underline{CM}(\omega) \bigtriangledown \underline{E_0}^2(r_{NP})\} \tag{5.1}$$

with the electric field $E_0(r_{NP})$, the distance r of the NP to the center of the nanogap, the frequency ω of the applied AC field, CM denotes the Clausius-Mosotti factor given by:

$$CM = \frac{\epsilon_p - \epsilon_m}{\epsilon_p + 2\epsilon_m} \tag{5.2}$$

where ϵ_p and ϵ_m are the complex permittivities of the capping molecule of the particle and the media (solvent), respectively. The Clausius-Mosotti factor, and thereby the DEP force, is maximal for small frequencies, thus for DC voltages. The electrostatic force is typically confined within 10 nm radius of the center of the nanoelectrodes, while the DEP extends to $\approx 100\,nm$ from the electrode gap, as described by [106]. In order to assemble NPs in between nanoelectrodes a threshold field must be exceeded in order

to overcome electrostatic repulsion between the NP and the electrodes/substrate, as described by Gierhart et al. [107]. The threshold field was defined as:

$$E_{th} \propto \sqrt{\frac{k_B T}{\epsilon_p r_{NP}^3}} \sim 0.056\,\mathrm{V/nm} \tag{5.3}$$

where k_b is the Boltzman constant, T the operating temperature, $r_{NP} = 7.5\,\mathrm{nm}$ the radius and $\epsilon_p = 6.9$ the permittivity of the capping molecule (MES) of the NP [107]. As a first approximation the threshold voltage scales linearly with the electrode separation, as observed by Stellacci et al. [106]. Hence, the smaller the nanoelectrode tip separation, the smaller the threshold value.
Moreover DEP trapping (DEPT) is most efficient for low frequencies and solvents with high permittivity. However, the DEP force also scales with the cube of the particle radius r_{NP}, which keeps the immobilization of small NPs in a nanoelectrode configuration challenging.
For uncharged NPs a combination of DC and AC voltage for trapping is the best solution. A charged NP is repelled from one electrode by an DC electrostatic field and covers only one of the metallic leads. Therefore AC DEP trapping is suitable in the case of a charged NP. AC DEPT has been successfully demonstrated for particles with a diameter of >15 nm with a high reproducibility by Stellacci et al. [106].

5.1. Detection of a trapping event

The DEPT was performed in a voltage divider circuit as depicted in Fig. 3.4 The trapping procedure was monitored by a lock-in amplifier, which measured the amplitude U_{ref} of the voltage and the phase drop p_{ref} over a serial reference resistor R_{ref} and the resistance over the nanoelectrodes R_{n-el}. Due to the unavoidable stray capacitance C_{ref}, C_{n-el} across resistor, the circuit is described by two serial impedances :

$$Z_{tot} = Z_{ref} + Z_{n-el}$$

using

$$Z_{ref} = (1/R_{ref} + i \cdot \omega C_{ref})^{-1} \text{ and } Z_{n-el} = (1/R_{n-el} + i \cdot \omega C_{n-el})^{-1}$$

The transfer function is:

$$H = \frac{U_{ref}}{U_{in}} = \frac{Z_{ref}}{Z_{ref} + Z_{n-el}} \tag{5.4}$$

In the limit of $\omega \to 0$ and $\omega \to \infty$ the transfer function becomes:

$$\begin{aligned} H_{\omega=0} &= \frac{R_{ref}}{R_{ref}+R_{n-el}} \\ H_{\omega=\infty} &= \frac{C_{n-el}}{C_{ref}+C_{n-el}} \end{aligned} \tag{5.5}$$

The resistance as well as the capacitance of the nanoelectrode in the voltage divider circuit the amplitude value was determined at the plateaus of the S-shaped impedance spectroscopy curve, which is plotted in the Bode diagram Fig. 5.1 for two characteristic resistances of the nanoelectrodes ($R_{n-el} = 1\,\mathrm{T\Omega}$ for empty electrodes),($R_{n-el} = 1\,\mathrm{G\Omega}$ with trapped NP) using the typical reference resistor $R_{ref} = 100\,\mathrm{M\Omega}$ and the capacitances of the DEPT setup ($C_{ref} = 8\,\mathrm{pF}, C_{n-el} = 0.1\,\mathrm{pF}$) by applying equations (5.5). Two characteristic frequencies were deduced using equation (5.4):

$$\begin{aligned} \omega_{n-el} &= \frac{1}{2\pi R_{n-el} C_{nel}} &&\approx 1.6\,\mathrm{Hz} \\ \omega_{ref} &= \frac{1}{2\pi R_{ref} C_{ref}} &&\approx 200\,\mathrm{Hz} \end{aligned} \tag{5.6}$$

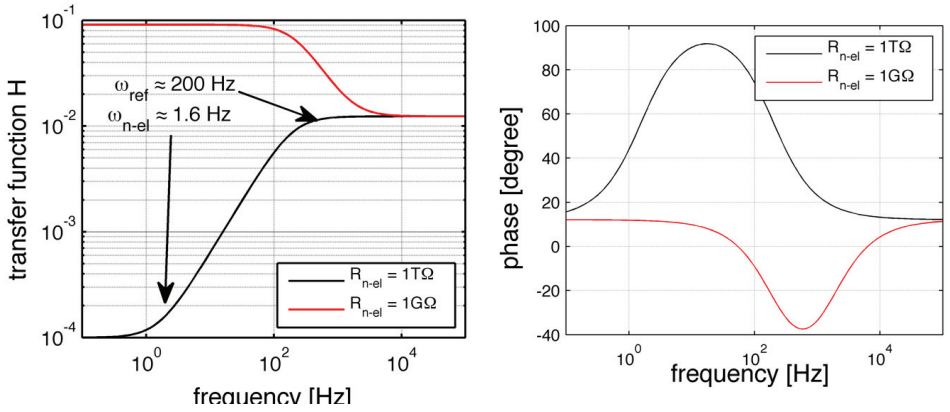

Figure 5.1.: Impedance spectroscopy calculated for two different values of $R_{n-el} = 1T\Omega$ and $R_{n-el} = 1G\Omega$, which simulates an empty nanoelectrode and a typical NP-nanoelectrode system, respectively, using the specific parameter of the trapping box: $C_{ref} = 8\,\mathrm{pF}$ and $C_{n-el} = 0.1\,\mathrm{pF}$.

calculated for the case of empty nanoelectrodes. The calculated frequencies describe the points in the S-shaped curve, where the dominating impedance changes from ohmic resistance to reactance. According to Fig. 5.1 the largest contrast between the transfer function for an empty nanoelectrode and a typical NP-nanoelectrode systems is expected for low frequencies $\omega_{n-el} \lesssim 1.6\,\mathrm{Hz}$.
In the following sections DEP trapping of:

(i) 4'-methyl-1,1'biphenyl-4-propanethiol (BP3) capped Au NPs with a core size of 4 nm.

(ii) Mercaptoethane sulfonic acid (MES) capped Au NPs with a core size of 13 nm.

(iii) MES and 4-(3',3'-dimethyl-6-nitrospiro [chromene-2,2'-indole]-1'-yl) butanethiol. (spiropyran) (2:3) capped Au NPs with a core size of 13 nm.

(iv) MES and spiropyran (6:1) capped NPswith a core size of 3-6 nm.

are described.

5.2. Immobilization of BP3 capped NPs (4 nm)

The biphenyl-propanethiol capped NP solution was synthesized by Kerstin Blech in the group of Prof. Ulrich Simon of the RWTH Aachen University, our cooperation partner in a DFG financed project. The synthesis of the BP3 capped gold NPs followed a modified route from Murray et al. [110]. Then the NP solution was precipitated with ethanol, washed, separated from solution by filtration and re-dispersed in toluene. A dialysis purified the solvent by removing the residual molecules from the synthesis process [111]. The BP3 Au NPs obtained, were characterized by TEM measurements on a Philipps CM200 with an acceleration voltage of 200kV, Fig. 5.2.
The NPs were solved in toluene, which has a high evaporation rate and a low surface tension. Due to the low surface tension of toluene the amount of solvent on each 6x6 mm sample was limited to $\sim 5\,\mu$l, which evaporates within 5 min. At the outline of the drop a 3D NP array structure appeared step wise during evaporation. Thereby,

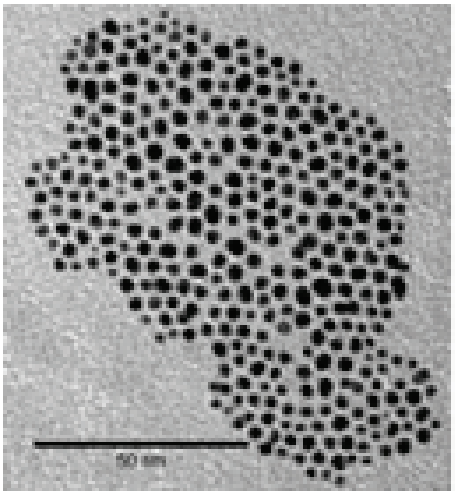

Figure 5.2.: Transmission electron micrograph of BP3 capped NPs, the size distribution was 3.6 nm ± 0.7 nm (derived from 208 particles by Kertin Blech RWTH Aachen).

potentially electrical conduction paths between the electrodes and the guard lines were created. As a consequence the drop-on-sample method is not suitable to immobilize a BP3 capped NP from toluol solution. Applying the DEPT trapping equipment as shown in section 3.1.2 in the bottom-drop top-sample approach with a saturated gas atmosphere of toluene, led to a time window for DEPT of approximately 45 min. The DEPT was performed applying a combination of DC and AC voltage to the voltage divider circuit:

$$U_{in} = U_{AC-detect}(t) + U_{DC-DEPT}(t) \tag{5.7}$$

with $U_{AC-detect}(t) = A_{detect}\cos(2\pi f_{detect}t)$, the frequency f_{detect}, the amplitude A_{detect} and the time t.

The trapping event was detected by a lock-in amplifier using a continuous detection voltage $U_{AC-detect}(t)$ with a frequency of 120 Hz and amplitudes of either $A_{detect}(A) = 0.1\,\mathrm{V_{rms}}$ and $A_{detect}(B) = 0.5\,\mathrm{V_{rms}}$ (rms denotes the root means square). The trapping event was indicated by a change in amplitude and phase measured over the reference resistor $R_{ref} = 100\,\mathrm{M\Omega}$ in a voltage divider circuit, as shown in Fig. 3.4. In both mea-

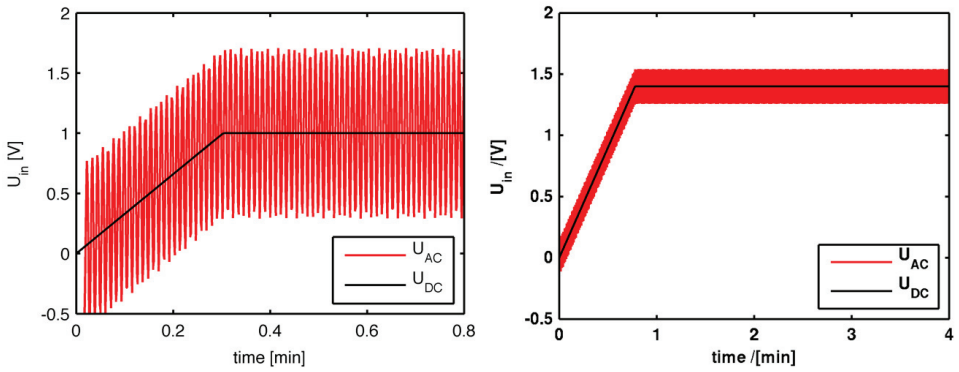

Figure 5.3.: Input voltage to the voltage divider circuit applied for DEPT of uncharged Au NPs with a core size of 4 nm.

surements (A,B) a clear change was observed in phase:
$\Delta p_{ref}(A) = 60°$, $\Delta p_{ref}(B) = 22°$ as well as in amplitude of $A_{ref}(A) = 73\,\mathrm{mV}$ (73% of $A_{detect}(A)$), $A_{ref}(B) = 140\,\mathrm{mV}$ (28% of $A_{detect}(B)$) over the reference resistor. The resistance over the nanogap in solution after the trapping event calculated with equation (5.5) was $R_{n-el}(A) = 0.4\,\mathrm{M\Omega}$ and $R_{n-el}(B) = 260\,\mathrm{M\Omega}$. The AC voltage ($A_{detect} = 0.5\,\mathrm{V}_{rms}$) applied generated an electrical field between the nanoelectrodes of approximately $E_{n-electrodes-AC} = (0.14 - 0.07)\,\mathrm{V/nm}$, assuming a distance between the tips of the nanoelectrodes of (5-10) nm. The electrical filed generated by the applied DC voltage ($U_{DC,max} = 1.4\,\mathrm{V}$) is $E_{n-el} = (0.14 - 0.28)\,\mathrm{V/nm}$.
According to the equation (5.3) a threshold electrical field, at which NPs with a radius $r_{NP} = 2\,\mathrm{nm}$ are DEP trapped into nanoelectrodes , is calculated at:

$$E_{th,NP}(R_{NP} = 2\,\mathrm{nm}) = (0.4)\,\mathrm{V/nm},$$

using a rough estimation for the permittivity of the capping molecule
$\epsilon_p = (\epsilon_{alkane} + \epsilon_{phenyl})/2) \approx 4.5$. By including the molecule into the calculation the threshold field of the combined NP - molecule system was calculated using equation (5.3) to $E_{th,NP+mol}(r_{NP} + l_{BP3}) = (0.18)\,\mathrm{V/nm}$.
Therefore the electrical field ($E_{n-el} \approx \frac{1.4\mathrm{V}}{7\,\mathrm{nm}} = 0.2\,\mathrm{V/nm}$) applied is slightly below the threshold field, where NP aggregation at the nanoelectrodes occur. Accordingly, the

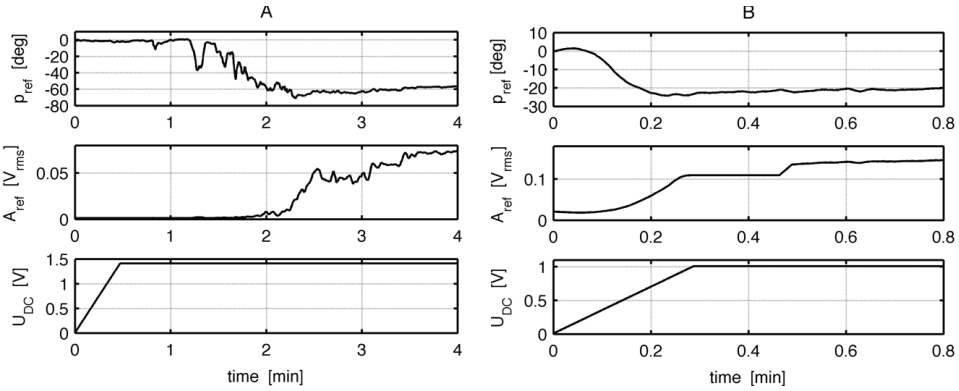

Figure 5.4.: DC-DEPT of a single BP3 capped Au NP (4 nm) of two representative trapping events were shown. The upper two subplots show the voltage and phase drop over a $R_{ref} = 100M\Omega$ reference resistor. The lower subplot illustrates the applied DC voltage ramp to U_{max}(Device A) = 1.4 V (left) and $U_{DC,max}$(Device B) = 1.0 V (right) with a ramp of 20 mV/s. The amplitude A_{detect} of the continuous detection voltage for impedance spectroscopy was $A_{detect}(A) = 0.1V_{rms}$ and $A_{detect}(B) = 0.5V_{rms}$, respectively. The first plateau in the voltage $A_{detect}(B)$ (right) is a measurement artifact (range-clipping) of the lock-in amplifier.

field strength applied makes it possible to detect trapping events of single molecule-capped NPs in between nanoelectrodes. Although this was not a representative study (4 trapping events) a faster trapping of 4 nm Au NPs was indicated by a higher AC amplitude A_{detect}, which is in accordance with Stellaci et al. [106], where a long range influence due to the AC component of U_{in} is described.

5.3. Immobilization of MES capped gold NPs (12 nm)

The MES capped NPs were synthesized by our cooperation partner, Itamar Willner of the Hebrew University of Jerusalem, in an EU financed project called Molecular Logic Circuits (MOLOC). The NPs were solved in 10mM HEPES (2-(4-(2-Hydroxyethyl)-1-piperazinyl)-ethanesulfonicacid, solved in demineralized water), which has a low evaporation rate and a high surface tension.Due to the high surface tension it is possible to

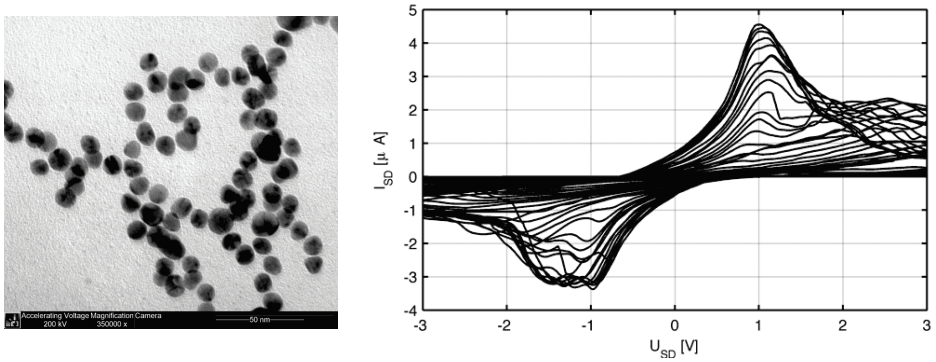

Figure 5.5.: Transmission electron micrograph (left) of MES capped Au NPs show a homogenious size distribution of $\sim$ 12 nm. Cyclo voltametry (right) of Au_3Pd_2 nanoelectrodes, suspended with 10 mM (aqueous) HEPES solution, measured at a rate of 50mV/s.

suspend each 6x6 mm sample with $\sim$ 15 μml solvent. In case of this NP-solvent combination the time window for DEPT is more than one hour, which makes the drop-on-sample method applicable for DEPT. The NPs have a size of $\sim$ 12 nm with a homogeneous size distribution, which was observed by transmission electron microscopy (TEM), shown in Fig. 5.5(left). The same trapping procedure as described in the previous section leaded to (i) a completely covered anode and (ii) a dis-solved cathode. Observation (i) led to the conclusion that the MES capped NPs were negatively charged. Thus the sulphonic acid was de-protonated in solution. Point (ii) was explained by cyclo-voltametric measurements on Au_3Pd_2 nanoelectrodes in 10 mM HEPES (aqueous) solution, where an oxidation peak at $U_{sd} \sim 1$ V, was observed. However, a recent study has shown that the piperazine ring in HEPES is able to generate nitrogen-centered free radicals, which can reduce gold [112]. Therefore it is a common solvent to grow gold nanoparticles in aqueous solution at very high yield (approximately 90%) [113]. For that reason a dissolution of only one side of the nanoelectrode at applied DC voltage was reasonable, see Fig. 5.5(right). As a matter of fact only AC DEPT with amplitudes smaller than 1 V were applicable for charged NPs in HEPES solution. The DEPT was performed applying a combination of two different AC signals to the voltage divider circuit, a continuous detection voltage $U_{AC-detect}(t)$ such as applied in DC-DEPT and a pulsed

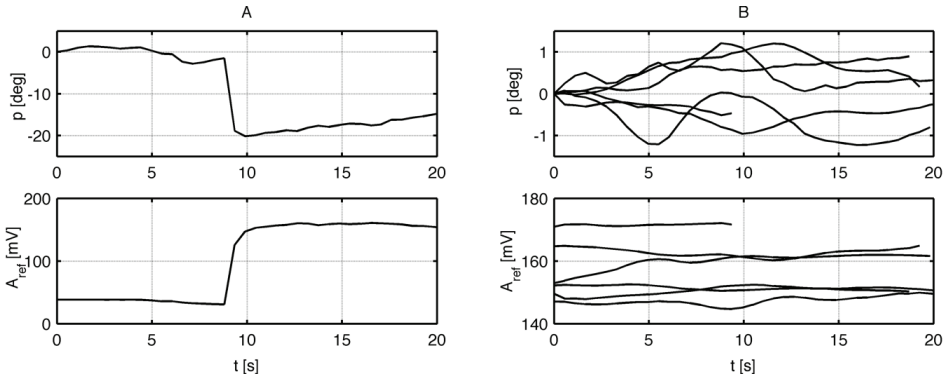

Figure 5.6.: AC DEPT trapping of a MES capped 12 nm gold NP is shown in the left graph. The DEPT was performed in a voltage divider circuit over a reference resistor $R_{ref} = 100\,\mathrm{M\Omega}$ with a detection signal: $A_{detect} = 200\,\mathrm{mV}$, $f_{detect} = 10\,\mathrm{Hz}$. Several measurements are shown on the right side, where NPs were already trapped unobserved by a applying an AC pulse with high amplitude ($A_{DEP} = 800\,\mathrm{mV}_{rms}$, $f_{DEP} = 15\,\mathrm{Hz}$) used for another nanoelectrode pair. Three different levels in amplitude are apparent $A_{ref1} \approx 151\,\mathrm{mV}_{rms}$, $A_{ref2} \approx 163\,\mathrm{mV}_{rms}$ and $A_{ref3} = 172\,\mathrm{mV}_{rms}$.

AC voltage:

$$U_{in} = U_{AC-detect}(t) + U_{AC-DEP}(t) \tag{5.8}$$

the contribution $U_{AC-DEP}(A_{DEP}, f_{DEP}, \Delta t, t)$ discribes an AC pulse with the amplitude A_{DEP}, the frequency f_{DEP} and a duration of Δt. Figure 5.6(A) shows a trapping event of a MES-capped, 12 nm gold NP measured with a detection signal, which has an amplitude $A_{detect} = 200\,\mathrm{mV}$ and frequency $f_{detect} = 10\,\mathrm{Hz}$. A MES capped NP was trapped before an AC pulse was applied. By applying an AC pulse with high amplitude ($A_{DEP} = 800\,\mathrm{mV}_{rms}$, $f_{DEP} = 15\,\mathrm{Hz}$) to one nanoelectrode pair, NPs were trapped unobserved in between other nanoelectrodes a shown in Figure 5.6(B). The applied AC voltage($A_{detect} = 0.8\,\mathrm{V}_{rms}$) generated an electrical field between the nanoelectrodes of approximately $E_{n-electrodes-AC} = (0.22 - 0.11)\,\mathrm{V/nm}$, assuming a distance between the tips of the nanoelectrodes of (5-10) nm. According to Equation (5.3) a threshold electrical field of:

$$E_{th,NP}(R_{NP} = 12\,\mathrm{nm}) = (0.078)\,\mathrm{V/nm}$$

was calculated, using $\epsilon_p = 6.9$ [107]. Thus the generated electrical field was greater than the threshold field $E_{threshold}$. This is probably the reason why a simultaneous trapping of NPs was observed in several nanoelectrodes. In Figure 5.6(B) three different amplitude levels were observed $A_{ref1} \approx 151\,\mathrm{mV}_{rms}$, $A_{ref2} \approx 163\,\mathrm{mV}_{rms}$ and $A_{ref3} = 172\,\mathrm{mV}_{rms}$. Correspondingly, resistances of
$R_{n-el1} \approx 32.5\,\mathrm{M\Omega}$, $R_{n-el2} \approx 22.7\,\mathrm{M\Omega}$ and $R_{n-el3} \approx 16.3\,\mathrm{M\Omega}$
were calculated with equation (5.5), respectively. On one hand the difference in resistance might correspond to a different vacuum gap in the tunneling contact. On the other hand the diameter of the NP $d = 12\,\mathrm{nm}$ is a factor of two greater than the distance between the nanoelectrodes, therefore probably no vacuum gap remains in the cases, where a resistance of R_{n-el1} was measured. Hence, we can assume that the resistance R_{n-el1} corresponds to a single trapped NP in a nanoelectrode. The lowest resistance could correspond to two NPs immobilized in between the nanoelectrodes $R_{n-el3} = (1/R_{n-el1} + 1/R_{n-el1})^{-1} = 16.2\,\mathrm{M\Omega}$. The intermediate resistance can be described by the immobilization of at least three NPs at the nanoelectrodes, e.g. two NPs in parallel to one NP: $R_{n-el2} = (1/R_{n-el1} + 1/(2R_{n-el1)})^{-1}$.

5.4. Immobilization of MES and Spiropyran (2:3) capped gold NPs (12 nm)

The MES and Spiropyran capped gold NPs were synthesized by our cooperation partner Itamar Willner of the Hebrew University of Jerusalem. The NPs were solved in 10mM Hepes (aqueous solution), thus the drop-on-sample method was applied to DEPT as well. The size of the gold NPs was $\sim (12 \pm 1)\,\mathrm{nm}$ as observed by transmission electron microscopy (TEM) shown in Fig. 5.8(left). A representative trapping event is shown in Fig. 5.8(right). After controlled or unobserved DEPT, a resistance of $R_{n-el1} \approx 430 - 490\,\mathrm{M\Omega}$ was measured in about 25 pairs of nanoelectrodes. In the case of a trapping event, the magnitude of the voltage drop U_{ref} over the reference resistor is different before and after the AC pulse.

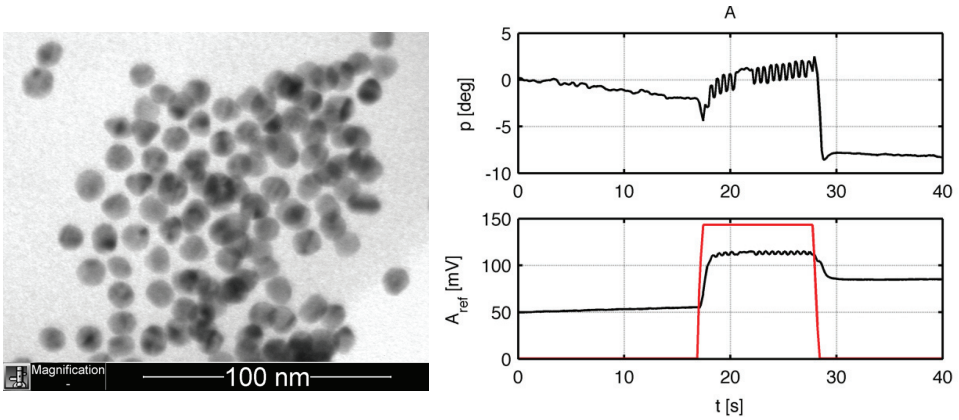

Figure 5.7.: Transmission electron micrograph (left) of Spiropyran capped Au NPs show a homogeneous size of $\sim (12 \pm 1)\,\mathrm{nm}$. On the right side a representative DEPT measurement is shown, ($R_{ref} = 100\,\mathrm{M\Omega}$, $A_{detect} = 500\,\mathrm{mV}$, $f_{detect} = 10\,\mathrm{Hz}$.The red colored line illustrates the AC-DEPT pulse with:$A_{DEP} = 1200\,\mathrm{mV}_{rms}$, $f_{DEP} = 15\,\mathrm{Hz}$ and a pulse duration of $\Delta t = 10\,\mathrm{s}$. The magnitude of the voltage drop A_{ref} over the reference resistor before and after the AC pulse is different, which indicates a trapping event.

5.5. Immobilization of Spiropyran capped CdSe NPs (4 nm)

The MES and Spiropyran capped CdSe NPs were synthesized by our cooperation partner Itamar Willner of the Hebrew University of Jerusalem. The NPs were as well solved in 10mM Hepes (aqueous solution), thus the drop-on-sample method was applied to DEPT. The size of the CdSe NPs was $(4.1 \pm 0.4)\,\mathrm{nm}$ as observed by transmission electron microscopy (TEM) shown in Fig. 5.8(left). A representative trapping event is shown in Fig. 5.8(right). After controlled DEPT a resistance of $R_{n-el1} \approx 251\,\mathrm{M\Omega}$ was measured in only one nanoelectrode pair. At fabrication step B such small nanoelectrode separations were not often observed.

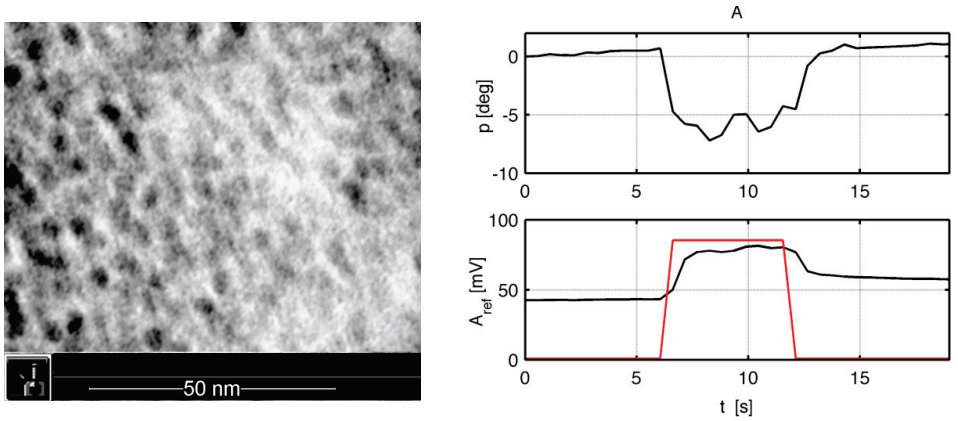

Figure 5.8.: Transmission electron micrograph (left) of Spiropyran capped CdSe NPs show a homogeneous size of $\sim (4 \pm 0.4)\,\mathrm{nm}$. The low quality in resolution was due to the lower density of CdSe (almost a factor of four) and a thick layer of organic residuals. The representative DEPT measurement is shown on the right, ($R_{ref} = 100\,\mathrm{M\Omega}$, $A_{detect} = 200\,\mathrm{mV}$, $f_{detect} = 10\,\mathrm{Hz}$.The red colored line illustrates the AC-DEPT pulse with:$A_{DEP} = 500\,\mathrm{mV}_{rms}$, $f_{DEP} = 15\,\mathrm{Hz}$ and a pulse duration of $\Delta t = 10\,\mathrm{s}$.

5.6. Conclusion of DEPT

The controlled immobilization of a single nanoparticle between the nanoelectrodes is required for the application of molecule-capped NPs in working devices. In this work procedures have been worked out to immobilize single charged and uncharged NPs between nanoelectrodes, which are based on dielectrophoretic trapping. Successful trapping events were detected live using a lock-in amplifier. To achieve conclusive AC measurements on a high ohmic system, all involved capacitances have to be minimized to a few pF or even in the sub pF range, in order to increase the cut-off frequency of the unavoidable high-pass RC-filter. In addition the charging of the molecule capped nanoparticle is playing a distinct role to use either AC or DC dielectrophoretic trapping. These measurements enabled a live monitoring of a single-nanoparticle trapping event.

6. Transport measurements on BP3 capped NPs

Charge transport measurements on 4'-methyl-1,1'biphenyl-4-propanethiol (BP3) capped gold nanoparticles, see Fig. 6.1 with a diameter of 4 nm were studied at various temperatures. The NPs have been synthesized by K. Blech in the group of U. Simon at the RWTH Aachen within the framework of a DFG financed project.
The synthesized gold nanoparticles were characterized by Kerstin Blech, using several methods such as: UV/VIS spectroscopy, transmission electron microscopy (TEM), dynamic light scattering (DLS), and small angle X-ray scattering (SAXS) [114]. As a result, the size of the NP((4.1 ± 0.5) nm), the inter-particle distance ((1.4 ± 0.4) nm)and an estimation of the length of the capping molecule BP3 (1.6 nm) was obtained. The results are available in the Supporting Information. At room temperature the total conductivity across the nanoelectrode-molecule-NP-molecule-nanoelectrode configuration is shown to be critically dependent upon how perfectly the NP fits between the nanoelectrodes [111]. In the electrode-molecule-NP-molecule-electrode devices the geometrical changes, even in the sub-nanometer region, influence the transport properties significantly. Possible reasons for changes in the geometry of a tunneling contact are: (1) moving of single gold atoms [4], (2) a temperature dependent expansion / contraction of nanoelectrodes, (3) a structural crossover between two morphologies of the nanoparticle as described by Barnard et al. [115], (4) molecular reorganization as described by [11]. One approach to probe the properties of a molecule-NP device is to bridge the gap between nanoelectrodes by a single nanoparticle, which was performed within my work as doctoral researcher. Another method is to assemble a 3D-array of NPs on inter digitating electrode structures(IDEs), which was performed by Kerstin Blech [114] in the group of Prof. U. Simon in the Anorganische Chemie, RWTH Aachen University, a cooperation partner in a DFG financed project. Temperature dependent transport measurements on NP arrays are well studied as described in [116–118].

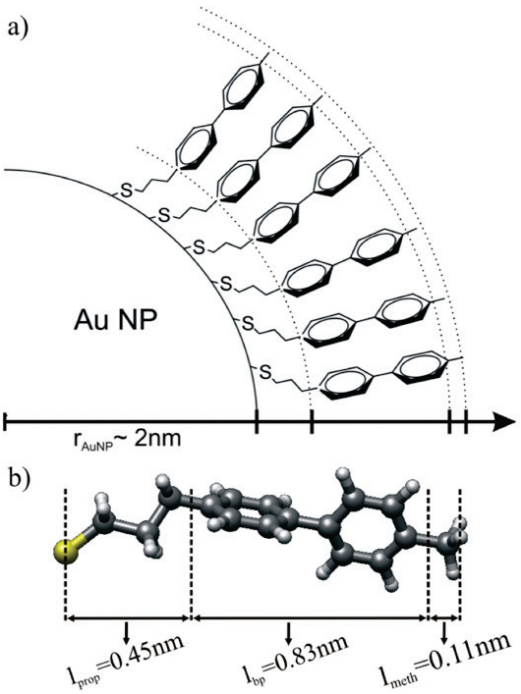

Figure 6.1.: a) Schematic drawing of biphenyl-propanethiol molecules stabilizing a gold nanoparticle. b) The characteristic lengths of the molecular subunits are indicated. Accordingly the total diameter of the BP3 capped NPs is calculated to ∼6-7 nm depending on the density and orientation of the BP3 molecules.

Possible transport mechanisms of 'nanoelectrode-(molecule-NP-molecule)-nanoelectrode' systems, i.e. in arrays of NPs (Aachen) and single NPs (Jülich) between nanoelectrodes, were explored by temperature dependent complex impedance or current/voltage measurements. Temperature dependent conductivity measurements revealed different types of transport mechanisms, such as hopping [79], transport according to the granular metals model [86], superexchange coupling [11] and tunneling [82]. In addition, a discontinuity in the conductivity as a function of temperature is discussed in terms of a possible structural crossover in particle morphologies. The transport mechanisms of BP3 capped gold NPs (4 nm) immobilized between two Au nanoelectrodes were studied depending of temperature and under illumination of light with different wavelength. The BP3 capped NPs were immobilized by DC-DEPT as described in section 5.2 in the nanoelectrode devices. Then cyclic $I(U)$ measurements were performed in the subpicoampere cryostat setup as shown in 3.1.4. The risk of a damage to the device during the interchange between the input lines of the cryostat was minimized by following an

interchange procedure, involving the interconnect switch box, as described in section 3.1.3.

6.1. Temperature dependent transport measurement on single BP3 capped NPs

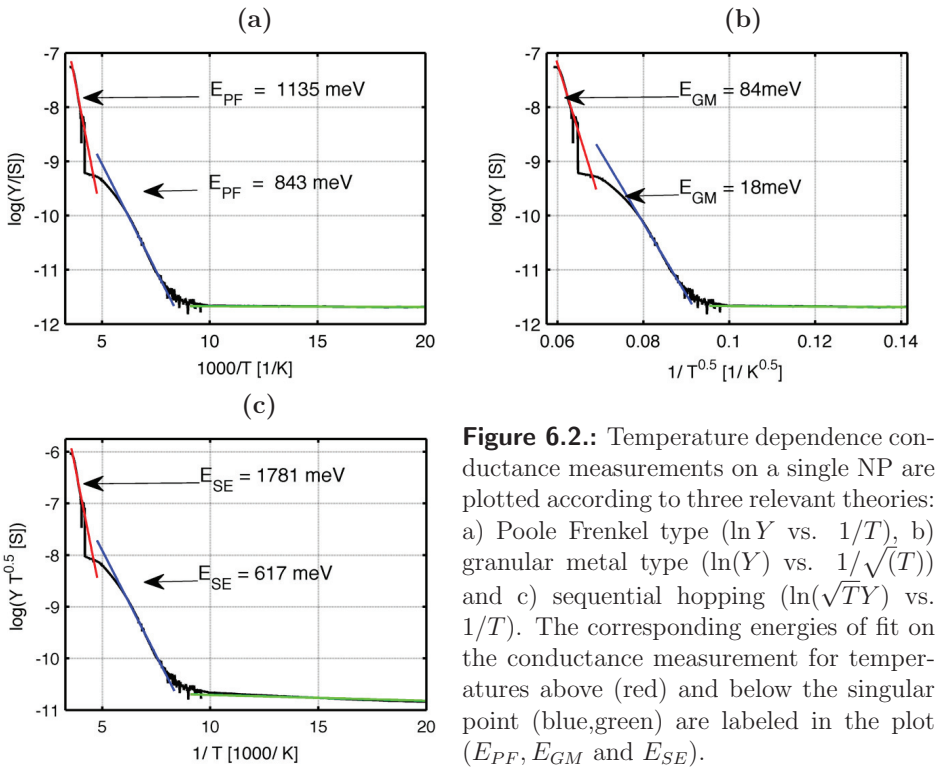

Figure 6.2.: Temperature dependence conductance measurements on a single NP are plotted according to three relevant theories: a) Poole Frenkel type ($\ln Y$ vs. $1/T$), b) granular metal type ($\ln(Y)$ vs. $1/\sqrt{(T)}$) and c) sequential hopping ($\ln(\sqrt{T}Y)$ vs. $1/T$). The corresponding energies of fit on the conductance measurement for temperatures above (red) and below the singular point (blue,green) are labeled in the plot (E_{PF}, E_{GM} and E_{SE}).

The temperature dependent conductance of a single BP3-capped NP, applying a source drain voltage of $U_{sd} = 1\,\mathrm{V}$, is investigated in this section. The electric conductivity Y through the nanoelectrode/BP3-NP-BP3/nanoelectrode device was measured over a wide range of temperatures, as plotted in an Arrhenius type of plot, see Fig. 6.2a). In Fig. 6.2a) four different transport regimes are identified clearly and can be attributed in principle, according to their temperature dependence, to different transport mechanisms.

In the highest temperature range (I), ($T_{red} = 265\,\mathrm{K} - 245\,\mathrm{K}$), an exponential decrease of the conductivity with decreasing temperature is observed pointing to a thermally activated charge transport. In this case of temperature dependent hopping between molecular moieties, either belonging to one molecule or neighboring molecules, the activation energy corresponds to the relevant motion. Regarding BP3 capped NPs the mobility of charge carriers is dependent on the dihedral angle between the phenylen units. The mobility is highest for a coplanar and lowest for a perpendicular orientation of the phenylen rings. However, since thermally activated hopping should be observed in case of poly-phenylen units according to Ratner [11] only for temperatures above $\sim$310 K, it is unlikely that a simple Arrhenius-type conduction mechanism can be applied here. Furthermore, in the case of conduction measurements through a single nanoelectrode/BP3-NP-BP3/nanoelectrode device, the strong electrical field induced by the applied voltage of , $U_{sd} = 1\,\mathrm{V}$ has to be considered. Assuming that there is no additional vacuum gap between the NP and the electrodes, U_{sd} drops over the length of twice the BP3 capping layer around the NP, that is over $l_{tot} = 2l_{BP3}\cos 30° = 2.58\,\mathrm{nm}$. The resulting electrical field amounts to $\sim$0.4 V/nm. Consequently, the thermally activated transport through the single NP device observed takes place in high electric fields and is described best by Poole-Frenkel-type transport, as described in section 2.3.2. From the least-square fits to the data points in Fig. 6.2a) in the temperature range (I), ($T_{red} = 265\,\mathrm{K} - 245\,\mathrm{K}$), $E_A = 440 \pm 20\,\mathrm{meV}$ and $E_{PF} = 1135 \pm 20\,\mathrm{meV}$ are obtained, respectively, using $U_{sd} = 1\,\mathrm{V}$ and $\epsilon_r = 4.5$. These activation energies, E_A and E_{PF}, respectively, for thermally activated transport are considerably higher than values given for the planarization energy of polyphenyl chains, like $E_A = 0.19\,\mathrm{eV}$ given for a biphenyl unit by Reed [28]. This points to the fact, that the planarization of the biphenyl unit is not the highest barrier in the hopping process observed in the nanoelectrode/BP3-NP-BP3/nanoelectrode device.

In the temperature range (II), ($T_{dis} = 245\,\mathrm{K} - 200\,\mathrm{K}$), the conductivity reveals a discontinuity, whose origin can not be explained within this data set. For further characterization additional temperature dependent conductivity and current/voltage measurements were performed, as shown in Fig. 6.4. The cyclic temperature sweep (Fig. 6.3b)) is showing a reproducible hysteresis in conductivity. The transition to the low conductance state is achieved by cooling below 235 K, while the transition to the high conductance

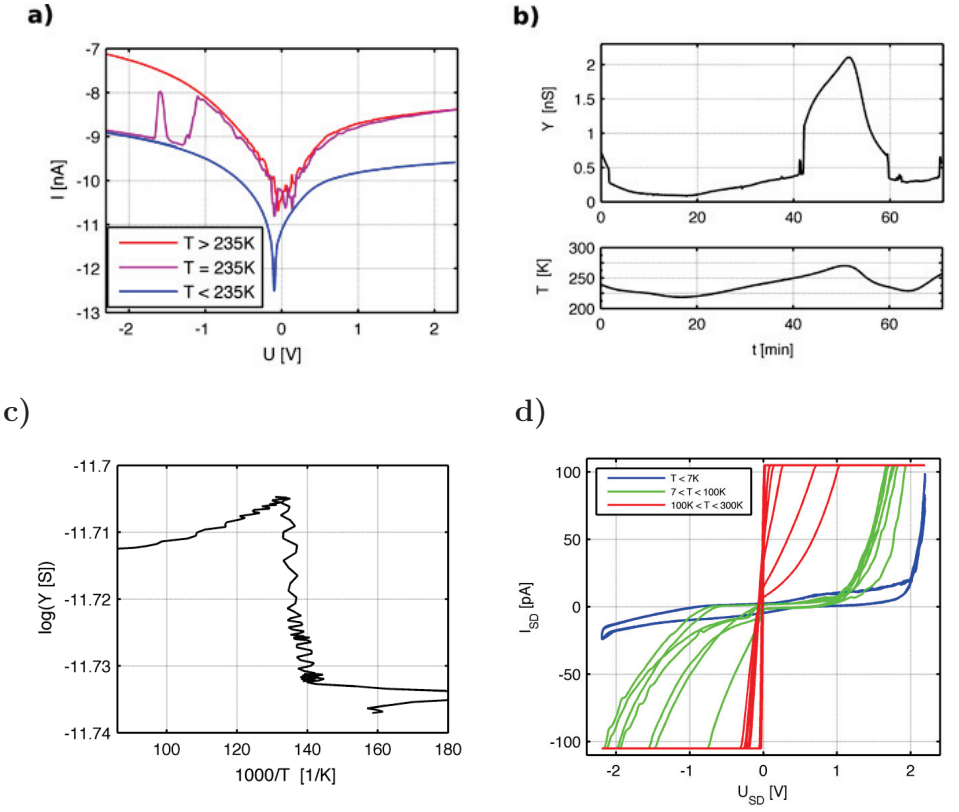

Figure 6.3.: Detailed investigation of the device in the temperature range ($\sim$ 235 K), where the singularity was observed in the temperature dependent conductance plot. a) Cyclic $I(U)$ measurements above 235 K (red), at 235 K (purple) and below 235 K (blue). The shape of the $I(U)$ curves taken before and after transition is similar, the transition between the two states is sharp. b) Cyclic temperature sweep shows a small hysteresis between the transition-temperature of the two conductance-states. c) Below a temperature of 7 K molecular vibrations are freezing out, which was observed as a small step in the temperature dependent conductance measurement. d) $I(U)$ curve during warmup of the device. Three different behaviors are indicated, below 7 K, between 7 K-100 K and above 100 K.

state is achieved by heating above 253 K. The $I(U)$-characteristics of the NP-device (Fig. 6.3a)) confirm this result. A significant difference in magnitude of current is ob-

served for $I(U)$ characteristics taken above or below the transition temperature. The high temperature $I(U)$-curve exhibits also a stronger voltage dependence than the low temperature curve. Most interestingly an $I(U)$-curve taken at $T = 235\,K$ reveals a switching between both conductance states. One possible reason for a sudden change of current in the order of one magnitude as observed here is a geometrical change in the distance between electrodes of about $0.1\,nm$ in vacuum. However, since this change of current is fully reproducible an accidental geometrical change seems to be rather unlikely. On the contrary a physical reason causing a geometrical rearrangement is probable.

In the third transport regime (III), identified in Fig. 6.2a) for temperatures $T_{blue} = 200\,\mathrm{K} - 110\,\mathrm{K}$, the activation energy becomes less temperature dependent indicating a different transport mechanism. Possible mechanisms for charge transport in this region are superexchange coupling (see section 2.3.4) and transport according to the granular metal model (see section 2.3.3). The superexchange charge transfer process is characterized by the transfer of electrons or holes in one step from a donor to an acceptor unit via bridge orbitals that are used as a medium for electronic coupling. The relevant energy for this process is the reorganization energy, E_{SE}, which is mainly determined by the structural differences between the equilibrium configurations of the respective donor and acceptor units in neutral and ionic states [11, 79]. In Fig. 6.2b) the temperature dependent conductivity is plotted as $\log(Y_{gm})$ vs $T^{-1/2}$ and in c) $\log(Y_{SE}T^{1/2})$ vs T^{-1} according to the granular metal model and superexchange coupling, respectively. For this temperature range (III) the experimental data show slightly stronger deviations from the granular metal model and thus, superexchange coupling is assumed to be the most probable transport mechanism. From the slope of 6.2c) the characteristic reorganization energy $E_{SE} = 617\,\mathrm{meV}$ is obtained that is well in the range of the calculated values given by Ratner [79] ranging from 360 meV to 1130 meV for 3-methylbiphenyl, depending on the theoretical functional applied, the basis set and electron or hole transfer. Moreover, a reorganization energy of 580 meV [79] was calculated for electron transport through the biphenyl unit and suggests that this mechanism should be considered also in this system.
For very low temperatures, ($T_{green} < 100\,\mathrm{K}$) there was no temperature dependence of the conductivity measured through the single BP3-NP device obtained (6.2). Therefore it is assumed that tunneling is the main conduction mechanism in this regime.

	characteristic energies				
	$E_{PF}[meV]$	$E_A[meV]$	$E_{GM}[meV]$	$E_{GM}[meV]$	$E_{SE}[meV]$
			$l_{vac} = 0nm$	$l_{vac} = 0.1nm$	
(I)$T \in [245\,K, 265\,K]$	1135 ± 20	440 ± 20	84 ± 19	55 ± 10	1781
(III) $T \in [110\,K, 200\,K]$	843 ± 3	148 ± 3	18 ± 5	12 ± 2	617

Table 6.1.: Activation energies obtained for a single BP3 capped NP in the temperature regimes (I), ($T_{red} = 265\,\mathrm{K} - 245\,\mathrm{K}$), and (III), ($T_{blue} = 200\,\mathrm{K} - 110\,\mathrm{K}$), assuming different transport mechanisms see text.

All values deduced for the activation energies in the respective temperature ranges are summarized in Tab. 6.1. For temperatures below 100 K the temperature-dependence of current transport do not show a significant slope for all models applied. Therefore, this temperature range corresponds to the direct tunneling regime, which is overlapped by the influence of the temperature related contraction of the nanoelectrodes and an increase in vacuum gap of about (0.066..0.133) nm in this temperature range. A small step in the conductance curve at 7.5 K is observed reproducibly at this temperature. According to Reed et al. [119] this feature is related to the freezing of molecular vibrations (Fig. 6.3)c) [119].

Temperature dependent conductance of a NP array

The measurements on single NP devices discussed above are supported by a temperature dependent conductance measurement on a three-dimensional array of BP3-stabilized gold NPs in an IDE structure. This measurement is a standardized method to characterize 3D arrays of molecular capped NPs, which was established and performed in the group of Prof. U. Simon at the RWTH Aachen University. The data obtained was analyzed using the same methods as for a single NP device. The corresponding Arrhenius ($\log(Y)$ vs. $1/T$), granular-metal-based ($\log(YT^{0.5})$ vs. $1/T$) and superexchange ($\log(Y)$ vs. $1/T^{0.5}$) plots were shown in Fig. 6.4. Here, as well, four different temperature regimes were observed:
(I) $T_{red} \in [300\,\mathrm{K}, 340\,\mathrm{K}]$, (II) $(220\,\mathrm{K} - 300\,\mathrm{K})$ (III) $T_{blue} \in [110\,\mathrm{K}, 220\,\mathrm{K}]$,(IV) $T_{green} \in [30\,\mathrm{K}, 80\,\mathrm{K}]$. In the temperature range (II) an atypical charge transport behavior was observed, which is discussed below.

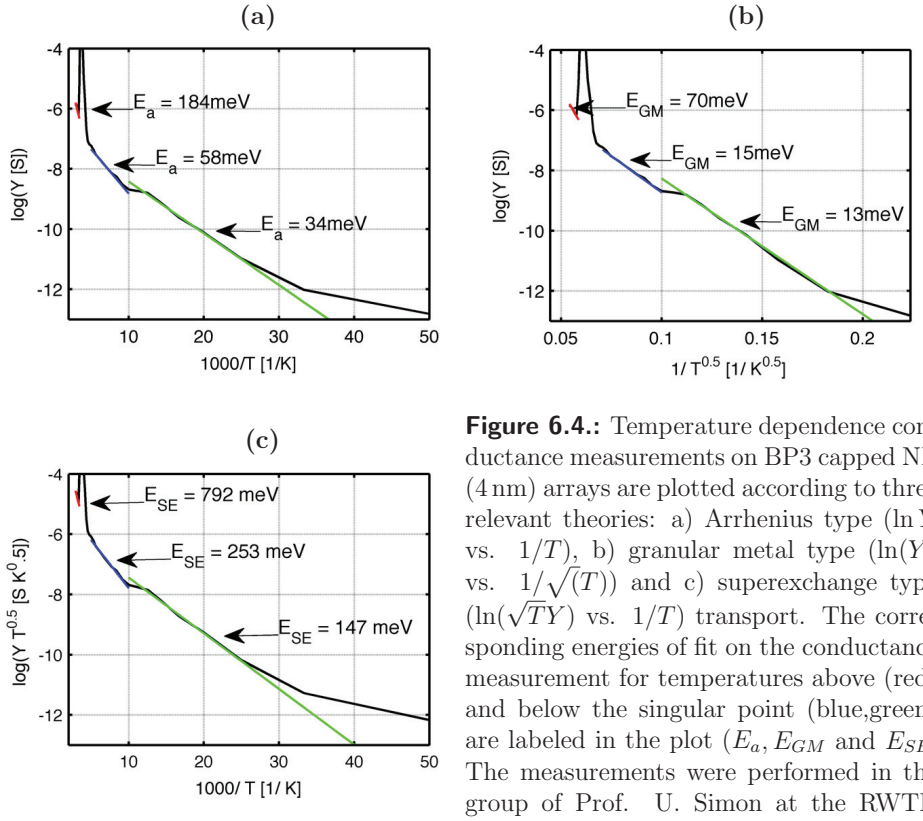

Figure 6.4.: Temperature dependence conductance measurements on BP3 capped NP (4 nm) arrays are plotted according to three relevant theories: a) Arrhenius type ($\ln Y$ vs. $1/T$), b) granular metal type ($\ln(Y)$ vs. $1/\sqrt{(T)}$) and c) superexchange type ($\ln(\sqrt{T}Y)$ vs. $1/T$) transport. The corresponding energies of fit on the conductance measurement for temperatures above (red) and below the singular point (blue,green) are labeled in the plot (E_a, E_{GM} and E_{SE}. The measurements were performed in the group of Prof. U. Simon at the RWTH Aachen University.

The fit of the corresponding energies as the activation energy E_A, E_{GM} (transport as described for granular metal films) and the reorganization energy E_{SE} (suggesting that electron transfer occurs based on an intramolecular superexchange process) of the respective temperature regimes were shown in table 6.2.
The charge transport according to the Poole-Frenkel model, which describes the field-enhanced electron emission, can be excluded for 3D NP arrays since the voltage drop in this case is negligible (appr. 1μV/NP) in comparison with the single nanoparticle experiments.

In the temperature regime (I) (300 K - 340 K) the activation energy of $E_a(I) = 184$ meV fitted is in great accordance with the planarization energy of biphenyl moieties [28].

	characteristic energies		
	$E_A[meV]$	$E_{GM}[meV]$	$E_{SE}[meV]$
(I)$T_{red} \in [300\,K, 340\,K]$	184	70	792
(III) $T_{blue} \in [100\,K, 200\,K]$	57	15	253
(IV) $T_{green} \in [30\,K, 100\,K]$	34	13	147

Table 6.2.: Activation energies obtained for an array of BP3 capped NP in the temperature regimes (I), ($T_{red} = 340\,\mathrm{K} - 300\,\mathrm{K}$), (III) ($T_{blue} = 200\,\mathrm{K} - 100\,\mathrm{K}$) and (IV) ($T_{green} = 100\,\mathrm{K} - 30\,\mathrm{K}$), assuming different transport mechanisms see text.

Consequently it can be deduced that the thermal activation energy associated with the phenyl rotation is the main energy barrier in this temperature range for BP3-NP arrays. In the ($\log(Y)$ vs. $1/T^{0.5}$)-plot a linear dependence with the same slope for both temperature regimes (III) and (IV) was observed. The corresponding energy was $E_{GM}(III - IV) \approx (14 \pm 1)\,\mathrm{meV}$. This might be an indication that in both regimes (III,IV) the transport is based on the same mechanism. The energy E_{GM} can be predicted by the electrostatic energy of a spheric two shell capacitance [86]:

$$E_{gm,theo} = E_c \approx \frac{e^2}{2C_{two-shell}} = \frac{e^2}{8\pi\epsilon_r\epsilon_0}\,(1/r_{NP} + 1/(r_{NP} + s)) \approx 13\,\mathrm{meV}$$

The value calculated is in excellent correspondence with the value obtained in the fit using granular metal theory. The Arrhenius type activation energy $E_A = 58\,\mathrm{meV}$ fitted in this regime (III) is in accordance with the coulomb blockade energy $\Delta U_c = 4E_c \approx 61\,\mathrm{meV}$ observed in $I(U)$ measurements on a single BP3 capped NP, as shown in section 6.2.1.

An atypical behavior expressed by a peak in the Arrhenius curve appeared in the temperature range 230 K-290 K of the BP3-stabilized AuNPs. The reason for the atypical peak in the Arrhenius plot is still unclear. In order to scrutinize this unexpected finding further a DCS measurement (compare Appendix A), The endothermal process occurs in the temperature range of 220 K - 250 K, was performed by Kerstin Blech [114]. This endothermal process appears in the same temperature range, where the peak in the Arrhenius plot was found. A tentative explanation might be a structural crossover in the morphologics of the Au core. This is in accordance with the phase map of gold nanoparticles, which was derived from a relativistic ab initio thermodynamic calculation

published recently by Barnard et al. [115]. The crossover between two morphologies may cause changes in the geometry in the range of (0.1-0.4) nm, corresponding to a change of the inter particle tunneling rate of 1-4 orders of magnitude, as calculated by the factor $exp(-\beta_{vac} l_{vac})$. Furthermore, the structural crossover might induce a reorganization of the ligand shell and therefore might cause a change in the electrical conductivity. This supports the theory of a spontaneous change in the length of the vacuum gap, as discussed for the unsteadiness in the temperature dependent conductance that was observed for a single NP at 235 K.

A similar charge transport phenomenon through 3D film of mercaptosuccinic acid capped gold NPs with different core sizes was observed by Kimura [116], where at around 205 K a reversible transition occurred, which could not be explained by the authors. The activation energy of a 4 nm mercaptosuccinic acid -stabilized gold NPs was fitted to $E_a(Kimura) = 57\,\text{meV}$ [116]. A similar atypical behavior in electrical resistances of 300 nm thick films of AuNPs linked by octanedithiol and hexanedithiol was reported by Mueller et al. [40]. In the temperature range 220 K - 285 K a hysteretic behavior occurred, which was attributed to the contraction/expansion of water/ice in the pores of the disordered nanoparticle films and the substrate. However, in the transport measurements on NP arrays, performed by Kerstin Blech at the RWTH Aachen University, this effect was excluded, since the NP arrays were prepared from dry toluene solutions. Furthermore other impedance measurements that have been performed using the same experimental set-up and under analogous drying conditions, do not show such discontinuities, which could be related to residual water.

6.1.1. Molecular orbital mediated transport at 4K

Below 100 K, the electrical transport mechanism through the 'nanoelectrode-molecule-NP-molecule-nanoelectrode system' was not temperature dependent. Therefore a pure tunneling mechanism is assumed. Step-like features are observed in the $I(U)$ characteristic, shown in Fig. 6.5. The steps indicate a resonant transport via molecular orbitals. According to section 2.1.3 the orbital mediated transport was fitted and as a result the parameters (σ_n, ϵ_n) of the Gaussian bells in the DOS curve was achieved. The result is:

$$(f_1 = 3.5, \sigma_1 = 0.1\,\text{eV}, \epsilon_1 = 0.55\,\text{eV})\ (f_2 = 1, \sigma_2 = 0.09\,\text{eV}, \epsilon_2 = 1.88\,\text{eV})$$

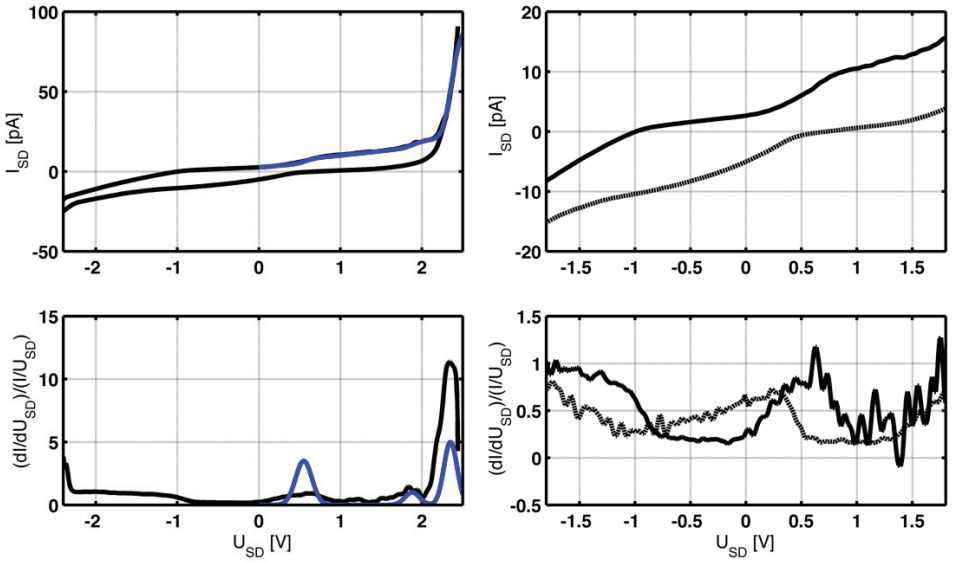

Figure 6.5.: (left) Current transport characteristic (top) and ndc (bottom) through a single BP3 capped NP at 4K. The blue colored line shows a fit according to the orbital mediated tunneling-theory (compare section 2.1.3). In the bottom plot the blue curve represents the DOS-curve containing three molecular levels. (right) This plot shows a zoom of the left plot. The ndc at 4K (bottom) shows periodic peaks with a peak distance of $\Delta U_{BP3,4K}(N, N+1) = 90\,\mathrm{mV}$

$(f_3 = 5, \sigma_3 = 0.08\,\mathrm{eV}, \epsilon_3 = 2.35\,\mathrm{eV})$

6.1.2. Coulomb blockade at 4K

A stepwise limited transport by coulomb blockade interaction is observed in the fine structure of the ndc in Fig. 6.5. The ndc of the $I(U)$-curve measured at 4K shows periodic peaks originated by coulomb blockade with a distance of 103 meV, which corresponds to a capacitance of $C_{\Sigma,BP3-A,4K} = 3.11\,\mathrm{aF}$, calculated with $C_{\Sigma,BP3-A,4K} = 2e^2/\Delta U_{BP3,4K}(N, N+1)$ [88]. The temperature dependent change in tip distance of the nanoelectrodes is estimated by the contraction of two circular plates with a diameter

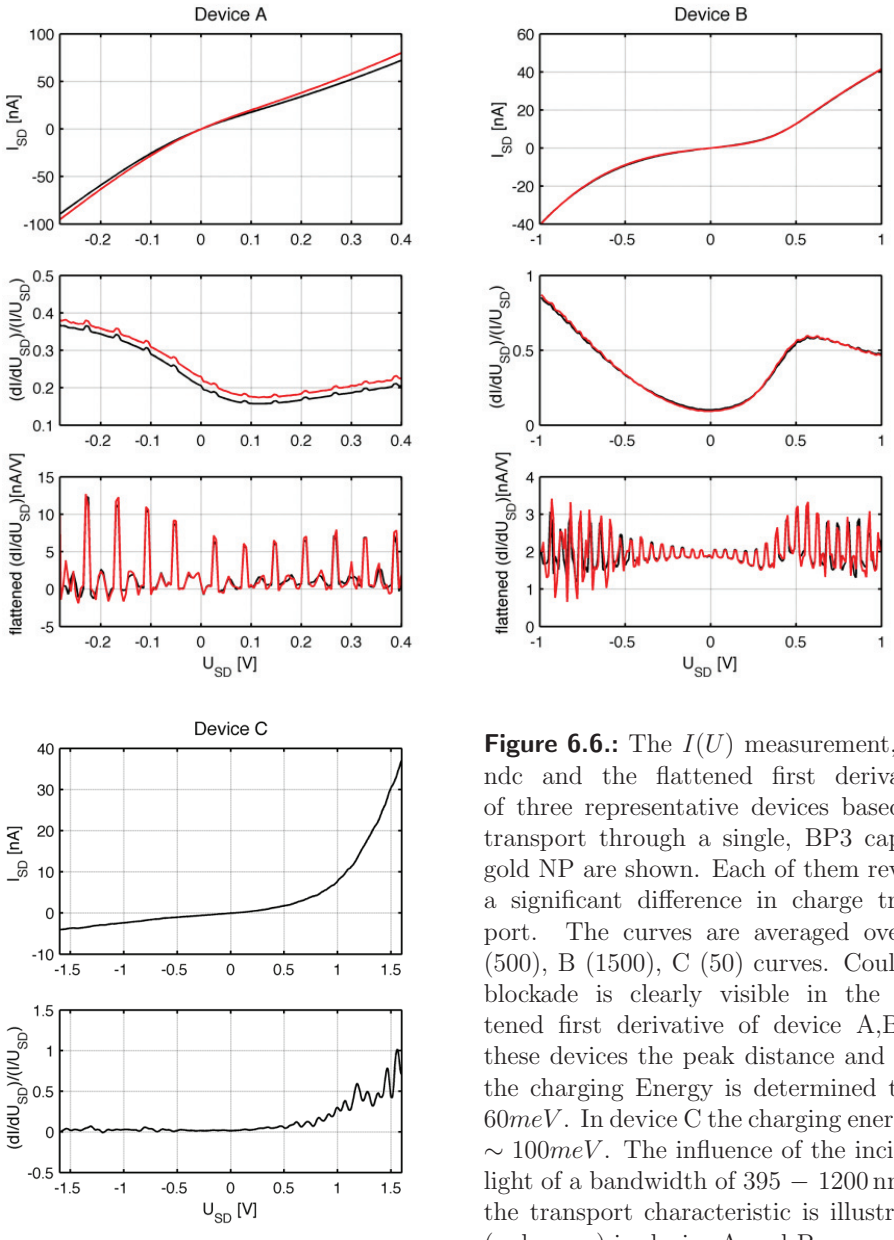

Figure 6.6.: The $I(U)$ measurement, the ndc and the flattened first derivative of three representative devices based on transport through a single, BP3 capped gold NP are shown. Each of them reveals a significant difference in charge transport. The curves are averaged over A (500), B (1500), C (50) curves. Coulomb blockade is clearly visible in the flattened first derivative of device A,B, in these devices the peak distance and thus the charging Energy is determined to $\sim 60meV$. In device C the charging energy is $\sim 100meV$. The influence of the incident light of a bandwidth of $395 - 1200\,\mathrm{nm}$ on the transport characteristic is illustrated (red curve) in device A and B.

of 50 nm (chosen as the width of the connection line). A change of $\Delta T = -300\,\mathrm{K}$ in temperature increases the distance of the nanoelectrodes by approximately $\Delta d_{gap} = 2 \cdot 50\,\mathrm{nm}(e^{k_{\alpha,Au}\Delta T} - 1) \approx 0.2 - 0.4\,\mathrm{nm}$, with $k_{\alpha,Au} = 14.2 \cdot 10^{-6}\,/\mathrm{K}$. It is assumed that the NP at 4K is in direct physical contact to one electrode and separated by a vacuum gap ($\approx 0.2 - 0.4\,\mathrm{nm}$) from the other electrode.
According to equations (2.35),(2.36) the capacitance of the molecular capped NP to the electrode with the vacuum gap is calculated to $C_{NP-plane}(l_{vac} = (0.2..0.4)\,\mathrm{nm}) = (1.8..1.6)\,\mathrm{aF}$ using a radius $r = r_{NP} + \cos(30°)l_{BP3} = 3.3\,\mathrm{nm}$. Using a relative permittivity of $\epsilon_r = \epsilon_{SiO_2}/2 \approx 2$ and considering that the applied substrate SiO_2 fills the half of the relevant room in the calculations. The coupling of the BP3 capped NP to the other electrode is estimated to $C_{NP-plane}(l_{vac} = (0.05)\,\mathrm{nm}) = (1.9)\,\mathrm{aF}$. The sum of both capacitances $C_{\Sigma,BP3,theory,4K} = C_{NP-plane}(l_{vac} = (0.2..0.4)\,\mathrm{nm}) + C_{NP-plane}(l_{vac} = (0.05)\,\mathrm{nm}) = (3.7..3.5)\,\mathrm{aF}$corresponds to the experimentally observed value of $C_{\Sigma,BP3-A,4K}$.

6.2. Transport measurement on single BP3 capped NPs at RT

The cyclic $I(U)$ measurements on three representative devices (Fig. 6.6 a),b),c)) show a significant difference in charge transport, i.e. the magnitude of the transport current and the ndc, which is clearly observable in the inset of Fig. 6.6c), where the $I(U)$ characteristic of all devices is plotted in the same graph. A possible reason for the different behavior of the three devices is discussed in the following sections.
The corresponding energy to the peak in the ndc of device B at $U_{sd} = 0.58\,\mathrm{eV}$ is in the order of the activation energy for superexchange coupling, compare sections 6.1 and 6.1.1, so that it is assumed that the transport mechanism in the device is changed.
The coulomb blockade behavior is discussed in more detail in section 6.2.1. In device A and B the influence of the illumination of light is observable in the charge transport measurement, which is discussed in more detail in section 6.2.5

6.2.1. Coulomb blockade at RT

In all devices, periodic peaks, indicating a CB-based transport mechanism, were observed at room temperature. The energy difference between the periodic peaks is equal

for constant temperatures T. Metallic nanoparticles in the size of <5 nm exhibit experimental capacitances in the order of $10^{18}F = 1 - 5\,\mathrm{aF}$ and hence a charging energy in the order of $E_c \approx 10 - 80\,\mathrm{meV}$. Therefore, in such systems, Coulomb blockade phenomena is observed in a range close to ambient temperatures, such as those shown in the ndc and the flattened first derivative of device A and B in Fig. 6.6. The cyclic $I(U)$ curves, averaged over 250 cycles (device A) and 750 cycles (device B), were obtained at RT. The $I(U)$ curves show nonlinear and slightly asymmetric behavior. In the flattened first derivative equidistant periodic peaks are clearly observable, with a distance of $\Delta U_{BP3,RT}(N, N+1) = 61\,\mathrm{mV}$. The corresponding coupling capacitance is $C_{\Sigma,BP3-A,RT} = 5.2\,\mathrm{aF}$ [88].
Compared to the coulomb blockade measurement at 4K, the peak separation observed is reduced, which is correlated to an increase of the capacitive coupling to one of the nanoelectrodes, due to the absence of a vacuum gap between the Au nanoelectrode and the NP. The capacitive coupling thereby is increased and thus the charging energy is lower ($\Delta U_{BP3,RT}(N, N+1) = 61\,\mathrm{mV}$) compared to the measurement at 4K ($\Delta U_{BP3,4K}(N, N+1) = 103\,\mathrm{mV}$).
The coulomb blockade peaks (Fig. 1b) were slightly asymmetric around zero, which is with a fractional residual charge Q_0 on the nanoparticle in equilibrium as described by Tinkham et al. [90]. The first coulomb steps of characterized NP-nanoelectrode systems are observed at source drain voltages of: ($U_{neg,BP3-A} = -50\,\mathrm{mV}$, $U_{pos,BP3-A} = 25\,\mathrm{mV}$) and ($U_{neg,BP3-B} = -55\,\mathrm{mV}$, $U_{pos,BP3-B} = 25\,\mathrm{mV}$). Using equation (2.30) the calculated fractional charging on the NP is determined to $Q_{0,BP3-A} = 0.19\,e$ and $Q_{0,BP3-B} = 0.37\,e$. The peak separations of $\Delta U_{neg-pos,BP3-A} = 75\,\mathrm{mV}$ and $\Delta U_{neg-pos,BP3-B} = 80\,\mathrm{mV}$ and at the first step corresponds to a capacitance of $C_{\Sigma,BP3-A/B,0} = 4.2\,\mathrm{aF}$ and $C_{\Sigma,BP3-B,0} = 4.0\,\mathrm{aF}$, which is almost 0.5 aF less, compared to the capacitance $C_{\Sigma,BP3-A,RT}$ calculated by the averaged peak separation $\Delta U_{BP3,RT}(N, N+1) = 61\,\mathrm{mV}$.

Since $k_B T < \Delta U e$, the measurement was performed in the 'strong' Coulomb blockade regime. According to [88], the theoretical value for the Coulomb blockade peak height is calculated using:

$$\Delta G_{CB,theo} = G_{lin,BP3-A,B} E_c / 6 k_b T \tag{6.1}$$

with the charging energy $E_c = \Delta U e/4$, the temperature $T = 300\,\mathrm{K}$ and the conductances around zero bias ($G_{lin,BP3-A} = 190\,\mathrm{ns}$ and $G_{lin,BP3-B} = 10\,\mathrm{ns}$), the theoretical

peak heights are calculated as $\Delta G_{CB,theo,A} = 19\,\mathrm{nS}$ and $\Delta G_{CB,theo,B} = 1\,\mathrm{nS}$, respectively. The peak heights measured $\Delta G_{CB,meas,A} \approx 10\,\mathrm{nS}$ and $\Delta G_{CB,meas,B} \approx 0.5\,\mathrm{nS}$, which are determined from the flattened first derivative of the $I(U)$ measurements. The theoretical value is a factor of two higher than the peak height measured. Consequently the fraction in conductance originated by CB-transport in the linear regime ($|U_{sd}|$<0.1), which is directly related to direct tunneling, was estimated to be:

$$(G_{CB-A,RT} = G_{lin,BP3-A}/2 = 100\,\mathrm{nS})$$

and

$$(G_{CB-B,RT} = G_{lin,BP3-B}/2 = 5\,\mathrm{nS}).$$

Including the considerations of the temperature dependent continuous increase

$$l_{vac,BP3-A}(T) = 2 \cdot 25\,\mathrm{nm}(e^{k_{\alpha,Au}\Delta T} - 1)$$

(contraction of the electrodes) and the unsteady change

$$\Delta l_{vac,jump}(T = 235\,\mathrm{K}) \approx 0.2\,\mathrm{nm}$$

(structural crossover) the temperature dependent conduction related to direct tunneling is estimated as:

$$G_{CB-A}(T) = G_{CB-A,RT} \exp\left(-\beta(l_{vac,BP3-A}(T) + 0.2\,\mathrm{nm}\sigma(235 - T))\right) \tag{6.2}$$

The Arrhenius-type hopping related temperature dependent conductance is estimated to:

$$G_{Arrhenius-A}(T) = (G_{lin,BP3-A} - G_{CB-A}(T)) \exp\left(-\frac{E_a}{k_B}(T^{-1} - 293^{-1})\right) \tag{6.3}$$

The sequential superexchange related temperature dependent conductance is estimated to:

$$\begin{aligned} G_{SE-A}(T) =& (G_{lin,BP3-A} - G_{CB-A}(T) - G_{Arrhenius-A}(T)) \\ & \cdot \left(T^{-1/2} - 293^{-1/2}\right) \exp -\frac{\lambda_r}{4k_B}(T^{-1} - 293^{-1}) \end{aligned} \tag{6.4}$$

The comparison of this theoretical approach with the measurement and an the partial contribution to the total transport current is shown in Fig. 6.7.

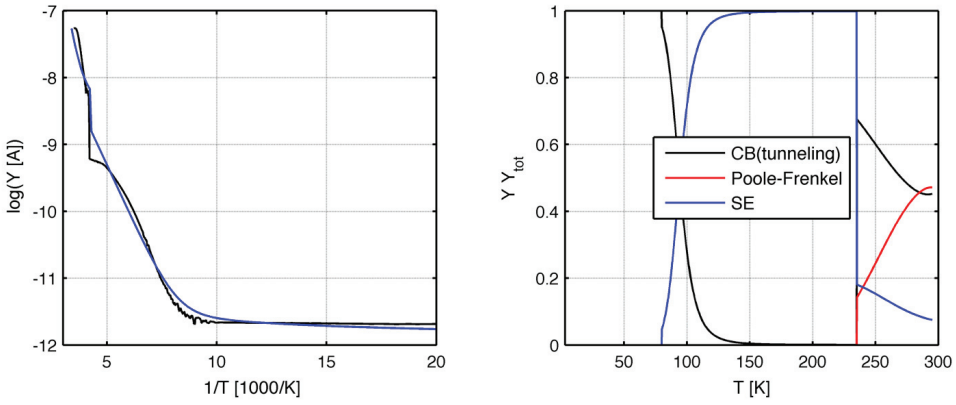

Figure 6.7.: (left) Simulation of the temperature-dependent transport, for further details compare with text. (right) The contribution of the three different channels (tunneling, hopping, sequential superexchange) to the total current.

6.2.2. Simmons fit of the $I(U)$ curve

The data of the $I(U)$ measurements across the junction were analyzed by applying a combination of an iterative fit sequence of the Simmons equation and the improved Transition Voltage Spectroscopy (TVS) as described in section 2.1.1 and 2.1.2. The height of the tunneling barrier as well as the remaining vacuum gap width were thereby determined for two representative 'electrode-molecule-NP-molecule-electrode' devices (A,C). According to the results shown in Fig. 6.7 the contribution of tunneling to the total current is estimated at 50% of the total current. According to [80] the hopping based transport current scales linearly with the source drain voltage U_{sd}, therefore the total tunneling related transport current is approximated using:

$$I_{tunneling,A} = I_{sd,A} - G_{Arrhenius-A,RT} \cdot U_{sd} \tag{6.5}$$

First the quotient $I_{tunneling,A}/U_{sd}$ was plotted versus U_{sd}^2, as depicted in Fig. 6.8. The conductance in the linear regime $G_{Sim,BP3,A/B}$ and the shaping factor $\rho_{BP3,A/C}$ were approximated using a linear fit, according to equation(2.6). The result of the linear fit,

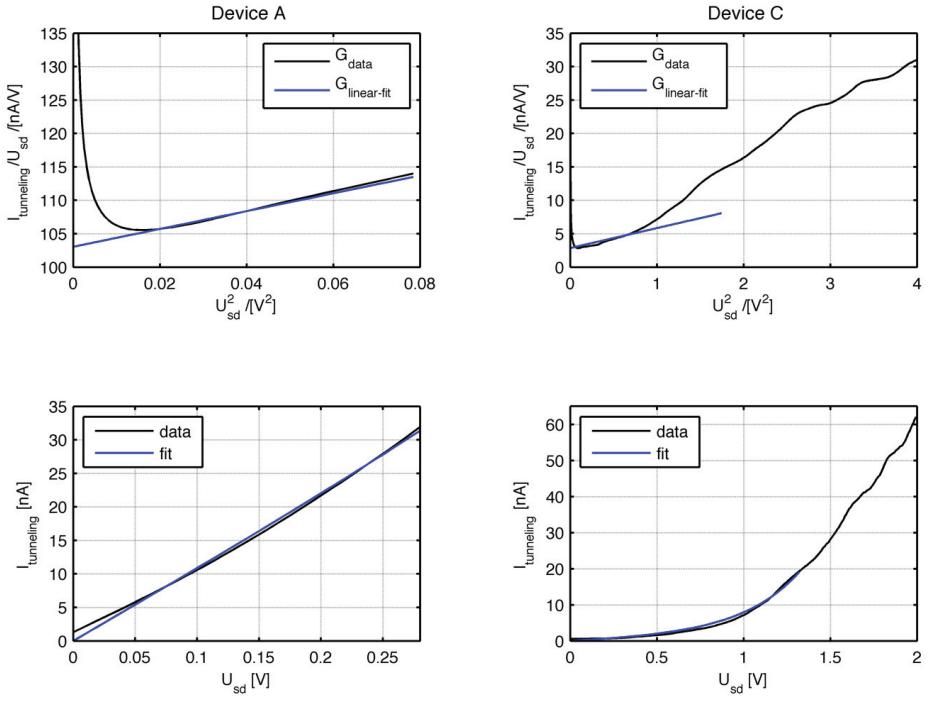

Figure 6.8.: (top) Linear fit of the quotient $I_{tunneling,A}/U_{sd}$ plotted versus U_{sd}^2.The blue colored line is a linear fit that reveals the shaping factor ($\rho_{BP3,A}(i=0) = 11.1\,(\mathrm{eV})^{-1}$, $\rho_{BP3,C}(i=0) = 10.5\,(\mathrm{eV})^{-1}$) from the slope of the curve. And the conductance in the linear regime ($G_{Sim,BP3-A} = 103\,\mathrm{nS}$, $G_{Sim,BP3-C} = 2.8\,\mathrm{nS}$) of the pure tunneling current is given by the axis intercept. (bottom) The result of the iterative Simmons sequence is in good agreement with the $I(U)$ measurement.

shown in 6.8, for the two representative devices was:

$$(G_{Sim,BP3-A} = 104\,\mathrm{nS} \text{ and } G_{Sim,BP3-C} = 2.8\,\mathrm{nS})$$

$$(\rho_{BP3-A}(i=0) = 11.1\,(\mathrm{eV})^{-1}, \rho_{BP3,C}(i=0) = 10.5\,(\mathrm{eV})^{-1})$$

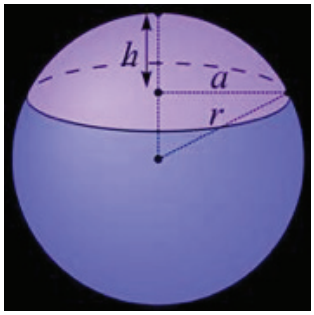

Figure 6.9.: Schematic diagram of a NP with radius $r_{NP,BP3} = 2\,\mathrm{BP3}$. The area of light purple colored calotte is $A_{calotte} = 2\pi r_{NP,BP3} h$.

The conductance in the linear regime can be estimated using equation (2.1):

$$(G_{Sim,BP3-A,theo.}(N_{molecules} = 5, l_{vac} = 0\,\mathrm{nm}) \approx 104\,\mathrm{nS},$$

$$G_{Sim,BP3-C,theo.}(N_{molecules} = 5..10, l_{vac} = 0.16..0.19\,\mathrm{nm}) \approx 2.5\,\mathrm{nS}).$$

Assuming that 5..10 molecules contribute to the tunneling transport process, this value is calculated, see Fig. 6.9 using the area of a calotte with a height between $h = 0.1..0.2\,\mathrm{nm}$, corresponding to an surface Area of $A_{calotte}(h) = 1.26..3.77\,\mathrm{nm}^2$. In the worst case all molecules on the calotte are parallel, thus the largest vacuum gap equals the height h, therefore the smallest contributing transport channel is a factor 10..100 lower than at the top of the calotte. According to Lüssem et al. [73] on $1\,\mathrm{nm}^2$ four BP3 molecules have place, therefor the number of molecules that contribute to charge transport is estimated at 5..10.

The conductance in the linear regime $G_{lin,tunneling}$ was set to fixed values ($G_{Sim,BP3-A/C}$) in the fitting sequences. The value obtained for the shaping factor is applied as starting parameter for the iterative fit sequence, as described in section 2.1.1. The other starting parameters for the first iteration step of the nonlinear least square fit were chosen to:

$$\phi_{BP3-A/C,1}(i = 0) = 0\,\mathrm{V},\ \phi_{BP3-A/C,2}(i = 0) = 7.5\,V$$
$$(\beta l)_{BP3-A/C,2}(i = 0) = \rho_{BP3-A/C,1}(i = 0)\phi_{BP3-A/C,2}(i = 0)$$

equally for both devices (A,C). The result of the iterative fitting sequence after 30 iteration steps was:

$$\rho_{BP3-A}(i = 30) = 7.0\,(\mathrm{eV})^{-1}, \rho_{BP3-C}(i = 0) = 9.5\,(\mathrm{eV})^{-1},$$
$$\phi_{BP3-A}(i = 30) = 1.65\,\mathrm{eV},\ \phi_{BP3-C}(i = 30) = 2.00\,\mathrm{eV},$$
$$(\beta l)_{BP3-A}(i = 30) = 11.5\,\mathrm{nm},\ (\beta l)_{BP3-C}(i = 30) = 18.9\,\mathrm{nm}.$$

6.2.3. Geometrical considerations out of electrical measurements

A concrete description of the geometry in the nanoelectrode junction is obtained by using equation (2.9), if molecular parameter such as the decay constant and length of the subunits are known.
The decay constant is well determined by STM measurements and documented in literature, for alkane $\beta_{alkane} = 8.1\,\mathrm{nm}^{-1}$ [48] and for the biphenyl unit $\beta_{BP} = 4.7\,\mathrm{nm}^{-1}$ [73]. The length of the molecular sections was calculated by a commercially available program (Argus Lab) $l_{methane} = 0.11\,\mathrm{nm}$, $l_{BP} = 0.83\,\mathrm{nm}$ and $l_{propane} = 0.45\,\mathrm{nm}$ as shown in Fig 6.1b). The tilt angle α had only a minor influence between 0°and 30°and was set to 30°taking into account the results given by NEXAFS measurements on BP3 [120]. Therefore, using the fitting result $(\beta l)_{fit} = (\beta l)_{BP3-A/C}(i = 30)$, the length of the vacuum gap is calculated as:

$$(\beta l)_{fit} = \beta_{vac} l_{vac} + \cos(\alpha)\,(\beta_{BP} l_{BP} + \beta_{alkane}(l_{propane} + l_{methane})) \tag{6.6}$$

As a result, the length of the vacuum gaps are estimated to be:

- for device A: $l_{vac,Sim,BP3-A} = (0.1 \pm 0.2)\,\mathrm{nm}$
- for device C $l_{vac,Sim,BP3-C} = (0.4 \pm 0.2)\,\mathrm{nm}$

These results are cross-checked calculating the averaged barrier heights, using Literature values for the barrier height of alkane $\phi_{alkane,Lit} = 1.4\,\mathrm{eV}$ [121], biphenyl $\phi_{BP,Lit} = 0.9\,\mathrm{eV}$ [122] and gold $\phi_{gold,Lit} = 5.2\,\mathrm{eV}$:

$$\begin{aligned}
\phi_{BP3-NP-A,theo} &= \phi_{alkane,Lit.}(l_{propane} + l_{methyl}) \\
&\quad + \phi_{BP,Lit.} l_{BP} + \phi_{Au,Lit.} l_{vac,Sim,BP3-A} \\
&\approx 1.5\,\mathrm{eV} \\
\phi_{BP3-NP-C,theo} &= \phi_{alkane,Lit.}(l_{propane} + l_{methyl}) \\
&\quad + \phi_{BP,Lit.} l_{BP} + \phi_{Au,Lit.} l_{vac,Sim,BP3-C} \\
&\approx 2.1\,\mathrm{eV}
\end{aligned}$$

These values calculated for the averaged tunneling barrier height are within the error bars of the values that are obtained by the iterative fit. At this point it is remarkable for device A that the resistance at zero bias $R_{BP3-A} = 1/G_{Sim,BP3-A} = 104\,\mathrm{nS} = 9.6\,\mathrm{M\Omega}$

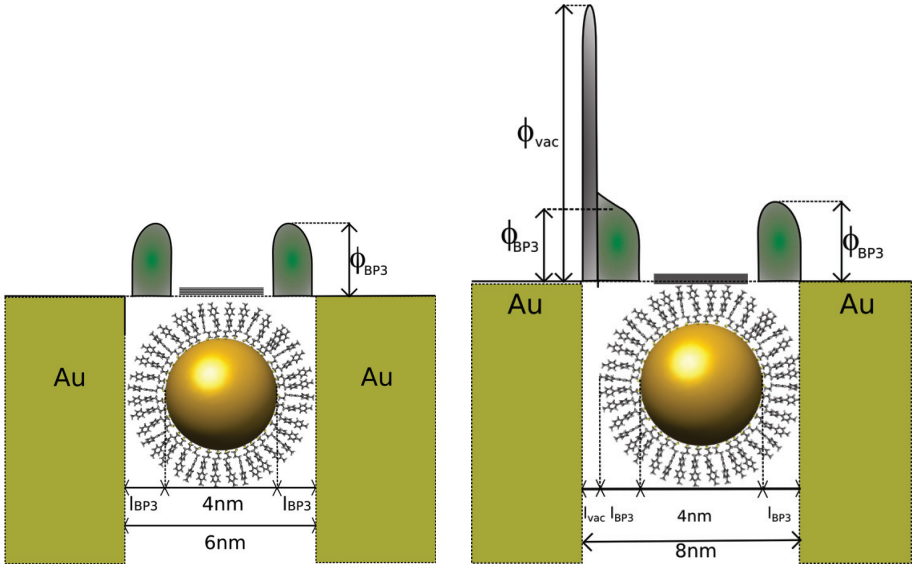

Figure 6.10.: a) Device A matches the height of the tunnel barrier the literature value for alkanethiols. This situation describes that the nanogap is completely filled by the hybrid nanoparticle. a) In device C the height of the tunnel barrier ϕ agrees with the work function of Au, therefore a small vacuum gap $l_{vac,Sim,BP3-C} \approx 3\,\mathrm{nm}$ remains.

is a factor of 5 lower than the typical contact resistance of alkanes ($54M\,\mathrm{M\Omega}$).

6.2.4. TVS

Besides the adapted Simmons equation, the electrical properties of the NP-nanoelectrode system is described by the TVS [62], compare section 2.1.2. TVS visualizes the transition from direct to Fowler-Nordheim tunneling (FNT), which is indicated by the minimum of the curve $\ln(I/U)$ plotted vs. $1/U$ (compare Device B,C in Fig. 6.11), i.e. by the transition voltage $U_{TVS,BP3}$.

In device A the Simmons fit revealed a vacuum gap of $l_{vac,TVS,BP3-B} \approx 0.1\,\mathrm{nm}$, so that the transport is dominated by molecular properties. The value of the transition voltage for different values of α is estimated using equations (2.16) to:
$U^{\alpha=2}_{TVS,BP3-A}(\eta_{BP3,A}) \approx 0.60\,\mathrm{V}$ and $U^{\alpha=1.5}_{TVS,BP3-A}(\eta_{BP3,A}) \approx 0.40\,\mathrm{V}$,
using $\eta_{BP3-A}(l_{vac} = 0.1\,\mathrm{nm}) = 0.78$ calculated with equation (2.12). The value of

the transition voltage is above the measured range, which is limited by the current of 100 nA. Experimental experience revealed that this current compliance is safe for the tested type of molecules. Therefore the transition from direct to Fowler-Nordheim tunneling was not observed in the TVS (Fig. 6.11a)).

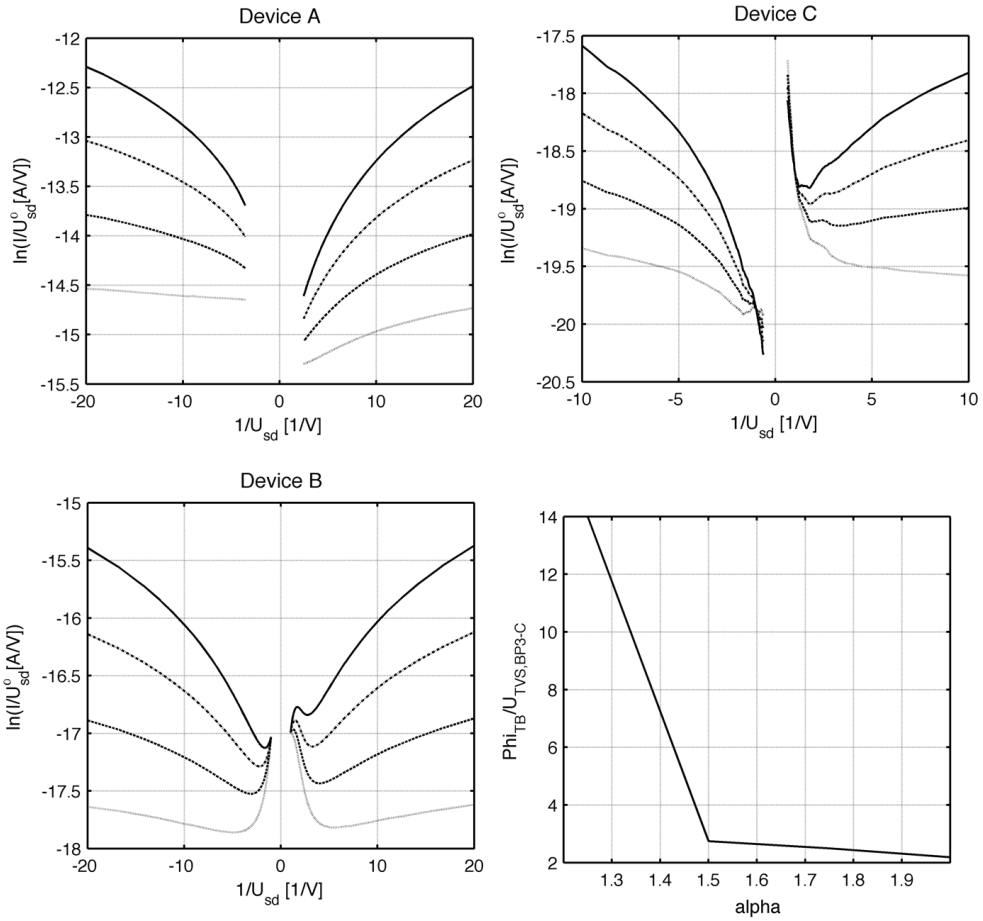

Figure 6.11.: Improved TVS plotted for different values of $\alpha = 2.0, 1.75, 1.5, 1.25$. (bottom right) Ratio of the fitted tunneling barrier height $\phi_{BP3-A/B/C}$ (Simmons) and the observed transition voltage $U_{TVS,BP3-A/B/C}$.

In the ndc of device B a peak is observed at $U_{DOS,BP3-B} = 0.61\,\mathrm{V}$, as shown in Fig. 6.6. The transition voltage is determined to $U^{\alpha=2}_{TVS,BP3-B} = 0.39\,\mathrm{V}$ and $U^{\alpha=1.5}_{TVS,BP3-B} = 0.25\,\mathrm{V}$, see Fig. 6.11, for $\alpha = 2$ and $\alpha = 1.5$, respectively. The contact factor η is calculated, using equation (2.16), to $\eta^{\alpha=2}_{BP3-B} = 0.75$ and $\eta^{\alpha=1.5}_{BP3-B} = 0.47$, which is in correspondance with the calculated value $\eta_{BP3,theo} = 0.63$, using equation (2.12) and $l_{vac,Sim,BP3-B} = 0.2\,\mathrm{nm}$.

The Simmons fit for device C revealed a tunneling barrier height of $\phi_{BP3-C} = 2.00\,eV$, as discussed in the previous section. The transition voltage is determined as $U_{TVS,BP3-C} = 0.85\,\mathrm{V}$, see Fig. 6.11. The contact factor η is calculated, using equation (2.16), as $\eta^{\alpha=2}_{BP3-C} = 0.34$, the theoretical value is calculated using equation (2.12) and the result of the Simmons fit $l_{vac,Sim,BP3-C} = 0.5\,\mathrm{nm}$ to $\eta_{theo,BP3} = 0.41$, which is in correspondence with measurements discussed by [62].

In conclusion, a set of two representatives I/U measurements across a BP3-NP immobilized in a nanogap are discussed. In this approach two independent methods were applied to crosscheck the characterized molecular properties achieved by $I(U)$ measurements, i.e. iterative Simmons fit sequence and improved TVS.

6.2.5. Photoconductivity in a single NP device

As shown by [123, 124] the incident light couples to the connection lines itself and the electrical field between the tips of the nanoelectrodes, thus at the position of the nanoparticle, is enhanced. The field enhancement is highly dependent on the exact geometry at the gap position and is strongest at the corner of the nanoelectrode tip [123]. Therefore the influence of light on the charge transport in such a system is significantly different, depending on the exact geometrical arrangement of the NP in the nanoelectrode device. The influence of the incident light on the current transport is shown in Fig. 6.6a),b). Depending on the exact geometrical arrangement of the NP in the nanoelectrode device the illumination of light increases the total current by 9 % (device A). Thus the contact resistance is reduced by $\approx 5\,\mathrm{M\Omega}$, originated from the photoelectric effect, which generates a cloud of electrons at the metal surface. Beside this other transport mechanisms, such as hopping or sequential superexchange, might be enhanced. In Device B the photocurrent increases the total current by less then

1 %, the contact resistance is increased for low voltages ($U_{sd} < 0.4V$) and reduced for high voltages ($U_{sd} > 0.4V$) by an amount of $\approx 1\,\mathrm{G\Omega}$ and $\approx 0.5\,\mathrm{G\Omega}$, respectively. As shown in section 6.2.3, Fig. 6.10, between the NP and the nanoelectrodes in device A,

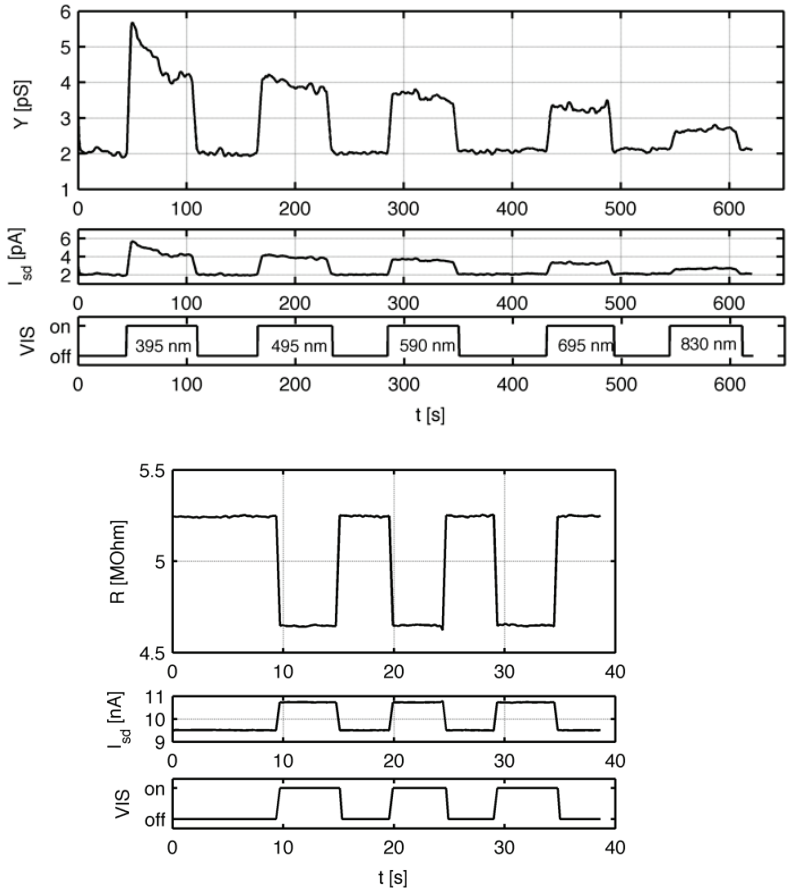

Figure 6.12.: (top) RT measurement of the photocurrent for an applied bias voltage of $U_{sd} = 50\,\mathrm{mV}$ at a single BP3 capped NP under switching light conditions (bandwidth 395 nm-1100 nm). The enhancement of the current of is 11%. (bottom) At low temperatures ($T = 4\,\mathrm{K}$) the photocurrent for an applied voltage of $U_{sd} = 1\,\mathrm{V}$ under exposure of light of different bandwidth, the observed enhancement of the conductance is 80 %.The denoted wavelength is the lower bond of the bandwidth, the upper bound is determined by a liquid IR filter at 1100 nm.

no vacuum gap and in device B a vacuum gap of approximately 0.1 nm remains. One possible explanation for a greater increase in photocurrent is a different geometrical arrangement, i.e. at the corner of the electrode tip (device A) or in the center of the electrode tip (device B).
In Fig. 6.12(left) the influence of an exposure of light with the bandwidth 395 nm-1100 nm on the transport current is shown. The measurement is performed at RT for an applied bias voltage of $U_{sd} = 50\,\mathrm{mV}$, the change in current is explained by a pure photocurrent [37]. At low temperatures, the vibrational modes of the molecule were frozen, therefore an exposure will enhance the excitation of vibrational modes in the molecule and metal electrodes and enhance the coupling of the molecule to the electrodes. Therefore the influence of the light is expected to be much higher (80 %) compared to the room temperature measurements, see Fig.6.12(right). This effect is reasonable if we assume that molecular vibrations are excited by the illumination with light, comparing the $I(U)$ characteristic (Fig. 6.3) below 7 K, where the molecular vibrations are frozen out, with the $I(U)$ characteristic above 7 K. The measurements are performed for an applied voltage of $U_{sd} = 1\,\mathrm{V}$. The influence of the exposure to light of the bandwidth of 830 nm - 1100 nm is much smaller, compared to the other bandwidth. This bandwidth is above the plasmon resonance of a NP-metal-electrode system [125]. The wavelengths 695 nm and 830 nm corresponds to an energy of 1.50 eV and 1.79 eV, respectively, which is in the order of the determined tunneling barrier height of the BP3 capped NP (as determined in sections 6.2.2 and 6.1.1), however a direct transition from the Fermi-level to a molecular level has not yet been described in literature. The reason for a lower photocurrent is currently not clear.

6.3. Conclusion of the BP3 capped NPs

The various investigations on a single BP3-capped NP, as shown in this chapter, elucidate the different mechanisms involved in charge transport in such a device and gives an impression about the type of contact of the BP3 capped NP to the nanoelectrodes, i.e. is there a vacuum gap remaining between the NP and the electrode or not.
First, approved tools are applied according to Poole-Frenkel, Arrhenius, granular metal and super-exchange coupling to elucidate different transport mechanisms in a NP device, commonly an array of NPs, using temperature dependent conductance measurements. However, this method elucidates the principles of charge transport mechanisms for the case of single BP3 capped NPs that are immobilized between nanoelectrodes as well. The results obtained are compared with measurements on a NP array, which was performed by Kerstin Blech in the group of our cooperation partner Prof. U. Simon.

In the case of a single NP four regions are identified in the Arrhenius plot, where charge transport is based on different transport mechanisms. The limiting barrier $E_{PF} = 1135\,\mathrm{meV}$ is dedicated by the Poole-Frenkel theory at high temperatures ($T \in [245\,\mathrm{K} - 265\,\mathrm{K}]$), which corresponds to the high voltage approximation of the Arrhenius equation. At intermediate temperatures ($T \in [110\,\mathrm{K} - 200\,\mathrm{K}]$) super-exchange coupling between the phenyl-units is the dominating transport mechanism. The related energy $E_{SE} = 617\,\mathrm{meV}$ is in correspondence with the reorganization between two adjacent phenyl units, as observed in literature [12]. The conductance is observed to be temperature independent at low temperatures ($T < 100\,\mathrm{K}$), which indicates a pure tunneling based transport [8].

In the case of a NP array, at high temperatures ($T \in [300\,\mathrm{K} - 340\,\mathrm{K}]$) the activation energy $E_A = 184\,\mathrm{meV}$ obtained is in correspondence with the rotation energy of 190 meV that was determined by Reed et al. [28] for a biphenyl in a nanopore device. At intermediate and low temperatures ($T \in [20\,\mathrm{K} - 170\,\mathrm{K}]$) the transport is shown to be dependent on the charging energy of the NP. The determined value of $E_{GM} \approx (14 \pm 3)\mathrm{meV}$ is in correspondence with the charging energy of

$$E_{gm,theo} = E_c \approx \frac{e^2}{2C_{two-shell}} = \frac{e^2}{8\pi\epsilon_r\epsilon_0}\left(1/r_{NP} + 1/(r_{NP}+s)\right) \approx 13\,\mathrm{meV}.$$

The charging energy obtained is in correspondence with the charging energy calculated using the peak distance ΔU_{RT}, which is determined of the $I(U)$ in the single NP measurement at room temperature.

$$E_c = \Delta U_{RT} e/4 \approx 15\,\mathrm{meV}$$

Comparing both experiments, charge transport in a 3D NP-array is considerably higher than in a single NP device due to the availability of multiple transport channels in parallel percolation paths. The observed activation energies in a 3D NP-array are remarkably lower, which is attributed to the interdigitating ligand shells, thus an insulating medium of closed packed molecules. On the contrary, only a few ($\sim$4) molecules are creating a contact between the NP and the electrodes. Consequently, the insulating medium between the NP and the nanoelectrode is regarded as higher insulating than in a 3D NP-array.
The temperature dependent transport through a single NP and a NP array shows a significant difference. In a NP array a voltage drop over each tunneling barrier is typically lower than $1\,\mu$V. Contrary, in a single NP device, the voltage drop over the limiting tunneling barrier is at least the half of the applied bias voltage. Therefore, in the case of a single NP, the high field equations for temperature dependent transport have to be considered, i.e. the hopping is described using the Poole-Frenkel equation [126] and the granular metal model for high electric fields [86]. In the case of the NP array pure tunneling is not observed, which is obvious, since the transition rate according to tunneling is exponentially dependent on the voltage drop over each tunneling barrier. In a NP array the molecules are interdigitating, so that the coupling between the NPs and hence the characteristic energies obtained for the transport mechanisms might be different.
The common feature observed in both measurements is a discontinuity in the temperature dependent conductance measurement. The postulated explanation for this phenomenon is a reversible, structural crossover between two morphologies of the NP, as well as the rearrangement of the capping molecule on the particle surface. The change in vacuum gap, due to the structural crossover, is estimated to be in the range of 0.1-0.3 nm in section 6.2.1.
It is not clear why this discontinuity appears in different forms, but it appears as a sudden change in conductance for a single NP, while it is broadened up to a width of 60 K

for the NP array. In fact this is an affirmation for the earlier made hypothesis that this discontinuity might be attributed to a crossover in the particle morphology, since the crossover is described as size dependent [115] and the NPs have a size distribution. Consequently, a temperature distribution for structural crossover in a NP array is expected.

Coulomb-blockade behavior is observed at room temperature as well as at 4 K. So far only in STM measurements on small Au NPs with a diameter of <4 nm CB behavior is observed at room temperature (RT) [127]. The observed peak separations at RT and 4 K ($\Delta U_{RT} = 61$ meV and $\Delta U_{4K} = 103$ meV) correspond to charging energies of $E_{c-RT} = 15$ meV and $E_{c-4K} = 26$ meV, respectively, which is typical for the size of the NPs [61, 128–131]. The difference in charging energy by a factor of 1.7 is explained by the change of the length of the vacuum gap between the nanoparticle and the nanoelectrode. Thereby, the capacitive coupling is reduced, which increases the charging energy E_c. A change in vacuum gap of 0.3-0.5 nm is composed of the temperature dependent contraction of the nanoelectrodes and the assumed structural crossover of the NP [115].

The total amount of coulomb blockade related transport is estimated comparing the measured peak heights of the Coulomb blockade peaks ($\Delta G_{CB,meas,A} \approx 10$ nS and $\Delta G_{CB,meas,B} \approx 0.5$ nS) with the theoretically calculated values ($\Delta G_{CB,theo,A} = 19$ nS and $\Delta G_{CB,theo,B} = 1$ nS). The Coulomb blockade based transport is a phenomenon that limits the tunneling related charge transport mechanism [82]. Therefore, the fraction in conductance, that is related to direct tunneling at zero bias voltage, can be estimated to (see section 6.2.1):

$$(G_{CB-A,RT} = 100\,\text{nS}) \text{ and } (G_{CB-B,RT} = 5\,\text{nS}).$$

Considering the temperature dependent continuous contraction of the electrodes and the unsteady change due to the structural crossover, the temperature dependent conduction based on direct tunneling is estimated to ($G_{CB-A}(T)$). Accordingly, the Arrhenius-type $G_{Arrhenius-A}(T)$ and the superexchange $G_{SE-A}(T)$ related temperature dependent conductance are approximated. In the first order the model developed is showing a good correspondence with the measurement, see Fig. 6.7.
Two of the three representative devices (A,C) are investigated applying the aprooved tools, the Simmons fit routine [111] and the TVS [62]. Although the measurements

are performed under the same condition as the applied electrode material, NP solution, trapping method and measurement settings, the $I(U)$ transport measurements show a significantly different behavior, as shown in Fig. 6.6. In device A the conductance $G_{lin,BP3-A} = 190\,\text{nA}$ is increased almost by a factor 100 compared to device C $G_{lin,BP3-C} = 2.8\,\text{nA}$. The iterative Simmons fit applied to the corrected $I(U)$ curve with the value of conductance $G_{CB-A}(T = 300\,\text{K}) = 100\,\text{nS}$ and $G_{CB-C}(T = 300\,\text{K}) = 2.8\,\text{nS}$ at zero bias, which was determined by the temperature dependent measurements, reveal a tunneling barrier height of $\phi_{BP3-A} = 1.65\,\text{eV}$ and $\phi_{BP3-C} = 1.8\,\text{eV}$, respectively. The tunneling barrier of device A is in the order of the barrier height of alkanethiol (1.4 eV-1.6 eV) [20, 121] and in correspondence with estimations of the averaged barrier height according to equations (6.7), using literature values of the molecular decay constants and the determined length of the vacuum gap.
Thereby, the remaining vacuum gap is calculated to be 0.1 nm and 0.4 nm, respectively, using the decay parameter $(\beta l)_{BP3-A/C}$ obtained in the Simmons fit. Thus, a small difference of only 0.3 nm in the length of the vacuum gap, which is in the length scale of two atomic bonds, has an tremendous influence on the $I(U)$ characteristic.

The TVS tool cannot be applied to device A, since the value of the transition voltage is above the range of bias voltage applied, which is limited by the current compliance of 100 nA. Experimental experience has shown that this current compliance is safe for BP3-capped NPs. In device B a division factor of $\eta^{\alpha=2}_{BP3-B} = 0.75$ is revealed and thereby an 'intermediate' length of the vacuum gap of 0.2 nm was achieved, i.e. a value between the achieved length of the vacuum gap for device A and device C. The division factor $\eta^{\alpha=2}_{BP3-B}$ obtained is 20% higher as the theoretically calculated value of 0.63 using equation (2.12). In device C a division factor of $\eta^{\alpha=2}_{BP3-C} = 0.34$ is revealed, which already gives a hint that the length of the vacuum gap (0.5 nm) is slightly larger as the obtained value for device B. The division factor $\eta^{\alpha=2}_{BP3-B}$ obtained is 17 % lower as the theoretical calculated value of 0.41 using equation (2.12).
In conclusion, three representative electrode/BP3-NP-BP3/electrode devices $I(U)$ measurements have been shown. The devices are characterized applying the well established analyzing tools: Simmons fit and TVS. The tunneling barrier heights obtained and the resulting length of the vacuum gaps are consistently interpreted on the basis of a geometrical model with the application of the Simmons model, TVS and literature values of the molecular properties.

The conductivity is measured across the electrode/BP3-NP-BP3/electrode junctions and have been found to be highly sensitive to small variations of the NP deposited into the gap and critically dependent on how perfectly the NP fills the nanogap. Furthermore, the total resistance at zero bias $R_{cont,BP3} = 9.6\,\mathrm{M\Omega}$ of the biphenyl unit is almost lowered by a factor of three compared to the contact resistance of alkanes $R_{cont,alkane} = 54\,\mathrm{M\Omega}$ [48], which supports the comparison of the contact resistance of the phenyl unit to that of a fullerene.
The change in conductance under illumination of light due to a photocurrent through the device could be correlated to the position of the nanoparticle, i.e. a high photocurrent ($> 5\%$ change in current) probably corresponds to a position close to a corner of the nanoelectrode tip, thus, the electrode tip separation is smaller than the size of the NP. While a low photocurrent ($< 5\%$ change in current) could be related to a position between the nanoelectrodes, the electrode tip separation is larger than the size of the NP.

7. Transport measurements on MES capped NPs

In the following chapters the study of three different molecule-NP systems is described. First the transport property as the tunneling barrier height and a consideration of the geometry in the nanoparticle-nanoelectrode system were determined for MES capped 12 nm gold NPs. The NPs have been synthesized by our cooperation partner I. Willner at the Hebrev University of Jerusalem, in the frame of a 7^{th} framework financed European project MOlecular LOgic Circuits (MOLOC). In the measurements that are described in the following chapters, the electrode material Au_3Pd_2 is chosen, since palladium is not so ductile as Au and enhances the stability of the nanoelectrodes. The MES capped NPs are a reference System for the following study of gold NPs that are capped with different ratios of Spiropyran and MES.

7.1. Mercaptoethanesulfonic acid

In literature, in a SAM of mercaptoethane sulfonic acid, it was shown that some of the acid groups are de-protonated and some are hydrogen-cross-linked [132–134]. An indication for the de-protonation of the MES molecule was also found in DC-DEPT measurements, as described in section 5.3, where only the positive charged electrode was covered with MES capped NPs.
Due to the electrostatic repulsion of the negative charged sulfonic acid end-groups the MES capped NPs show a good geometric stability in solution, although MES are short chain molecules [133]. The MES molecule has two possible conformations of the Au-S-C-C-chain: trans and cis. Accordingly MES in cis conformation has a different length and dipole moment in direction of the tunneling barrier [135]. The effective length of the MES in trans and cis conformation was calculated by a freeware program (Chimera) to $l_{MES,trans} = 0.52\,\text{nm}$ and $l_{MES,cis}(MES) = 0.43\,\text{nm}$ respectively.

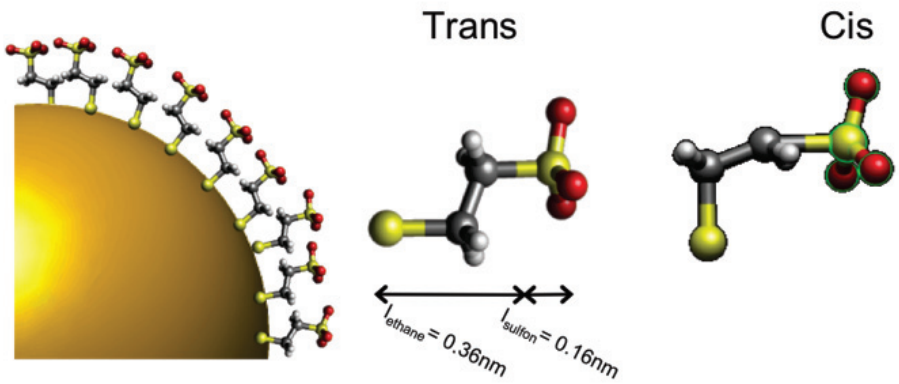

Figure 7.1.: (left) A MES capped gold NP with a diameter of (12 nm) is depicted. (right) The MES molecule has two conformational sates: trans and cis. [136].

7.1.1. UV-Vis spectroscopy on MES molecules

The UV/VIS absorption spectrum of MES molecules in aqueous solution ($c \approx 10^{-3}$ mol/l) is depicted in Fig. 7.4 [136]. The onset of absorption (absorption edge), located at an energy of about 3.75 eV, possibly corresponds to the HOMO-LUMO gap of the MES molecule. Thus the first derivative of the absorption spectrum represents the transition between two DOS-levels of a molecular system [137, 138], therefore the peaks are expected to have a Gaussian shape [139]. In the UV/Vis absorption spectrum a second level was observed. The distance between the two levels $\Delta E_{MES,2-1}$ was estimated by the distance of the Gaussian peaks of the first derivative to $\Delta E_{MES,2-1} = (0.95 \pm 0.01)$ eV, as shown in the blue curve of Fig. 7.4b). This level might correspond to other first order transitions in the MES, for example the [(HOMO-2) $\leftrightarrow$ LUMO],[(HOMO-1) $\leftrightarrow$ LUMO], [HOMO $\leftrightarrow$ (LUMO+1)] or [HOMO $\leftrightarrow$ (LUMO+2)] transition, since the [(HOMO-1) $\leftrightarrow$ HOMO] and other second order possible transitions have a much lower probability, as discussed in [140].

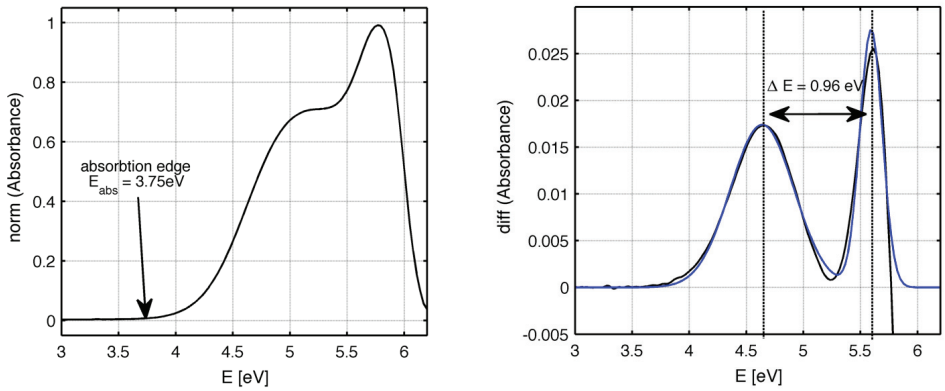

(a) **(b)**

Figure 7.2.: a) Optical absorption spectrum of MES molecules dissolved in di-water. b) First derivative of the absorption spectrum. The blue curve is a fit of two overlapping gaussian peaks $f_i(E) = H_i exp(-(E - E_{MES,i})^2/\sigma^2_{MES,i})$ with $i \in [1, 2]$. The result of the fit was $H_1 = 0.0174$, $H_2 = 0.0276$, $E_{MES,1} = 4.64\,\text{eV}$, $E_{MES,2} = 5.59\,\text{eV}$, $\sigma_{MES,1} = 0.39\,\text{eV}$ and $\sigma_{MES,2} = 0.14\,\text{eV}$. The measurement was performed by [136].

7.1.2. Approximation of the dipole moment of MES

Next the dipole moments of MES in the trans and cis conformation were calculated by a PhD student (Tristan Lespagnard) of our cooperation partner F. Remacle at the university of Liege, to $P_{MES,trans} = 2.75\,\text{Debye}$ and $P_{MES,cis} = 4.02\,\text{Debye}$. The dipole moment of the de-protonated MES along the transport axis was estimated by a commercially available program (Argus Lab) as $P_{MES,deprot.} = 6.0\,\text{Debye}$. The packing density in a SAM of MES on a Au(111) was estimated to $5\,\text{molecules/nm}^2$ by [141] in linear sweep voltammetric measurements, which correlates to the density of alkanethiol. However, in a lower ordered layer, such as on a NP surface, the packing density is assumed to be $4\,\text{molecules/nm}^2$ in trans and 3 molecules/nm^2 in cis conformation, and thus a lower packing as alkanethiol ($\approx 5\,\text{molecules / nm}$). Thereby the surface dipole moment of MES on gold was calculated to $P_{MES-Au,trans} = 11\,\text{Debye/nm}^2$, $P_{MES-Au,cis} = 12.06\,\text{Debye/nm}^2$, $P_{MES-Au,deprot.} = 24.0\,\text{Debye/nm}^2$ respectively.
According to equation (2.21) in section 2.2, the change in work function was estimated to $W_{MES-Au,trans} = 4.1\,\text{eV}$, $W_{MES-Au,cis} = 4.5\,\text{eV}$ and $W_{MES-Au,deprot.} = 9.4\,\text{eV}$. The

relative difference between the work functions of the two MES species trans and cis was estimated as:

$$\Delta W_{MES-Au,trans,cis} \approx 0.4\,\mathrm{eV}$$

7.2. Transport measurement on single MES capped NPs at RT

The transport properties of MES capped gold NPs (12 nm), which were immobilized between two AuPd nanoelectrodes, are studied in this section. The MES NPs were immobilized by AC-DEPT as described in section 5.3. Then cyclic $I(U)$ measurements were performed in a triaxial shielded box under normal atmosphere conditions on the vibration isolated cryostat platform. The cyclic $I(U)$ measurement was performed with the settings: $dU = 10\,\mathrm{mV}$, $dt = 0.2\,\mathrm{s}$, $NPLC = 1$ and a fixed range of 1 nA.
An amazing good conformity was found, comparing the $I(U)$ measurements on SAM MES on Au(111) [136] with the cyclic $I(U)$ measurements on MES capped NPs in a nanoelectrode configuration, as shown in Fig. 7.3(b).
The branch with the solid line was measured with a positive dU (up), and the dashed line with a negative dU (down). The features in the ndc of the 'up-' and the 'down-branch' were qualitatively similar, as shown in the inset of Fig. 7.3b), where the 'up branch' was plotted mirrored with respect to the ordinate. Therefore only the 'down-branch' is discussed in the following part. Comparing the ndc of the NP- measurement with the DOS curve achieved by STM measurement, for $U_{sd} < 0$ two peaks were found at:
($U_{MES,DOS,1} = -1.78\,\mathrm{V}$,$U_{MES,DOS,2} = -1.08\,\mathrm{V}$),
which were assigned as the relevant density of states features and thus are attributed to molecular energy levels (HOMO, HOMO-1). The distance between the peaks is $\Delta U_{MES,DOS,1-2} = (0.72 \pm 0.03)\,\mathrm{V}$. For positive voltages $U_{sd} > 0$ one peak is observed at ($U_{MES,DOS,3} > 2.2\,\mathrm{V}$), which is correlated to the LUMO level. Beside the $I(U)$ measurements described previously, extremely unsteady devices, that have a much higher conductance that is expected for such a short molecule were observed.

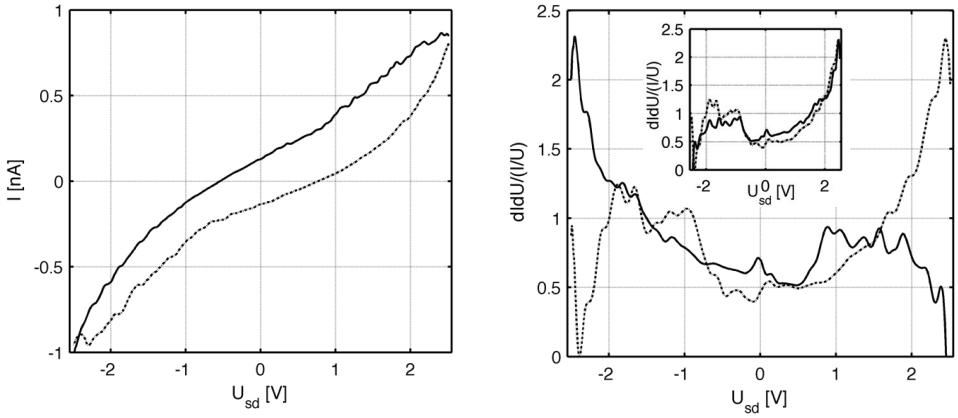

Figure 7.3.: a) Cyclic $I(U)$ curve of a single MES capped gold NP with a diameter of 12 nm and b) ndc curve. Three peaks in the ndc are described, as relevant density of states features, compare STM measurements. The up and the down branches of the ndc are similar in shape, which is illustrated in the inset of (b), where the U_{sd} of the up branch (solid line) is flipped for clarity.

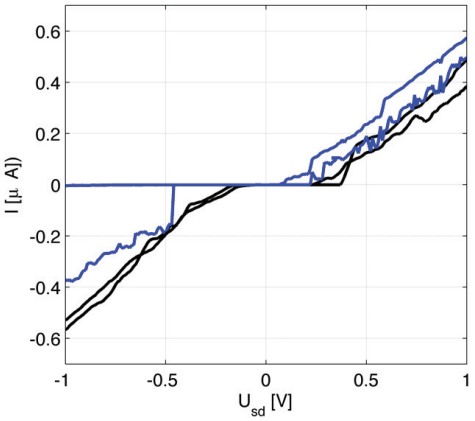

Figure 7.4.: In the $I(U)$ measurement on MES capped 12 nm Au NP extremely fluctuating $I(U)$-curves were observed, which show a conductance in the order of 1 μS.

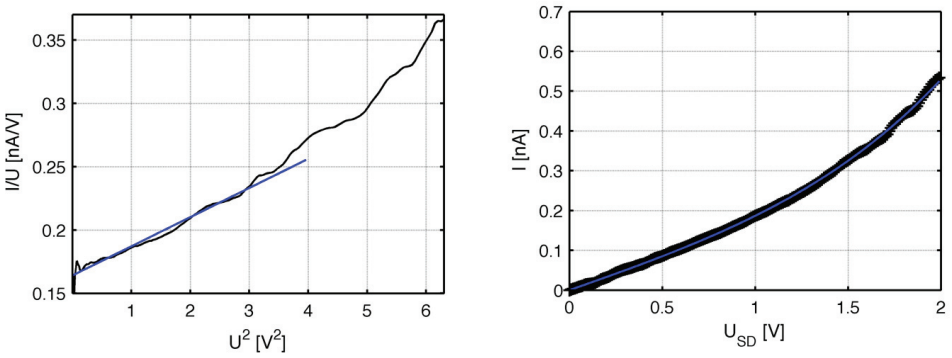

(a) (b)

Figure 7.5.: a) Linear fit of the quotient I/U plotted versus U^2. The blue colored line is a linear fit that reveals the parameter $\rho_{MES,pos}(i=0) = 3.6\,/(\mathrm{eV})^{-1}$ from the slope of the curve and the conductance in the linear regime $G_{MES,lin-pos} = 0.165\,\mathrm{nS}$ from the axis interception.

7.2.1. Simmons fit of the $I(U)$ curve

An exponential fit with the Simmons model is associated with high uncertainties, which were reduced by applying an iterative fit sequence, as described in section 2.1.1. First the quotient I/U was plotted versus U^2, as depicted in Fig. 7.5. The conductance in the linear regime G_{lin} and the shaping factor $\rho_{neg/pos}(i=0)$ were fitted using a linear fit, according to equation (**??**).The result of the linear fit for the negative and positive side of the 'down-branch':
($G_{MES,lin-neg} = 0.165\,\mathrm{nS}$, $G_{MES,lin-pos} = 0.165\,\mathrm{nS}$)
and ($\rho_{MES,neg}(i=0) = 5.3\,(\mathrm{eV})^{-1}$,$\rho_{MES,pos}(i=0) = 3.6\,(\mathrm{eV})^{-1}$),
was applied as starting parameter for the iterative fit sequence, as described in section 2.1.1. The result of the iterative fitting sequence after 30 iteration steps was:
$\rho_{MES,neg} = 5.0\,(\mathrm{eV})^{-1}$, $\rho_{MES,pos} = 3.6\,(\mathrm{eV})^{-1}$ and
$\phi_{MES,neg} = 5.4\,\mathrm{eV}$, $\phi_{MES,pos} = 5.6\,\mathrm{eV}$ and
$(\beta l)_{MES,neg} = 27$, $(\beta l)_{MES,pos} = 20.0$.
The width of the vacuum gap of the fitting result (βl) was approximated by using:

$$(\beta l)_{MES,tot} = \beta_{vac} l_{vac} + \cos(\gamma)\beta_{MES} l_{MES} \tag{7.1}$$

The decay constant for MES is estimated, using [59]:

$$\beta_{MES} = \frac{2}{\hbar}\cos(\gamma)\sqrt{2m^* m_e \phi_{MES}}$$

with $\phi_{MES} = U_{MES,DOS,1-3}$(MES-NP) as observed in Fig. 7.3, to be in the range $\beta_{MES} = (10-15)\,\mathrm{nm}^{-1}$, thereby the uncertainty of the calculation of the vacuum gap is 0.2 nm. The lengths of the molecular subsections are $l_{ethane} = 0.36\,\mathrm{nm}$ and $l_{sulfonate} = 0.16\,\mathrm{nm}$ as shown in Fig. 7.1b). The tilt angle γ of the molecule had only a minor influence between 0°and 30°and was set to 0°, assuming the sulfonate group of the MES is aligned in parallel to the electrical field.
The length of the vacuum gap was estimated as:
$l_{vac,MES,Sim-neg} = (0.9 \pm 0.2)\,\mathrm{nm}$, $l_{vac,MES,Sim-pos} = (0.6 \pm 0.2)\,\mathrm{nm}$.

7.2.2. Transition Voltage Spectroscopy

According to [62,65], the minimum in Fowler Nordheim plot is called transition Voltage. The transition voltage U_{trans} is correlated with the distance of the closest molecular level to the fermi level by a factor f, which is dependent on the exponent α and the symmetry parameter η, as described in section 2.1.2. The TVS is plotted for two different exponents $\alpha = 2$ and $\alpha = 1.5$, as described in [62]. For $\alpha = 2$ two minima are observed in the 'up-' and the 'down-branch' at $U_{MES,TVS-up} = 2.22\,\mathrm{V}$ and $U_{MES,TVS-down} = 1.92\,\mathrm{V}$ respectively, as shown in Fig. 7.6a). In the Fowler Nordheim plots with $\alpha = 1.5$

	down		
	peak i=1	peak i=2	peak i=3
$U(MES,DOS,i)[eV]$	-1.08	-1.78	> 2.2
	$\alpha = 1.5$		
$U_{MES,TVS-down}(\alpha = 1.5)$ [eV]	-0.39	-0.67	1.40
$U(MES,DOS,i)/U_{MES,TVS-down}$	2.77	2.66	1.72
η	0.24	0.34	0.28
$l_{vac,MES,TVS}$ [nm]	0.7	0.8	0.8

Table 7.1.: Compilation of voltages $U(MES,DOS,i)$, where peaks are observed in the DOS-curve and the corresponding transition voltages $U_{MES,TVS-down}(\alpha = 1.5)$. Therewith the symmetry parameter η (using equation (2.16)) and thus the remaining vacuum gap in the tunneling contact are estimated (using equation (2.12)).

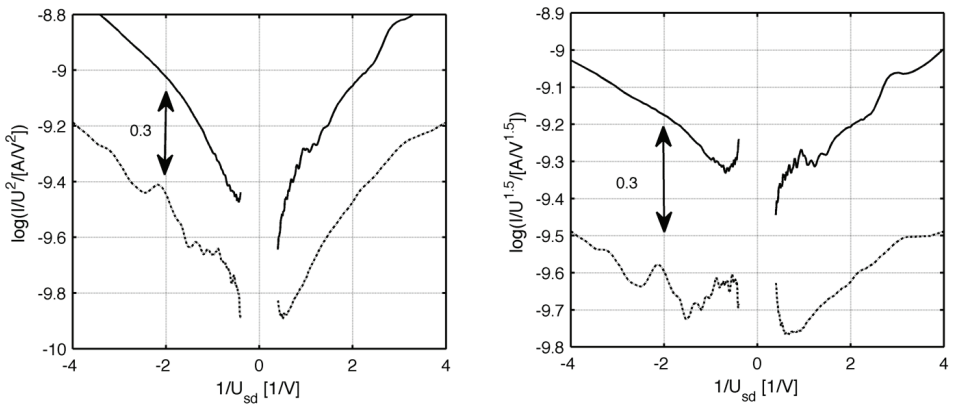

(a) **(b)**

Figure 7.6.: a) Fowler Nordheim plot with $\alpha = 2$ calculated from a cyclic $I(U)$ measurement of a single MES capped gold NP with a diameter of 12 nm. The solid line in the plot corresponds to the 'up' and the dashed to the 'down-branch'. The two branches (up and down) were separated by 0.3, for clarity. b) Fowler Nordheim plots with $\alpha = 1.5$ emphasize the minima in each branch.

(Fig. 7.6) the minima in each branch are more emphasized, compared to plots with $\alpha = 2$. The 'down-branch' for $\alpha = 1.5$ is discussed according to equations (2.16) in section 2.1.2, using $l_{molecule} = l_{vac,MES,TVS}$ in equation (2.12).

7.3. Results and discussion

The representative measurement of the 'nanoelectrode-MES-NP-MES-nanoelectrode' system is in excellent agreement with the STM measurements of a SAM of MES on Au(111) surface, to be published by A. Soltow [136]. Although the measurements were performed under completely different conditions, such as :

1. the electrode material [AuPd vs. (Au(substrate), W(tip))]
2. MES capped gold NP vs. SAM of MES on Au(111)
3. measurement setup in normal atmosphere condition vs. UHV STM

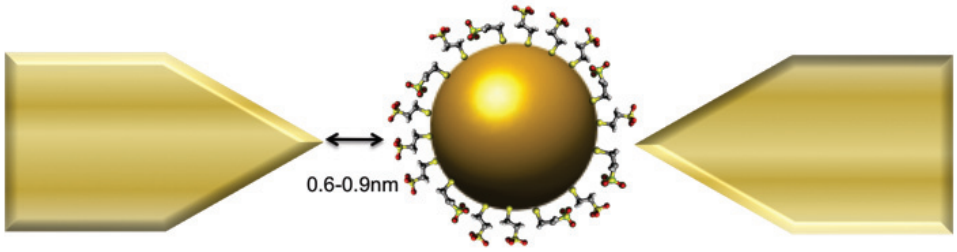

Figure 7.7.: The vacuum gap between the MES capped NP and the electrodes was determined to $l_{vac} \approx (0.6 - 0.9)\,\mathrm{nm}$, using the results of the iterative Simmons fitting sequence.

the $I(U)$ and ndc obtained in both types of measurements (STM / nanoelectrodes) corresponds amazingly, see Fig. 7.3. The ndc obtained of the investigated molecule using STM technique, mirrors the DOS curve of the molecule, therefore the two groups of peaks were assigned to the occupied molecular levels HOMO and HOMO-1 level of the MES molecule. In both types of measurement devices (STM, nanoelectrodes) the conductance in the linear regime ($U_{sd} \approx 0\,\mathrm{V}$) was comparable $G_{lin}(U_{sd} = 0.20\,\mathrm{V}) \approx 0.16\,\mathrm{nS}$. The iterative Simmons fit revealed a tunneling barrier height of $\phi_{MES-NP} \approx (5.5 \pm 0.3)\,\mathrm{eV}$, which is in the order of the work function of gold [65]. With the decay parameter $(\beta l)_{MES,neg/pos}$ the remaining vacuum gap was calculated to $l_{vac,MES,Sim-neg/pos} = (0.6 - 0.9)\,\mathrm{nm}$, which is comparable to the length of the vacuum gap achieved by TVS measurements $l_{vac,MES,TVS} = (0.8 \pm 0.2)\,\mathrm{nm}$, see Tab. 7.1. This leads to the conclusion, that the nanoelectrodes were not completely filled by the MES capped NP, a small vacuum gap of (0.6 - 0.9) nm remains as shown in Fig. 7.7. From TVS, (compare Fig. 7.6) a transition voltage of $U_{MES,TVS} = (2.2 \pm 0.2)\,\mathrm{V}$ was determined, which corresponds with the peak (p2) observed in the ndc [65], compare Fig. 7.3.

In conclusion a MES-gold contact has been studied in a 'electrode-MES-AuNP-MES-electrode' device and compared to STM measurements. Molecular properties have been characterized by $I(U)$ measurements and TVS. The tunneling barrier heights obtained and the resulting vacuum gap are consistently interpreted on the basis of a geometrical model with the help of the Simmons model and TVS.

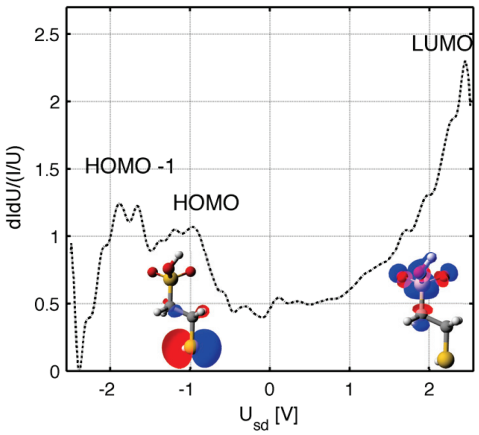

Figure 7.8.: The negative branch of the ndc from a cyclic $I(U)$ measurement of a single MES capped gold NP with a diameter of 12 nm. The peaks in the ndc were correlated with the molecular energy levels corresponding to the observations in STM measurements. The molecular HOMO and LUMO orbitals were calculated with the commercially available Software ArgusLab.

8. Transport measurements on SP / MES capped NPs

Electronic transport measurements on spiropyran (SP) / MES capped gold NPs were studied under illumination with light and at various temperatures (RT,4 K). The NPs have been synthesized by our cooperation partner I. Willner at the Hebrev University of Jerusalem, in the 7^{th} framework financed european project MOLOC. The properties of the reference NP, which is only capped with MES molecules, have been discussed in the previous chapter.
Measurements on gold NPs, which are capped with different ratios of SP/MES and have different sizes, are shown in this chapter. In the first section charge transport for single SP/MES (3:2) capped 12 nm gold NPs (device type A) is investigated under illumination of light at RT. Next, charge transport in single SP/MES (1:6) capped 4 nm gold NPs (device type B) is investigated in transistor geometry at RT and 4K. In device type B Gundlach oscillations and Coulomb blockade behavior was observed at low temperatures.

As shown in chapter 6, a delocalized π-electron system has a lower tunneling barrier and a lower contact resistance compared to an alkane chain. The charge transport measurements exhibits a significant difference in conductance, if the length of the tunnel barrier, the dipole moment along the transport axis and most importantly the HOMO-LUMO gap of a molecule is manipulated. This kind of manipulation is possibly induced in a photoisomerizable molecule. As functional ligand molecules the photo-isomerizable molecule spiropyran is used, compare Fig. 8.3. Spiropyran is a well-characterized photochrome that can be reversibly isomerized. SP has a closed carbon-ring form and under UV (350 ± 50 nm) photoexcitation, it undergoes reversible photoisomerization to the zwitter ionic, open-chain merocyanine (MC) form. The reverse reaction can be induced by thermal activation or VIS light (550 ± 50 nm). It is expected that the

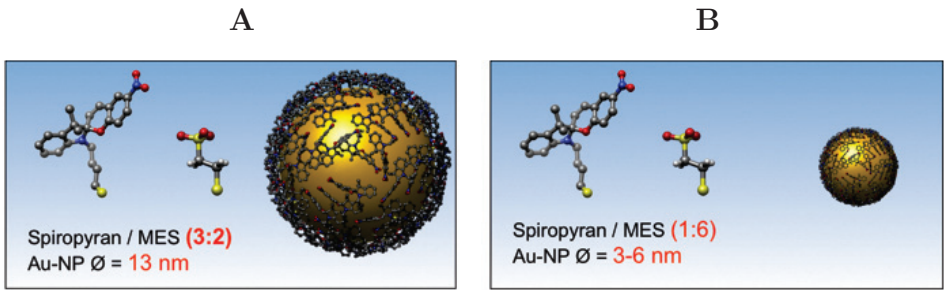

Figure 8.1.: Schematic drawing of the two types of NPs applied: **A** SP/MES (3:2) capped 12 nm gold NPs and **B** SP/MES (1:6) capped 4 nm gold NPs. The NP were synthesized in the group of I. Willner at the Hebrev University Israel.

open-chain MC form, which has a widely delocalized π-electron system, conducts more than the closed SP form. The open form has also a much larger dipole moment (13.6 D compared to 8.13 D for SP), since it is zwitter-ionic. The change of these molecular properties under illumination with UV light is described as switch in conductivity of the NP-nanoelctrode device.

8.1. DFT calculations of the SP/MC photoisomer and the MES / SP capped gold NP

The calculations that are shown in this section were performed by our cooperation partner F. Remacle at the University of Liege in Belgium, in the EU financed project MOLOC. The calculations are performed at DFT level using (B3LYP parameterization) with the 6- 31G(d,p) basis set or the 6-311++G(d,p) for field effects using the GAUSSIAN 09 suite of programs.

The central part of Fig. 8.3 shows the calculated localization of the HOMO and LUMO of SP and MC, it is observed that the MOs of SP are more localized as the MOs of MC, which is completely delocalized over the MC molecule head-group. The field free HOMO-LUMO gap at the B3LYP/6-31++G(d,p) level is 3.3 eV for SP and 2.7 eV for MC [142]. When anchored on a thiol capped Au25 cluster, where it is surrounded by 4 MES molecules ($Au25(SCH_3)_{13}(MES)_4$ SP) to mimic the studied NP, a decrease of

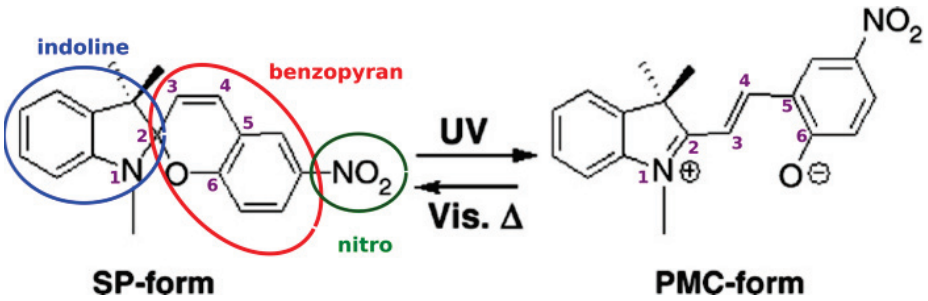

Figure 8.2.: Structural formula of spiropyran and merocyanin during photochromism. The subunits of SP (indoline,benzopyrane, nitro) were defined, as used in the text. The metastable conformers of the metastable states where defined with the planes $PL_{ind-benzo} = \{N1, C2, C3, C4\}$, $PL_{benzo1} = \{C2, C3, C4, C5\}$ and $PL_{benzo2} = \{C3, C4, C5, C6\}$, see Fig. 8.4. The structural formula is adopted from [52].

the HOMO-LUMO gap to 2.2 eV for SP and 2.1 eV for MC (B3LYP LANL2DZ for Au/6- 31G(d,p) for the other atoms) was achieved. Field effects on the position of the HOMO and LUMO of the isolated SP have been investigated at the B3LYP/6-31++G(d,p) level as well. An applied field (∼1 V/nm) along the molecular axis of SP increases the HOMO-LUMO gap to 3.7 eV, while a field in the opposite direction (∼-1.0 V/nm) results to a HOMO-LUMO gap of 2.8 eV. Applying a field perpendicular to the molecular axis also increases the HOMO-LUMO gap (3.5 eV at + 1V/nm) while the HOMO- LUMO slightly decreases for a field in the opposite direction (3 eV at 1 V/nm). The MOs of the conjugated MC forms are delocalized π-orbitals and therefore much more stable in external fields. In a trapped configuration of the SP functionalized Au-NPs in a nanogap the SP is not systematically oriented with respect to the directions of the bias and gate voltages applied. For this reason, the HOMO-LUMO gap in such an experiment is expected to be between 2.8 eV and 3.7 eV.

Also the computed UV-VIS spectra for the isolated SP and MC molecule, using TD-DFT/6-31+G(d,p), were shown in Fig. 8.3(bottom). For the SP form, the lowest excited state (at 430 nm) is a charge transfer (CT) state corresponding to the HOMO-LUMO excitation. The MC excited states have a $\pi - \pi^*$ character. Their absorption is in the range of VIS light, with a computed wavelength of the most intense transition at 500 nm. These wavelengths are in agreement with the UV-VIS spectra of the 100 nm layer on quartz [144], as one expects a red shift in condensed phase and a larger one for

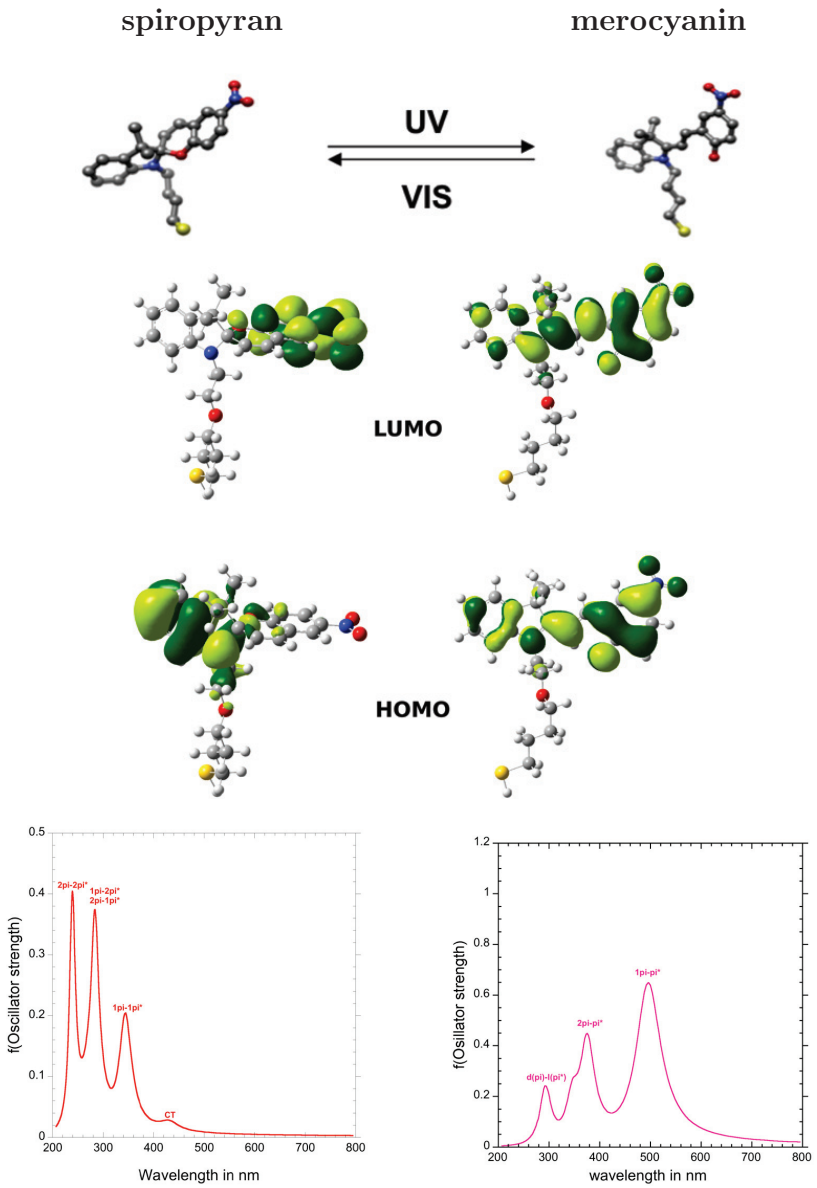

Figure 8.3.: (top) Schematic drawing of the photoisomeres molecules SP and MC, as bond on the Au surface. The SP state is thermally stable. A transition to the MC state is induced under illumination of UV light (∼350 nm). (center) Calculated HOMO and LUMO of spiropyran and merocyanin. (bottom) Calculation of the absorption spectra of SP and MC. The numerical calculations have been performed by Renuka Ganesan [143], a PhD researcher in the group of F. Remacle University of Liege, Belgium.

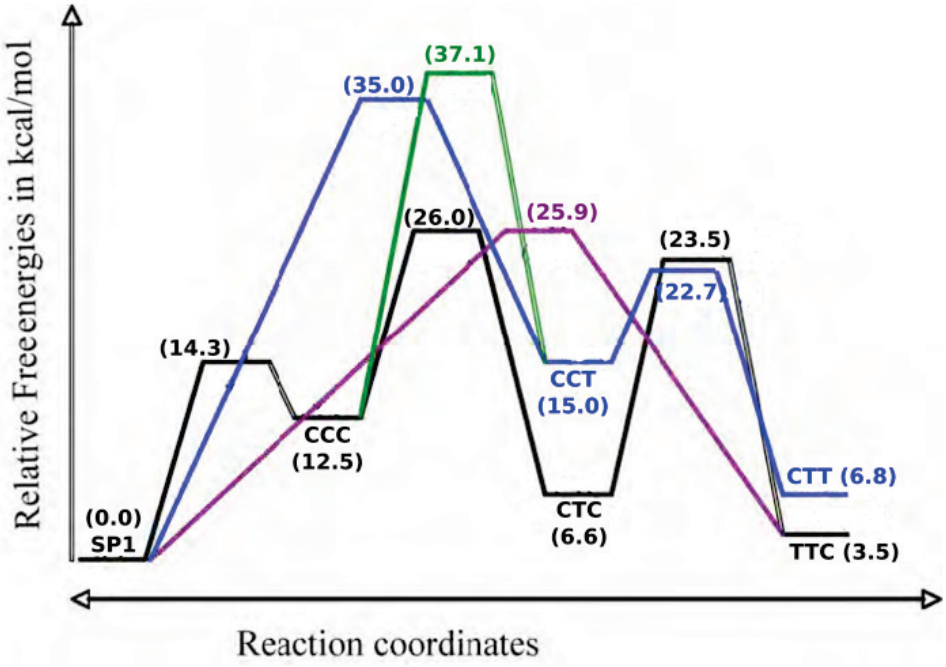

Figure 8.4.: Thermal reaction pathways of SP computed at the B3LYP/6-31G(d,p) level. Four possible transition paths from SP to MC are shown, which contains of different transition states. The reaction path, plotted with a black line, is stated to be the most probable one. The numerical calculations have been performed by Renuka Ganesan [143], a PhD researcher in the group of F. Remacle University of Liege, Belgium.

the conjugate form because of larger cooperative effects.

Four isomerization pathways have been identified for the thermal isomerization of the neutral SP molecule. Their free energy profiles at room temperature are shown in Fig. 8.4. Among them, the multistep reaction profile path 1 is the most favorable one but the pathways involving higher energy of the transition state (TS) are important for the understanding of the photo induced isomerization mechanism. The metastable intermediate states are defined by the abbreviatives CCC, CCT, CTC, CTT and TTC, which are defined by cis and trans states in the planes $PL_{ind-benzo} = \{N1, C2, C3, C4\}$, $PL_{benzo1} = \{C2, C3, C4, C5\}$ and $PL_{benzo2} = \{C3, C4, C5, C6\}$, see Fig. 8.2. The isomerization rates at room temperature have been computed using Transition State

Theory. In agreement with experiments as described later, it was found that the thermal rate of isomerization from SP to MC is slow (about $70\,s^{-1}$). The rate of the isomerization back is much slower (about $0.2\,s^{-1}$). However, since the MC form is slightly higher in energy than the SP form (by 1.5 eV for the MC conformer), the back isomerization can occur spontaneously.
In thorough calculations no single orientation of the external field was found that clearly favors the isomerization all the way to the most stable MC form. By removing or adding an electron or adding a proton, the relative stability of the SP and MC and the isomerization pathways are significantly different from that of the neutral form. There are two donation sites (see Fig. 8.2), either a negative charge atom can be bound on the N of the indole moiety or a proton on the O of the benzopyran. However, on one hand the O-protonated form is not stable in the closed form and spontaneously isomerizes to an open CCC conformer. On the other hand, the barriers, remain of the order of those of the neutral to reach the more stable protonated MC. It is important to note that the O-protonated MC is significantly more stable than the (protonated) SP conformers (by circa 3.2 eV). The same is true upon electron attachment. The MC anion is more stable by 0.9 eV than the SP one. The stabilization of the open MC form for the cation is less important (0.2 eV for the MC cation). In both cases, there is no variation (cation) or there is an increase (anion) of the electron density on the benzopyran part, which does not favor the ring opening, unlike case of the protonation on the O of the benzopyran part. Overall, the rates of isomerization to the open form are not faster for the SP cation and anion than for the neutral but the reaction is spontaneous since the open forms are more stable than the closed ones.

8.2. UV - VIS spectroscopy on Spiropyran molecules

The UV-VIS measurements that are shown in this section were performed by a PhD student Karsten Schulz **??** in the group of R. Weinkauf at the University of Düsseldorf, our cooperation partner in the EU financed project MOLOC. The most interesting question was whether SP without solvent and in the solid state could switch to MC. As Fig. 8.3 shows, MC has a zwitterionic structure and is expected to be metastable. The necessary time for back-isomerize is dependent on the temperature as well as on the

surrounding medium. In solid state, however, cooperative effects can be present. The SP was deposited by thermal vaporization on quartz plates and on which the switching properties were investigated. The experiments show (see Fig. 8.5) that SP as solid state material can be switched back and forth and that MC is stable in the absence of light and heat, which is explained by dimerization/aggregation of the zwitterionic molecules. This is in contrast to solution experiments where MC switches back by thermal motion within a few seconds. In the energy-resolved laser photo-electron spectrum as illustrated in Fig. 8.5) it is observed that the cross section of MC is greater than of SP.

8.3. Excitation spectroscopy on SP/MES NP devices

The optical setup as described in section 3.1.5 was tested using a multi-NP-device that was obtained by a drop drying method using the SP/MES (3:2) 12 nm NPs between nanoelectrode with 5 ± 1 nm tip separation. These devices are stable at RT and bias voltages of several volts can be applied at low temperatures. In the further text the measurement of a source drain current for a fixed source drain voltage and under illumination of light with discrete wavelength is referred to as excitation spectroscopy. Fig.8.6(left) shows the excitation spectroscopy (black) of a multi-NP device using a Xe arc-bow lamp. It is observed that the device maps the intensity profile of the light source, this effect can be described as photo-conductance. However, since the irradiance (red) over the wavelength 350 nm to 750 nm in the first order is flat, two peaks in the excitation spectroscopy can be assigned to the molecule-NP-nanoelectrode system ($\lambda_1 = 430$ nm and $\lambda_2 = 558$ nm). The peak observed at $\lambda_1 = 430$ nm is exactly in the flank of the raising optical power, so that the exact peak position is probably at lower wavelengths. The dotted graph is obtained by using a cuvette with solution of MES NPs (12 nm) as additional filter. It is observed that only the second peak is reduced in height, therefor this peak can be related to the molecule-NP system. In Fig.8.6 (right) the excitation spectra of a multi-NP devices for different source drain voltages ($U_{sd} = 0.2$ V (black), $U_{sd} = 0.4$ V (green), $U_{sd} = 0.8$ V (blue)) are shown using an intensity controlled Xe arc-bow lamp. Due to the constant amount of photocurrent, the peaks observed are more pronounced compared to the peaks obtained previously. The current of the spectroscopy measurements with different applied bias

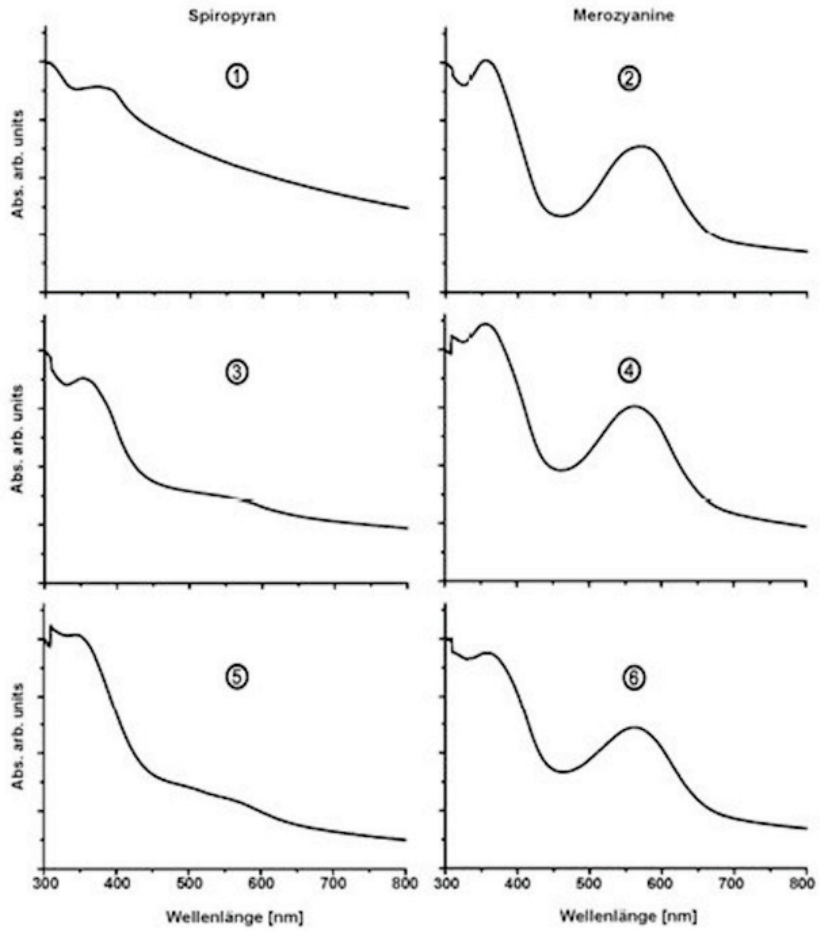

Figure 8.5.: UV-VIS spectra show in the order of the numbering the back and forth switching between SP and MC molecules in a 100 nm dry surface layer on quartz using LEDs (532 nm, 355 nm). The switching of SP to MC is performed by UV (355 nm) excitation and the back-switching by VIS (532 nm) light. The spectra of the MC-form is showing two resonance peaks at 360 nm and 560 nm, while the 560 nm peak is absent for the SP-form. The measurements have been performed by Karsten Schulz, a PhD researcher in the group of R. Weinkauf Universität Düsseldorf.

voltage obtained, was normalized to have two points equal: $\mathrm{norm}(I(\lambda = 200\,\mathrm{nm}, U_{sd}))$ and $\mathrm{norm}(I(\lambda = 450\,\mathrm{nm}, U_{sd}))$. It was assumed that optical power at $\lambda = 200\,\mathrm{nm}$ is

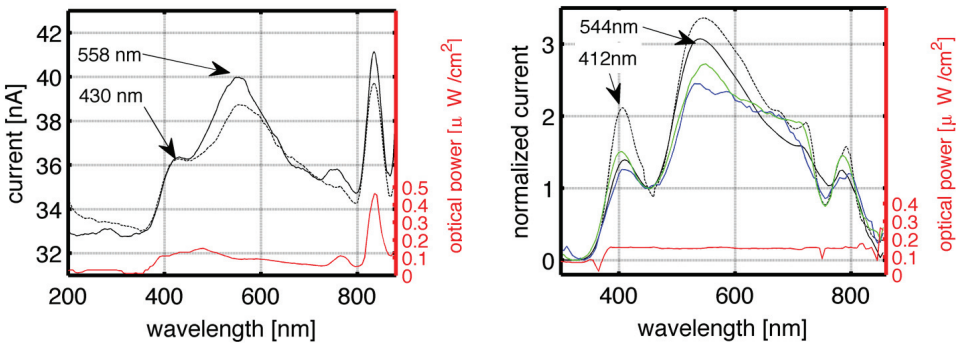

Figure 8.6.: (left) Excitation spectroscopy of a multi-NP device of SP:MES (3:2) capped 12 nm NPs. The current through the NP device, for a constant source drain voltage of $U_{sd} = 0.8V$, is measured under illumination of light with a discrete (± 10 nm) wavelength. The dotted graph is obtained using an additional filter (cuvette with MES capped NPs 12 nm). The red curve illustrates the power spectrum of the Xe arc bow lamp (Oriel) applied. (right) The excitation spectroscopy using light with discrete wavelength and constant intensity is plotted. The current, obtained for source drain voltages of $U_{sd} = 0.2$ V (black), $U_{sd} = 0.4$ V (blue), $U_{sd} = 0.8$ V (green), is normalized so that the minimum of all curves is equally set to one values and the value obtained at 450 nm is equal. The normalized current is plotted vs. the wavelength of the illuminated light. The graphs with bold lines are obtained using a scan speed of 70 s /5 nm, the dotted line is obtained with a speed of 140 s /5 nm.

zero and at $\lambda = 200$ nm a pure photocurrent (creating the baseline) is observed. In addition to Fig.8.6 (leftt), a shoulder is observed at about 680 nm. The height of the shoulder is constant for the source drain voltage applied, while the height of the peak at 412 nm and at 544 nm changes for all source-drain voltages. Furthermore, the height changes as well with the scan speed, which is for the dashed black graph, twice as slow as for the solid black graph. This effect is a strong indication that this peak is related to the isomerization of the spiropyran to merocyanin. Hence, it is assumed that the peak at 412 nm is related to the isomerization of SP to MC, and the peak at 544 nm is related to the back-isomerization of MC to SP. The peak at 800 nm cannot assigned to a physical origin at this moment.

8.3.1. Simulation of surface plasmon polaritons in the NP-nanoelectrode system

The excitation of slow localized surface plasmon polaritons, for the case of a single moleular-capped, gold NP that is immobilized in between Au_3Pd_2 nanoelectrodes, was simulated by the PhD student Ulli Paetzold in the group of R. Carius of the IEK-5 in the Forschungszentrum Jülich. In Fig. 8.7 (left,top) the geometry of the simulated

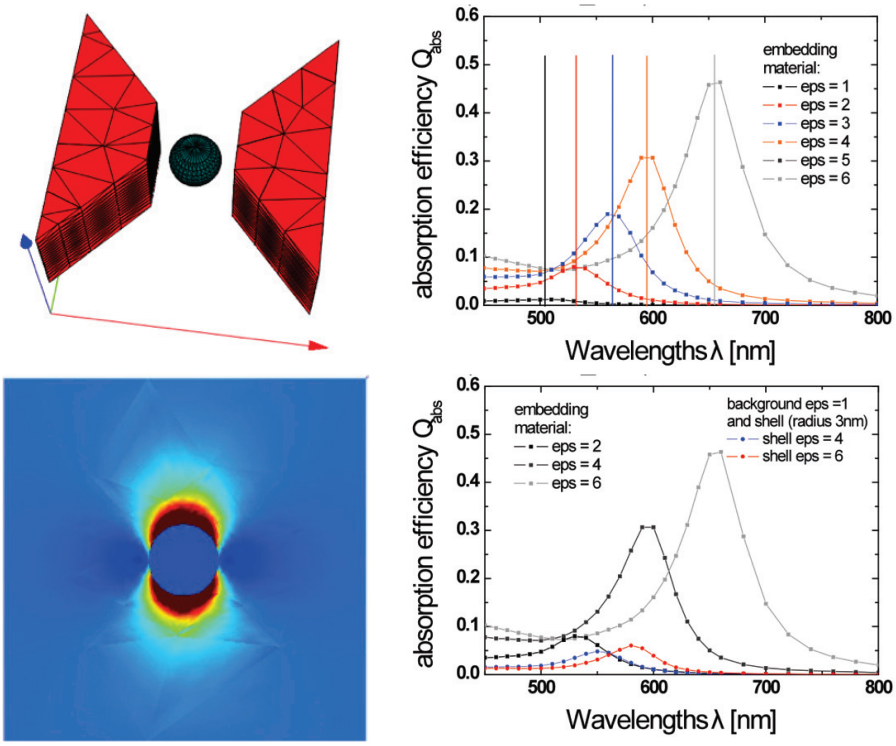

Figure 8.7.: (left) Geometry of the simulated model (top), simulated electric field around a gold NP (10nm) during illumination with light. **(right)** Absorption efficiency of a gold NP in a Au_3Pd_2 nanoelectrode configuration, embedded in media with different ϵ (top) and with different ligand shells (bottom). These calculations were performed by Ulli Paetzold in the group of Prof. Carius IEK-5 in the Forschungszentrum Jülich.

device is shown, the bottom graph illustrates the electric field that is generated close to a gold NP under illumination of light. The absorption efficiency for a NP in a nanoelectrode configuration that is embedded in different media, i.e. for different permittivities $\epsilon = 1..8$, is shown in Fig. 8.7(right,top). The graph can be summarized with the statement:
The higher the permittivity ϵ of the embedding medium, the higher is the wavelength λ_{max} at which the absorption efficiency Q_{abs} is maximal ($Q_{abs,max}$).

The bottom right graph shows the absorption efficiency of a molecule-capped NP (with $l_{mol} = 1.5\,\text{nm}$) calculated, which has a permittivity of $\epsilon = 4 - 6$. The influence on the peak position and peak height is much smaller compared to the case of the NP-nanoelectrode configuration in the embedded medium. Comparing the measured above excitation spectra that are achieved by a drop-drying method, with the case of the embedded medium, we find a good agreement for $\epsilon = 3$, which is in a really good agreement with the literature value for spiropyran ($\epsilon_{Lit} = 2.75$).

8.4. Transport measurements on Type A: SP/MES (3:2) with 12 nm Au core

In a similar electrode configuration as described in the previous chapter a 12 nm gold NP capped with two molecular species: the photo-isomerizable SP and MES (3:2) was immobilized by DEP trapping, as described in chapter 5, in between Au_3Pd_2 nanoelectrodes. Then cyclic $I(U)$ measurements were performed in the sub-picoampere cryostat setup as shown in 3.1.4. The risk of a damage of the device during the interchange between the input lines of the cryostat was minimized by following an interchange procedure, involving the interconnect switch box, as described in section 3.1.3.
In contrast to the molecules discussed previously the spiropyran is a photo-isomer, which changes the geometrical and electrical configuration and thus the electronic properties under illumination with UV light. The connecting lines of the nanoelectrodes act as antenna, which enhances the electrical field of the incident light at the gap position. This effect is theoretically described by Søndergaard et al. [123, 145]. In this way the incident light can couple to a nanometer-scaled NP even with a low power light source of $< 1\,\text{mW/cm}^2$.

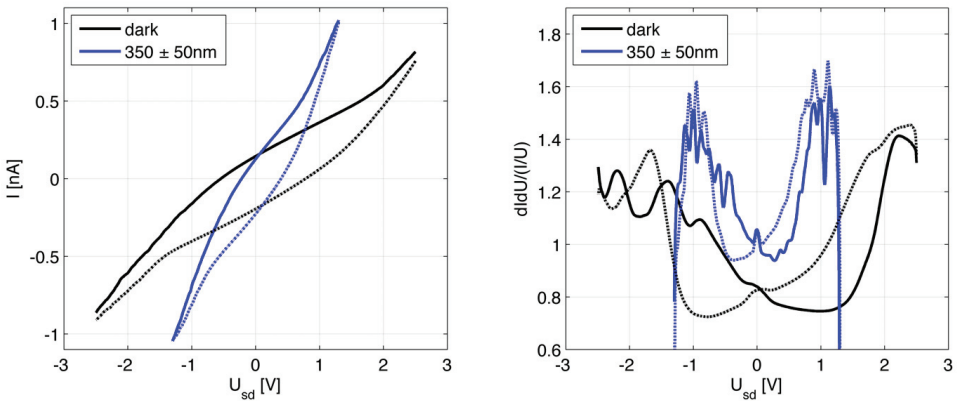

Figure 8.8.: $I(U)$ SP/MES (3:2) capped 12 nm NPs. Cyclic $I(U)$ curve of a single SP/MES (3:2) capped 12 nm gold NP without exposure to light (black) and with exposure to UV-light (350 ± 50 nm) and b) ndc curve. (black line) Two peaks in the ndc are ascribed, as relevant density of states features, comparing STM measurements.(blue line) Two peaks in the ndc are ascribed, as relevant density of states features, comparing STM measurements.

Measurements of the SP/MES type A NP in a nanoelectrode configuration were performed with the settings: $dU = 10\,\text{mV}$, $dt = 0.2\,\text{s}$, $NPLC = 1$ and a fixed range of 1 nA.

Under illumination with UV light the current magnitude was increased by a factor of three during exposure with UV light, see Fig. 8.8. While the increase in conductance of BP3-capped NP devices, due to a photocurrent was significantly lower ($\Delta I(U_{sd})/I_{sd} \approx 11\,\%$). The branch with the solid line was measured with a positive dU (up), and the dashed line with a negative dU (down). The features in the ndc of the 'up-' and the 'down-branch' were mirrored but qualitatively similar. This effect is explained with the symmetry of the device, since two MMM junctions were present in the electrode/SP-NP-SP/electrode device. Only the 'down-branch' is discussed below. In the ndc of the NP-measurement for $U_{sd} < 0$ two relevant DOS features were found at :

$$(U_{DOS,SP-A,1} = -2.19\,\text{V} \quad \text{and } U_{DOS,SP-A,2} = -1.40\,\text{V})$$

the peak at $U_{sd} = -0.9\,\mathrm{V}$ is assigned as relevant density of states features of the MES capped NP as described in the previous Chapter. For positive voltages $U_{sd} > 0$ one peak is observed at ($U_{DOS,SP-A,3} = 2.24\,\mathrm{V}$).
The difference of $e\Delta U_{DOS,SP-A,3-2} = e(U_{DOS,SP-A,3} - U_{DOS,SP-A,2}) = 3.64\,e\mathrm{V}$ corresponds to a wavelength of 341 nm thus $\pi - \pi^*$ transition (HOMO-LUMO gap) of spiropyran. As shown by R. Ganesan [143] a transition from the excited SP molecule to merocyanin is possible (see Fig. 8.4). In the ndc of the NP-measurement under illumination with UV light of a bandwidth of $350 \pm 50\,\mathrm{nm}$, two peaks were found at :

$$(U_{DOS,MC-A,1} = -1.01\,\mathrm{V} \quad \text{and } U_{DOS,MC-A,2} = 0.99\,\mathrm{V})$$

which are assigned as relevant density of states features of merocyanin, and thus to molecular energy levels. The difference of $\Delta eU_{DOS,MC-A,3-1} = e(U_{DOS,MC-A,3} - U_{DOS,MC-A,1}) = 2\,e\mathrm{V}$ corresponds to a wavelength of 619 nm. This is in the order of the $\pi - \pi^*$ transition (HOMO-LUMO gap) of merocyanin. The exited MC molecule relaxes to the SP molecule over a reaction path, similar to the case of SP (see Fig. 8.4). The red-shift of about 100 nm might be explained by an impact of the nanoelectrodes to the delocalized molecular levels of merocyanin and thus on the electronic structure. Besides this, the continuous illumination of UV light probably also influences the electronic structure.
However, since there are two molecules present on the NP (SP/MES) a clear indication of the molecular orbitals using this technology is not possible. Unfortunately, we did not obtain NPs that were only capped with SP or in a matrix of well-known alkanethiols. STM measurements on SP and MC molecules in a octanethiol matrix were performed to correlate the features observed in the ndc to molecular orbitals. The black curve of the ndc (see Fig. 8.8(right) of the NP-nanoelectrode device obtained are in amazing good correspondence with STM measurements on isolated spiropyran molecules in a matrix of octanethiol on Au(111) [136]. Comparing the blue curve ndc, which is performed during exposure with light of a bandwidth of $350 \pm 50\,\mathrm{nm}$, with the DOS curve of MC achieved by STM measurement, a great correspondence is found as well.

8.4.1. Simmons fit of the $I(U)$ curve

An exponential fit with the Simmons model is associated with high uncertainties, which were reduced by applying an iterative fit sequence, as described in section 2.1.1. First

the quotient I/U was plotted versus U^2, as depicted in Fig. 8.9. The conductance in the linear regime $G_{Sim,SP-A}$ and the shaping factor ρ_{SP-A} were fitted using a linear fit, according to equation (2.6).The result of the linear fit for the 'up-branch' is :

$$(\rho_{SP-A,neg}(i=0) = 3.6\,(\mathrm{eV})^{-1}, \rho_{SP-A,pos}(i=0) = 7.8\,(\mathrm{eV})^{-1})$$

and a conductance at zero bias of $G_{Sim,SP-A} = 120\,\mathrm{pS}$.
was applied as starting parameter for the iterative fit sequence, as described in section 2.1.1. The result of the iterative fitting sequence after 30 iteration steps was:

$\rho_{SP-A,neg}(i=30) = 3.3\,(\mathrm{eV})^{-1}$, $\rho_{SP-A,pos}(i=30) = 7.0\,\mathrm{eV}^{-1}$ and
$\phi_{SP-A,neg}(i=30) = 2.1\,\mathrm{eV}$, $\phi_{SP-A,pos}(i=30) = 1.2,\mathrm{eV}$ and
$(\beta l)_{SP-A,neg}(i=30) = 6.9$, $(\beta l)_{SP-A,pos}(i=30) = 9.5$.

The fitting routine did not converge properly in the fit of the negative branch. The reason for this might be that the peaks in the DOS are not defined very well or too close together. The results for $U_{sd} < 0\mathrm{V}$ shown are chosen from the iterative simmons fit with the parameter set (ρ, ϕ). The width of the vacuum gap of the fitting result (βl) was approximated by using:

$$(\beta l)_{tot} = \beta_{vac} l_{vac} + (\beta_{alkane} l_{butane} + \beta_{SP} l_{SP} \tag{8.1}$$

The decay constant for spiropyran is estimated, using [59]:

$$\beta_{spiro} = \frac{2}{\hbar}\cos(\gamma)\sqrt{2m^* m_e \phi_{SP1}} \approx 7..10\,\mathrm{nm}^{-1}$$

with the decay parameter of SP $\beta_{spiro} = (4-5)\,\mathrm{nm}^{-1}$, the uncertainty of the calculation of the vacuum gap is 0.1 nm. The length of the molecular sections is $l_{butane} = 0.72\,\mathrm{nm}$ and $l_{spiro} = 0.4\,\mathrm{nm}$. The tilt angle was set to $\gamma = 0°$, assuming the spiropyran group is aligned in parallel to the NP surface.
The length of the vacuum gap was estimated to $l_{vac,Sim,SP-A,neg} = (0.1 \pm 0.1)\,\mathrm{nm}$ and $l_{vac,Sim,SP-A,pos} = (0.3 \pm 0.1)\,\mathrm{nm}$.

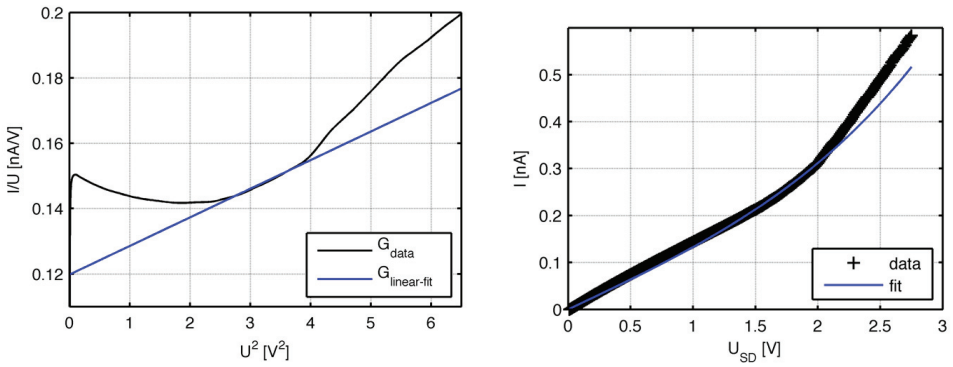

(a) (b)

Figure 8.9.: a) Linear fit of the quotient I/U plotted versus U^2. The blue colored line is a linear fit that reveal the parameter $\rho_{SP-A,pos} = 2.6\,(\mathrm{eV})^{-1}$ from the slope of the curve and the conductance in the linear regime $G_{Sim,SP-A} = 0.120\,\mathrm{nS}$ from the axis interception. b) The current voltage characteristic and the fit (blue) of the $I(U)$ curve obtained are shown.

8.4.2. Transition Voltage Spectroscopy

According to [62, 65], the minimum in Fowler Nordheim plot is called transition voltage. The transition voltage $U_{TVS,SP-A}$ is correlated with the DOS feature $U_{DOS,SP-A,i}$ by a factor f. This factor was shown to be dependent on the exponent α and the symmetry parameter η, as described in section 2.1.2. The TVS is plotted for three different exponents $\alpha = 2$, $\alpha = 1.75$ and $\alpha = 1.5$, as described in [62]. For simplicity only the up branch is discussed. For $\alpha = 2$ a minima is observed for positive voltages at $U_{TVS,SP-A,pos} = 2.22\,\mathrm{V}$ and for negative voltages at $U_{TVS,SP-A,neg} = 1.92\,\mathrm{V}$, respectively, as shown in Fig. 8.10. These values are in correspondence with the observed DOS features in the ndc. A compilation of the minima in the TVS plot observed were shown in Tab. 8.1 and the length of the vacuum gap was estimated according to section 2.1.2. The values for the division factor obtained and the remaining vacuum gap of either SP and MC are in agreement with the expectations:
(i) the device measured is created by a 12 nm particle that was trapped in a 5 nm sized nanogap, therefore no vacuum gap is expected ($l_{vac} < 0.1\,\mathrm{nm}$)
(ii) the division factor is in correspondence with the value $\eta^{\alpha=2}_{BP3-B} = 0.75$ obtained for

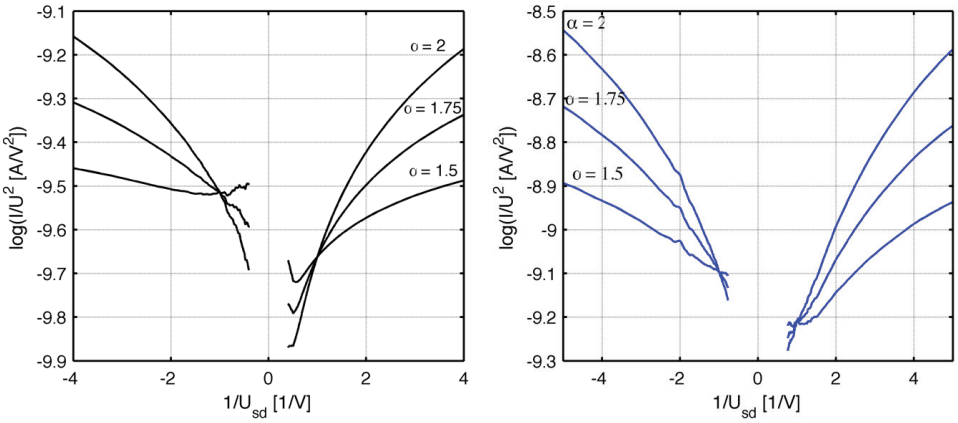

(a) (b)

Figure 8.10.: (left) Fowler Nordheim plot with $\alpha = 2$, $\alpha = 1.75$ and $\alpha = 1.5$ calculated from a cyclic $I(U)$ measurement of a single SP/MES (3:2) capped gold NP with a diameter of 12 nm. The TVS plot is created from data that were obtained in the dark, though the molecule is in the spiropyran conformation. (right) The measurements on the right side were obtained during illumination with light of the bandwidth 350±50 nm, though the molecule is in the merocyanin configuration.

a BP3 capped NP. The division factor describes the fraction of bias voltage that drops over the molecule, which is dependent on the type of contact between the molecule and the nanoelectrode. Since the SP has a delocalized π-electron system that could create the contact to the electrode, it is comparable to the contact created by the BP3 molecule.

In the data of the MC molecule for negative bias voltages obtained no minimum in the Fowler Nordheim plot was observed. The delocalized π-electron system is spread over the whole MC molecule, therefore on the first view a higher division factor could be expected.

The calculated vacuum gap of 0.1 nm is in correspondence wit the value determined using the Simmons fit.

Spiropyran				Merocyanin	
	peak 1	peak 2	peak4		peak2
$U_{DOS,SP-A}[eV]$	-2.19	-1.40	2.24	$U_{DOS,MC-A}$[eV]	0.99
	$\alpha = 1.5$				$\alpha = 1.5$
$U^{\alpha=1.5}_{TVS,SP-A}$ [eV]	-2.03	1.25	1.89	$U^{\alpha=1.5}_{TVS,MC-A}$ [eV]	0.95
$U_{DOS,SP-A}/U_{TVS,SP-A}$	1.08	1.16	1.19	$U_{DOS,MC-A}/U_{TVS,MC-A}$	1.05
η	0.71	0.68	0.62	η	0.75
$l_{vac,TVS,SP-A}$ [nm]	0.1	0.1	0.1	$l_{vac,TVS,MC-A}$ [nm]	0.1

Table 8.1.: Compilation of voltages of the peaks in the DOS-curve observed at $U_{DOS,SP-A}$, $U_{DOS,MC-A}$ and the transition voltages $U_{TVS,SP-A}$,$U_{TVS,MC-A}$ for $\alpha = 1.5$, determined for spiropyran and merocyanin respectively. In this way the division parameter η (using equation (2.16)) and thus the remaining vacuum gap in the tunneling contact are estimated (using equation (2.12)).

8.5. Electrical switch created by photo-isomerisation of spiropyran

In the previous sections the influence of the isomerization on the electronic structure and the distance of the HOMO and the LUMO level was discussed. In this section the switching between SP and MC and the thermal stability of the uncharged MC form is investigated. In Fig. 8.11 the time dependent normalized current is measured. The time, where the UV light of the bandwidth 350±50 nm was turned off, corresponds to the time, where the spontaneous decay begins. The half life time determined is $T_{1/2,MC-A} = 108\,\mathrm{s}$, which is close to the half-life time (84 s) of $10^{-4}M$ SP in Chloroform solution [52]. As conclusion, the SP / MC molecule can be considered in a matrix similarly to solution. It is assumed that not (only) the SP/MC molecules in between the NP-nanoelectrode play a role in charge transport process, but the SP/MC molecules of the whole capping layer as well. That means a switching from the SP to the MC form increases the dielectric constant of the medium and thereby reduces the decay parameter, see equation (2.14). The maximum absorption is observed at $\lambda_{max} \approx 580\,\mathrm{nm}$ [52], in UV-VIS transmission measurements of SP-$(CH_2)_{18}$ in chloroform and this is a bit higher than the peak at 566 nm observed in the excitation spectroscopy measurement as shown in Fig. 8.6. The fast decay of the MC on the NP in the nanoelectrode device, which is in the same order of SP in chloroform, is surprising. The decay of the MC between the NP and the

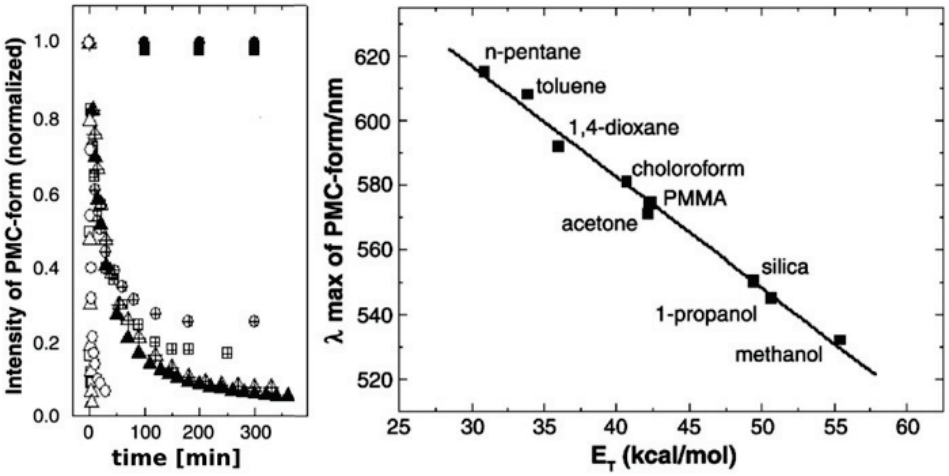

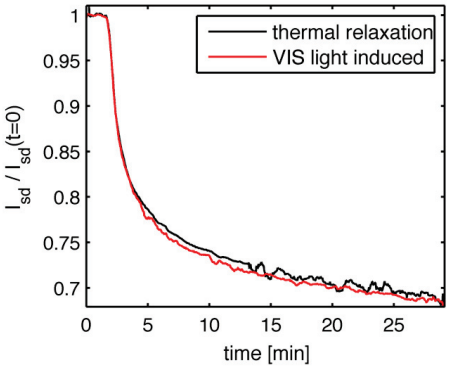

Figure 8.11.: (top, left) A time dependent absorption intensity at λ_{max} of different MC forms (triangle) MC-$(CH_2)_{18}$, (square) MC-OH, (circle) MC-COOH) in various matrices (open) chloroform, (cross) PMMA, (filled) silica [52]. (right, right) experimentally found transition energies E_T of MC to SP for different solvents and the correlated absorption maximum λ_{max} of the MC form. (bottom) Thermal relaxation of the photoisomer merocyanin to spiropyran measured by (left) a time dependent conductance measurement after turning off the UV light (350 ± 50 nm) and

nanoelectrode would expected to be in the range of MC in a PMMA matrix or even in silica. But this might be an indication that the SP/MC molecules, which are not directly between the NP and nanoelectrode, were involved in the charge transport as well.

8.5.1. Application as multi valued logic device / full adder

Over the last three decades electronic bricks using multiple- valued logic have been receiving considerable attention [146]. As the number of devices in a chip increases, the interconnection between active devices inside and outside a silicon chip becomes complicated. The theoretical advantages of multiple-valued logic in reducing the number of interconnection required to implement logical functions have been well established and widely acknowledged [147–150].

The system described in the previous section has two inputs ('U_{sd}' and UV light 'on|off'). Choosing the input values of the source drain voltage of e.g. $U_0 = 1\,\mathrm{V}$, $U_1 = 1.2\,\mathrm{V}$ corresponding to the logical (0) and (1) state, respectively and two optical input values off(0) | on(1), a four level output (<0>, <1>, <2> and <3>) is generated, which is defined by the resistive state R_{1-4}, see Fig. 8.12.

The ultimate challenge for molecule-based systems is a complete mimicry of electronic

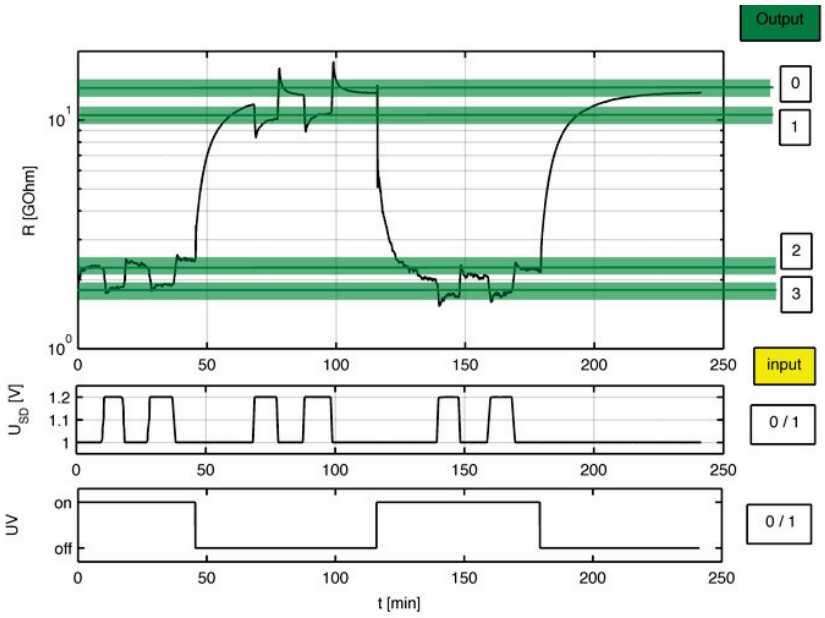

Figure 8.12.: Using two input channels ($U_{sd} \leftrightarrow [U_0, U_1]$ and UV light on|off) a four level system system is created. The input values are $U_0 = 1\,\mathrm{V}$, $U_0 = 1.2\,\mathrm{V}$ and UV-light on|off .

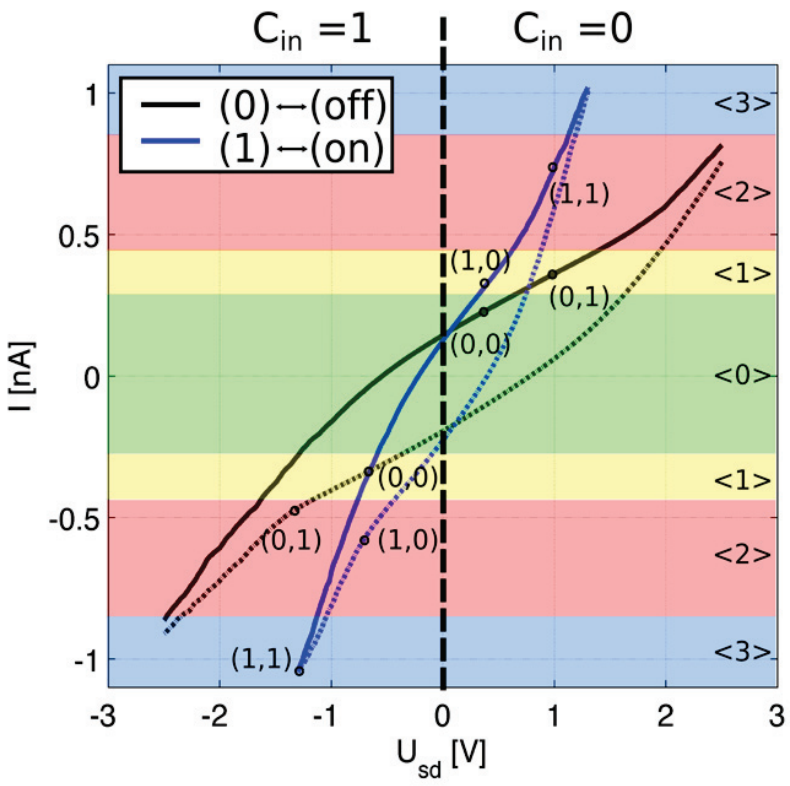

Figure 8.13.: Implementation of a Full adder logical circuit on the obtained $I(U)$ curve.

calculators. An electronic calculator, such as the Full Adder, was implemented in a scheme on the $I(U)$ curve, see Fig. 8.13. In the full adder operation the sum of three input parameter (A_{in},B_{in},C_{in}) is encrypted in two output parameter (S,C_{out}), i.e. the sum S and a carrier out variable C_{out}. The input parameter A_{in} is attributed to the exposure with UV light (off|on) $\leftrightarrow$ (0|1) with the bandwidth of 350 ± 50 nm. The input parameter B_{in},C_{in} is attributed to two values of the bias voltage U_{sd}, while C is denoted by the sign of the input voltage, see Tab. 8.2. The output values S, C_{out} are created by the magnitude of current and compressed to one multi valued logic parameter S_n. The logic output value S_n is implemented in this device as the

amplitude of current. Four different ranges of current were defined $(0.00 - 0.30)$ nA, $(0.31 - 0.45)$ nA, i$(0.46 - 0.80)$ nA and $(0.80 - 1.20)$ nA that correspond to the logical values <0>, <1>, <2> and <3>, respectively.

There are new features that exhibit logical capabilities far more complex than a switch.

A	UV	B	$\lvert U_{sd}\rvert$ [V]	C	sign(U_{sd})	$U_{sd}(BC)$ [V]	$\lvert I_{sd}[nA]\rvert$	S_n
0	off	0	0.5	0	+	0.3	$0.00 - 0.30$	<0>
0	off	1	1.2	0	+	1	$0.31 - 0.45$	<1>
1	on	0	0.5	0	+	0.3	$0.31 - 0.45$	<1>
1	on	1	1.2	0	+	1	$0.46 - 0.80$	<2>
0	off	0	0.5	1	-	-0.7	$0.31 - 0.45$	<1>
0	off	1	1.2	1	-	-1.4	$0.46 - 0.80$	<2>
1	on	0	0.5	1	-	-0.7	$0.46 - 0.80$	<2>
1	on	1	1.2	1	-	-1.4	$0.80 - 1.20$	<3>

Table 8.2.: Translation of the input parameters A, B and C to the physical parameter , UV (on|off), $|U_{sd}|$ and sign(U_{sd}), respectively. The bias voltage applied in dependence on the input values is calculated with: $U_{sd}(BC) = -0.2 + (-1)^C(0.5 + B \cdot 0.7)$. The logical output value S_n was defined by the different ranges of current.

The magnitude of current as output signal allows the full adder operation on such a device.

8.6. Transport measurements on Type B SP/MES (1:6) with 4 nm Au core

In this section a 4 nm gold NP capped with SP and MES (1:6) was immobilized by DEP trapping, as described in chapter 5, in between Au_3Pd_2 nanoelectrodes on devices fabricated with a full plain backgate and 26 nm SiO_2 as insulating material. The cyclic $I(U)$ measurements were performed in the sub-picoampere cryostat setup as shown in 3.1.4. The risk of a damage to the device during the interchange between the input lines of the cryostat was minimized by following an interchange procedure, involving the interconnect switch box, as described in section 3.1.3.

In the previous measurements that are performed using the Type A NPs (SP/MES (3:2)) the metal-molecule-NP-molecule-metal device is found to be almost symmetric and the tunneling barrier was defined by the SP/MC molecule. In this type of NPs the

number of molecules that may contribute to the total magnitude of charge transport was reduced by a factor of three due to the reduction of the NP-radius, see Fig. 6.9. In addition the fraction of SP in the capping layer is reduced by a factor of four. In total Type B NPs are capped by a smaller amount (factor of twelve) of SP molecules, compared to Type A NP molecules. Therefore the dielectric medium in the nanogap and the bundle of molecules in the nanoelectrode-molecule-NP junction is changed significantly, which already should have a huge impact on the charge transport in this device. The total number of SP/MES molecules that contribute to the charge transport is estimated to 2-6 molecules, in analogy to section 6.2.2, see Fig. 6.9. Due to the fact that only one of seven molecules (SP/MES (1:6)) in Type B NPs is an SP with an estimated range of 2-6 molecules contributing to the charge transport on each side of the NP, an asymmetric metal-molecule-NP-molecule-metal contact is most probable, see Fig. 8.14. Due to this fact a significant difference in transport characteristic between the two types (A/B) of devices is expected.In this device the illumination with UV light or light of other wavelength did not have a huge impact (<5%) on the magnitude of current, see Fig. 8.15, which might be a consequence that the number of SP molecules between the nanoelectrodes is dramatically reduced by a factor of 36 (factor four by the different ratio (2:3), (1:6) and a factor of nine due to the smaller surface of the NP). The shape of the $I(U)$ characteristic is mirrored compared to the devices which were shown in the next sections. The reason for this behavior might be that the NP is coupled with the MES molecule to the opposite nanoelectrode.

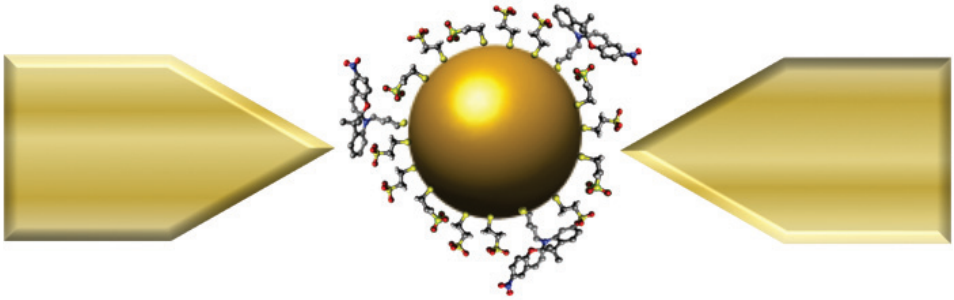

Figure 8.14.: Type B NP SP/MES (1:6) with 4 nm Au core immobilized in a small nanogap.

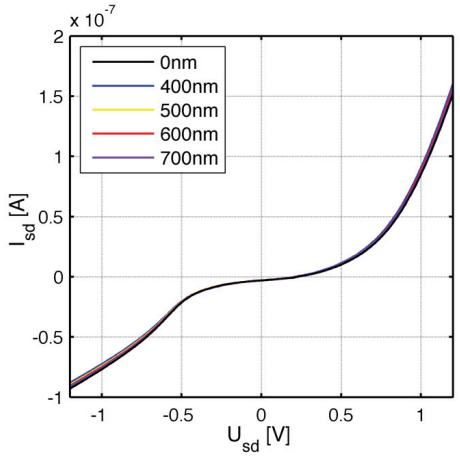

Figure 8.15.: Device 0: Current voltage characteristic of Type B SP/MES (1:6) with 4 nm Au core under illumination of light with discrete wavelength (bandwidth 30 nm). The cyclic $I(U)$ measurement was performed with the settings: $dU = 10\,\mathrm{mV}$, $dt = 0.2\,\mathrm{s}$, $NPLC = 1$.

8.6.1. Device1: Current voltage characteristic and TVS at RT

The cyclic $I(U)$ measurement was performed with the settings: $dU = 2\,\mathrm{mV}$, $dt = 0.2\,\mathrm{s}$, $NPLC = 1$ In Fig. 8.16(left) in the differential conductance a peak is observed at $U_{DOS,SP-B1} = 0.7\,\mathrm{V}$, which is attributed to the HOMO-level of MES, compare section 7. The Fowler Nordheim plot, Fig. 8.16(right), shows a minimum at $U_{TVS,SP-B1} = 0.83\,\mathrm{V}$. The transition voltage is within the errorbars consistent with the DOS peak observed in the ndc.

8.6.2. Device1: Gundlach oscillations in molecular vacancies at 4K

The cyclic $I(U)$ measurements at 4 K show oscillating behavior. In the Fowler-Nordheim regime the bias voltage applied exceeds the tunneling barrier height of the molecule. Under this condition an interference phenomenon, namely Gundlach oscillations, is observed. The electrons at the Fermi level that dominantly contribute to the tunneling current, are partly reflected either at the metal surface or at the molecular energy level that is defined by the LUMO of the molecule [151–154]. Thus, electron standing waves can be excited in the vacuum gap in front of the molecular surface, see Fig. 8.17. With the increase of the bias voltage, the width of the region classically available changes and thereby the interference between the reflected electrons oscillates between constructive and destructive interference of the electron wave function. In STM measurements this

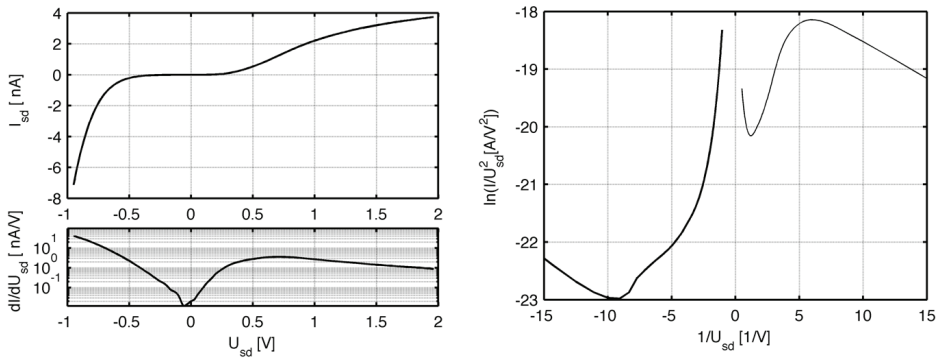

Figure 8.16.: (left) Current voltage characteristic of Type B SP/MES (1:6) with 4 nm Au core and the differential conductance. (right) Fowler Nordheim plot.

phenomenon is observed only for a positive bias voltage, thus for reflections at the LUMO orbital. Since in a NP-device two barriers are present, the phenomenon is observed for both, negative and positive bias.

Gundlach [154] calculated the tunneling current/transmission coefficient as a function of the applied bias voltage for a metal/insulator/metal system. A resonance condition is fulfilled if an integer number of half- wavelengths of the electron wave function fit into the well between molecule and the rising vacuum gap potential. Coombs and Gimzewski derived the condition [155]:

$$U_N = \phi + c(NF)^{2/3} \tag{8.2}$$

with $c = 4.39(\mathring{A}\sqrt{V})^{2/3}$. U_N is the voltage of the N$^{\text{th}}$ resonance state, ϕ is the tunneling barrier, and F is the field strength in volts per angstrom. In addition a quasi-one-dimensional electrical field distribution is considered, whereas in reality the distribution is essentially three-dimensional:

$$F \approx \frac{U_{sd}}{l_{tot}} \tag{8.3}$$

with $l_{tot} = l_{butane} + l_{SP} + + l_{MES} + l_{vac}$.

The result of these considerations is summarized in Tab. 8.3. From this table the averaged value $\bar{l}_{tot} \approx 2.7\,\text{nm}$ is calculated, which leads to an estimation of the remaining vacuum gap of $l_{vac} \approx 0.7\,\text{nm}$. The first peaks (N=-0 and N=0) were observed at bias voltages that were in correspondence with the DOS feature $U_{DOS,SP-B1} = 0.7\,\text{V}$.

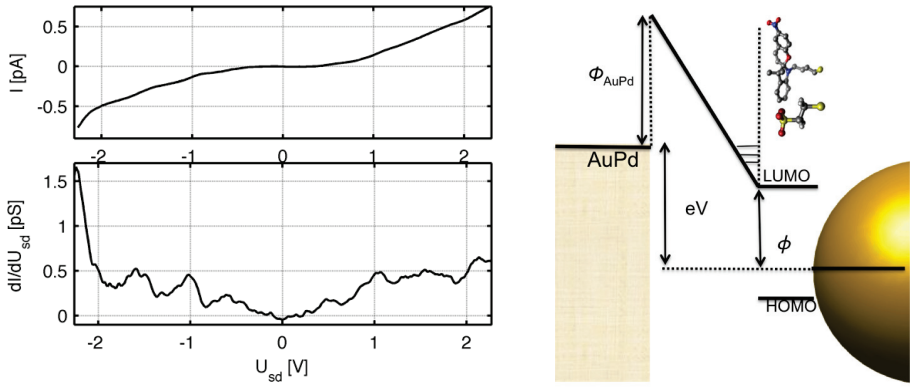

Figure 8.17.: (left) $I(U)$ characteristic obtained at 4 K shows periodic oscillations with peak distances in the order of 0.5-0.6 V. Schematic of Gundlach oscillations for an applied bias $|eU_{sd}| > |E_{Fermi} - E_{LUMO}|$ classical availabe regions appear in the tunneling barrier. According to the electron in a triangular box several a constructive interference is observed, if the distance between the 'walls' is an half integer value of the wavelength of an electron.

N	-3	-2	-1	-0	0	1	2	3
U_N [V]	-2.21	-1.59	-1.01	-0.57	0.50	1.05	1.56	2.14
l_{tot} [nm]	2.9	2.8	2.9			2.4	2.6	2.8

Table 8.3.: Peak positions of the Gundlach oscillations of the order N observed for positive and negative bias voltages and the calculated length of l_{tot}, see equation (8.2).

8.6.3. Device2: Current voltage characteristic and TVS at RT

The type B of NPs was immobilized in between a nanoelectrode configuration applying nanoelectrodes with a full-plain backgate configuration using a 26 nm insulating SiO_2 layer. The differential conductance (dc) of cyclic $I(U)$ measurements is shown for various gate voltages, see Fig. 8.18(left). The right graph shows a magnification of the differential conductance at positive bias voltages. The peak $U_{DOS,SP-B}(U_g)$ obtained in the dc for positive bias is two orders of magnitude lower than for negative bias. The ndc, obtained for zero gate voltage and at negative bias voltages, is in accordance

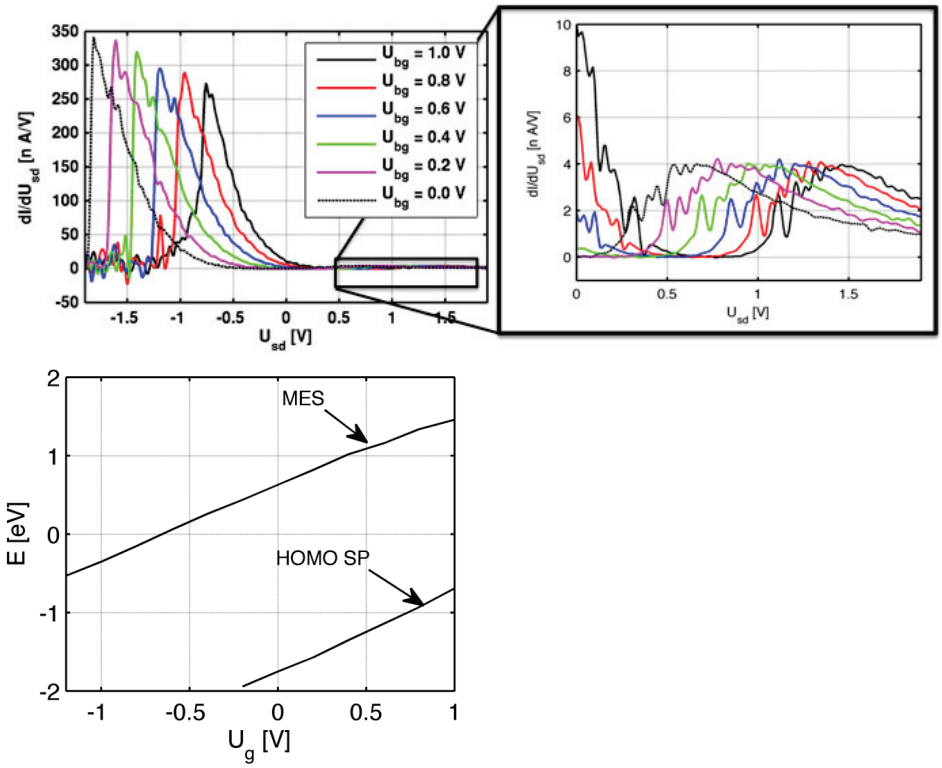

Figure 8.18.: (top) The graph show the dc of the current voltage characteristics for different gate voltages U_g of Type B SP/MES (1:6) with 4 nm Au core. The right graph shows a magnification of the dc for positive bias, since the observed peak is two orders of magnitudes smaller than the peak observed at negative bias. (bottom) A plot of the peak position in dependence of the gate voltage.

with spiropyran molecules in a matrix of SAM of octanethiol on Au(111) [136]. Taking these measurements into account, the DOS-feature at negative bias can be identified as the HOMO level of SP $U_{DOS-HOMO,SP-B}$. The DOS feature at positive voltages is attributed to a MO of the MES molecule. The assumption of the geometric arrangement of the molecules in the two tunneling barriers (see Fig. 8.14) is supported by the assignment of the DOS features described above. In this picture, it is plausible that the resonant case for the SP molecule has a higher impact than for the MES molecule, since SP is part in the current limiting junction in this device. In addition to the DOS

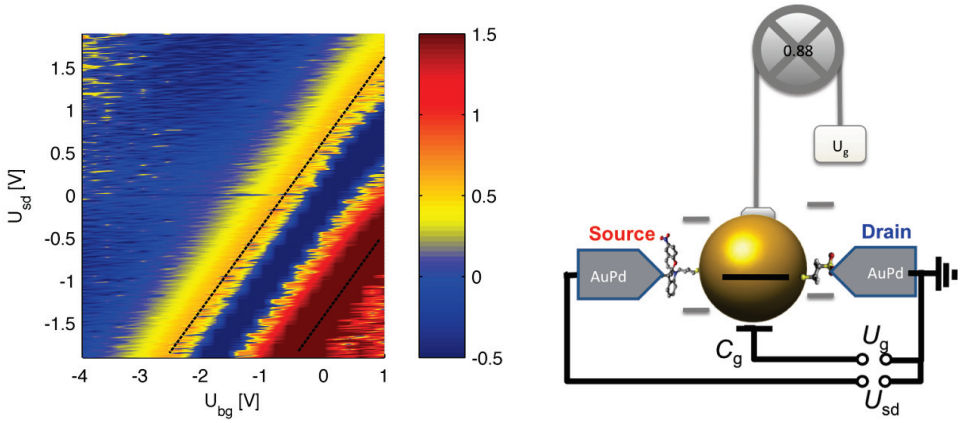

Figure 8.19.: (left) Color map of ndc curves obtained for various gate and source drain voltages, the color map is plotted in logarithmic scale so that the HOMO levels of both molecules were visible. (right) Schematic of molecular orbital lifting, the molecular orbitals are correlated to the energy level of the NP, a change in backgate voltage elevates the energy level of the NP and therebye the molecular levels.

peaks an oscillatory variation of the DOS curve was observed. The distance between the peaks was found to be 65 meV. This value is comparable to the value of 61 meV determined in RT measurements on BP3 capped NPs with 4 nm Au core. Metallic NPs in the order of 5 nm or below exhibit experimental capacitances of the order of 1-5 aF, and therefore Coulomb blockade phenomena can be observed at ambient temperatures. Electron transfer occurs by tunneling through the ligands between the electrodes and the NP.

A controllable gate-voltage dependence of $U_{DOS-HOMO,SP-B}$ was observed in the molecule-capped NP device. The DOS feature observed shifts to a lower bias as a more negative U_g is applied, see Fig. 8.18(top). Thus by changing the gate voltage the molecular energy levels were shifted relative to the Fermi energy and can be pushed to resonance. The $U_{DOS-HOMO,SP-B}(U_g)$ values measured against U_g is shown in Fig. 8.18(bottom). It is observed that $U_{DOS-HOMO,SP-B}(U_g)$ scales linearly and reversibly as a function of U_g. The slope, $f_{eff} = \Delta U_{DOS-HOMO}/\Delta U_g = 0.88$, is the gate efficiency factor, which describes the effectivity of the molecular orbital gating. This factor is more than three times larger than the value (0.25) obtained by Reed et al. [119], for single alkanedithiol

molecules. The devices, used by Reed et., al were fabricated using electromigration technique of a continuous gold wire (coated with the desired molecules, in vacuum, at 4.2 K). In the design used, the weaklink of the wire is placed over an oxidized aluminum gate electrode with 3 nm oxide layer. The large gate coupling was explained by Reed et al. that the molecule resides close to the gate metal-dielectric interface, which reduces the screening by the electrodes [119]. The high coupling in the case of the type B NP device has not been understood. Indications for a measurement artifact were distorted by the fact that of both source-meters in the measurement setup the voltage between the output is measured and saved as data as well as the outgoing current of the two sources, see Fig. 8.19. The gate-controlled tunneling transport is fully illustrated in Fig. 8.19, where a two-dimensional color map of $\log(dI/dU_g)$ is shown. This type of two-dimensional color map is later referred to as energy level plot, which is attributed to the fact that the energy levels of the molecules and the gate induced shift were clearly observable. The dashed line indicates the HOMO energy level of the spiropyran $U_{DOS-HOMO,SP-B}(U_g)$ and of MES $U_{DOS-HOMO,MES}(U_g)$, thus the boundary between two distinct transport regimes (direct and resonant tunneling). The transport characteristic shows typical direct tunneling for a bias and gate voltage applied in the boundaries of the dashed lines

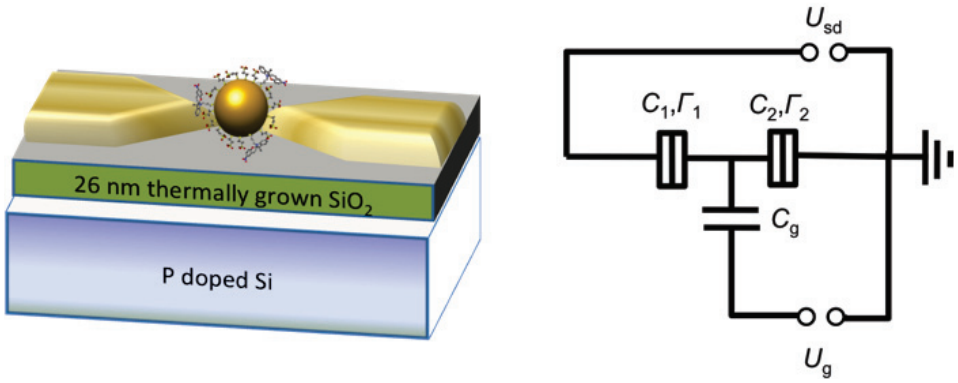

Figure 8.20.: (left) Schematic of the molecule-capped NP device in transistor geometry. (rigth) Equivalent circuit of the system.

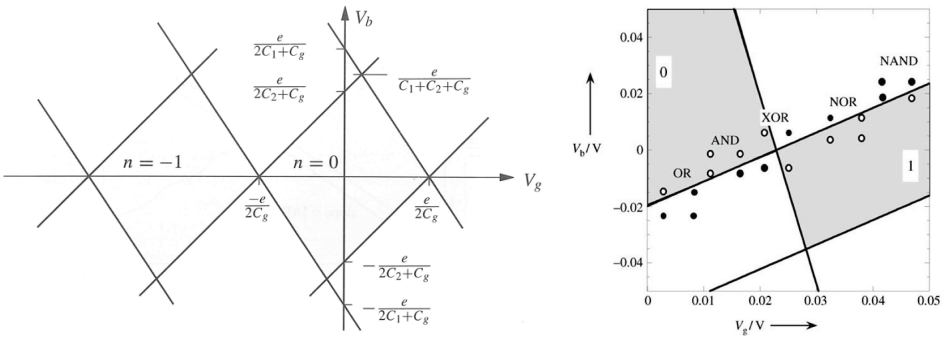

Figure 8.21.: (left) Typical stability diagram of a SET device, the capacitive coupling between the NP and the gate and the electrodes can be calculated as illustrated [88]. (right) 'Stability map showing two stable regions (grey background) in which the (negative) charge is either n=0 or n=1, as indicated. Points in the stable regions are shown as circles. The full dots show points that are read as a "yes" answer to the question "is there current flowing?". The two current-carrying regions differ in the sign of the current because of the change in the sign of the source-drain voltage. The different Boolean functions of two variables (=four values of the read-ins) have outputs that can be in either region depending on their truth table. [156]

Setting a gate and bias voltage outside of these boundaries, a molecular level comes between the energy window (see Fig. 8.19) of the electrodes and resonant transport is

observed.
In a three-terminal device, a negative or positive gate voltage would raise or lower the orbital energies in the molecules relative to E_F, respectively. Hence, a positive value of f_{eff} indicates HOMO-mediated (hole) tunneling. Conversely, f_{eff} is negative for LUMO-mediated (electron) tunneling [119].

8.6.4. Device2: Coulomb diamonds at 4K

In this section cyclic $I(U)$ measurements that were performed at liquid helium temperature (4.2 K) are discussed. The building block of the device and the equivalent circuit is schematically depicted in Fig. 8.20. The tunneling resistances $R_1 \approx R_{SP} \approx 1\,\mathrm{G\Omega}$ and $R_2 \approx R_{MES} \approx 10\,\mathrm{M\Omega}$ of the two tunneling barriers are much higher than the quantum resistance $R_0 = 25.8\,\mathrm{k\Omega}$. Therefore the tunneling can be described by the rates (Γ_1, Γ_2) through the left and the right contacts, which are calculated with [157]:

$$\Gamma_1 = \frac{1}{e^2 R_1} \frac{-\Delta E_1}{1 - \exp(\Delta E_1/(k_B T))} \tag{8.4}$$

$$\Gamma_2 = \frac{1}{e^2 R_2} \frac{-\Delta E_2}{1 - \exp(\Delta E_2/(k_B T))} \tag{8.5}$$

ΔE_1 and ΔE_2 are the changes in electrostatic energy between the occupation states n and n+1 of the nanoparticle. Since the resistances of the ligands are much higher than R_0, electrons are localized on the nanoparticle. This allows calculating the change in electrostatic energy using the orthodox theory:

$$\Delta E_1 = \pm \frac{e^2}{C_\Sigma} \left(\frac{1}{2} + n - \frac{C_g U_g}{e} - \frac{(C_2 + C_g) U_{sd}}{e} \right) \tag{8.6}$$

$$\Delta E_2 = \mp \frac{e^2}{C_\Sigma} \left(\frac{1}{2} + n - \frac{C_g U_g}{e} + \frac{C_1 U_{sd}}{e} \right) \tag{8.7}$$

where C_g,C_1 and C_2 are the capacitances between the NP and the gate, the left and the right electrodes, respectively. The stability map (see Fig. 8.21) shows the lines $\Delta E_1 = 0$ and $\Delta E_2 = 0$, which divides the plane into regions where the charge transfer is or is not energetically allowed [157]. In the stability diagram (see Fig. 8.22) diamond-like features are clearly observable.

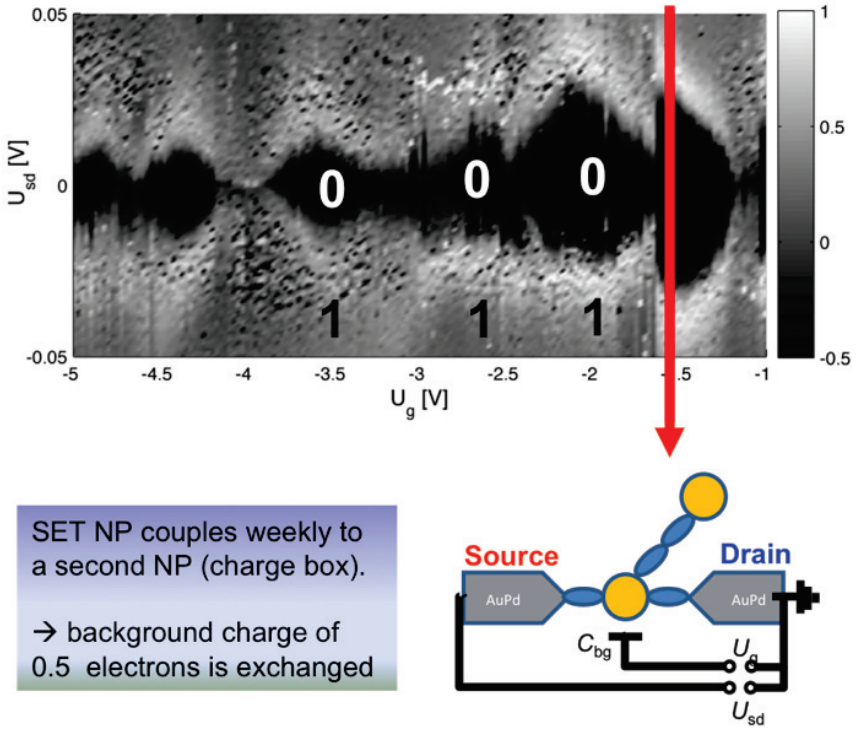

Figure 8.22.: Coulomb diamond-like stability diagram measured at 4K. The switching like behavior might be explained with a partial charging and discharging of the NP.

The 'jumping' of the diamonds can be explained by a fluctuating residual charge Q_0 between the NP and a coupled 'charge box' / trap site close to the NP [14]. The charge box could be either the molecule (MES / Spiropyran / Na^+ ion), a coupled additional NP or trap sites in the SiO_2. The stabililty plot and the transconductance of one coulomb diamond is shown in Fig.8.23. Using Fig. 8.21 the capacitance between the NP, the electrodes and the backgate can is estimated to:

$$C_g = 0.14\,\text{aF},\ C_1 = 2\,\text{aF} \text{ and } C_2 = 2.6\,\text{aF}$$

Fig. 8.24 shows the single $I(U)$ curves obtained for different gate voltages. On the experimental results obtained a complete set of binary logic gates can be realized on

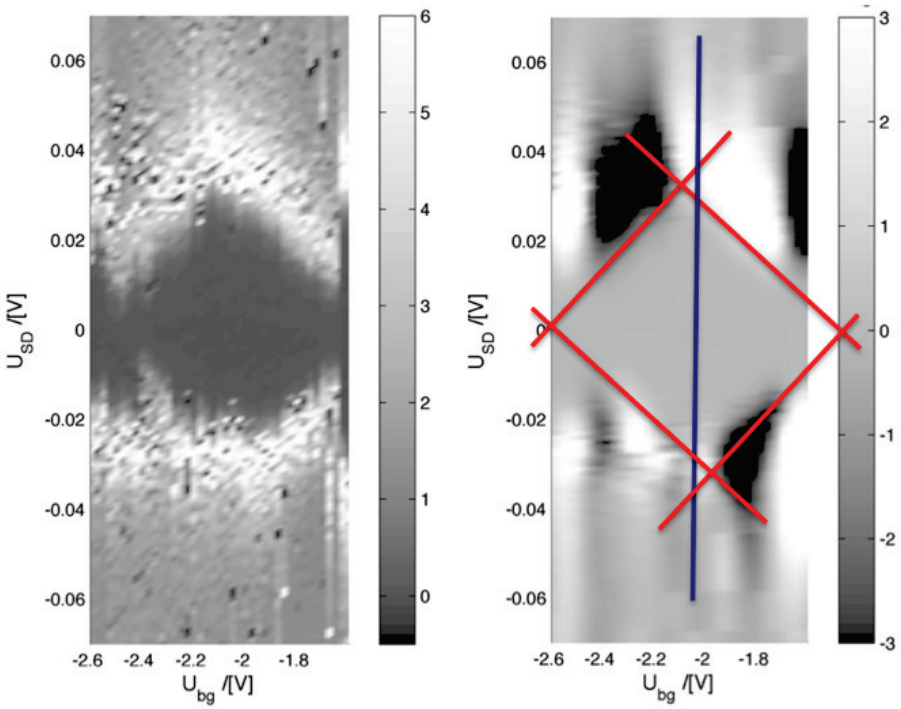

Figure 8.23.: Stability plot (left) and transconductance plot (right) of a Coulomb diamond that is obtained by a measurement of a Type B SP/MES (1:6).

the same hardware, see Fig.8.21. According to Klein et al. [156] these gates can be operated in parallel so that logic on the level of a full adder can be implemented.

8.7. Conclusion: Light induced conduction switch in devices with SP and MES capped NPs

Molecules with tailored functionalities are chosen to create a switch that changes the electronic properties during the illumination with light of a distinct wavelength. For this purpose the photoisomer SP, which has one stable (SP) and one metastable (MC) conformer, is chosen. The two conformers show fundamental different transport characteristics. The NPs investigated are capped with different ratios of the functionalized

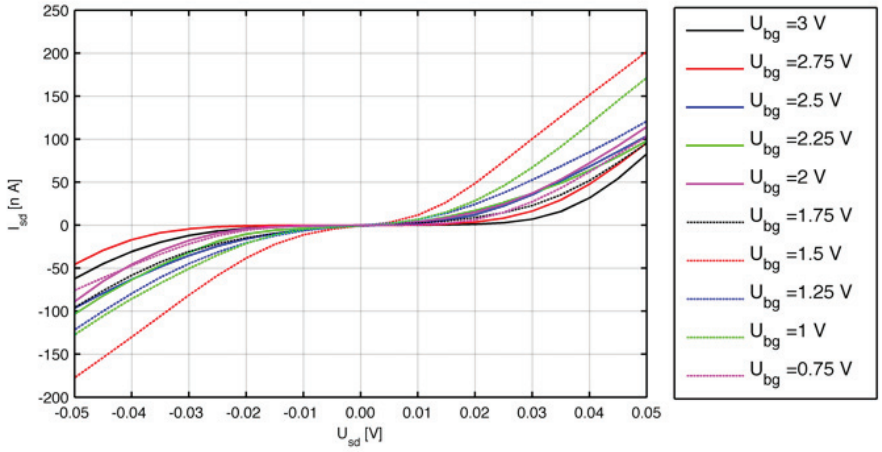

Figure 8.24.: Single $I(U)$ curves of coulomb blockade.

photoisomer spiropyran (SP) and the NP-stabilizing mercaptoethane sulphonic-acid (MES), which is found to be accompanied by fundamental different transport characteristics.

MES

However, since there are two molecules present on the NP (SP/MES) a clear indication of the molecular orbitals using this technology is not possible. Unfortunately, we did not obtain NPs that are only capped with SP or in a matrix of for example well-known alkanethiols.

Firstly, a reference NP, a MES capped gold NP with 12 nm core size, had to be characterized, since the electrical properties of MES are not known. In the ndc of a cyclic $I(U)$ measurement DOS features are observed at ($U_{MES,DOS,1} = -1.78\,\mathrm{V}$,$U_{MES,DOS,2} = -1.08\,\mathrm{V}$) and $U_{MES,DOS,3} > 2.2\,\mathrm{V}$, the difference $\Delta U_{MES,DOS,1-2} = (3.28 \pm 0.03)\,\mathrm{V}$ is assigned to the HOMO-LUMO gap of MES, which is determined to be 3.75 eV by a UV-VIS spectra of MES molecules dissolved in di-water. The double-peak $U_{MES,DOS,1,2}$ observed can be related to MES molecules present in different conformations (cis, trans) in the tunneling barrier. A theoretical approximation of the change of molecular energy levels due to different dipole moments in the

tunneling barrier is approximated using [20]. The different surface dipole moments ($P_{MES-Au,trans} = 11\,\text{Debye/nm}^2$, $P_{MES-Au,cis} = 12.06\,\text{Debye/nm}^2$) of the two conformers lead to a theoretical difference between the work functions of the two MES species trans and cis: $\Delta W_{MES-Au,trans,cis} \approx 0.4\,\text{eV}$. The difference $\Delta W_{MES-Au,trans,cis}$ is 43% smaller than the observed peak distance $\Delta U_{MES,DOS,1-2}$, so that the peaks (1,2) can be assigned as the relevant density of states features and, thus, are attributed to molecular energy levels: HOMO-1, HOMO, respectively. Consequently, peak number three can be assigned to the LUMO level. These assignments of the energy levels are only possible due to the comparison with STM measurements [136], in which the geometrical arrangement in the tunneling barrier is well defined. The STM measurements are performed on a SAM of MES molecules on Au(111) [136]. Surprisingly, the $I(U)$ and ndc obtained in both types of measurements (STM / nanoelectrodes) are in good correspondence, although the measurements are performed under completely different conditions such as: (i) the electrode material [AuPd vs. (Au(substrate), W(tip))], (ii) MES capped gold NP vs. SAM of MES on Au(111) and (iii) measurement setup in normal atmosphere condition vs. UHV STM.

In both types of measurement devices (STM, nanoelectrodes) the conductance in the linear regime ($U_{sd} \approx 0\,\text{V}$) is comparable ($G_{MES,lin} \approx 0.165\,\text{nS}$). Using the iterative Simmons fit a tunneling barrier height of $\phi_{MES-NP} \approx (5.3 \pm 0.3)\,\text{eV}$ is revealed, which is in the order of the work function of gold [65]. This is in correspondence with (i) the estimated length of the vacuum gap $l_{vac,MES} = (0.6 - 0.9)\,\text{nm}$, which is determined using the Simmons fit and TVS, using the division factor $\sim$0.3.

In conclusion a MES-gold contact has been studied in an 'electrode-MES-AuNP-MES-electrode' device and compared to STM measurements. Molecular properties have been characterized by $I(U)$ measurements and TVS. The tunneling barrier heights obtained and the vacuum gap determined are consistently interpreted on the basis of a geometrical model with the help of the Simmons model and TVS.

Type A SP/MES (3:2) capped NPs

Type A gold NPs are capped with SP/MES (3:2) and have a core size of 12 nm. In such devices symmetric contacts, i.e. the contact between the NP and the left/right electrode, are created by a similar bundle of molecules. Since the NP is surely larger (12 nm) as the nanogap (5 nm) the $I(U)$ curves obtained have shown similar characteristics for all measured devices.

The expertises of several cooperation partners, namely:
(i) R. Ganesan, T. Lespagnard in the group of F. Remacle at the university of Liege (theoretical calculations),
(ii) K. Schulze in the group of R. Weinkauf at the university of Düsseldorf (spectroscopic measurements),
(iii) U. Paetzold in the group of Prof. Carius IEK-5 in the Forschungszentrum Jülich (simulations on plasmonics in nanometer-scaled devices) and
(iv) A. Soltow, a STM collegue in our group,
are incorporated in the interpretation of the obtained data.
On the electrode/molecules-NP-molecules/electrode device cyclic $I(U)$ measurements are performed in the dark and under illumination of UV light with the bandwidth of $350 \pm 50\,\mathrm{nm}$.
In the dark the molecule is in the SP-form, the ndc of the electrode/SP|MES-NP-SP|MES/electrode device is showing three relevant DOS features at :
($U_{DOS,SP-A,1} = -2.19\,\mathrm{V}$, $U_{DOS,SP-A,2} = -1.40\,\mathrm{V}$) and $U_{DOS,SP-A,4} = 2.24\,\mathrm{V}$. The peak at $U_{DOS,SP-A,1}$ is assigned as relevant density of states features of the MES capped NP ($U_{DOS,MES,2}$). The difference of $e\Delta U_{DOS,SP-A,4-2} = 3.64\,e\mathrm{V}$ corresponds to a wavelength of 341 nm, which is in correspondence with the $\pi - \pi^*$ transition (HOMO-LUMO gap) of spiropyran as theoretically predicted by R. Ganesan [143] and experimentally measured in a 100 nm dry surface layer by K. Schulze [144], using UV-Vis spectroscopy.
The transition between the SP-form and the MC-form can be induced over several reaction paths, the highest difference in free energy between the SP molecule and a transition state is in the order of 1.6 eV. R. Ganesan [143] has shown that a transition from the excited SP molecule to merocyanin is induced (see Fig. 8.4).
Under the illumination of UV light in the bandwidth of $350 \pm 50\,\mathrm{nm}$ the molecule is in the MC-form. The ndc of the electrode/MC|MES-NP-MC|MES/electrode device is showing two relevant DOS features at:
$U_{DOS,MC-A,1} = -1.01\,\mathrm{V}$ and $U_{DOS,MC-A,2} = 0.99\,\mathrm{V}$.
Between the two molecular states a significant difference in the magnitude of current is observed. The difference is explained by the reduced height of the tunneling barrier of the MC-form.
Supported by STM measurements, which are found to be in good correspondence to the single NP-device, the observed energy levels, without and under illumination of UV light, are dedicated to the molecular energy levels of the SP and MC molecule [136]. It

is observed that the up and the down branches of the cyclic $I(U)$ measurements appear again mirrored, which is explained by the symmetric tunneling contact of the NP to the right and the left nanoelectrode. In the down branch of the ndc the peak at negative bias is attributed to the HOMO energy level and hence, the peak at positive bias to the LUMO energy level.
The difference in energy of $e\Delta U_{DOS,MC-A,2-1} = e(U_{DOS,MC-A,2} - U_{DOS,MC-A,1}) = 2\,eV$ corresponds to a wavelength of 619 nm. This is in the order of the calculated $\pi - \pi^*$ transition (HOMO-LUMO gap) of merocyanin and the obtained peak position ($\lambda = 560\,nm$) of the UV-Vis spectra of the MC-form. The excited MC molecule relaxes to the SP molecule over a reaction path, similar to the case of SP (see Fig. 8.4) [143]. The redshift of about 40-100 nm can be explained by an impact of the nanoelectrodes to the delocalized molecular levels of merocyanin and thus, on the electronic structure.
The determined half life time is $T_{1/2,MC-A} = 108\,s$, which is determined from the observed decay of the current after switching off the UV-light. This value is only marginal higher than the half-life time (84 s) of $10^{-4}M$ of SP dissolved in chloroform solution [52]. Hence, the MC molecules on the NP can be assumed as weakly coupled to the surrounding media, i.e. the MES molecules and the nanoelectrodes. Additionally, the chemisorption of the SP molecule on a gold NP seem to have not a great impact on the half-life time and on the difference between the HOMO and LUMO energy levels of the molecule. This leads to the conclusion that the molecular orbitals of the MC and SP molecule are only weakly coupled to the NP via the alkane chain.
The power of the UV light applied in this measurement is in the range of 10μW, which corresponds to $\sim 10^{13}$ photons per second. The cross section of the SP molecule is about 0.5 nm x 1 nm, so that the rate with which photons hit a single molecule, is $< 10^{-6}/s$.
The explanation of the observed coupling is found in slow localized surface plasmon polaritons (SLSPP). The SLSPP are generated in metal structures under illumination of light, in this case in the connection-lines that act as antenna. The SLSPP were localized close to the corners of metallic structures and were concentrated at the nanogap position. These polaritons are generating an AC electric field with the frequency of the applied light at the nanogap position. Thus, the connection lines to the nanoelectrodes act as antenna and focus the electric field of the incident light at the nanogap position.
The excitation spectroscopy measurement, i.e. the measurement of the conduction of the NP device at a fixed bias voltage under illumination of light with different wavelengths, is showing two distinct peaks at 412 nm and 544 nm. The height of the peaks

is found to be dependent on the applied bias voltage as well as on the sweep rate. The light is generated with a Xenon lamp and the intensity is held at a constant value. The observed peaks are in correspondence with the UV/Vis measurements obtained on merocyanin in the solid state on a surface (360 nm and 560 nm). Theoretical SLSPP calculations of this nanometer-sized device, using AuPd electrodes and molecule capped Au NPs, show a huge impact of the surrounding dielectric medium on the wavelength λ of the incident light, where the absorption efficiency is maximal. The impact of the plasmon resonance on the conductivity is not clear at the moment. In the device created by the BP3-capped NPs the influence of light on the conductance was about 10%. The magnitude of the impact of the intensity controlled sweep of light on the conduction through the NP device is shown in Fig. 8.6(right) to be in the order of three, which is in agreement to the observed cyclic $I(U)$ curves, see Fig. 8.8.

Using the analyzation tools Simmons and TVS conclusive results are obtained, i.e the length of the vacuum gap is determined to be 0.1 nm for the device with the capping molecule in the SP-form and the MC-form. The difference between the HOMO and LUMO energy, that are obtained by the iterative Simmons fit, is 3.3 eV, which is a bit lower than the distance between the peaks observed in the ndc $e\Delta U_{DOS,SP-A,4-2} = 3.64\,e$V. The division factor obtained for the SP-form $\eta^{\alpha=1.5}_{SP-A} \approx 0.62 - 0.71$ is found to be lower as for the MC-form ($\eta^{\alpha=1.5}_{MC-A} \approx 0.75$), which is in correspondence with the calculated widely delocalized π-electron system of the MC-form.

In conclusion, the optical and electrical properties of the type A SP/MES (3:2) capped 12 nm gold NPs were investigated using the analyzing tools Simmons and TVS. With the incorporation of the interdisciplinary expertise of our cooperation partners, which have performed studies on the SP molecule, a consistent impression of such a complicated system was achieved. The observed DOS features in the ndc were assigned to molecular energy levels (HOMO, LUMO) according to STM measurements. Finally a logical scheme was drawn, with which it is possible to mimic a complex logic device such as the full adder on a single NP device, whereby a conventional full adder consists of 24 transistors [158].

Type B

In type B devices gold NPs with a core size of 4 nm and capped with SP/MES (3:2) are applied. The number of molecules that contribute to the charge transport is estimated to be in the range of 2-6. Therefore, it is most probable that the bundle of molecules at the two adjacent contacts of the NP and the nanoelectrodes are different. It is observed that the $I(U)$ curves are asymmetric. This is a strong indication that the obtained NP-based devices have asymmetric contacts, i.e. an electrode/SP-NP-MES/electrode contact (see Fig. 8.15) or electrode/MES-NP-SP/electrode contact (see Fig. 8.16).

The ndc of device 1 shows a DOS feature at $U_{DOS,SP-B1} = 0.7\,\mathrm{V}$, which is attributed to the HOMO-level of MES (compare with section 7). The Fowler Nordheim plot (compare with Fig. 8.16(right)) shows a minimum at $U_{TVS,SP-B1} = 0.83\,\mathrm{V}$, which is within the error-bar in correspondence with the observed DOS peak in the ndc.
The magnitude of current of the cyclic $I(U)$ measurements is in the pA range at 4 K, which is a clear indication that a vacuum gap between the NP and the electrode arose. Oscillations in the ndc (see Fig. 8.17) are indicating an interference phenomenon called Gundlach oscillations. Thus, in the case, where a molecular orbital is within the window of the applied bias voltage, there is a region in the tunneling contact that is classically available (see Fig. 8.17) and can be described by a triangular box. In this classically available region standing electron waves occur between the potential drop of the metal and the molecular orbital (see Fig. 8.17). With the increase of the bias voltage, the width of the classically available region (the triangular box) changes and thereby the interference of the electrons in the triangular box oscillate between constructive and destructive interference of the electron wave function. In STM measurements this phenomenon is observed only for a positive bias voltage, thus, for reflections at the LUMO orbital. Since in a NP-device two barriers are present, the phenomenon is observed for both, negative and positive bias. Coombs and Gimzewski derived a condition [155], with which the field strength $F \approx \frac{U_{sd}}{l_{tot}}$ and therefore the length of the tunneling barrier $l_{tot} = l_{butane} + l_{SP} + l_{MES} + l_{vac}$ is determined. The averaged value $\bar{l}_{tot} \approx 2.7\,\mathrm{nm}$ is calculated, hence the remaining vacuum gap is approximated to $l_{vac} \approx 0.7\,\mathrm{nm}$. The size of the vacuum gap is in correspondence with the magnitude of the current observed. This is the first time that Gundlach oscillations have been observed in an electrode/molecule-NP-molecule/electrode device. However, in molecule based systems using STM it is

already published [153, 159]. Gundlach oscillations in a metal-vacuum-metal contact are widely investigated using STM technology [68, 152, 160, 161].

In device 2 the $I(U)$ curve obtained is asymmetric as well. The device is measured in transistor geometry, using a p-doped silicon substrate as full plain backgate that is electrically isolated from the electrode structure by a 26 nm thick, thermally grown SiO_2 layer. For zero gate voltage two DOS features are observed In the ndc at:
$U_{DOS-HOMO,MES}(U_g = 0\,\mathrm{V}) = 0.70\,\mathrm{V}$ and
$U_{DOS-HOMO,SP-B}(U_g = 0\,\mathrm{V}) = -1.85\,\mathrm{V}$,
which are assigned to the HOMO energy levels of MES and SP, respectively, comparing with STM measurements. On top of the DOS features a periodic, oscillatory behavior is observed. The distance between the periodically appearing peaks is 65 meV. This value is comparable to the value of 61 meV determined in RT measurements on BP3-capped NPs with 4 nm Au core.
For various gate voltages U_g the ndc is plotted in logarithmic scale in a color-map plot, which is referred to as energy level plot. The position of the energy levels of the molecules (DOS features) shifts with the applied gate voltage, the slope is determined to be $f_{eff} = \Delta U_{DOS-HOMO}/\Delta U_g = 0.88$. This factor is more than three times larger than the value (0.25) obtained for single alkanedithiol molecules by Reed et al. [119]. The devices used by Reed et al. were fabricated using electromigration technique of a continuous gold wire (coated with the desired molecules in vacuum at 4.2 K). In the used design the weaklink of the wire is placed over an oxidized aluminum gate electrode with a 3 nm thick oxide layer. The large gate coupling was explained by Reed et al. as that the molecule resides close to the gate metal-dielectric interface, which reduces the screening by the electrodes [119]. The high coupling in the case of the type B NP device is not understood until now. Indications for a measurement artifact are distorted by the fact that at both source-meters in the measurement setup the voltage between the output is measured and saved as data as well as the outgoing current of the sources (see Fig. 8.19).
In the measurements, that are performed at 4 K, coulomb diamond like features in the stability plots are observed. The jumping-like shift of the diamonds can be explained by a fluctuating residual charge Q_0 on the NP. The charge might be transferred by either the molecule (MES / Spiropyran / Na^+ ion), a coupled additional NP or trap sites in the SiO_2. The different sizes of the diamonds in the stability plot are an additional in-

dication that more than one NP is present close to the nanogap region [88]. The height of the diamond of ∼65 meV is in correspondence with the peak distance obtained at RT and to the BP3 capped NP device. The fact, that the peak distance at RT and 4 K is the same, is an indication that the nanogap is smaller than the size of the NP. The obtained values of the capacitances ($C_g = 0.14$ aF, $C_1 = 2$ aF and $C_2 = 2.6$ aF) are in correspondence with the capacitance calculated according to the model of a metal sphere coupled to an infinite plane, which is calculated to be $C_{MES}(r = 2\,\text{nm}, l_{MES} = 0.5\,\text{nm}) = 2.7$ aF and $C_{SP}(r = 2\,\text{nm}, l_{SP} = 1.1\,\text{nm}) = 1.8$ aF. The coupling of the NP to the applied gate voltage is determined to be 6 %, which is typical for such a device.

In conclusion, we can state that the BP3-capped NPs as well as the Type B (SP:MES) (1:6) NPs, which both have a core size of ∼4 nm, show coulomb blockade at RT. Both molecules (SP, BP3) are composed of an alkane chain (propane, butane) and an additional delocalized π-electron system (BP and SP). The peak distance in both devices was $61 - 65$ meV at RT, which indicates a comparable capacitve coupling of the NP to the electrodes and thus, similar dielectric constants and lengths. The change in the order of magnitude of current in transport measurements at different temperatures is a good indicator if the geometrical situation in the nanogap, i.e. the length of the vacuum gap changes with temperature. In the case of the BP3 capped NPs at low temperatures the current is almost five orders of magnitude lower compared to RT measurements. Therefore, a vacuum gap of ∼0.4 nm is assumed, which is in correspondence to the larger peak separation of ∼103 meV.
Contrary, in the measurements of Type B (SP:MES) (1:6) NPs the peak distance of the Coulomb blockade peak as well as the order of magnitude of current was only a factor of ten lower, which can be explained by the freezing of the contribution to charge transport according to Poole-Frenkel and super-exchange.

Various logical schemes (OR, AND, XOR, NOR, NAND) can be implemented on a single Coulomb blockade device just by the choice of proper values for gate and the bias voltage as shown by [156].

9. Conclusion

The studies described in this thesis elucidate the electronic properties and charge transport mechanisms in nanoelectrode/molecule-nanoparticle-molecule/nanoelectrode systems. It was demonstrated that it is possible to implement such a system using CMOS compatible technology and even in transistor geometry. The charge transport mechanisms were clearly attributed to molecular properties, as well as to the properties of the metal-nanoparticles. In combination with STM measurements a clear indication of the observed molecular energy levels was possible. A systematic manipulation of molecular orbitals was demonstrated using the application of a backgate as well as the change of the electronic properties of the functionalized, photoisomerizable capping molecule under illumination of light. The molecular properties were determined using several analyzing methods. A descriptive picture of the molecule-NP-electrode system were drawn for various systems that are based on the molecular properties. Before a molecule-nanoparticle system can be tailored to the demands of a working device, the fundamental understanding, if possible of all charge transport phenomenas observed, is required. Investigation tools of charge transport in molecule based devices are: (1) source-drain dependent cyclic $I(U)$-curves at various temperatures, (2) gate dependent cyclic $I(U, U_g)$-curves at various temperatures, (3) temperature dependent conductance measurements, (4) change in conductance due to the illumination of light. Analyzing tools to interpret the measurements performed are: (i) the Simmons model and (ii) transition voltage spectroscopy. Besides this, various other phenomena such as Coulomb blockade, photoconductance, orbital mediated tunneling and temperature dependent charge transport models (Arrhenius, granular metal based transport, super-exchange and tunneling) are discussed. The application of molecular capped nanoparticles as bricks in working devices demands structuring techniques to fabricate nanoscale electrodes with high accuracy and reproducibility.

Fabrication of nanoelectrodes

An essential part of this work is the establishment of a fabrication recipe for metallic nanoelectrodes that have a tip separation of a few nanometer in CMOS compatible technology. In this thesis an E-beam lithographical fabrication process has been worked out to provide nanometer-spaced metal electrodes and multi-terminal devices. The E-beam lithographical fabrication process was optimized to fabricate nanoelectrodes with a tip separation of only a few nanometer with an accuracy in the nanometer scale. The optimization included the enhancement of (i) the contrast in the exposed pattern, (ii) the optimization of E-beam machine parameters and (iii) the resist/developer combination.
(i) The increase in contrast of the dose pattern by a factor of 1.5 was achieved on the one hand by reducing the exposed area around the electrode tip position according to the regimes in a Monte Carlo based simulation of backscattered electrons in the substrate and on the other hand by a reduction of the dose applied using an enhanced dose setting.
(ii) The exposure dose pattern with best contrast and steepest steps at the border region is created with the lowest possible beam current and beam-step size.
(iii) The new type of developer (H_2O/IPA) enhances the sensitivity by 15 % and the contrast by 10 %. Almost no dark development is observed. A double layer resist was chosen that is developed in two subsequent steps. Thereby, the stability of the mask bridge is increased.
The contrast of the realistic exposure dose pattern was improved with (i) and (ii). In combination with (iii) the sidewall of the mask layer bridge is steeper and therefore, the mask layer bridge itself remained thicker. Therefore, it is more rigid and this results in a high yield fabrication process ($\sim$ 55 %) of nanoelectrodes that have a tip separation of 2-4 nm and a geometric control, which is in the nanometer scale. These results are unrivaled in comparison with other single-step E-beam lithographic fabricated nanoelectrodes.
There are indications that the limiting factor is the beam shape/focus. The dose in the 2 nm and 4 nm lines have to be increased by a factor of two compared to the previous tip design.

Three different methods were investigated to fabricate multi terminal devices using 4-terminal-in-plane sidegates, lithographically defined metal backgate and semiconducting

full plane backgate. In the case of four terminal devices (in plane gating) the yield was noticeably reduced due to the increased stray dose. Additionally, the attempt to contact the four electrodes with the measurement equipment led to the destruction of the device, probably due to electrostatic dis-chargement. Contrary, in metal backgated structures that were isolated by a 25 nm thick SiO_2 layer the yield did not change dramatically. But in such devices the voltage applied to the backgate was limited to a few volt (3 V-4 V). Otherwize a breakdown of the device was observed. The best choice for the realization of a gated structure was the approach using the semiconducting full-plane as backgate. In this solution no influence on the yield was observed and the device was stable for an applied gate voltage of -20 V to 2 V at room temperature.

Immobilization of nanoparticles between nanoelectrodes

The controling of the immobilization of a single nanoparticle between the nanoelectrodes is required for the application of molecular capped nanoparticles in working devices. In this work procedures have been developed to immobilize single charged and uncharged nanoparticles between nanoelectrodes, which are based on dielectrophoretic trapping. A successful trapping event is detected by using a lock-in amplifier. To achieve conclusive AC measurements on a high ohmic system all capacitances involved have to be minimized to a few pF or even in the sub pF range in order to avoid RC-filter effects. Additionally the charging of the molecule capped nanoparticle plays a distinct role to use either AC or DC dielectrophoretic trapping. These measurement setup enabled a live monitoring of a single-nanoparticle trapping event.

Charge transport in nanoelectrode-nanoparticle devices with BP3 capped NPs

This chapter shows representative electrical measurements on nanoelectrodes in which a single BP3 capped NP is immobilized. The properties of the subunits, of which the molecule (BP3) investigated is composed, are well documented in literature. It was surprising that it is possible to apply well established analyzing tools (Simmons, TVS), which are developed for pure molecular devices that consist of only one junction, to the case of a molecular capped NP in a nanoelectrode configuration. It is shown that the application of the Simmons equation and TVS as analyzing tools reveal a detailed geometrical picture of the situation of the NP at the nanoelectrodes, i.e. the length of

a remaining vacuum gap, if the decay constant and length of the molecular subunits are known.

In the case, where between the molecule-capped NP and the nanoelectrodes no vacuum gap remains, the tunneling barrier height $\phi_{Sim,BP3-A} = 1.65\,\mathrm{V}$ of the iterative Simmons fit obtained was in correspondence with the literature value of the tunneling barrier height of alkane ϕ_{alkane}. Therefore, it can be assumed for future investigations that the largest tunneling barrier height of the subunits, of which the molecule is composed, dominates the transport, if the molecular orbitals of which the subunits are composed are still localized in the subunit. Furthermore, it was observed that the total resistance at zero bias $R_{BP3} = 9.6\,\mathrm{M\Omega}$ of the BP3 molecules is at least lowered by a factor of four lower compared to the contact resistance of alkane $R_{cont,alkane} = 54\,\mathrm{M\Omega}$ (achieved for a device with one chemsiorbed and one physisorbed contact). The contact resistance of the phenyl units and the assumption of direct phenyl-metal contacts is considerably lower than a for a typical physical contact and likely the reason to cause this resistance lowering. In conclusion, in the nanoelectrode-nanoparticle configuration molecular properties were tested.
Moreover, Coulomb-blockade behavior was observed at room temperature as well as at 4 K. So far only in STM measurements on small Au NPs with a diameter of <4 nm CB behavior is observed at room temperature (RT) [127]. Up to now CB at RT is not observed in a CMOS compatible device, which is based on a molecule-NP-system. Small changes in the contact geometry have a tremendous influence on the peak distance. A vacuum gap of approximately 0.4 nm causes an increase in peak distance by a factor of 1.7, as it was observed for device A, comparing the measurements performed at RT and 4 K.
An approved tool to elucidate different transport mechanisms in a NP device, commonly an array of NPs, is the temperature dependent conductance measurement. However, this method elucidates the principles of charge transport mechanisms for the case of single BP3 capped NPs that are immobilized between gold nanoelectrodes as well. The comparison of the temperature dependent transport through a single NP and a NP array exhibits significant difference.
(1) In the single NP-device temperature independent and thus, tunneling based transport was observed for temperatures below 100 K. However, in a NP array pure tunneling was not observed.

(2) The voltage drop over each tunneling barrier is in a single NP device at least the half of the applied bias voltage over the limiting tunneling barrier, while in a NP array a voltage drop between neighbouring NPs is typically less than 1 μV.
(3) In the case of a NP array the molecules are interdigitating so that the coupling between the NPs and the transport mechanisms might be different. The feature commonly observed in both measurements was a discontinuity in the temperature dependent conductance measurements. The explanation postulated for this phenomenon is a reversible, structural crossover between two geometrical configurations of the NP as well as the rearrangement of the capping molecule on the particle surface. The change in vacuum gap, due to the structural crossover, was estimated to be in the range of 0.1-0.3 nm.
In the case of a NP array at high temperatures (above RT) the highest activation energy in the system was given by molecular planarisation of two phenyl units. At intermediate and low temperatures the transport was shown to be dependent on the charging energy of the NP.
In the case of a single NP at high temperatures the limiting barrier was dedicated by the Poole-Frenkel theory. At intermediate temperatures super-exchange coupling between the phenyl-units was the dominating transport mechanism, while at low temperatures pure tunneling was observed.
Furthermore, the change in conductance under illumination of light due to a photocurrent through the device could be correlated to the position of the nanoparticle, i.e. a high photocurrent ($>$ 5% change in current) probably corresponds to a position close to a corner of the nanoelectrode tip, i.e. the electrode tip separation is smaller than the size of the NP. A low photocurrent ($<$ 5% change in current) could be related to a position between the nanoelectrodes, i.e. the electrode tip separation is larger than the size of the NP.

Light induced conduction switch in nanoelectrode-nanoparticle devices with SP and MES capped NPs

Molecules with tailored functionalities were chosen to create a switch, which can be activated by illumination of light, that changes electronic properties. In particular with the view to a possible application as a device, which comprises complex logical functionality already at room temperature, makes the systems attractive.

The NPs investigated were capped with different ratios of the photoisomer spiropyrane (SP) and mercaptoethane sulphonic-acid (MES), which was found to be incorporated with fundamental different transport characteristics.
Firstly, as a reference NP a MES capped gold NP with 12 nm core size was characterized. Supported by STM measurements, which were found to be in amazing correspondence to the single NP-device, the energy levels observed were dedicated to the molecular energy levels of the MES molecule.

Type A NPs, SP/MES (3:2) gold NPs with a core size of 12 nm create devices with symmetric contacts. It is observed that the $I(U)$ curves were symmetric as well. Since the NP is surely larger than the nanogap, the $I(U)$ curves obtained have shown similar characteristics for all devices. With the illumination of UV light in the bandwidth of 350 ± 50 nm a switch between two molecular states that show a significant difference in the magnitude of current was observed. The difference in the $I(U)$-curve is explained by the change in the height of the tunneling barrier. Supported by STM measurements, which were found to be in correspondence to the single NP-device, the energy levels observed, without and under the exposure of UV light, were dedicated to the molecular energy levels of the SP and MC molecule, respectively. The decay rate of the current after switching off the UV-light corresponds to the rate of SP molecules dissolved in chloroform.
The power of the UV light applied in this measurement was in the range of 10μW. With this power the chance that the molecule is hit by a single photon within a minute is less than the chance to win a Lotto game. The explanation of the coupling observed is found in slow localized surface plasmon polaritons (SLSPP). The SLSPP were generated under illumination of light in metal structures that have dimensions in the range of the wavelength of visible light, in this case the connection-lines that act as antenna. The SLSPP were localized close to the corners of metallic structures and were concentrated at the nanoelectrode position. These SLSPPs generate an AC electric field at the nanoelectrodes position, which has the frequency of the applied light. Thus, the connection lines to the nanoelectrodes act as antenna and focus the electric field of the incident light at the nanoelectrode position.
Surprisingly, the excitation spectroscopy measurement, i.e. the measurement of the conduction of the NP device at a fixed bias voltage under illumination of light with different

wavelengths, was in correspondence with UV/ VIS measurements on merocyanin in the solid state on a surface. Therefore, the charge transport in Type A based nanoelectrode-NP configurations is dominated by the properties of the spiropyrane molecule.
In conclusion, the optical and electrical properties of the type A SP/MES (3:2) capped 12 nm gold NPs were investigated using the analyzing tools Simmons and TVS. With the incorporation of the interdisciplinary expertise of our cooperation partners, which have performed studies on the SP molecule, a consistent impression of such a complicated system was achieved. The observed DOS features in the ndc were assigned to molecular energy levels (HOMO, LUMO) according to STM measurements. Finally a logical scheme was drawn, with which it is possible to mimic a complex logic device such as the full adder on a single NP device, whereby a conventional full adder consists of 24 transistors.
Type B NPs, SP/MES (1:6) gold NPs with a core size of 4 nm, create devices with asymmetric contacts, i.e. an electrode/SP-NP-MES/electrode contact. It is observed that the $I(U)$ curves were asymmetric as well. In the case, where the right electrode (with contact to the MES) is grounded, the HOMO of the SP molecule is tested for negative bias voltage and, verse visa, when the left electrode is grounded. There was a second molecular energy level observed in the normalized differential conductance (ndc) curve, which was two orders of magnitude lower as the HOMO of the SP molecule. An explanation for this huge difference might be that the SP molecule creates the current limiting barrier in the device. The full plane backgate coupling to the molecular orbitals was unexpectedly high. The reason for this effect cannot yet be explained. Coulomb diamonds were observed at low temperatures. Due to a fluctuating residual charge Q_0 on the NP the diamonds shift/jump in position. The fluctuation in the charge Q_0 can be explained by the charging of (i) the capping molecules (MES,SP), (ii) the presence of weakly coupled NPs (charge boxes) or trap sites in the SiO_2 layer. The coupling determined from CB observed was in the range of 7%, which is typical for a 26 nm thick SiO_2 layer and a NP with a core size of 4 nm.

Outlook

Molecule-based devices will not shrink the density of the brickets in a CMOS compatible device further to keep the validity of Moores Law. Instead the density in logic per device bricket is improved, for instance a Full Adder, which is created by 24 transistors

using classical CMOS technology, can be implemented in a single nanoparticle device. Although the use of single molecular capped NPs improved the device stability and reproducibility compared to single molecule devices, the devices are still far away from mass production. The main problem in the reproducibility of current single molecular capped nanoparticle devices is (i) the contact of the molecules to the nanoelectrode and (ii) the exact geometrical situation. This would be improved by a molecule, which is chemisorbed on both the nanoparticle and the nanoelectrode. A molecular capping layer with an end-group that prefers to create an electrical conduction with the nanoelectrode material and not with other NPs would solve the problem. Alternatively, the nanoelectrodes could be capped with molecules that have two thiol-endgroups. The fragility of devices, which are based on a few molecules, makes it unpromising that such a type of device will be applied as logical circuits in future commercially available computer technology. However, the application as memory, sensors or light converting units is more promising.

To summarize the current states of industrial computer technology: (i) the clock speed of the CPU unit stagnates due to the increasing stray capacitance, which gets worse in a downscaling system,
(ii) the device geometry of logical gate units is almost at the limit of downscale,
(iii) L1-L3 cache uses more than 60 % of the space of a processor.
The mission to keep Moores Law valid focusses current industrial investigations (e.g. IBM, Intel, HP) on the downscaling of L1-L3 cache, which are currently micrometer sized objects. Therefore, current CPU manufactures focus their investigations on fast L1-L3 caches, with sub-micrometer dimensions. The application of redox-active molecules in 'medium' area junctions (50 nm x 50 nm) might be a possible application in future devices. Thereby, the molecules can be deposited on the metal surface either in a self assembled monolayer (SAM) or mixed in an isolating thin film polymer and covered with a conducting polymer or a metal electrode. Indeed such devices could be used as resistive switches. Such a system is commonly described as a finite state machine, thus a machine, whose state is based on the history of the device. A network of such finite state machines is called cellular automata, which is handled to be able to simulate biological neural networks.

The use of NPs in industrial fabrication is widely spread. According to the report

”Nanostructured Materials for the Biomedical, Pharmaceutical and Cosmetic Markets” from BCC Research four types of nanoparticle materials, including gold, accounted for more than 90% of the market. Titanium dioxide, zinc oxide and calcium phosphate were the other dominant materials. The global market for these nanoparticles in biomedical, pharmaceutical and cosmetic applications was worth $200 million in 2006. This sector looks set to increasingly use gold with clinical trials, using gold nanoparticles to deliver anticancer drugs already underway.

New uses envisaged in the electronics industry include gold nanomaterials to enhance solar cells, liquid crystal displays and even flash memory devices, although these have yet to emerge from the research laboratories that are working on them.

Bibliography

[1] Lin, B. *Microelectronic engineering* **83**(4), 604–613 (2006).

[2] Prins, F., Hayashi, T., Steenwijk, B. J. A. D. V. V., Gao, B., Osorio, E. A., Muraki, K., and Zant, H. S. J. V. D. *Appl. Phys. Lett.* **94**(12), 123108 Jan (2009).

[3] Zhang, H., Barsotti, R., Wong, C., Xue, X., Liu, X., Stellacci, F., and Thong, J. *Small* **5**(24), 2797–2801 (2009).

[4] Martin, C., Ding, D., van der Zant, H., and Ruitenbeek, J. *New Journal of Physics* **10**, 065008 (2008).

[5] Herwald, S. W. and Angello, S. J. *Science* **132**(3434), 1127–1133 Oct (1960).

[6] Mann, B. and Kuhn, H. *Journal of Applied Physics* **42**(11), 4398–4405 (1971).

[7] Aviram, A. and Ratner, M. *Chemical Physics Letters* **29**(2), 277–283 (1974).

[8] Simmons, J. G. Jan (1963).

[9] Salomon, A., Cahen, D., Lindsay, S., Tomfohr, J., Engelkes, V., and Frisbie, C. *Adv Mater* **15**(22), 1881–1890 (2003).

[10] Holmlin, R., Haag, R., Chabinyc, M., Ismagilov, R., Cohen, A., Terfort, A., Rampi, M., and Whitesides, G. *Journal of the American Chemical Society* **123**(21), 5075–5085 (2001).

[11] Weiss, E., Tauber, M., Kelley, R., Ahrens, M., Ratner, M., and Wasielewski, M. *Journal of the American Chemical Society* **127**(33), 11842–11850 (2005).

[12] Selzer, Y. and Allara, D. *Annu. Rev. Phys. Chem.* **57**, 593–623 (2006).

[13] Nero, J. D., Souza, F. M. D., and Capaz, R. B. *Jnl of Comp & Theo Nano* **7**(3), 503–516 Mar (2010).

[14] Osorio, E. A., Bjørnholm, T., Lehn, J.-M., Ruben, M., and Zant, H. S. J. V. D. *Journal of Physics: Condensed Matter* **20**(37), 374121 Aug (2008).

[15] Ancona, M., Kruppa, W., Rendell, R., Snow, A., Park, D., and Boos, J. *Physical Review B* **64**(3), 033408 (2001).

[16] Bezryadin, A., Dekker, C., and Schmid, G. *Applied Physics Letters* **71**(9), 1273–1275 (1997).

[17] Wheeler, W. and Dahnovsky, Y. *The Journal of chemical physics* **129**, 154112 (2008).

[18] Choi, S. H., Kim, B., and Frisbie, C. *Science* **320**(5882), 1482 (2008).

[19] Akkerman, H., Blom, P., Leeuw, D. D., and Boer, B. D. *Nature* **441**(7089), 69–72 (2006).

[20] Karthäuser, S. *Journal of Physics: Condensed Matter* **23**, 013001 (2011).

[21] Ferrara, V. L., Alfano, B., Fiorentino, G., Polichetti, T., Massera, E., and Francia, G. D. *Microelectronic engineering* **Article in press** (2011).

[22] Moore, J. *Current Opinion in Solid State and Materials Science* **1**(6), 777–788 (1996).

[23] Binnig, G., Rohrer, H., Gerber, C., and Weibel, E. *Physical Review Letters* **49**(1), 57–61 (1982).

[24] Binnig, G., Rohrer, H., Gerber, C., and Weibel, E. *Physical Review Letters* **50**(2), 120–123 (1983).

[25] Bumm, L., Arnold, J., Cygan, M., Dunbar, T., Burgin, T., Jones, L., Allara, D., Tour, J., and Weiss, P. *Science* **271**(5256), 1705 (1996).

[26] Reed, M., Zhou, C., Muller, C., Burgin, T., and Tour, J. *Science* **278**(5336), 252 (1997).

[27] Reichert, J., Ochs, R., Beckmann, D., Weber, H., Mayor, M., and Löhneysen, H. *Physical Review Letters* **88**(17), 176804 (2002).

[28] Zhou, C., Deshpande, M., Reed, M., Ii, L. J., and Tour, J. *Appl. Phys. Lett.* **71**, 611 (1997).

[29] Morpurgo, A., Marcus, C., and Robinson, D. *Applied Physics Letters* **74**, 2084 (1999).

[30] Li, C., He, H., and Tao, N. *Applied Physics Letters* **77**, 3995 (2000).

[31] Meszaros, G., Kronholz, S., Karthäuser, S., Mayer, D., and Wandlowski, T. *Applied Physics A: Materials Science & Processing* **87**(3), 569–575 (2007).

[32] Park, H., Lim, A., Alivisatos, A., Park, J., and McEuen, P. *Applied Physics Letters* **75**, 301 (1999).

[33] Strachan, D., Smith, D., Johnston, D., Park, T., Therien, M., Bonnell, D., and

Johnson, A. *Applied Physics Letters* **86**, 043109 (2005).

[34] Moth-Poulsen, K. and Bjørnholm, T. *Nature nanotechnology* **4**(9), 551–556 (2009).

[35] Wang, G., Yoo, H., Na, S., Kim, T., Cho, B., Kim, D., and Lee, T. *Thin Solid Films* **518**(2), 824–828 (2009).

[36] Wang, W., Lee, T., and Reed, M. A. *Physical Review B* **68**(3), 1–7 Jul (2003).

[37] Nakanishi, H., Bishop, K., Kowalczyk, B., Nitzan, A., Weiss, E., Tretiakov, K., Apodaca, M., Klajn, R., Stoddart, J., and Grzybowski, B. *Nature* **460**(7253), 371–375 (2009).

[38] Bernard, L., Kamdzhilov, Y., Calame, M., van der Molen, S., Liao, J., and Schönenberger, C. *The Journal of Physical Chemistry C* **111**(50), 18445–18450 (2007).

[39] Beverly, K., Sampaio, J., and Heath, J. *J. Phys. Chem. B* **106**(9), 2131–2135 (2002).

[40] Müller, K., Herrmann, J., Wei, G., Raguse, B., and Wieczorek, L. *The Journal of Physical Chemistry C* **113**(42), 18027–18031 (2009).

[41] Martin, S., Haiss, W., Higgins, S., and Nichols, R. *Nano letters* **10**(6), 2019–2023 (2010).

[42] Sutanto, J., Smith, R., and Collins, S. *J. Micromech. Microeng.* **20**, 045016 (2010).

[43] Jafri, S., Blom, T., Wallner, A., Welch, K., Stromme, M., Ottosson, H., and Leifer, K. *Microelectronic engineering* **88**, 2629–2631 (2010).

[44] Kuemmeth, F., Bolotin, K., Shi, S., and Ralph, D. *Nano letters* **8**(12), 4506–4512 (2008).

[45] Klein, D., McEuen, P., Katari, J., Roth, R., and Alivisatos, A. *Applied Physics Letters* **68**, 2574 (1996).

[46] Kervennic, Y., der Zant, H. V., Morpurgo, A., Gurevich, L., and Kouwenhoven, L. *Applied Physics Letters* **80**, 321 (2002).

[47] Krahne, R., Dadosh, T., Gordin, Y., Yacoby, A., Shtrikman, H., Mahalu, D., Sperling, J., and Bar-Joseph, I. *Physica E: Low-dimensional Systems and Nanostructures* **17**, 498–502 (2003).

[48] Akkerman, H. B. and Boer, B. D. *Journal of Physics: Condensed Matter* **20**(1), 013001 Dec (2007).

[49] Guldi, D., Illescas, B., Atienza, C., Wielopolski, M., and Martín, N. *Chemical Society Reviews* **38**(6), 1587–1597 (2009).

[50] Martin, C., Ding, D., Sørensen, J., Bjørnholm, T., van Ruitenbeek, J., and van der Zant, H. *Journal of the American Chemical Society* **130**(40), 13198–13199 (2008).

[51] Sridharan, D., Waks, E., Solomon, G., and Fourkas, J. *Applied Physics Letters* **96**, 153303 (2010).

[52] Kinashi, K., Harada, Y., and Ueda, Y. *Thin Solid Films* **516**(9), 2532–2536 (2008).

[53] Fragouli, D., Persano, L., Paladini, G., Pisignano, D., Carzino, R., Pignatelli, F., Cingolani, R., and Athanassiou, A. *Advanced Functional Materials* **18**(11), 1617–1623 (2008).

[54] Chen, Q., Feng, Y., Zhang, D., Zhang, G., Fan, Q., Sun, S., and Zhu, D. *Advanced Functional Materials* **20**(1), 36–42 (2010).

[55] Katz, E., Lion-Dagan, M., and Willner, I. *Journal of Electroanalytical Chemistry* **382**(1-2), 25–31 (1995).

[56] Hobley, J., Oori, T., Kajimoto, S., Gorelik, S., Hönig, D., Hatanaka, K., and Fukumura, H. *Applied Physics A: Materials Science & Processing* **93**(4), 947–954 (2008).

[57] Pluntke, Y., Kibler, L., and Kolb, D. *Phys. Chem. Chem. Phys.* **10**(25), 3684–3688 (2008).

[58] Favier, F., Walter, E., Zach, M., Benter, T., and Penner, R. *Science* **293**(5538), 2227 (2001).

[59] Vilan, A. *The Journal of Physical Chemistry C* **111**(11), 4431–4444 (2007).

[60] Kornyshev, A., Kuznetsov, A., and Ulstrup, J. *PNAS* **103**(18), 6799–6804 (2006).

[61] Wuelfing, W., Green, S., Pietron, J., Cliffel, D., and Murray, R. *Journal of the American Chemical Society* **122**(46), 11465–11472 (2000).

[62] Markussen, T., Chen, J., and Thygesen, K. *Physical Review B* **83**(15), 155407 (2011).

[63] Tomfohr, J. and Sankey, O. *Physical Review B* **65**(24), 245105 (2002).

[64] Beebe, J. M., Kim, B., Frisbie, C. D., and Kushmerick, J. G. *ACSNano* **2**(5), 827–832 (2008).

[65] Huisman, E., Guédon, C., van Wees, B., and van der Molen, S. *Nano letters* **9**(11), 3909–3913 (2009).

[66] Fowler, R. and Nordheim, L. *Proceedings of the Royal Society of London. Series A, Containing Papers of a Mathematical and Physical Character* **119**(781), 173–181 (1928).

[67] Kim, B., Beebe, J., Jun, Y., Zhu, X., and Frisbie, C. *Journal of the American Chemical Society* **128**(15), 4970–4971 (2006).

[68] Yoneya, N., Noda, M., Hirai, N., Nomoto, K., Wada, M., and Kasahara, J. *Applied Physics Letters* **85**, 4663 (2004).

[69] Engelkes, V., Beebe, J., and Frisbie, C. *Journal of the American Chemical Society* **126**(43), 14287–14296 (2004).

[70] Guisinger, N., Yoder, N., and Hersam, M. *P Natl Acad Sci Usa* **102**(25), 8838 (2005).

[71] Akiyama, R., Matsumoto, T., and Kawai, T. *Physical Review B* **62**(3), 2034 (2000).

[72] Sabatani, E., Cohen-Boulakia, J., Bruening, M., and Rubinstein, I. *Langmuir* **9**(11), 2974–2981 (1993).

[73] Lüssem, B., Müller-Meskamp, L., Karthäuser, S., Homberger, M., Simon, U., and Waser, R. *The Journal of Physical Chemistry C* **111**(17), 6392–6397 (2007).

[74] Krzeminski, C., Delerue, C., Allan, G., Vuillaume, D., and Metzger, R. *Physical Review B* **64**(8), 085405 (2001).

[75] Lafferentz, L., Ample, F., Yu, H., Hecht, S., Joachim, C., and Grill, L. *Science* **323**(5918), 1193 (2009).

[76] Beebe, J., Kim, B., Gadzuk, J., Frisbie, C. D., and Kushmerick, J. *Physical Review Letters* **97**(2), 026801 Jul (2006).

[77] Crispin, X., Geskin, V., Crispin, A., Cornil, J., Lazzaroni, R., Salaneck, W., and Brédas, J. *Journal of the American Chemical Society* **124**(27), 8131–8141 (2002).

[78] Hoft, R., Ford, M., and Cortie, M. *Nanoscience and Nanotechnology, 2006. ICONN '06. International Conference on* (2006).

[79] Yuri, A., Hutchison, G., Rempala, P., Ratner, M., and Michl, J. *The Journal of Physical Chemistry A* **107**(19), 3970–3980 (2003).

[80] Trudeau, P., Escorcia, A., and Dhirani, A. *The Journal of Chemical Physics* **119**, 5267 (2003).

[81] Beverly, K., Sample, J., Sampaio, J., Remacle, F., Heath, J., and Levine, R. *Proceedings of the National Academy of Sciences* **99**(90002), 6456–6459 (2002).

[82] Korotkov, A. and Nazarov, Y. *Physica B: Condensed Matter* **173**(3), 217–222 (1991). test.

[83] Arrhenius, S. *Zeitschrift für physikalische Chemie* Jan (1889).

[84] Shklovskiĭ. . . , B. *Soviet Physics Uspekhi* **117**, 401–435 Jan (1975).

[85] Jain, S., Radhakrishna, S., of Scientific Unions Committee on Science, I. C., in Developing Countries, T., and of Technology (Madras, I. I. I. *Physics of semiconductor devices: proceedings of the Third International Workshop, Madras, India, November 27-December 2, 1985.* (1985).

[86] Abeles, B., Sheng, P., and Coutts, M. *Advances in Physics* **24**(3), 407–461 Jan (1975).

[87] Marcus, R. *The Journal of chemical physics* **24**, 966–978 Jan (1956).

[88] Wasshuber, C. *Springer* , 278 Jan (2001).

[89] Hanna, A. and Tinkham, M. *Physical Review B* **44**(11), 5919 (1991).

[90] Hanna, A., Tuominen, M., and Tinkham, M. *Phys. Rev. Lett.* **68**(21), 3228–3231 (1992).

[91] Zeng, N. and Murphy, A. *Nanotechnology* **20**, 375702 (2009).

[92] Landis, S. *Nano-lithography.* Number John Wiley & Sons, London. (2011).

[93] Naulleau, P. *SPIE Newsroom* , 10.1117 (2009).

[94] Hughey, L., Williams, R., Rife, J., Nagel, D., and Peckerar, M. *Nuclear Instruments and Methods in Physics Research* **195**(1-2), 267–271 (1982).

[95] Lu, B.-R., Chen, Y., Huq, E., Qu, X.-P., and Liu, R. *J. Nanosci. Nanotech.* **10**(11), 7130–7133 Nov (2010).

[96] Chen, J., Krecinic, F., Chen, J.-H., Chen, R., and Lin, B. *Design Automation Conference (ASP-DAC), 2011 16th Asia and South Pacific* , 403 – 404 (2011).

[97] Yasutake, Y., Kono, K., Kanehara, M., Teranishi, T., Buitelaar, M. R., Smith, C. G., and Majima, Y. *Appl. Phys. Lett.* **91**(20), 203107 Jan (2007).

[98] Steinmann, P. and Weaver, J. M. R. *J. Vac. Sci. Technol. B* **22**(6), 3178 Jan (2004).

[99] Liang, X. and Chou, S. *Nano letters* **8**(5), 1472–1476 (2008).

[100] Fischbein, M. and Drndic, M. *Nano letters* **7**(5), 1329–1337 (2007).

[101] Sidorkin, V., van Run, A., van Langen-Suurling, A., Grigorescu, A., and van der Drift, E. *Microelectronic engineering* **85**(5-6), 805–809 (2008).

[102] Yasin, S., Hasko, D., and Ahmed, H. *Microelectronic engineering* **61**, 745–753 (2002).

[103] Manakli, S., Docherty, K., Pain, L., Todeschini, J., Jurdit, M., Icard, B., Leseuil, S., and Minghetti, B. *Microprocesses and Nanotechnology Conference, 2005 International* , 242 (2005).

[104] Ocola, L. *J. Vac. Sci. Technol. B* **27**, 2569 (2009).

[105] Pohl, H. *Dielectrophoresis: the behavior of neutral matter in nonuniform electric fields*. (1978).

[106] Barsotti, R., Vahey, M., Wartena, R., Chiang, Y.-M., Voldman, J., and Stellacci, F. *Small* **3**(3), 488–499 (2007).

[107] Gierhart, B., Howitt, D., Chen, S., Smith, R., and Collins, S. *Langmuir* **23**(24), 12450–12456 (2007).

[108] Bernard, L., Calame, M., Molen, S. V. D., Liao, J., and Schönenberger, C. *Nanotechnology* **18**, 235202 (2007).

[109] Boccaccini, A., Roether, J., Thomas, B., Shaffer, M., Chavez, E., Stoll, E., and Minay, E. *Nippon Seramikkusu Kyokai Gakujutsu Ronbunshi(Journal of the Ceramic Society of Japan)* **114**(1), 1–14 (2006).

[110] Templeton, A., Wuelfing, W., and Murray, R. *Accounts of Chemical Research* **33**(1), 27–36 (2000).

[111] Manheller. *Nanotechnology (IEEE-NANO), 2010 10th IEEE Conference on* , 919 – 923 (2010).

[112] Habib, A. and Tabata, M. *Bulletin of the Chemical Society of Japan* **78**, 262–269 Jan (2005).

[113] Xie, J., Lee, J., and Wang, D. *Chemistry of materials* **19**(11), 2823–2830 (2007).

[114] Blech, K. *RWTH Aachen University, inorganic chemistry* , Dissertation Jan (2012).

[115] Barnard, A., Young, N., Kirkland, A., van Huis, M., and Xu, H. *ACS nano* **3**(6), 1431–1436 (2009).

[116] Kimura, K. *Phys Chem Chem Phys* **11**(41), 9346–9350 (2009).

[117] Wessels, J., Nothofer, H., Ford, W., von Wrochem, F., Scholz, F., Vossmeyer, T., Schroedter, A., Weller, H., and Yasuda, A. *Journal of the American Chemical Society* **126**(10), 3349–3356 (2004).

[118] Beverly, K., Sample, J., Sampaio, J., Remacle, F., Heath, J., and Levine, R. *P Natl Acad Sci Usa* **99**(Suppl 2), 6456 (2002).

[119] Song, H., Kim, Y., Jang, Y., Jeong, H., Reed, M., and Lee, T. *Nature* **462**(7276), 1039–1043 (2009).

[120] Rong, H., Frey, S., Yang, Y., Zharnikov, M., Buck, M., Wühn, M., Wöll, C., and Helmchen, G. *Langmuir* **17**(5), 1582–1593 (2001).

[121] Akkerman, H. and de Boer, B. *Journal of Physics: Condensed Matter* **20**, 013001 (2008).

[122] Chen, J., Markussen, T., and Thygesen, K. *Physical Review B* **82**(12), 121412 (2010).

[123] Søndergaard, T. and Bozhevolnyi, S. *Physical Review B* **75**(7), 073402 (2007).

[124] Søndergaard, T., Jung, J., Bozhevolnyi, S., and Valle, G. D. *New Journal of Physics* **10**, 105008 (2008).

[125] Abe, S. and Kajikawa, K. *Physical Review B* **74**(3), 035416 (2006).

[126] Shirota, Y. and Kageyama, H. *Chemical reviews* **107**(4), 953–1010 (2007).

[127] Andres, R., Bein, T., Dorogi, M., Feng, S., Henderson, J., Kubiak, C., Mahoney, W., Osifchin, R., and Reifenberger, R. *Science* **272**(5266), 1323 (1996).

[128] Park, K., Ha, J., Yun, W., Shin, M., and Park..., K. *Applied physics ...* **71**(11), 1469–1471 Jan (1997).

[129] Likharev, K. *Proceedings of the IEEE* **87**(4), 606–632 (1999).

[130] Trudeau, P., Orozco, A., Kwan, E., and Dhirani, A. *The Journal of Chemical Physics* Jan (2002).

[131] Ohgi, T., Sakotsubo, Y., Fujita, D., and Ootuka, Y. *Surface Science* **566**, 402–405 (2004).

[132] Imae, T. and Torii, H. *The Journal of Physical Chemistry B* **104**, 9218–9224 Jan (2000).

[133] Zou, X., Bao, H., Guo, H., Zhang, L., Qi, L., Jiang, J., Niu, L., and Dong, S. *Journal of colloid and interface science* **295**(2), 401–408 (2006).

[134] Donten, M., Krolikowska, A., and Bukowska, J. *Phys. Chem. Chem. Phys.* **11**, 3390–3400 Jan (2009).

[135] Kudelski, A. *Langmuir* **18**(12), 4741–4747 (2002).

[136] Soltow, A. *Dissertation* Jan (2013).

[137] Morales, A., Mora, E., and Pal, U. *Revista Mexicana de Fisica S* **53**(5), 18 (2007).

[138] Jiménez-Becerril, J. and Solache-Rios, M. *Microporous and Mesoporous Materials* **69**, 109–118 Jan (2004).

[139] Freire, J. and Tonerzer, C. *The Journal of chemical physics* **130**, 134901 Jan (2009).

[140] Barone, V. and Polimeno, A. *Chem. Soc. Rev.* **36**, 1724–1731 Jan (2007).

[141] Ooi, Y., Hobara, D., Yamamoto, M., and Kakiuchi, T. *Langmuir* **21**, 11185–11189 Jan (2005).

[142] Lespagnard, T. *Dissertation: theory electronic levels.* (2013).

[143] Ganesan, R. *Dissertation: theory.* (2013).

[144] Schulze, K. *Dissertation: STM.* (2013).

[145] Søndergaard, T., Beermann, J., Boltasseva, A., and Bozhevolnyi, S. *Physical Review B* **77**(11), 115420 (2008).

[146] Smith, K. *Computers, IEEE Transactions on* **100**(9), 619–634 (1981).

[147] Patel, V. and Gurumurthy, K. *Advances in Computing, Control, & Telecommunication Technologies, 2009. ACT'09. International Conference on* , 752–755 (2009).

[148] Klein, M., Mol, J., Verduijn, J., Lansbergen, G., Rogge, S., Levine, R., and Remacle, F. *Applied Physics Letters* **96**, 043107 (2010).

[149] Raychowdhury, A. and Roy, K. *Nanotechnology, IEEE Transactions on* **4**(2), 168–179 (2005).

[150] Lin, S., Kim, Y., and Lombardi, F. *Circuits and Systems, 2009. MWSCAS'09. 52nd IEEE International Midwest Symposium on* , 435–438 (2009).

[151] Untiedt, C., Yanson, A., Grande, R., Rubio-Bollinger, G., Agrait, N., Vieera, S., and van Ruitenbeek, J. *Physical Review B* **66**(085418) Jan (2002).

[152] Pauly, C., Grob, M., Pezzotta, M., Pratzer, M., and Morgenstern, M. *Physical Review B* **81**(12), 125446 (2010).

[153] Meskamp, L. M., Karthäuser, S., Zandvliet, H., Homberger, M., Simon, U., and Waser, R. *Small* **5**(4), 496–502 (2009).

[154] Gundlach, K. *Solid-State Electronics* **9**(10), 949–957 (1966).

[155] Coombs, J. H. and Gimzewski, J. K. *Journal of Microscopy* **152**(3), 841–851 (1988).

[156] Klein, M., Lansbergen, G. P., Mol, J. A., Rogge, S., Levine, R. D., and Remacle, F. *ChemPhysChem* **10**(1), 162–173 Jan (2009).

[157] Cervera, J. and Mafe, S. *ChemPhysChem* **11**, 1654–1658 Jan (2010).

[158] Navi, K., Foroutan, V., Mazloomnejad, B., Bahrololoumi, S., Hashemipour, O., and Haghparast, M. *World Applied Sciences Journal* **4**(1), 142–149 (2008).

[159] Zandvliet, H. and van Houselt, A. *Annual Review of Analytical Chemistry* **2**, 37–55 (2009).

[160] Chang, H., Wu, B., Yao, Y., Su, W., and Chang, C. *J. Nanosci. Nanotech.* **10**(7), 4663–4666 (2010).

[161] Lin, C., Lu, S., Su, W., Shih, H., Wu, B., Yao, Y., Chang, C., and Tsong, T. *Physical Review Letters* **99**(21), 216103 (2007).

A. Investigation of BP3-capped NP by Kerstin Blech

A.1. DSC Analysis using: UV/Vis, TEM, SAXS

The synthesized gold nanoparticles were characterized by UV/Vis spectroscopy, TEM analysis, small angle X-ray scattering (SAXS) in solution and from solid 3D films, dynamic light scattering (DLS) and differential scanning calorimetry (DSC). The results are presented in the following sections.

UV/Vis

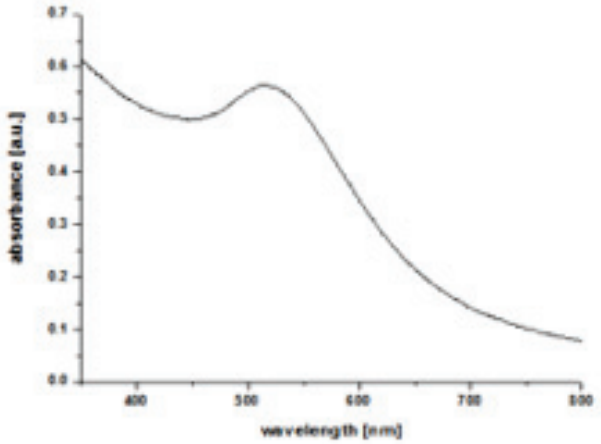

Figure .1.: The UV/Vis spectra shows an absorbance maximum at 521 nm, which is characteristic for Au nanoparticles in this size range.

The TEM analysis of BP3 capped NPs displays almost spherical nanoparticles with a mean diameter of 4.1±0.5 nm. The determined mean interparticle spacing of 1.4±0.4 nm has the same length as the BP3 molecule (1.39 nm), which can be explained by an interdigitating of the ligand shells, as described in [ACS nano]. Complex impedance measurements were performed on IDE structures (interdigitated electrode structures) on which the cluster solution was drop-casted to form a densely packed film. In these

Distribution of interparticle spacing derived from TEM analysis

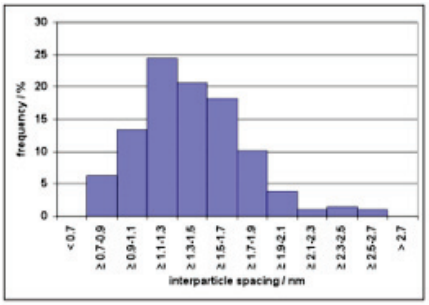

Figure .2.: A mean interparticle spacing of 1.4 ± 0.4 nm could be calculated from 209 measured interparticle distances from TEM analysis.

SAXS

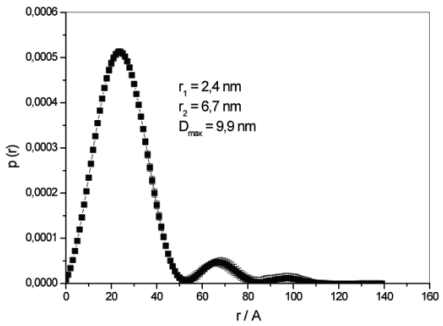

Figure .3.: The small angle X-ray scattering experiment shows in the distance distribution function curve one significant maximum at a radius of 2.4 nm for the Au nanoparticles. Besides another maximum at r = 6.7 nm is noticeable. This second maximum can be explained by strong $\pi - \pi$-interactions between BP3 molecules of neighboring particles caused by a high nanoparticle concentration in the capillary tube. Additionally SAXS measurements of films of BP3 stabilized Au NP were performed. A surface-to-surface distance of 0.6 nm could be calculated from the structure-factor peak in the scattering curve.

DLS: $R_H = 3.2\,\text{nm}$ (mean value)
30°> 2.85 nm 60°> 2.81 nm
40°> 3.31 nm 90°> 3.72 nm

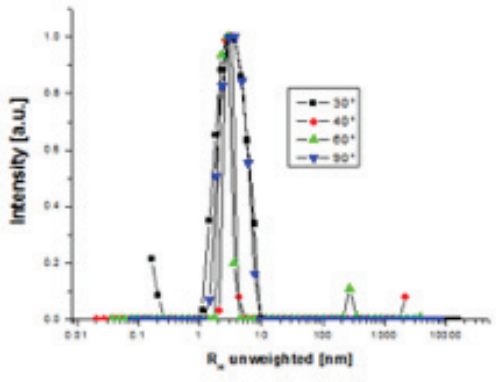

Figure .4.: From DLS measurements at four different angles a mean hydrodynamic radius of 3.2 nm could be obtained.

measurements the complex impedance was recorded as a function of frequency (1 MHz - 10 mHz) and temperature (340 K - 10 K) at a constant voltage of 100 mV.

DSC measurement of BP3-stabilized AuNPs

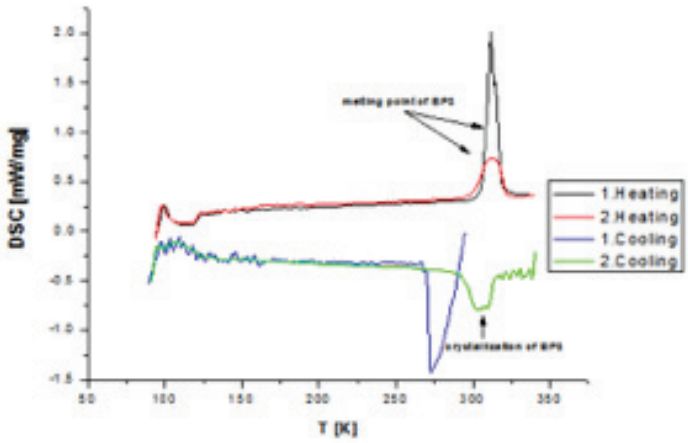

Figure .5.: The DSC measurements of the free ligand shows at 311K a sharp peak in the first heating curve, which is caused by the melting of the BP3 molecules. In the second heating curve this peak is broader and can be explained by a possible partially destruction of the molecules during the heating process upon 330K. In the cooling curve a broad peak at 305K could be identified as crystallization process of BP3. In comparison to the DSC measurements of the AuNP-BP3-system the curves show no endothermal processes in the temperature range in which the atypical behavior could be observed.

A.2. Impedance spectroscopy measurement

An atypical behavior expressed by a peak in the Arrhenius curve appeared in the temperature range 230K-290K of the Arrhenius plot (Figure 2) of the BP3-stabilized AuNPs. In order to further scrutinize this unexpected finding we performed DSC measurements, which reveal in the low temperature range the glass transition and melting point of toluene, which was used as solvent for the Au nanoparticles, and an additional endothermal process. This endothermal process appears in the same temperature range, where the peak in the thermally activated conductivity was found.

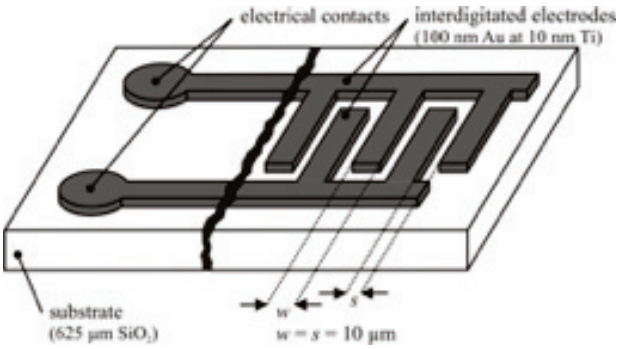

Figure .6.: Schematic illustration of the Interdigitated Electrode (IDE) structure used for impedance measurements. The 100 nm thick gold electrodes have a separation of 10 μm.

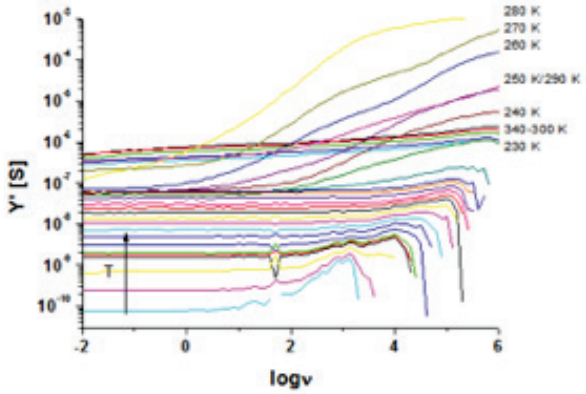

Figure .7.: The admittance spectra show nearly over the whole frequency range a frequency independent conductance except for temperatures between 220K-280K. This DC conductance, extrapolated to log ?->0, is increasing with increasing temperature according to a temperature dependent conductivity in this system. In the temperature range between 230K-280K the conductivity becomes frequent-dependent, which can be explained by a change in the nanoparticle network and accordingly by a change in the nanoparticle morphologics.

B. Influence of light on the sample-temperature

A test device (50% Nb capped SiO_2) was cooled below the transition temperature $T_C = 9.2\,\mathrm{K}$ where Nb becomes superconducting. The critical current in a superconductor represents the maximum current that a superconductor can carry. Also note that, as the current flowing through a superconductor increases, the transition temperature T_c will usually decrease.

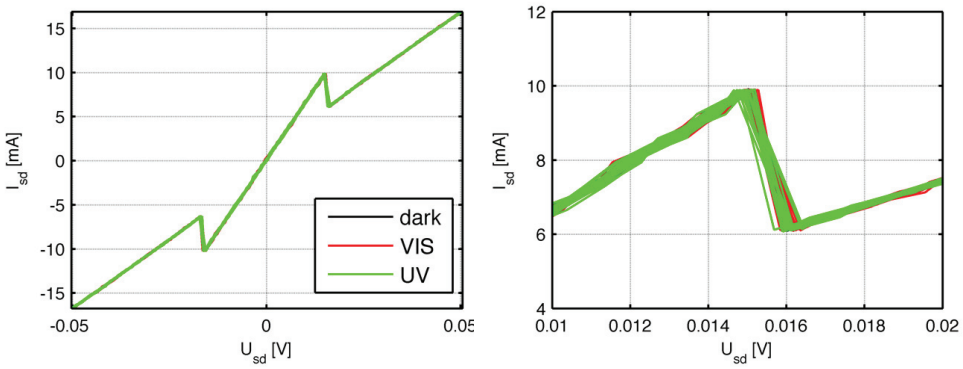

Figure .8.: The critical current of the Nb film at 4.2 K is shown to be $\sim 10\,\mathrm{mA}$. This value did not change under illumination of visible light (Bandwidth 495 nm - 1200 nm), UV light (Bandwidth 200 nm - 1200 nm) and in the dark.

1. **Ferrocenes as Potential Building Blocks for Molecular Electronics**
   Self-Assembly and Tunneling Spectroscopy
   by L. Müller-Meskamp (2008), 153 pages
   ISBN: 978-3-89336-509-8

2. **Magnetic Proximity Effects in Highly-ordered Transition Metal Oxide Heterosystems studied by Soft x-Ray Photoemission Electron Microscopy**
   by I. P. Krug (2008), XX, 180 pages
   ISBN: 978-3-89336-521-0

3. **Seltenerd-basierte ternäre Oxide als alternative Gatedielektrika**
   von J. M. Roeckerath (2008), 148 Seiten
   ISBN: 978-3-89336-543-2

4. **Strominduzierte Magnetisierungsdynamik in einkristallinen Nanosäulen**
   von R. Lehndorff (2009), I, 86 Seiten
   ISBN: 978-3-89336-564-7

5. **Magnetization Dynamics in Magnetically Coupled Heterostructures**
   von A. Kaiser (2009), X, 121 pages
   ISBN: 978-3-89336-577-7

6. **Resistive switching in Pt/TiO_2/PT**
   by D. S. Jeong (2009), vii, 133 pages
   ISBN: 978-3-89336-579-1

7. **Electromechanical Force Microscopy and Tip-Enhanced Raman Spectroscopy for Polar Oxide Nanoparticles**
   by S. Röhrig (2009), vi, 114 pages
   ISBN: 978-3-89336-600-2

8. **Investigation of resistive switching in barium strontium titanate thin films for memory applications**
   by W. Shen (2010), 114 pages
   ISBN: 978-3-89336-608-8

9. **Nanostrukturierte Metallelektroden zur funktionalen Kopplung an neuronale Zellen**
   von D. Brüggemann (2010), vii, 160 Seiten
   ISBN: 978-3-89336-627-9

10. **Integration of resistive switching devices in crossbar structures**
    by Chr. Nauenheim (2010), XII, 142 pages
    ISBN: 978-3-89336-636-1

11. **Correlation between Raman spectroscopy and electron microscopy on individual carbon nanotubes and peapods**
by C. Spudat (2010). xiv, 125 pages
ISBN: 978-3-89336-648-4

12. **DC and RF Characterization of NiSi Schottky Barrier MOSFETs with Dopant Segregation**
by C. J. Urban (2010), iv, 151 pages
ISBN: 978-3-89336-644-6

13. **Alternative Systems for Molecular Electronics: Functionalized Carboxylic Acids on Structured Surfaces**
by M. C. Lennartz (2010), 183 pages
ISBN: 978-3-89336-667-5

14. **Highly conductive electrodes as diffusion barrier for high temperature applications**
by B. Mešić (2010), VII, 138 pages
ISBN: 978-3-89336-670-5

15. **Modeling, Fabrication and Characterization of Silicon Tunnel Field-Effect Transistors**
by C. P. Sandow (2010), XIII, 112 pages
ISBN: 978-3-89336-675-0

16. **Substituted Coronenes for Molecular Electronics: From Supramolecular Structures to Single Molecules**
by P. Kowalzik (2010), ix, 149 pages
ISBN: 978-3-89336-679-8

17. **Resistive switching in TiO2 thin films**
by L. Yang (2011), VII, 117 pages
ISBN: 978-3-89336-707-8

18. **Crystal- and Defect-Chemistry of Fine Grained Thermistor Ceramics on $BaTiO_3$ Basis with BaO-Excess**
by H. Katsu (2011), xxvii, 163 pages
ISBN: 978-3-89336-741-2

19. **Flächenkontakte zu molekularen Schichten in der Bioelektronik**
von N. Sanetra (2012), XIII, 129 Seiten
ISBN: 978-3-89336-776-4

20. **Stacked device structures for resistive memory and logic**
by R. D. Rosezin (2012), 137 pages
ISBN: 978-3-89336-777-1

21. **Optical and electrical addressing in molecule-based logic circuits**
by M. Manheller (2012), XIV, 183 pages
ISBN: 978-3-89336-810-5

Information / Information
Band / Volume 21
ISBN 978-3-89336-810-5

JÜLICH
FORSCHUNGSZENTRUM